EMERGING CLASSES OF SMART MATERIALS:

ORGANIC SINGLE CRYSTALS TO BIOLOGICAL NANO PARTICLES

by

Madushani Dharmarwardana

APPROVED BY SUPERVISORY COMMITTEE:

Dr. Jeremiah J. Gassensmith, Chair

Dr. Yves J. Chabal

Dr. John W. Sibert

Dr. Ronald A. Smaldone

To my loving mother, father and brother.

EMERGING CLASSES OF SMART MATERIALS:

ORGANIC SINGLE CRYSTALS TO BIOLOGICAL NANO PARTICLES

by

MADUSHANI DHARMARWARDANA, BS

DISSERTATION

Presented to the Faculty of

The University of Texas at Dallas

in Partial Fulfillment

of the Requirements

for the Degree of

DOCTOR OF PHILOSOPHY IN

CHEMISTRY

THE UNIVERSITY OF TEXAS AT DALLAS

August 2018

ACKNOWLEDGMENTS

EMERGING CLASSES OF SMART MATERIALS:

ORGANIC SINGLE CRYSTALS TO BIOLOGICAL NANO PARTICLES

Madushani Dharmarwardana, PhD
The University of Texas at Dallas, 2018

Supervising Professor: Jeremiah J. Gassensmith

Stimuli responsive materials, also known as "smart" materials, are capable of altering their properties in a controllable fashion in response to external stimuli. While most reported smart materials are based on synthetic polymeric systems, there exists a need to develop a novel class of smart materials with properties better suited for commercial settings. In this dissertation, we investigate two emerging classes of smart materials—organic single crystals and viral nanoparticles. First, we report novel class of thermo-responsive single crystalline compounds known as naphthalene diimides (NDIs). The single crystalline butoxyphenyl N-substituted NDI (BNDI), a derivative of NDI, exhibits thermo-mechanical and thermochromic behavior. The monoclinic phase of BNDI can be thermally transformed to its triclinic polymorph and the stress accumulated due to this phase transition can be released in the form of mechanical energy. In fact, we demonstrated that the energy associated with this phase transition could be utilized to lift a metal ball ~100 times heavier than the single crystal itself. Furthermore, BNDI exhibits colossal anisotropic thermal expansion with highest positive expansion coefficient reported for an organic compound so far.

Next, we investigated the thermochromic and thermo-salient behavior of alkoxyphenyl N-substituted NDI (ANDIs). It was clear that the thermo-salient behavior of ANDIs can be tuned by changing the alkyl substituents over a wide range of temperatures. Thermochromic ANDIs can be incorporated to commercially available polymers and we show that ANDI polymer composites also exhibit reversible thermochromism. The reasoning behind thermochromism in BNDI was further investigated using both experimental data and computational simulations.

The developments in nanotechnology have also produced smart materials that can respond to external stimuli in a controllable fashion. Viral nanoparticles—particularly symmetrical, polyvalent biological macromolecules are very attractive in nanomaterial-based research. Among viral nanoparticles, tobacco mosaic virus (TMV) is one of the most extensively-studied plant viruses, particularly known for its rod-shaped structure and stability in extreme conditions. Herein, we report proton relaxation properties and redox responsiveness of organic radical contrast agents (ORCAs) conjugated to TMV nano-particles. The ORCA-TMV particles show enhanced T_1 contrast at low fields and T_2 contrast at high fields compare to ORCA small molecules. Furthermore, we created a quenchless bimodal probe for fluorescence/MR imaging by conjugating a fluorescence dye to the interior and ORCAs to the exterior surfaces of TMV. We have also shown that the reduced from of ORCA-TMV can respond to enzymatically produced superoxides.

Biomimetic mineralization is another promising area of research as this process can significantly increase the stability of biological macromolecules such as enzymes, proteins, and viral nanoparticles. Previous reports show that TMV can act as a template for ZIF-8 growth, resulting in core shell bio nanoparticles (CSBNs). Finally, we investigate the responsiveness for biomimetics mineralization by TMV when its surface is modified with charged molecules. The

formation of CSBN was not prevented by the surface charge of the viral nano particle. However, we show that higher loading of positive charge on the surface of TMV will reduce the encapsulation efficiency of biomimetics mineralization process.

TABLE OF CONTENTS

LIST OF FIGURES

LIST OF TABLES

CHAPTER 1

INTRODUCTION

1.1 Introduction to smart materials

Recent advances in science are enabling scientists to design novel high-tech materials with predictable and controllable properties. These materials, also called smart materials or stimuli responsive materials (SRMs), can alter their properties in response to external or internal stimuli and have gained much attention within the scientific community as they can be used for many applications including drug delivery, sensing,[1] artificial muscles, actuating[2, 3] and smart coatings.[4] Mother nature also provides inspiration to create novel smart materials. Mimicking natural systems, however, can be challenging as it requires periodically-responsive behavior. To overcome this challenge, numerous SRMs or smart materials have been developed and reported in literature, the majority of which are polymeric systems.[4-8]

1.2 Thermo-responsive materials

Three main types of external stimuli have been identified—physical, chemical, and biological.[5] Physical stimuli such as light, temperature, and magnetism can affect the physical appearance of such materials. In contrast, chemical stimuli such as pH, changes in ion concentration and solvent can regulate the molecular interactions. Biological stimuli such as receptors and enzymes are more likely to impact the molecular functioning in the bulk material. Among the above-mentioned stimuli, temperature is the most extensively studied and well-understood type of trigger.[3] Thermo-responsive materials can change their physical or chemical properties when exposed to temperature changes. They are used in a wide range of applications such as drug delivery, artificial

muscles, and tissue engineering.[9] Thermo-responsive polymers have gained attention due to their favorable elastic properties, ease of fabrication, and high degree of reversibility.[9, 10] However, molecular single crystals are highly advantageous relative to polymeric systems as they can transform energy very rapidly due to their highly-ordered periodic structure.[10] Upon exposure to the heat, some crystals can exhibit a variety of responses including motion (thermo-mechanical), color changes (thermochromic), and size changes (colossal expansions).

1.2.1 Thermo-mechanically responsive molecular crystals
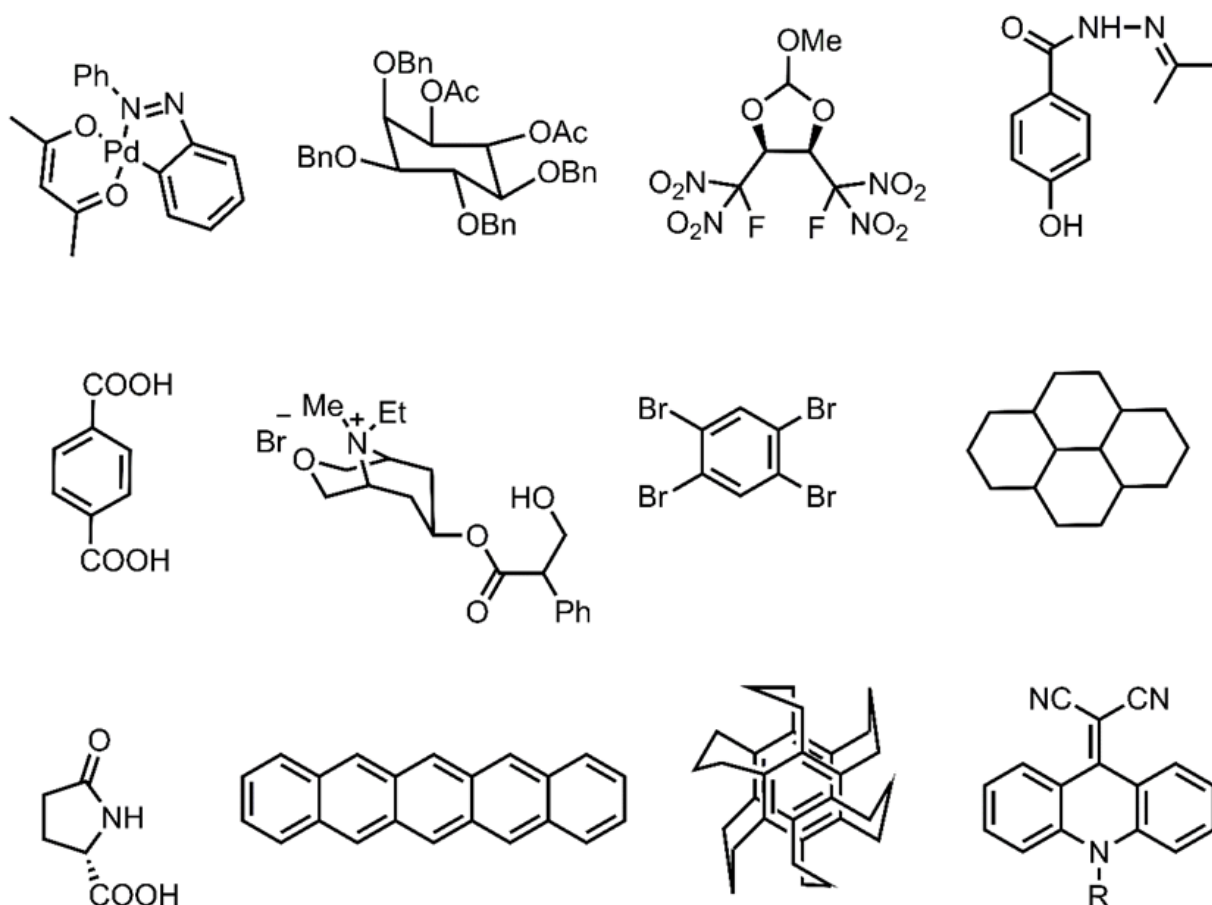
Figure 1.1. Molecular structures of reported thermo-salient crystals.[11]

Thermo-mechanically responsive molecular crystals are capable exhibiting self-actuating properties upon exposure to heat. These thermally actuating single crystals can be potentially used in a broad range of applications such as artificial muscles, sensors, electromechanical devices, nano- or macro-actuators, and smart medical devices and implants.[12] Polymeric and liquid crystalline thermo-responsive self-actuating systems are common; however, very few thermo-mechanically responsive single crystals have been reported (Figure 1.1, Figure 1.2 and Table 1.1). The mechanical responses in these molecular crystals can be varied depending on the molecular structure of the compounds. Table 1.1 gives summery of quantitative and qualitative comparison of the mechanical property of the state-of-the-art materials.
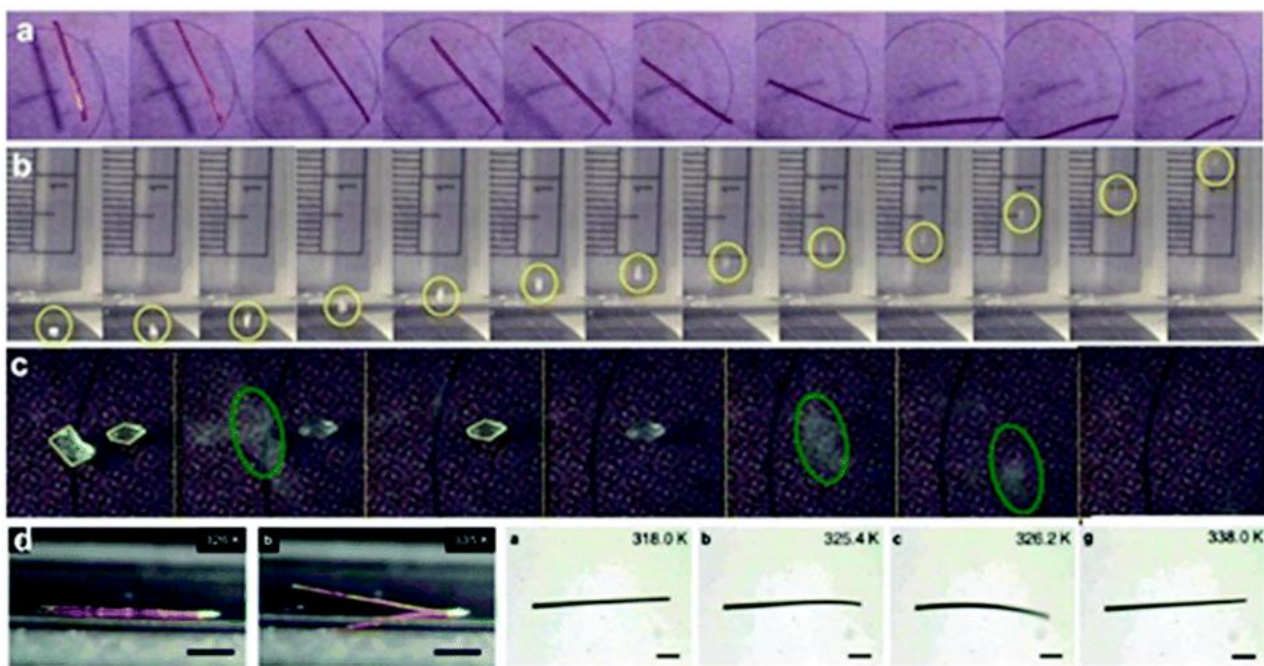
Figure 1.2. Examples of thermo-salient molecular solids. (Reprinted with permission from reference 12. Copyright 2016 The Royal Society of Chemistry).

Table 1.1. Quantitative & qualitative comparison of the mechanical property with the state-of-the-art materials.[10]

Reference	Material	Mechanical property	Reversible	Speed of the phase transition	Expansion or contraction of the unit cell parameters
10	BNDI (Organic)	Primarily bending. Also splitting, jumping,	No	Several Seconds	$a \approx -20\%$ $b \approx -75\%$ $c \approx +150\%$ Average velocity of expansion=5.435 μms^{-1}
13	Co-crystals of coronene and 1,2,4,5-tetracyanobenzene (Organic)	Self-healing behavior	Yes	Several seconds	—
14	PHBH[b] (Organic)	Thermosalient effect followed by colossal expansion	No	Few milliseconds	$a = +8.8\%$ $b = +12.3\%$ $c \approx -15\%$
15	L-pyroglutamic acid (Organic)	Thermosalient effect followed by colossal expansion	No	0.2 milliseconds	$\alpha \rightarrow \beta$ L-PGA $a = +1.58\%$ $b = -1.57\%$ $c = -0.55\%$ D-PGA $a = +1.66\%$ $b = -1.35\%$ $c = +0.57\%$
16	DCBFN[c] (Organic)	Thermosalient effect	No	Few milliseconds	$a = +5.88\%$ $b = +1.5\%$ $c = -2.5\%$
17	Amphiphiles containing tetra(ethylene glycol) moieties (Organic)	Bending	Yes	Several seconds	$a = +2.6\%$ $b = +0.68\%$ $c = -1.2\%$
18	TBB[d] (Organic)	Thermosalient effect	No	Few milliseconds	$\Delta a = -0.323$ Å $\Delta b = +0.475$ Å $\Delta c = +0.052$ Å
19	Oxitropium bromide (Organic)	Thermosalient effect	No	10^{-7} s	$a = $ — $b = 10\%$ $c = 8\%$
20	PPHA[e]	Colossal expansion and thermosalient effect (Jumping)	No	Few milliseconds	Average velocity of expansion=0.0418 ms^{-1}

[b]PHBH = N′-2-propylydene-4-hydroxybenzohydrazide

4

[c]DCBFN = 2,6-dichlorobenzylidine-4-fluoro-3-nitroanilin

[d]TBB = 1,2,4,5-tetrabromobenzene

[e]PPHA = (phenylazophenyl)palladium hexafluoroacetylacetonate

1.2.2 Thermochromic molecular crystals
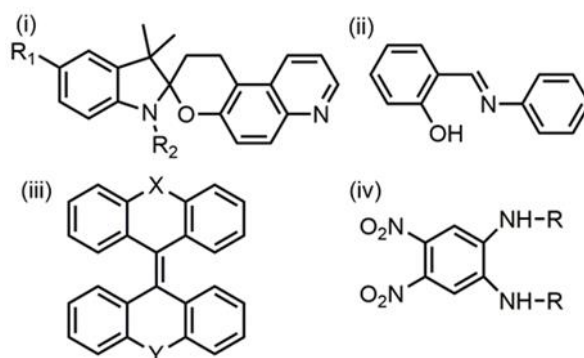
Figure 1.3. General structures of extensively studied thermochromic compounds (i) spiroheterocyclic compounds, (ii) Schiff bases, (iii) overcrowded ethylenes, and (iv) 1,3-diamino-4,6-dinitrobenzene dyes.

Thermochromism refers to reversible color changes of materials when exposed to an external heat source.[21] The mechanism responsible for thermochromism varies based on the molecular structure of a compound. Most studies have shown that thermochromism may occur due to an equilibrium between two molecular species, acid-base, keto-enol, stereoisomers or crystal structures (Figure 1.3).[22-25] However, organic compounds that show thermochromism in the solid, single crystalline state are very rare.

1.2.3 Colossal anisotropic thermal expansion

Thermal expansion in materials is another way of responding to external stimuli and can be easily identified as responsiveness at the molecular level. Positive thermal expansion (PTE) is a very common property for most materials.[26] The rate of thermal expansion (α) usually lies between $0 \times$

10^{-6} K^{-1} and 20×10^{-6} K^{-1}. In contrast, negative thermal expansion (NTE) materials—those that contract upon heating—can be used to tune the overall expansion of the system.[26] Unusually large PTE and NTE systems are very rare and are of interest. When the expansion coefficient of these materials exceeds 100×10^{-6} K^{-1}, their expansion can be described as "colossal." There are several inorganic, organo-metallic, and metal organic framework (MOF) systems that exhibit colossal thermal expansion;[26, 27] however, very few organic single crystals have been reported to exhibit this property.
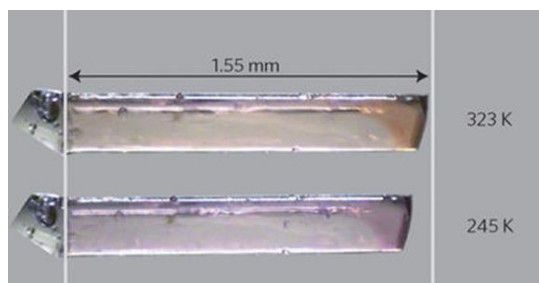
Figure 1.4. Anisotropic thermal expansion of (S,S)-octa-3,5-diyn-2,7-diol. (Reprinted with permission from reference 28. Copyright 2010 Springer Nature).

In 2010, Barbour et al. reported that (S,S)-octa-3,5-diyn-2,7-diol has an exceptionally large thermal expansion coefficient,[28] adding to the literature of organic colossal thermal expansion materials (Figure 1.4). Moreover, in 2016, Naumov et al. reported another class of organic single crystals that possess colossal anisotropic thermal expansion. This material exhibits the largest NTE coefficient observed for an organic compound.[14]

1.2.4 Naphthalene diimides

Naphthalene diimides (NDI) are the smallest homologues of the rylene diimide family (Figure 1.5).[29] These molecules are strong candidates for use in organic electronic applications as they have moderately high charge carrier mobility, high electron affinity, and very good thermal and

oxidative stability.[29] Apart from their uses in optoelectronics, NDIs are also used in several other fields such as fluorescent spectroscopy, supramolecular architectures, DNA intercalators, *etc*. The stimuli-responsive behavior of NDIs has been explored in several studies making them ideal candidates for sensing applications.[29]
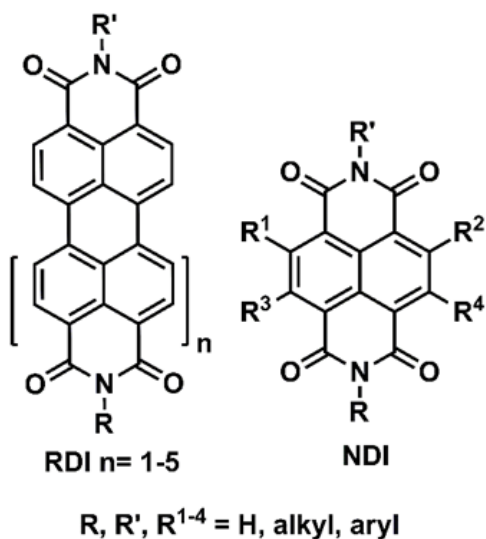
Figure 1.5. Aromatic diimide structures

1.3   Redox responsive materials
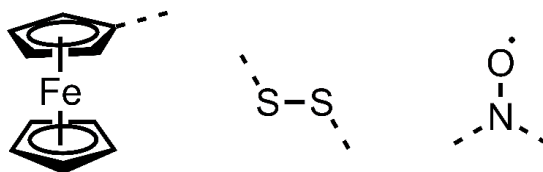
Figure 1.6. Redox responsive functional moieties

Reduction-oxidation (redox) stimuli can alter the oxidation state of the redox sensitive group. While there are several transition metal complexes that are sensitive to redox stimuli, redox sensitive organic compounds are far more applicable for medicinal applications. There are several redox sensitive organic moieties such as ferrocenes, disulfides, and paramagnetic organic radicals (Figure 1.6).[7]

1.3.1   Organic radical contrast agents (ORCAs)

Among redox sensitive organic moieties, paramagnetic organic radicals have been investigated in applications including magnetic resonance imaging (MRI), probes in biomedicines, and energy storage. These applications of nitroxide radicals are mainly due to their unique properties such as paramagnetic or redox activity.
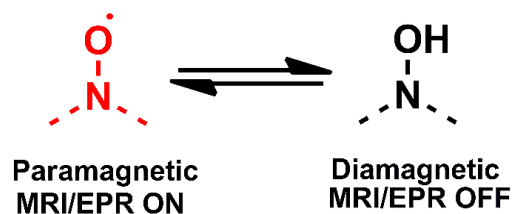
Figure 1.7. Sensing of redox species using ORCAs

Nitroxyl radicals possess a single unpaired electron in their outer shell. Thus, they can easily participate in redox reactions. Reduction of nitroxyl radicals can lead to diamagnetic hydroxylamines (Figure 1.7).[30] The reduced nitroxyl radicals can be easily oxidized to its paramagnetic form using oxidants such as air or peroxides. The electrochemistry of nitroxides has been widely studied. Existing literature reports a huge impact on oxidation potential stemming from the molecular structure and substituents of the nitroxides.[31] Another unique feature of nitroxide is the existence of the paramagnetic behavior whereas most organic compounds are diamagnetic. The paramagnetism of nitroxides is owing to the existence of a single unpaired electron. The detection of nitroxide radicals can be done using electron paramagnetic resonance (EPR), cyclic voltammetry (CV), and magnetic resonance imaging (MRI).

When paramagnetic nitroxide radicals are conjugated adjacent to a fluorophore, the fluorescence of the fluorophore can be quenched.[31,8] The unpaired electron of the radical can interact with the electrons of the fluorophore by changing the multiplicity of the excited state.[31] The triplet spin

state and the singlet spin state can both be converted to the doublet state, reducing spin-forbidden interactions.[31] This increases inter-system crossing and non-radioactive decay, eventually minimizing fluorescence decays (Figure 1.8).[31] This behavior is elegantly used in polymeric systems such as ratiometric sensors.[8]
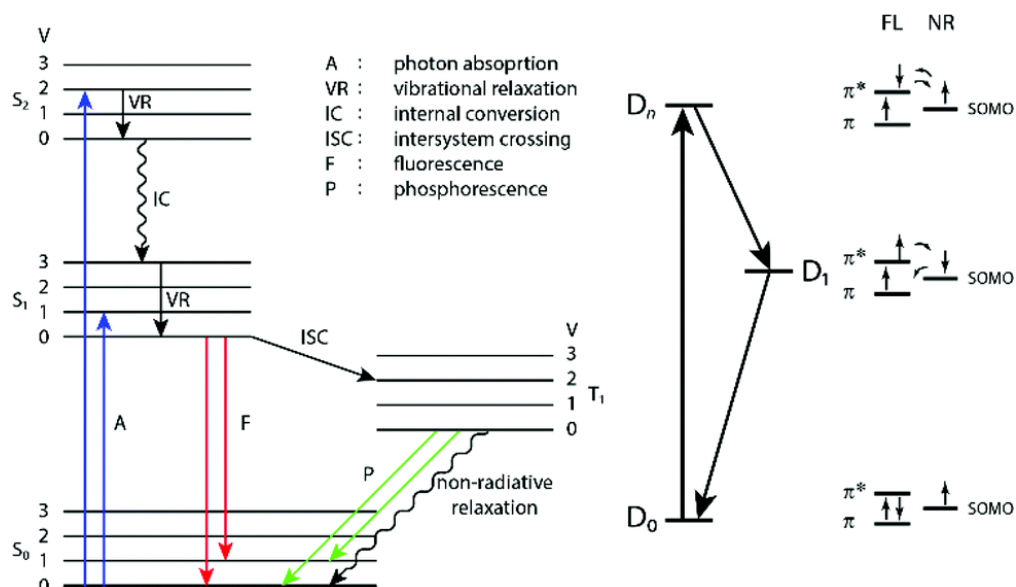
Figure 1.8. Fluorescence quenching of nitroxides. (Reprinted with permission from reference 31. Copyright 2018 The Royal Society of Chemistry).

Nitroxides are very useful as metal-free contrast agents due to their paramagnetic behavior. However, the single unpaired electron of the radical makes it less effective as a contrast agent. The incorporation of radicals to the polymeric backbone will enhance their relaxivity as well as increase the redox potential. Several extensive studies have been done on nitroxide conjugated polymeric systems as MRI contrast agents. Among these studies, Rajica *et al*. developed a dendrimer-based contrast agent, which shows enhanced relaxivity compare to the small molecule nitroxides. In 2014, Johnson *et al*. developed a bimodal sensor based on nitroxyl radicals for both MRI and NIR imaging. They showed that the reduction of the radical can enhance the emission of the system by nearly 250% (Figure 1.9).[8]
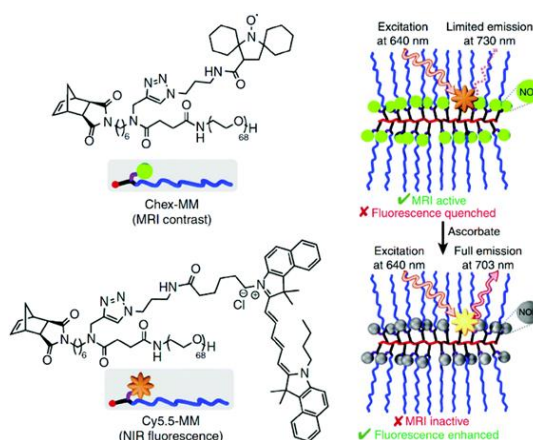
Figure 1.9. Bimodal sensor based on nitroxyl radicals for both MRI and NIR imaging. (Reprinted with permission from reference 8. Copyright 2014 Springer Nature).

1.4 Viral Nano particles

Different nanoparticle-based platforms have been developed for applications such as biomedicine, imaging, and drug delivery.[35] Among existing nanoparticles, viral nanoparticles (VNPs) are specifically attractive as they are naturally occurring, biocompatible, and biodegradable (Figure 1.10).[35] VNP-based chemistries and modification strategies have been developed for their functionalization with contrast agents, anti-cancer drugs, and targeting ligands.[32-34] Tobacco mosaic virus (TMV) is one of the oldest plant viruses and is among the most-studied plant viruses in plant pathology. Wild-type TMV can infect several plant species, among which *Nicotiana benthamiana* (tobacco) is widely used for the propagation of the TMV nanoparticle for research purposes. These viral nanoparticles are highly stable up to temperatures of 60 °C, pH values from 2-10, and organic solvents up to 80% by volume. TMV is a 300 nm hollow, rod-shaped nanoparticle with an interior diameter of 4 nm and exterior diameter of 18 nm (Figure 7a-b).
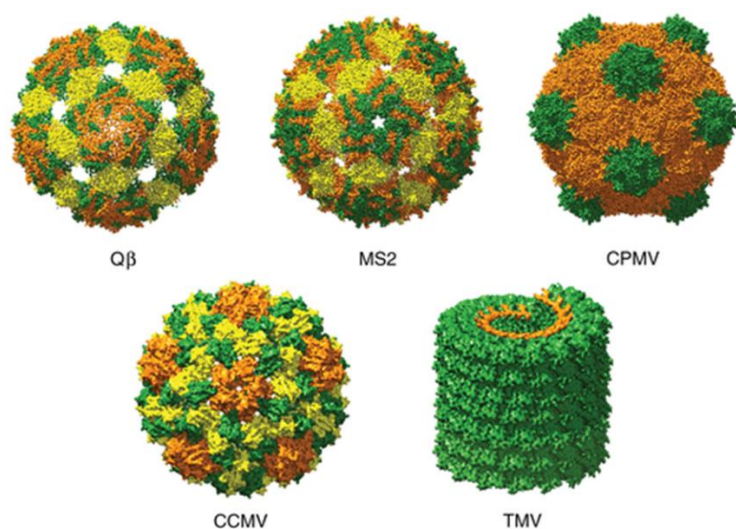
Figure 1.10. Crystallographically-obtained structures of common VLPs and VNPs Qβ, MS2, Cowpea Mosaic Virus (CPMV), Cowpea Chlorotic Mottle Virus (CCMV), and Tobacco Mosaic Virus (TMV). (Reprinted with permission from reference 35. Copyright 2016 John Wiley and Sons).

Each TMV nanoparticle is composed of 2130 coat protein monomers helically wrapped around an *ss*RNA molecule (Figure 1.11). TMV can be modified chemically via established bioconjugation reactions.[35] The exterior surface of TMV consists of solvent-exposed tyrosine (Y139) residues, which can be modified via diazonuim coupling reactions. The interior surface of TMV consists of solvent-exposed glutamic acid residues (E106 and E97), which can be modified easily via EDC coupling (Figure 1.12). The morphology of the nanoparticle after chemical modifications is confirmed by TEM and SEC. The efficiency of bioconjugation reactions in the context of TMV functionalization can be characterized by ESI-MS, MALDI-TOF, SDS-PAGE, SEC and UV-Vis absorption spectroscopy. The modified TMV nanoparticle has been utilized for numerous applications including in light harvesting systems, sensing, energy storages, cell growth, and as MRI contrast agents.[36-39]
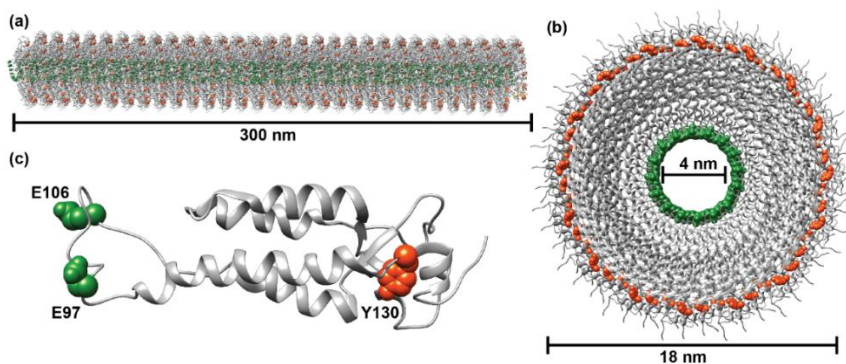
Figure 1.11. Crystallographically obtained structure of TMV (PDB ID 2TMV). (a) cylindrical shape of TMV nanoparticle (b) Side view of TMV showing its hollow shape and arrangement of solvent-exposed amino acid residues in the exterior and interior surface of TMV (c) coat protein monomer showing the solvent exposed amino acid residues available for bioconjugation.
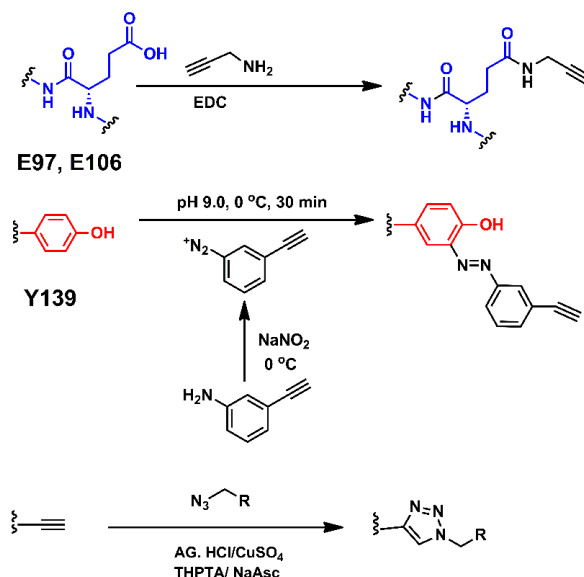
Figure 1.12. Bioconjugation reactions on the exterior and interior surfaces of TMV.[40]

1.5   Summary

While most smart materials or SRMs are polymeric systems, designing a novel class of SRMs represents a new frontier in the development of organic chemistry. Though temperature is arguably the most widely-studied stimulus, there are very few systems that have been identified as thermo-responsive materials that are not polymeric systems. Furthermore, redox conditions have been

shown to be extremely useful and versatile stimuli in biological systems. Redox responsive systems have been fabricated by incorporating redox responsive moieties into polymers. This dissertation will primarily focus on engineering novel classes of stimuli responsive materials for sensing applications in both non-biological and biological systems.

Chapter 1 will focus on introducing stimuli responsive materials and their applications. Chapters 2-4 will investigate an emerging class of thermo-responsive materials. Specifically, Chapter 2 will report the thermo-mechanical behavior of a butoxyphenyl N-substituted naphthalene diimide (BNDI) and its fabrication as a single crystal actuator. Chapter 3 will focus on thermo-responsive behaviour of alkoxyphenyl N-substituted naphthalene diimides and their application as thermochromic sensors. Based on our observations discussed in Chapters 2 and 3, we observed that alkoxyphenyl N-substituted naphthalene diimides exhibited thermochromic properties as well as colossal anisotropic expansion behavior. The reasoning behind the thermo-responsive behavior of BNDI using experimental data and computational studies will be explained in Chapter 4.

Remaining Chapters 5 and 6, the discussion will transition to the use of virus nano particles as responsive materials. The development of redox responsive materials is very important for controlled delivery and sensing applications. Specifically, designing sensors for the *in vivo* detection of reactive oxygen species (ROS) is very crucial as ROS can cause significant damage to human body. While fluorescence sensors are widely used for this purpose, none have emerged for the sensing of ROS in deep tissues. Thus, in Chapter 5 we investigate ROS sensing of a nitroxyl radical-modified tobacco mosaic virus. Biomimetic mineralization is one of the fascinating area of research as this process can enhances the stability of biological macromolecules such as enzymes, proteins and viral nano-particles. Previously our group showed that tobacco mosaic virus

can encapsulated with zeolitic imidazole framework (ZIF-8) to form core shell bio nanoparticles (CSBNs).[38] We also showed that bioconjugation reactions can still performed on the viral nanoparticle inside the TMV@ZIF-8 CSBN. In Chapter 6, we study the effect of surface charge of TMV for the formation of CSBNs. Finally, Chapter 7 discusses the future of each project and plans for further investigation.

1.6   References

1. Hu, J.; Liu, S. Responsive Polymers for Detection and Sensing Applications: Current Status and Future Developments. *Macromolecules* **2010,** *43*, 8315-8330.

2. Zhao, Q.; Dunlop, J. W.; Qiu, X.; Huang, F.; Zhang, Z.; Heyda, J.; Dzubiella, J.; Antonietti, M.; Yuan, J. An instant multi-responsive porous polymer actuator driven by solvent molecule sorption. *Nat. Commun.* **2014,** *5*, 4293.

3. Ma, M.; Guo, L.; Anderson, D. G.; Langer, R. Bio-inspired polymer composite actuator and generator driven by water gradients. *Science* **2013,** *339*, 186-189.

4. Wei, M.; Gao, Y.; Li, X.; Serpe, M. J. Stimuli-responsive polymers and their applications. *Polym Chem.* **2017,** *8*, 127-143.

5. Roy, D.; Cambre, J. N.; Sumerlin, B. S. Future perspectives and recent advances in stimuli-responsive materials. *Prog. Polym. Sci.* **2010,** *35*, 278-301.

6. Theato, P.; Sumerlin, B. S.; O'Reilly, R. K.; Epps, T. H., 3rd. Stimuli responsive materials. *Chem. Soc. Rev.* **2013,** *42*, 7055-7060.

7. Morrow, B. J.; Keddie, D. J.; Gueven, N.; Lavin, M. F.; Bottle, S. E. A novel profluorescent nitroxide as a sensitive probe for the cellular redox environment. *Free Radic. Biol. Med.* **2010,** *49*, 67-76.

8. Sowers, M. A.; McCombs, J. R.; Wang, Y.; Paletta, J. T.; Morton, S. W.; Dreaden, E. C.; Boska, M. D.; Ottaviani, M. F.; Hammond, P. T.; Rajca, A.; Johnson, J. A. Redox-responsive branched-bottlebrush polymers for in vivo MRI and fluorescence imaging. *Nat. Commun.* **2014,** *5*, 5460.

9. Kim, Y.-J.; Matsunaga, Y. T. Thermo-responsive polymers and their application as smart biomaterials. *J Mater Chem* **2017,** *5*, 4307-4321.

10. Dharmarwardana, M.; Welch, R. P.; Kwon, S.; Nguyen, V. K.; McCandless, G. T.; Omary, M. A.; Gassensmith, J. J. Thermo-mechanically responsive crystalline organic cantilever. *Chem. Commun.* **2017,** *53*, 9890-9893.

11. Takeda, T.; Akutagawa, T. Anisotropic Dissociation of π-π Stacking and Flipping-Motion-Induced Crystal Jumping in Alkylacridones and Their Dicyanomethylene Derivatives. *Chem. Eur. J.* **2016,** *22*, 7763-70.

12. Commins, P.; Desta, I. T.; Karothu, D. P.; Panda, M. K.; Naumov, P. Crystals on the move: mechanical effects in dynamic solids. *Chem. Commun.* **2016,** *52*, 13941-13954.

13. Liu, G.; Liu, J.; Ye, X.; Nie, L.; Gu, P.; Tao, X.; Zhang, Q. Self-Healing Behavior in a Thermo-Mechanically Responsive Cocrystal during a Reversible Phase Transition. *Angew. Chem.* **2017,** *56*, 198-202.

14. Panda, M. K.; Centore, R.; Causa, M.; Tuzi, A.; Borbone, F.; Naumov, P. Strong and Anomalous Thermal Expansion Precedes the Thermosalient Effect in Dynamic Molecular Crystals. *Sci Rep.* **2016,** *6*, 29610.

15. Panda, M. K.; Runcevski, T.; Husain, A.; Dinnebier, R. E.; Naumov, P. Perpetually self-propelling chiral single crystals. *J. Am. Chem. Soc.* **2015,** *137*, 1895-1902.

16. Ghosh, S.; Mishra, M. K.; Ganguly, S.; Desiraju, G. R. Dual Stress and Thermally Driven Mechanical Properties of the Same Organic Crystal: 2,6-Dichlorobenzylidene-4-fluoro-3-nitroaniline. *J. Am. Chem. Soc.* **2015,** *137*, 9912-9921.

17. Shima, T.; Muraoka, T.; Hoshino, N.; Akutagawa, T.; Kobayashi, Y.; Kinbara, K. Thermally Driven Polymorphic Transition Prompting a Naked-Eye-Detectable Bending and Straightening Motion of Single Crystals. *Angew. Chem.* **2014**, *126*, 7301-7306.

18. Sahoo, S. C.; Sinha, S. B.; Kiran, M. S.; Ramamurty, U.; Dericioglu, A. F.; Reddy, C. M.; Naumov, P. Kinematic and mechanical profile of the self-actuation of thermosalient crystal twins of 1,2,4,5-tetrabromobenzene: a molecular crystalline analogue of a bimetallic strip. *J. Am. Chem. Soc.* **2013,** *135*, 13843-13850.

19. Skoko, Z.; Zamir, S.; Naumov, P.; Bernstein, J. The thermosalient phenomenon. "Jumping crystals" and crystal chemistry of the anticholinergic agent oxitropium bromide. *J. Am. Chem. Soc.* **2010,** *132*, 14191-202.

20. Panda, M. K.; Runcevski, T.; Sahoo, S. C.; Belik, A. A.; Nath, N. K.; Dinnebier, R. E.; Naumov, P. Colossal positive and negative thermal expansion and thermosalient effect in a pentamorphic organometallic martensite. *Nat. Commun.* **2014,** *5*, 4811.

21. Day, J. H. Thermochromism. *Chem. Rev.* **1963,** *63*, 65-80.

22. Biedermann, P. U.; Stezowski, J. J.; Agranat, I. Thermochromism of overcrowded bistricyclic aromatic enes (BAEs). A theoretical study. *Chem. Commun.* **2001**, 954-955.

23. Lee, S. C.; Jeong, Y. G.; Jo, W. H.; Kim, H.-J.; Jang, J.; Park, K.-M.; Chung, I. H. Thermochromism of a novel organic compound in the solid state via crystal-to-crystal transformation. *J. Mol. Struct.* **2006,** *825*, 70-78.

24. Bohm, A.; Krieger, M.; Becker, S.; Mullen, K. Thermochromic Rylene Dyes. US 6,890,377 B2, 2005.

25. Lambi, E.; Gegiou, D.; Hadjoudis, E. Thermochromism and photochromism of N-salicylidenebenzylamines and N-salicylidene-2-aminomethylpyridine. *J. Photochem. Photobiol. A* **1995,** *86*, 241-246.

26. Goodwin, A. L.; Calleja, M.; Conterio, M. J.; Dove, M. T.; Evans, J. S.; Keen, D. A.; Peters, L.; Tucker, M. G. Colossal positive and negative thermal expansion in the framework material Ag3[Co(CN)6]. *Science* **2008,** *319*, 794-797.

27. Goodwin, A. L.; Kepert, C. J. Negative thermal expansion and low-frequency modes in cyanide-bridged framework materials. *Phys. Rev. B* **2005,** *71*.

28. Das, D.; Jacobs, T.; Barbour, L. J. Exceptionally large positive and negative anisotropic thermal expansion of an organic crystalline material. *Nat. Mater.* **2010,** *9*, 36-39.

29. Kobaisi, M. A.; Bhosale, S. V.; Latham, K.; Raynor, A. M.; Bhosale, S. V. Functional Naphthalene Diimides: Synthesis, Properties, and Applications. *Chem. Rev.* **2016**.

30. Bobko, A. A.; Kirilyuk, I. A.; Grigor'ev, I. A.; Zweier, J. L.; Khramtsov, V. V. Reversible reduction of nitroxides to hydroxylamines: roles for ascorbate and glutathione. *Free Radic. Biol. Med* **2007,** *42*, 404-412.

31. Hansen, K.-A.; Blinco, J. P. Nitroxide radical polymers – a versatile material class for high-tech applications. *Poly. Chem.* **2018,** *9*, 1479-1516.

32. Liepold, L.; Anderson, S.; Willits, D.; Oltrogge, L.; Frank, J. A.; Douglas, T.; Young, M. Viral capsids as MRI contrast agents. *Magn. Reson. Med.* **2007,** *58*, (5), 871-9.

33. Prasuhn, D. E., Jr.; Yeh, R. M.; Obenaus, A.; Manchester, M.; Finn, M. G. Viral MRI contrast agents: coordination of Gd by native virions and attachment of Gd complexes by azide-alkyne cycloaddition. *Chem. Commun.* **2007**, 1269-1271.

34. Chan, J. M. W.; Wojtecki, R. J.; Sardon, H.; Lee, A. L. Z.; Smith, C. E.; Shkumatov, A.; Gao, S. J.; Kong, H.; Yang, Y. Y.; Hedrick, J. L. Self-Assembled, Biodegradable Magnetic Resonance Imaging Agents: Organic Radical-Functionalized Diblock Copolymers. *ACS Macro Lett.* **2017,** *6*,176-180.

35. Chen, Z.; Li, N.; Li, S.; Dharmarwardana, M.; Schlimme, A.; Gassensmith. Viral chemistry: the chemical functionalization of viral architectures to create new technology. J. J. *WIREs Nanomed. Nanobiotechnol.* **2016,** *8,* 512–534.

36. Bruckman, M. A.; Randolph, L. N.; Gulati, N. M.; Stewart, P. L.; Steinmetz, N. F. Silica-coated Gd(DOTA)-loaded protein nanoparticles enable magnetic resonance imaging of macrophages. *J. Mater. Chem. B* **2015,** *3*, 7503-7510.

37. Hu, H.; Zhang, Y.; Shukla, S.; Gu, Y.; Yu, X.; Steinmetz, N. F. Dysprosium-Modified Tobacco Mosaic Virus Nanoparticles for Ultra-High-Field Magnetic Resonance and Near-Infrared Fluorescence Imaging of Prostate Cancer. *ACS nano* **2017,** *11*, (9), 9249-9258.

38. Li, S.; Dharmarwardana, M.; Welch, R. P.; Ren, Y.; Thompson, C. M.; Smaldone, R. A.; Gassensmith, J. J. Template-Directed Synthesis of Porous and Protective Core-Shell Bionanoparticles. *Angew. Chem.* **2016,** *55*, 10691-10696.

39. Bruckman, M. A.; Jiang, K.; Simpson, E. J.; Randolph, L. N.; Luyt, L. G.; Yu, X.; Steinmetz, N. F. Dual-modal magnetic resonance and fluorescence imaging of atherosclerotic plaques in vivo using VCAM-1 targeted tobacco mosaic virus. *Nano lett.* **2014,** *14*, 1551-1558.

40. Schlick, T. L.; Ding, Z.; Kovacs, E. W.; Francis, M. B. Dual-surface modification of the tobacco mosaic virus. *J. Am. Chem. Soc.* **2005,** *127*, 3718-3723.

CHAPTER 2

THERMO-MECHANICALLY RESPONSIVE CRYSTALLINE

ORGANIC CANTILEVER[1]

Authors – Madushani Dharmarwardana, Raymond P. Welch, Sunah Kwon, Victoria K. Nguyen,

Gregory T. McCandless, Mohammad A. Omary, Jeremiah J. Gassensmith

The Department of Chemistry, BE26

The University of Texas at Dallas

800 West Campbell Road

Richardson, Texas 75080-3021

2.1 Summary

We report thermo-mechanically responsive and thermochromic behavior in the single crystalline organic semiconductor butoxyphenyl N-substituted naphthalene diimide (BNDI). We show that initially monoclinic single crystals of BNDI undergo a single-crystal to single-crystal transition to a triclinic phase. This transition accompanies large changes in the crystal packing, a visible decrease in crystal size, reversible thermochromic behavior, and motion including bending, jumping, and splitting. We have shown that by fixing single crystals to a surface, we can harness the energy of the phase transition to create a single crystal cantilever capable of lifting small weights.

2.2 Introduction

Kinetic stimuli responsive behavior—the ability to move in response to the input of energy from an external source—has been engineered in a wide range of flexible materials from bulk polymers[1-7] to viral nanoparticles.[8-10] These soft materials readily undergo chemical functionalization and stimuli responsiveness can be straightforward to introduce.[1] Finding such motion in highly crystalline solids is still unusual and surprising.[11, 12] That said, recent examples of single crystals that bend, jump[13, 14] split,[15, 16] coil,[17] and explode[18] when prodded into undergoing either a phase transition or topochemical reaction[19-23] have emerged in the literature. This rapid and controllable dynamic behavior has attracted some interest owing to potential applications as micron or nanoscale actuators for smart medical devices, artificial muscles, sensors, and memory devices.[12, 24-27] In most cases, this induced motion leads to disintegration after the phase transition; thus, such crystals are not suitable for structure determination following actuation. In contrast, only a few

19

examples[14-29] of organic molecular crystals showing thermo-mechanical single crystal-to-single crystal (SC-SC) transitions have been reported. Donor-accepter stacks containing electron deficient naphthalene diimide subunits and electron rich dialkoxynaphthalene subunits have been shown to undergo phase transitions in response to temperature changes—giving rise to thermochromism.[28] What is not clear is if this thermal responsiveness is a general phenomenon to planar aromatics or if it is unique to donor-acceptor systems.[29-31] In other words, we wondered if similar thermo-responsive behavior could be achieved with just a single type of subunit—either single crystals containing only an electron donor or an electron acceptor. In the course of this study, we discovered that the monoclinic polymorph (α-phase) of single crystals containing exclusively butoxyphenyl N-substituted naphthalene diimide (BNDI) (Figure 1a) not only undergo significant intermolecular changes in stacking distance, but also, when heated, undergo a thermo-mechanical responsive SC-SC change to a reversibly thermochromic triclinic (β-phase) system. This is made all the more interesting because naphthalene diimide structures are one of only a handful of n-type organic semiconductors[32] and BNDI is known to have n-type semiconducting properties[32, 33] in the solid state. Intriguingly, the concurrent existence of polymorphism[34] and thermo-mechanical behavior in the solid state have yet to be reported for any naphthalene diimide—or any perylene derivative for that matter—despite several examples of liquid crystalline systems[35-37] and polymers[38] of these materials showing such behavior.[39]

20

2.3   Experimental

2.3.1   Materials

All the chemicals and solvents used for the synthesis and crystallizations (1,4,5,8-naphthalenetetracarboxylic dianhydride, 4-butoxyaniline, N,N-dimethylformamide, chloroform, tetrabutylammonium bromide, chloroform-d) were purchased from Sigma Aldrich.

2.3.2   Instrumentation

Nuclear Magnetic Resonance (NMR)

NMR spectra were measured using a Bruker AVANCE III 500 MHz spectrometer in $CDCl_3$ with $Si(CH_3)_4$ used as reference standard.

Single Crystal X-Ray Diffraction (SXRD)

SXRD data were collected for the two BNDI polymorphs, α-phase and β-phase using a Bruker Kappa D8 Quest diffractometer. Bruker Kappa D8 Quest diffractometer is equipped with an Incoatec microfocus Mo Kα radiation source, HELIOS multilayer optics, Oxford Cryosystems cryostream, and a Photon 100 CMOS detector. Bruker SAINT was used for all data sets for integration and scaling, SADABS was used for absorption correction (multi-scan) and analysis of systematic absences of hkl reflections and XPREP was used for space group selection. All initial triclinic and monoclinic models of the two polymorphs were generated with SHELXT (intrinsic phasing method)[40] and least-squares refinement was carried out with SHELXL2014.[41]

Temperature-dependent Powder X-Ray Diffraction (PXRD)

Temperature-dependent PXRD was collected using a Rigaku Ultima III XRD equipped with an HT 1500 high temperature attachment with Cu Kα radiation. Samples were placed on the sample holder and measured with 2θ range from 3–40° in a nitrogen gas environment. The temperature of

the experiment was programmed from room temperature to 493 K with 10 min equilibration time and 10 K/min heating rate. PXRD data were collected while the sample was heating to 493 K and cooling the sample to room temperature under nitrogen gas.

<u>Thermal Analysis</u>

Thermal properties of BNDI samples were analyzed with differential scanning calorimetry (DSC) using a TA Instruments Q2000. The samples were heated from 200 K to 500 K at a heating rate of 10 K/min, under a flow of nitrogen (50 mL/min).

<u>Hot-stage Polarized Optical Microscopy</u>

Thermo-mechanical behavior was analyzed using a MEIJI TECHNO ML9000 series polarizing microscope equipped with an Instech hot stage. The maximum temperature that the sample can be heated on this stage is 473 K. The sample was placed on a 1 mm thick glass slide and it was heated to 423 K. The actual temperature of the stage was determined by a Phidget Temperature Sensor (P/N 1051_2). After the phase transition, the sample was cooled by sending cooled nitrogen gas through the stage.

2.3.3   Quantification of thermo-mechanical effect

1.5 mm – 4.0 mm sized BNDI crystals were picked using a microscope and one end of the crystal was glued to the 1 mm glass cover slide. Then, a metal ball (4.1 mg steel or 1 mg tungsten carbide) was glued to the other end of the crystal. The cover slide with this BNDI cantilever was placed on the hot stage, heated to about 473 K, and monitored using a microscope which was placed perpendicular to the crystal. The angle of the BNDI cantilever before and after the phase transition was measured using the MU300 microscope software (AmScope, Irvine, California, USA).

22

2.3.4 Synthesis and Characterization

<u>Synthesis of BNDI</u>

A mixture of 1,4,5,8-naphthalene-tetracarboxylic dianhydride (NDA) (0.8045 g, 3.000 mmol) and

p-butoxyaniline (0.9914 g, 6.000 mmol) in DMF (20 mL) was heated under reflux at 110 °C for

24 hours. When the reaction mixture cooled to room temperature, a crystalline solid precipitated,

which was collected by filtration as an orange crystalline solid with a 70% yield. ^{1}H–NMR (500

MHz, CDCl$_3$, ppm): 1.01 (t, 7.0 Hz, 6 H), 1.54 (tq, 3.8, 7.2 Hz, 4 H) 1.82 (tt, 6.5, 8.0 Hz, 4 H),

4.04 (t, 4 H, 6.5 Hz) 7.07 (d, J= 8.5 Hz, 4 H) 7.23 (d, 8.5 Hz, 4 H) 8.82 (s, 4 H). ^{13}C–NMR (125

MHz, CDCl$_3$, ppm): 13.88, 19.30, 31.31, 67.99, 115.41, 126.70, 127.08, 127.19, 129.36, 131.43,

159.59, 163.24.

<u>Growth of the α-phase Single Crystals for SXRD</u>

Crude BNDI solid (0.056 g, 1.0 mmol) was placed in a scintillation vial and dissolved in 2.0 ml of

CHCl$_3$. The solution was boiled until the solid particles disappeared. The resultant solution was

loosely covered with a lid and kept for 2-3 days until crystals appeared.

<u>Growth of the β-phase Single Crystals for SXRD</u>

Crude BNDI (0.056 g, 1.0 mmol) and tetrabutylammonium bromide (0.064 g, 2.0 mmol) were

mixed in a scintillation vial and 2.0 ml of CHCl$_3$ was added. The resulting solution was boiled

until the solid particles disappeared. The resultant solution was loosely covered with a lid and kept

for 2-3 days until crystals appeared.

2.3.5 Single Crystal X-Ray Structure for α-phase and β-phase

Crystallographic data for the α-phase and β-phase have been submitted to the Cambridge Crystallographic Data Center with deposition number CCDC 1497526 and CCDC 1497523, respectively.

SXRD data for α-phase: Blade shape yellow crystal ($0.84 \times 0.14 \times 0.10$ mm^3) was used for the SXRD analysis, $C_{34}H_{30}N_2O_6$, M = 592.29, F(000) = 592, Monoclinic, $a = 5.026(2)$, $b = 33.756(5)$, $c = 7.9533(14)$, $\alpha = 90°$, $\beta = 99.997(10)°$, $\gamma = 90°$, V = 1328.9(6) Å^3, T = 100 K, Space group $P2_1/c$, Z = 2, D_x = 1.406 gcm^{-3}, 16317 measured reflections, 4061 independent reflections, 3266 reflections with $I > 2\sigma(I)$, $R[F^2 > 2\sigma(F^2)] = 0.050$, $wR(F^2) = 0.138$, S = 1.029, R_{int} = 0.045

SXRD data for β-phase: blade shape orange color crystal ($0.30 \times 0.14 \times 0.08$ mm^3) was used for SXRD analysis, $C_{34}H_{30}N_2O_6$, M = 592.29, F(000) = 296, Triclinic, $a = 4.1636(8)$, $b = 8.1371(18)$, $c = 20.104(5)$, $\alpha = 100.182(11)°$, $\beta = 93.124(14)°$, $\gamma = 94.102(14)°$, V = 667.1(3) Å^3, T = 100(2) K, Space group P1, Z = 1, D_x = 1.400 gcm^{-3}, 23801 measured reflections, 4086 independent reflections, 2918 reflections with $I > 2\sigma(I)$, $R[F^2 > 2\sigma(F^2)] = 0.052$, $wR(F^2) = 0.136$, S = 1.05, R_{int} = 0.060

2.4 Results and Discussion

During our initial investigation of BNDI single crystals, we found we could induce the quantitative growth of two phase-pure BNDI derivatives by changing the solution growth conditions. Specifically, we found the known yellow monoclinic polymorph (α-phase shown in Figure 2.1b), which we initially believed to be thermally inert based on temperature dependent single crystal X-ray diffraction (SXRD) experiments and a thermochromic triclinic polymorph (β-phase), which

produces orange crystals at room temperature (Figure 2.1c). While testing the presumed "thermal-inertness" of the yellow α-phase crystals, we discovered that, after heating to around 400 K and then upon cooling, the crystals became orange and displayed identical thermochromic behavior as the triclinic β-phase. We suspected that the crystals interconverted between the two polymorphs, which would have been surprising given the large difference in unit cell parameters (Table 2.1).

Table 2.1. Comparison of crystallographic parameters before and after phase transition

		α-phase	β-phase	Before phase transition	After phase transition
Temperature/ K		100	100	298	100
Crystal System		monoclinic	triclinic	monoclinic	triclinic
Space group		$P2_1/c$	$P1$	$P2_1/c$	$P1$
Unit cell/ Å	$a =$	5.026(2)	4.1636(8)	5.092(4)	4.16(1)
	$b =$	33.756(5)	8.1371(18)	33.62(2)	8.18(2)
	$c =$	7.9533(14)	20.104(5)	8.148(5)	20.21(5)
	$\alpha =$	90°	100.182(11)°	90°	100.10(5)°
	$\beta =$	99.997(10)°	93.124(14)°	100.11(2)°	93.03(6)°
	$\gamma =$	90°	94.102(14)°	90°	94.16(6)°
Volume/ Å^3		1328.8(6)	667.1(3)	1373(2)	675(3)
Crystal color		yellow	red/orange	yellow	red/orange
Z		2	1	2	1
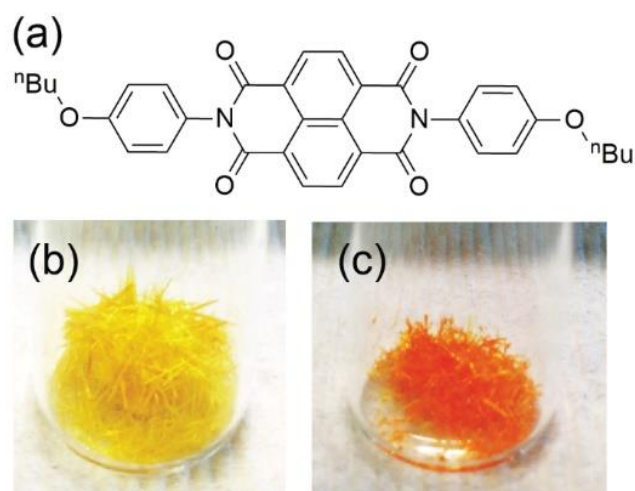
Figure 2.1. (a) Chemical structure of BNDI; Photographs of polymorphs: the (b) non-thermochromic α-phase and the (c) thermochromic β-phase.

Monoclinic α-phase → Triclinic β-phase
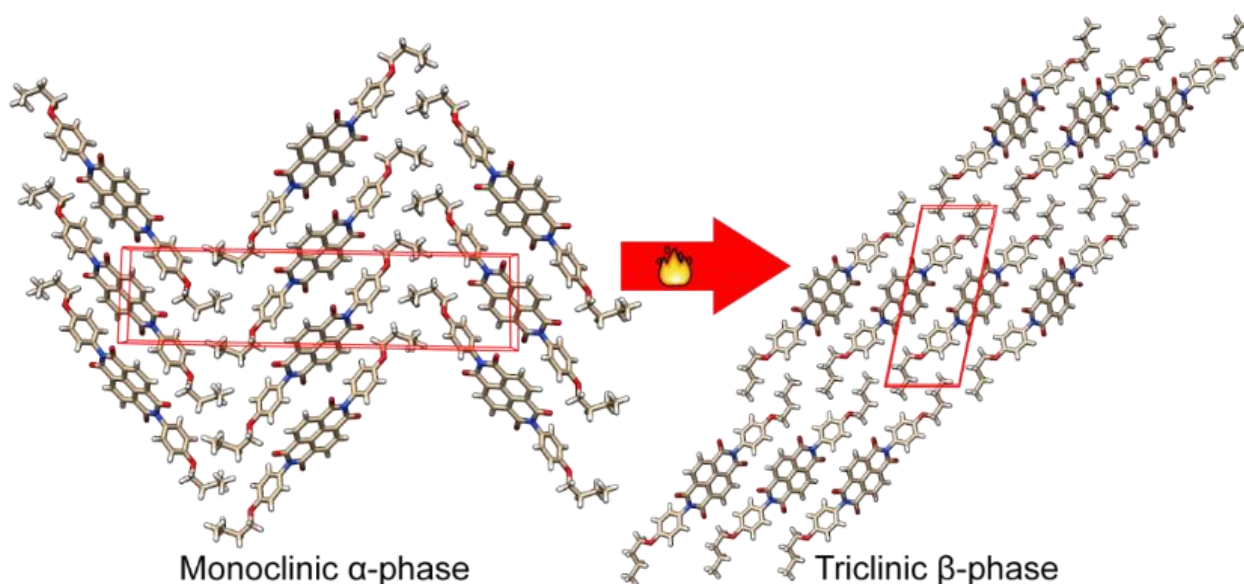
Figure 2.2. Perspective projections of the crystallographic packing in the SC-SC transition from the monoclinic α-phase to the triclinic β-phase. Upon heat treatment, the crystal lattice changes from herringbone packing to infinite 1D chains stacked co-facially along their π surfaces. The red box represents the unit cells of the respective crystals. Both images are oriented along the crystallographic a-axis.

In most reported cases, thermo-mechanically responsive molecular crystals are isosymmetric after

the phase transition and only minor changes of the unit cell are noted.[42-46] In the instance of BNDI,

however, crystal symmetry is not preserved and a comparatively massive change in the unit cell is

26

observed. Figure 2.2, for instance, shows both polymorphs along the crystallographic *a*-axis and clearly illustrates these large anisotropic changes in packing. We witnessed this first-hand when a single crystal of the monoclinic α-phase was evaluated by SXRD analysis at room temperature. The crystal was then heated in a round bottom flask using an oil bath to around 400 K, cooled down to 90 K, and SXRD data were collected. The thermally transformed polymorph, now in the β-phase, continued to diffract, though with some attenuation in long range order (Figure 2.3-2.4 and Table 2.1) and the emergence of disorder presumed to be associated with twinning. Frequently, we found that the crystals would undergo even more extreme motion; for instance, rapid vibration and jumping were seen, though, about 75% of the time, the crystals would bend out of plane (Figure 2.4). We characterized this dynamic behavior using hot-stage microscopy to analyze the morphological and color changes of the α-phase during this anomalous transition.
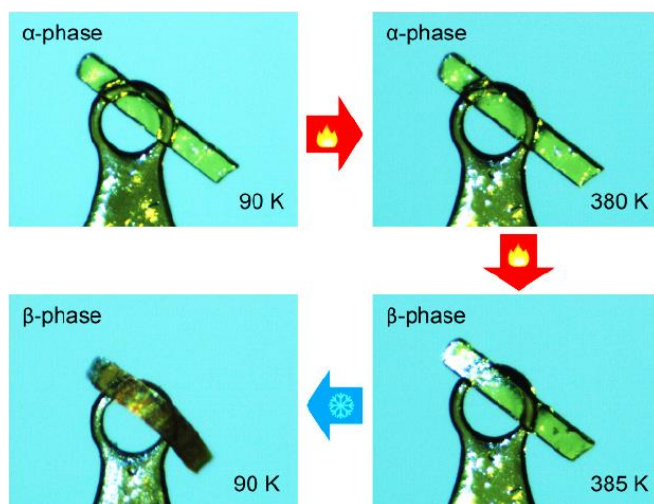
Figure 2.3. SC-SC phase transition of α-phase to β-phase. Images were taken when the crystal was mounted on a loop for SXRD. The yellow color α-phase started bending as the temperature increased to 385 K due to the phase transition from the α-phase to the β-phase. As the temperature decreased to 90 K using the cryostream, the bending of the single crystal was more obvious due to the shrinking of the unit cell of β-phase, and the crystal converted to a red/range color.
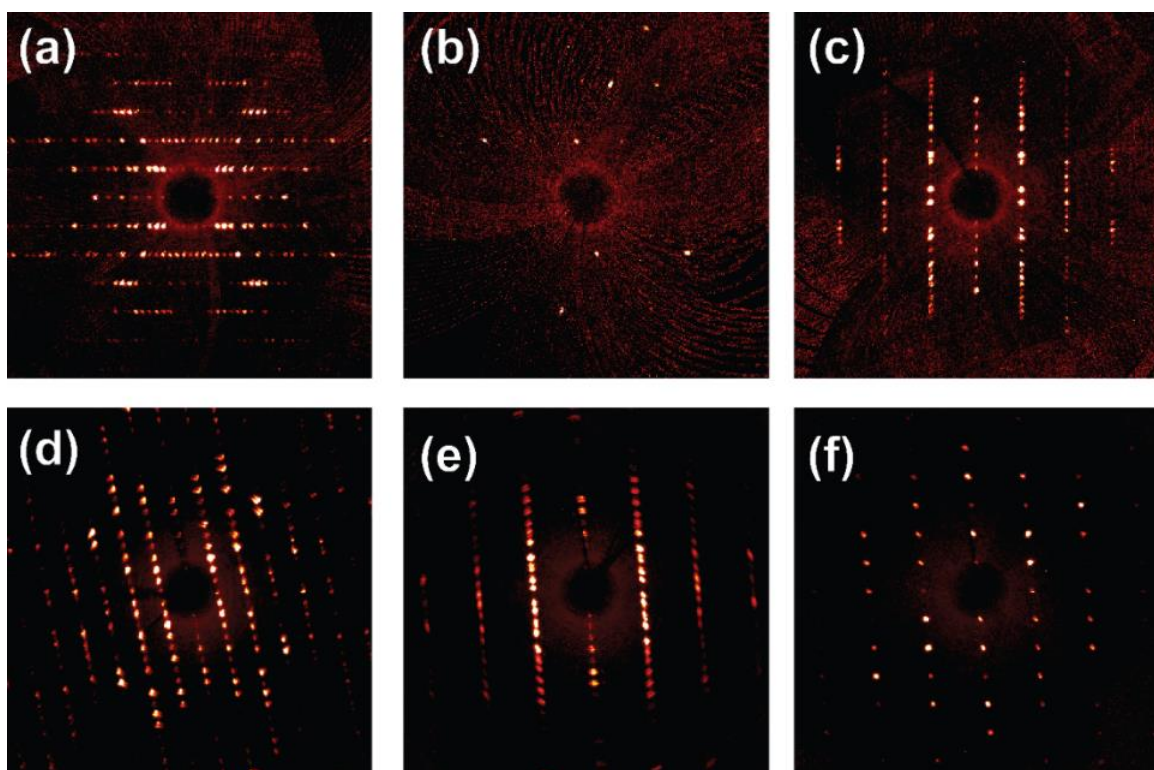
Figure 2.4. Single crystal diffraction data for α-phase to β-phase transition; Precession images (hk0, h0l, and 0kl) for before (a, b, c) and after (d, e, f) α-phase to β-phase transition. As shown in the (a, b, c) images, the α-phase shows strong diffraction spots in all directions. After the phase transition, the crystal still strongly diffracted, and the unit cell parameters were successfully determined. However, as shown in the (d, e, and f) images, weak diffraction spots were observed indicating the emergence of more than one crystalline domain
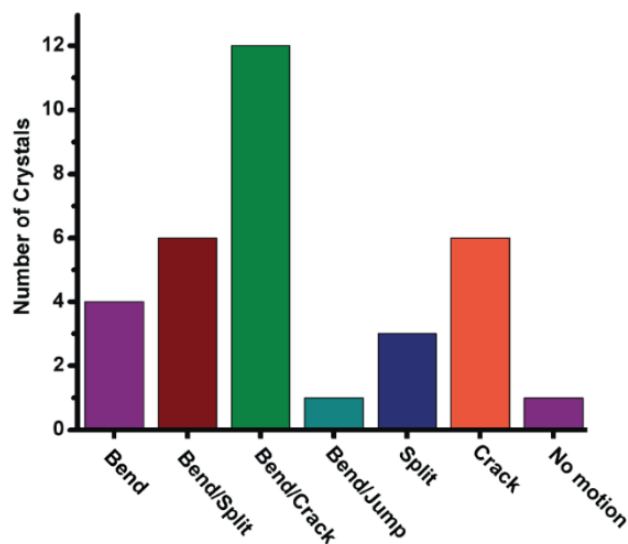
Figure 2.5. Different thermo-mechanical effects exerted by the BNDI crystals with respect to temperature changes. Total number of crystals used in this graph is 33.

When millimeter-sized single crystals in the α-phase were heated on the stage of a polarized optical microscope, the crystal initially expanded, but no movement was observed until the temperature reached around 400 K. At that point, a clear "wave front" began at one extreme end of a crystal and propagated to the other end followed by a change from bright yellow to dark yellow (Figure 2.6). At this point the crystal started showing movements such as cracking, splitting, jumping, and bending (Figure 2.6).
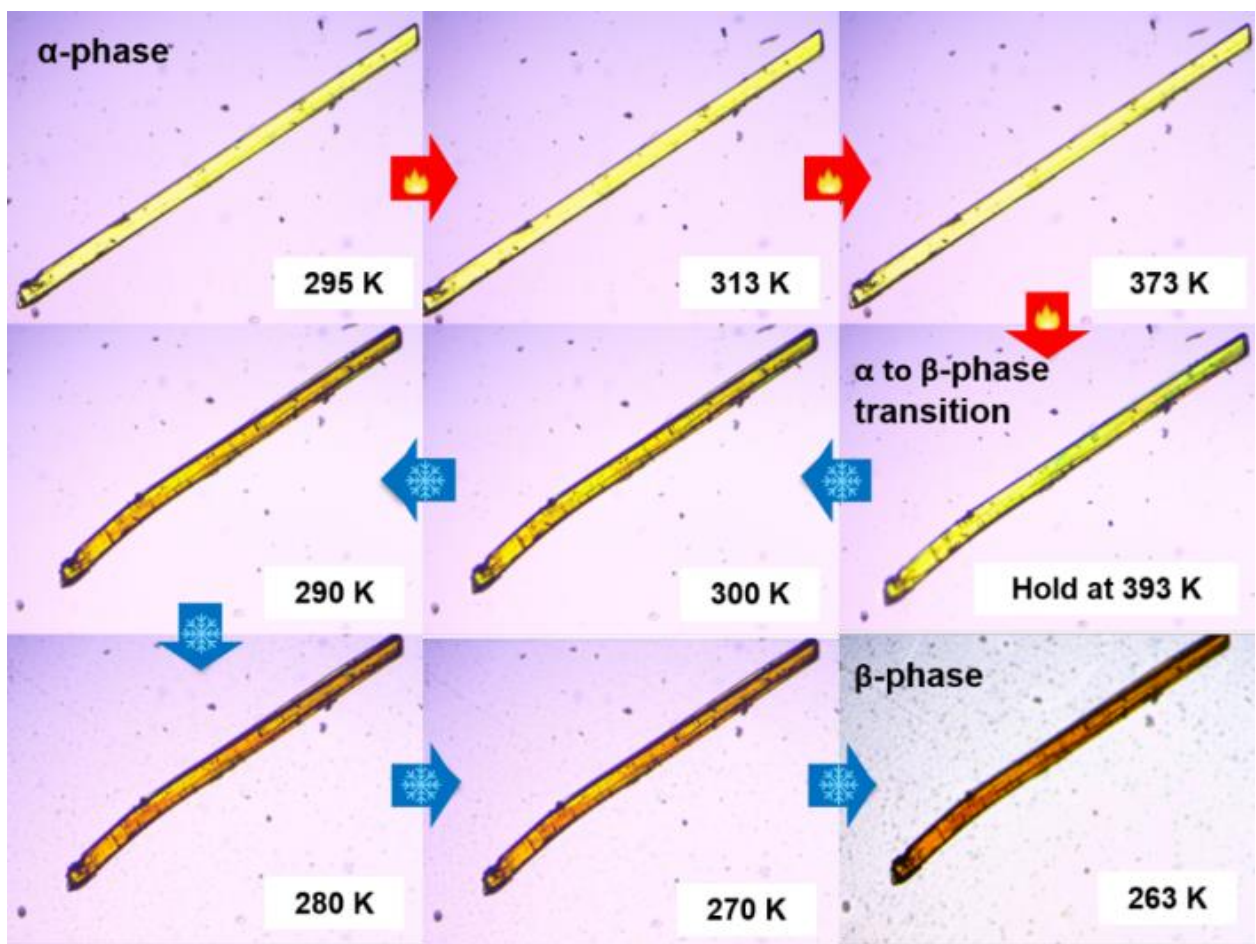
Figure 2.6. Polarized optical micrographs of α-phase upon heating and cooling. The crystal was placed on a 1 mm think glass slide on the heating stage and the changes of morphology and color were recorded as the crystal was heated continuously beyond the phase transition.
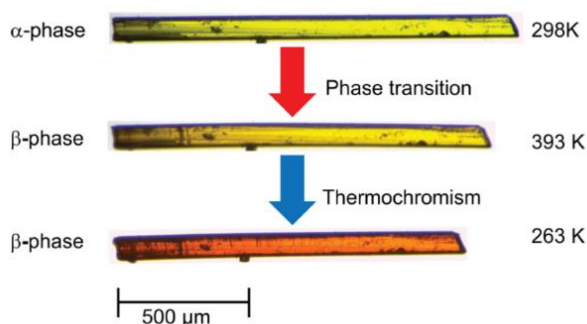
Figure 2.7. Changes of crystal dimensions during the α-phase to the β-phase transformation.

If the crystal did not jump out of view, we could then lower the temperature of the stage. Once the crystals underwent a transformation to the thermochromic β-phase, they changed color to red/orange as the stage was reduced to cryogenic temperatures (Figure 2.6). While most of the crystals ended up irreversibly bending during the phase transition, some crystals of the α-phase were either much less dramatic in movement (Figure 2.7) or bent back into plane following the transition. This allowed us to record the contraction of the crystal while it was heated beyond the phase transition and then cooled. The crystal contracted approximately 5% following the phase transition and a further 13% upon cooling to 263 K (Table 2.2, Figure 2.7). From our SXRD data it is clear that the transition from α-phase to β-phase results in a radically different unit cell and it is quite clear the crystals themselves change in size.

Table 2.2. Changes of the α-phase BNDI crystal dimension with respect to temperature of three individual crystals[a]

Temperature/ K	Crystal 1		Crystal 2		Crystal 3	
	Length/mm	Width/mm	Length/mm	Width/mm	Length/mm	Width/mm
298	1.509	0.094	1.604	0.105	1.957	0.073
323	1.508	0.095	1.607	0.103	1.961	0.075
383	1.514	0.094	1.616	0.106	1.966	0.075
393	1.418	0.088	1.498	0.098	1.814	0.071
373	1.417	0.086	1.486	0.103	1.816	0.068
323	1.370	0.094	1.423	0.101	1.753	0.069
298	1.340	0.094	1.408	0.097	1.736	0.063

[a]We have only considered the length and width of the crystal.

Table 2.3. Velocity of expansion of BNDI crystals during the transition from the α-phase to the β-phase (the same three crystals listed in above)

Δl/ mm	Δt/ s	Velocity of expansion Δl /Δt (μms^{-1})
0.096	24.48	3.921
0.118	24.76	4.765
0.152	19.95	7.619
Average velocity/ (μms^{-1})		5.535(±1.938)
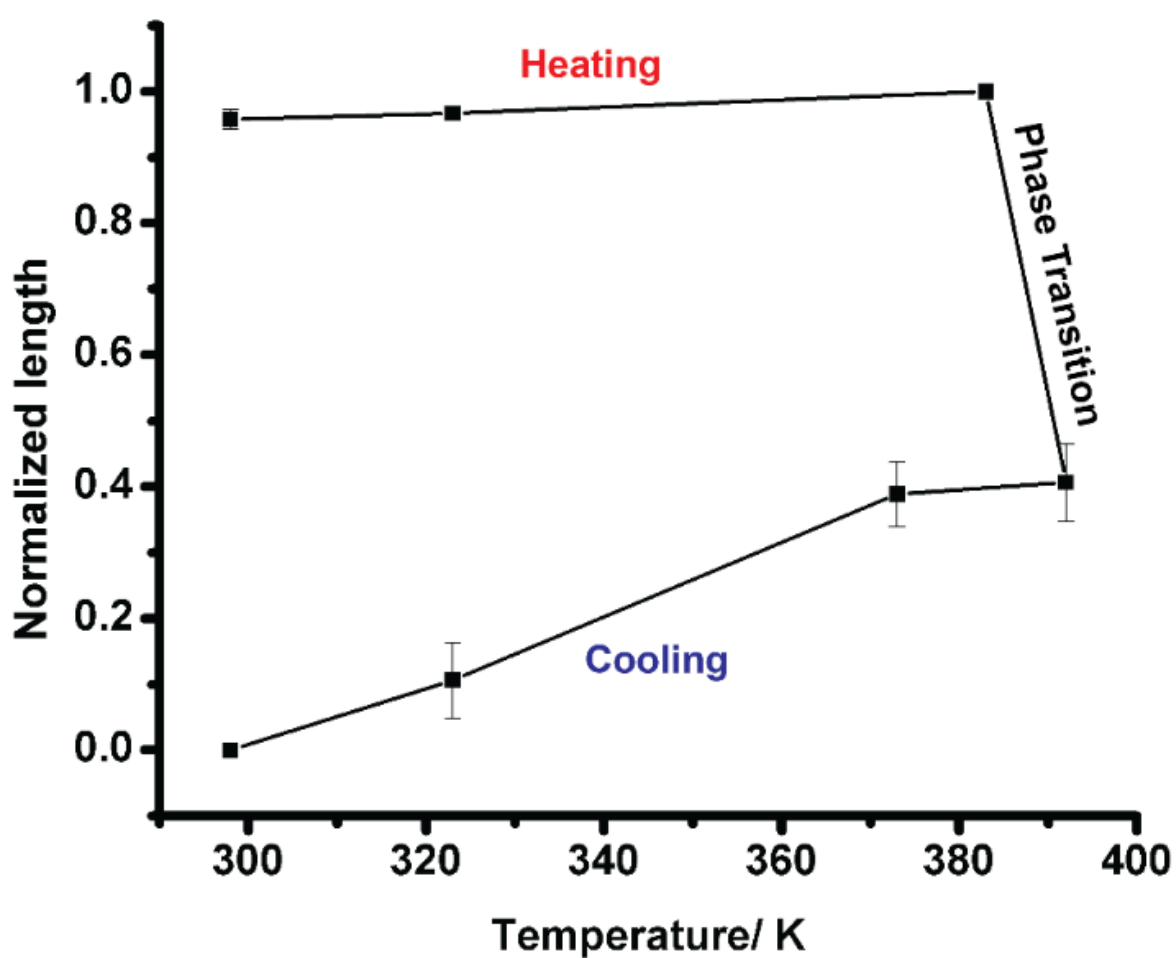
Figure 2.8. Changes of the crystal length with respect to the temperature. Some error bars are too small to be visible at this scale.
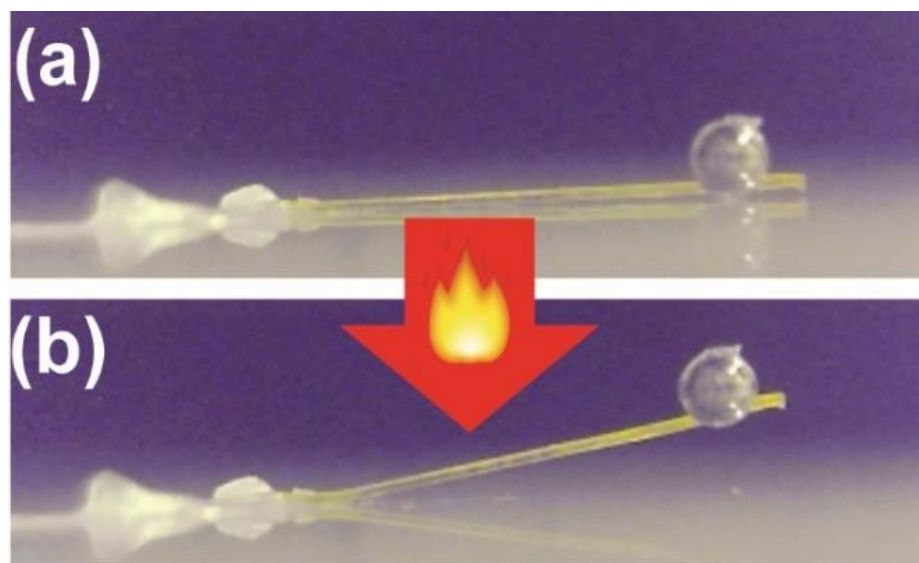
Figure 2.9. Thermo-mechanical work of a BNDI cantilever. (a) Before the phase transition. (b) After the phase transition. The crystal was heated on a glass slide on the heating stage of polarized optical microscope. The mass of the crystal and a 0.5 mm diameter tungsten carbide ball is ~ 0.0100 mg and 0.8320 mg, respectively.

Whilst the dynamic behavior we describe here is uncommon, several elegant studies[13, 16, 18, 43-45, 47-49] have postulated that the stress accumulation within the crystal due to the molecular rearrangement is transformed into mechanical force. We sought to quantify this mechanical force, at least rudimentarily, by converting the single crystals into molecular single crystal cantilevers. To do this, we glued one end of the crystal to the surface of a glass cover slip and a metal ball was loaded onto the other end of the crystal (Figure 2.9). The coverslip was then placed onto a heated stage and we recorded its behavior as the temperature passed and then retreated from the phase transition temperature.
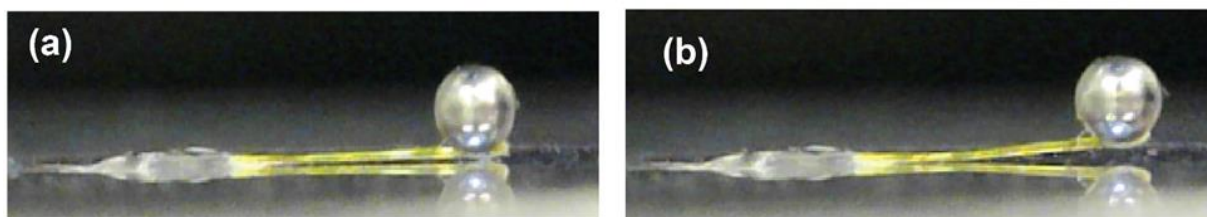
Figure 2.10. Lifting of a 4.1 mg steel ball by a long BNDI cantilever. The length of the crystal is 3498 μm.
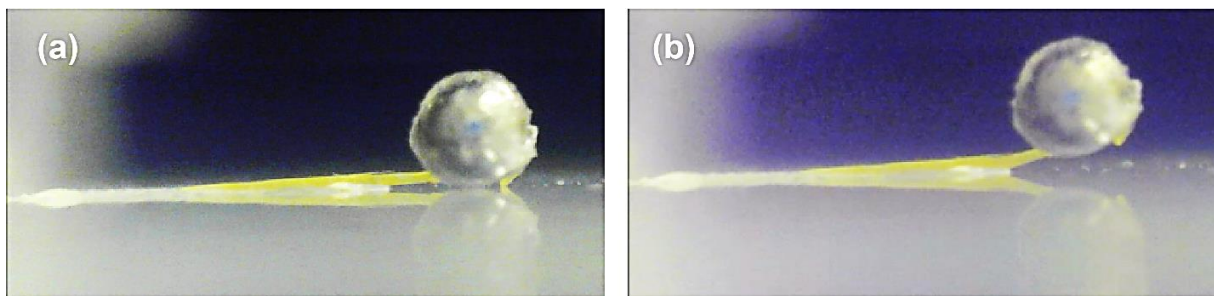
Figure 2.11. Lifting of a 4.1 mg steel ball by a short BNDI cantilever. The length of the crystal is 1120 µm.
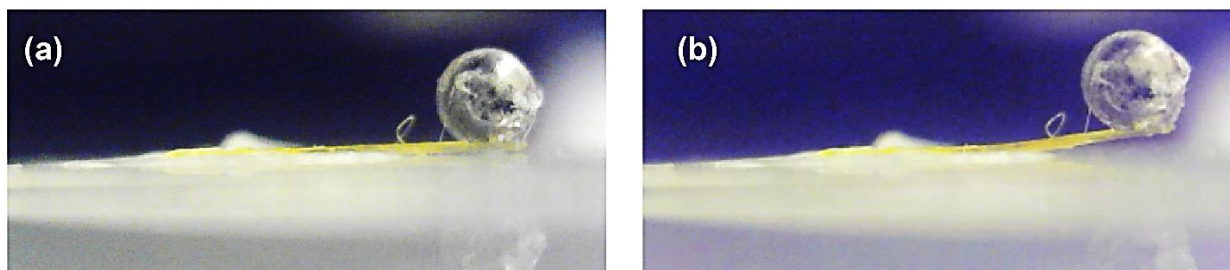
Figure 2.12. Lifting of a 4.1 mg steel ball by a medium length BNDI cantilever. The length of the crystal is 1476 µm.
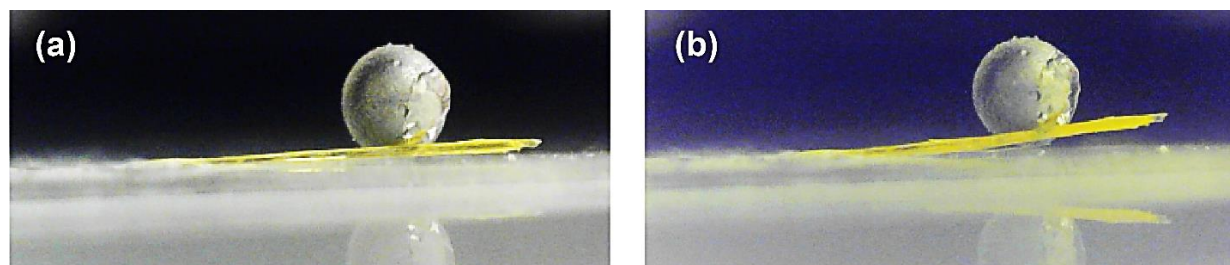
Figure 2.13. Lifting of a 4.1 mg steel ball by a long BNDI cantilever. The length of the crystal is 3055 µm.
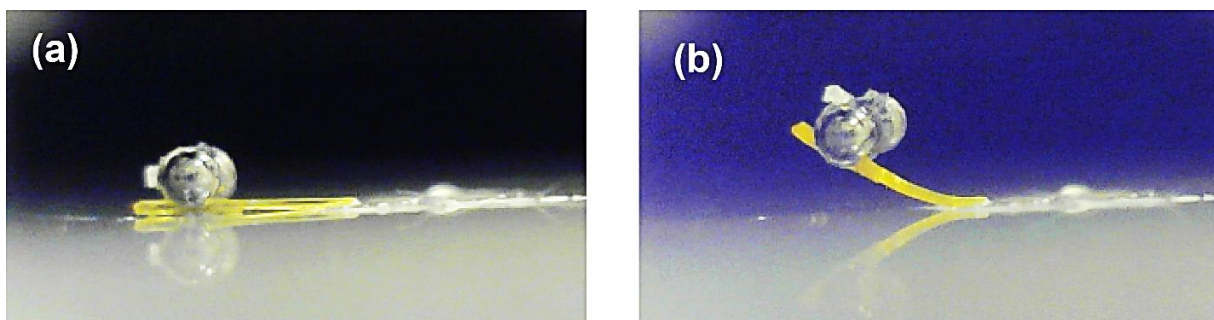
Figure 2.14. Lifting of two 1 mg tungsten carbide balls by a short BNDI cantilever. The length of the crystal is 1632 µm.

We tried a range of crystal sizes and two sizes of metal balls to quantify the thermo-mechanical behaviour of this unique system (Figure 2.9-2.14 and Table 2.4). The maximum load we were able

33

to lift with 3.5 mm long BNDI crystal was a 4.113 mg stainless steel metal ball to a height of 0.24 mm (Figure 2.9). In this case, *the metal ball is 91 times heavier than the BNDI crystal*, the amount of work done by the BNDI cantilever is about 0.01 µJ, and the force generated from the α-phase to the β-phase transition is 40 µN.

Table 2.4. Work done by the BNDI cantilever with different crystal lengths

Figure number	Crystal Length/ µm	ΔAngle/ °	Mass lifted/ mg	ΔHeight/ µm	Work Done/ µJ
2.10	1120	15	4.113	289.8	0.01164
2.11	1476	11	4.113	281.6	0.01131
2.12	3055	8	4.113	425.2	0.01708
2.9	3489	4	4.113	243.3	0.00977
2.13	1632	30	1.667	816.0	0.01599
2.8	3307	11	0.832	631.0	0.00618

Differential scanning calorimetry (DSC) analysis on bulk samples of the yellow monoclinic α-phase had yet another surprise in store for us—a second transition at an even higher temperature. The DSC scans shown in Figure 5a reveal the multiple phase transitions: (1) the expected transition from the α-phase to the β-phase at 388 K; (2) followed by a transition to a new γ-phase at 479 K; and (3) a return to the β-phase upon cooling below 408 K. When this thermal cycle is repeated on the same sample, only the transition between the β-phase and γ-phase is observed, indicating that this transition is reversible. The DSC data of both polymorphs clearly indicated that this phase transition is transforming the α-phase to a more thermodynamically stable and highly thermochromic β-phase (Figure 2.15a and Figure 2.16). During the β-phase to γ-phase

transformation, the crystals lose some of their crystallinity which results in the peak shifting in the second heating cycle (Figure 2.10a).[50, 51]
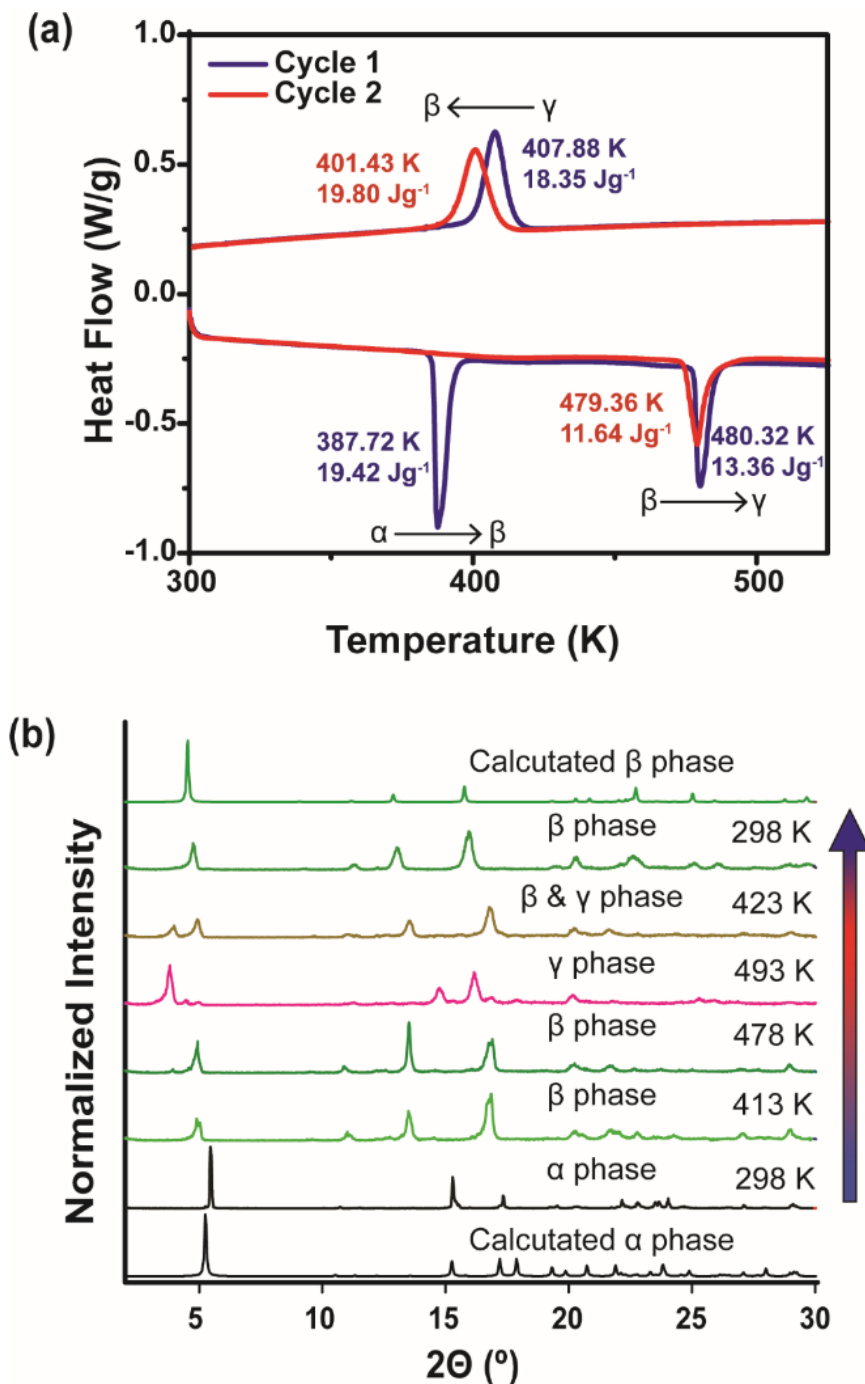
Figure 2.15. (a) DSC curves for the α-phase; Heating rate is 10 K/min (b) Variable temperature PXRD data for the α-phase.
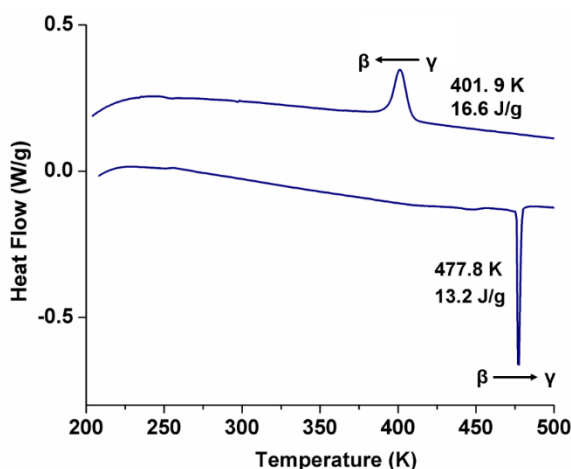
Figure 2.16. DSC curve for the β-phase; the heating rate is 10 K/min.

We confirmed the bulk material underwent reversible crystallographic phase transitions using variable temperature powder X-ray diffraction (PXRD). As shown in Figure 2.15b, as the temperature increases on a sample of pure α-phase BNDI, the reflections of the α-phase peaks decrease and a new set of reflections corresponding to the β-phase appears. As we further increase the temperature, the α-phase completely transforms to the β-phase, which then gives way to the γ-phase at temperatures above 480 K. As we cool down the sample to room temperature, the intensity of the β-phase peaks increases, and the γ-phase completely disappears. Thus far, we have been unable to obtain SXRD data of this high temperature γ-phase, as the single crystals become polycrystalline. Curiously, at these high temperatures, the β-phase is a bright yellow. Once it enters the γ-phase it suddenly becomes orange, indicating that the packing conformation has clearly changed into something quite distinct. Notably, upon cooling, the crystals again turn yellow at the phase transition and then are again thermochromic, and they still strongly diffract by PXRD.[52]

2.5   Conclusions

In summary, we have demonstrated the SC-SC polymorphic transition of the α-phase of the organic semiconductor BNDI to its highly thermochromic β-phase followed by a reversible polymorphic transition to a γ-phase, which only exists at high temperatures. During the polymorphic α-phase to β-phase transition, the crystal symmetry has been changed from monoclinic to triclinic, which accompanied massive stress accumulation within the crystal. According to our polarized optical microscope data, the α-phase of BNDI shows mechanical responses such as bending, jumping, cracking, and splitting upon heating. This thermally induced phase transition could be very useful in microelectronic devices. As a proof of principle, we used the force generated by this thermally driven phase transition to lift a metal ball nearly two orders of magnitude heavier than the crystal itself. Further, the notion that polymorphs of naphthalene diimides—an important class of organic semiconducting materials—are thermo-mechanically sensitive, with each polymorph showing distinct solid-state behavior, could have important implications for the field of organic semiconductors.

2.6   References

1. Yu, Y.; Nakano, M.; Ikeda, T. Photomechanics: directed bending of a polymer film by light. *Nature* **2003,** *425*, 145.

2. Smela, E. Conjugated Polymer Actuators for Biomedical Applications. *Adv. Mater.* **2003,** *15*, 481-494.

3. Spinks, G. M.; Wallace, G. G.; Fifield, L. S.; Dalton, L. R.; Mazzoldi, A.; De Rossi, D.; Khayrullin, I. I.; Baughman, R. H. Pneumatic Carbon Nanotube Actuators. *Adv. Mater.* **2002,** *14*, 1728-1732.

4. Baughman, R. H. Carbon Nanotube Actuators. *Science* **1999,** *284*, 1340-1344.

5. Pelrine, R. High-Speed Electrically Actuated Elastomers with Strain Greater Than 100%. *Science* **2000,** *287*, 836-839.

6. Li, M. H.; Keller, P.; Li, B.; Wang, X.; Brunet, M. Light-Driven Side-On Nematic Elastomer Actuators. *Adv. Mater.* **2003,** *15*, 569-572.

7. Natansohn, A.; Rochon, P. Photoinduced Motions in Azo-Containing Polymers. *Chem. Rev.* **2002,** *102*, 4139-4176.

8. Li, S.; Dharmarwardana, M.; Welch, R. P.; Ren, Y.; Thompson, C. M.; Smaldone, R. A.; Gassensmith, J. J. Template-Directed Synthesis of Porous and Protective Core-Shell Bionanoparticles. *Angew. Chem.* **2016,** *55*, 10691-10696.

9. Chen, Z.; Li, N.; Li, S.; Dharmarwardana, M.; Schlimme, A.; Gassensmith, J. J. Viral chemistry: the chemical functionalization of viral architectures to create new technology. *WIREs Nanomed. Nanobiotechnol.* **2016,** *8*, 512-534.

10. Chen, Z.; Li, N.; Chen, L.; Lee, J.; Gassensmith, J. J. Dual Functionalized Bacteriophage Qbeta as a Photocaged Drug Carrier. *Small* **2016,** *12*, 4563-4571.

11. Terao, F.; Morimoto, M.; Irie, M. Light-driven molecular-crystal actuators: rapid and reversible bending of rodlike mixed crystals of diarylethene derivatives. *Angew. Chem.* **2012,** *51*, 901-904.

12. Kobatake, S.; Takami, S.; Muto, H.; Ishikawa, T.; Irie, M. Rapid and reversible shape changes of molecular crystals on photoirradiation. *Nature* **2007,** *446*, 778-781.

13. Lusi, M.; Bernstein, J. On the propulsion mechanism of "jumping" crystals. *Chem. Commun.* **2013,** *49*, 9293-9295.

14. Panda, M. K.; Runcevski, T.; Husain, A.; Dinnebier, R. E.; Naumov, P. Perpetually self-propelling chiral single crystals. *J. Am. Chem. Soc.* **2015,** *137*, 1895-1902.

15. Medishetty, R.; Sahoo, S. C.; Mulijanto, C. E.; Naumov, P.; Vittal, J. J. Photosalient Behavior of Photoreactive Crystals. *Chem. Mater.* **2015,** *27*, 1821-1829.

16. Liu, G.; Liu, J.; Ye, X.; Nie, L.; Gu, P.; Tao, X.; Zhang, Q. Self-Healing Behavior in a Thermo-Mechanically Responsive Cocrystal during a Reversible Phase Transition. *Angew. Chem.* **2017,** *56*, 198-202.

17. Chen, Z.; Majidi, C.; Srolovitz, D. J.; Haataja, M. Tunable helical ribbons. *Appl. Phy. Lett.* **2011,** *98*, 011906.

18. Nath, N. K.; Panda, M. K.; Sahoo, S. C.; Naumov, P. Thermally induced and photoinduced mechanical effects in molecular single crystals—a revival. *CrystEngComm* **2014,** *16*, 1850.

19. Pathigoolla, A.; Sureshan, K. M. Synthesis of triazole-linked homonucleoside polymers through topochemical azide-alkyne cycloaddition. *Angew. Chem.* **2014,** *53*, 9522-9525.

20. Lauher, J. W.; Fowler, F. W.; Goroff, N. S. Single-crystal-to-single-crystal topochemical polymerizations by design. *Acc. Chem. Res.* **2008,** *41*, 1215-1229.

21. Pathigoolla, A.; Gonnade, R. G.; Sureshan, K. M. Topochemical click reaction: spontaneous self-stitching of a monosaccharide to linear oligomers through lattice-controlled azide-alkyne cycloaddition. *Angew. Chem.* **2012,** *51*, 4362-4366.

22. Barbour, L. J. Single Crystal to Single Crystal Transformations. *Aust. J. Chem.* **2006,** *59*, 595.

23. Li, Z.; Fowler, F. W.; Lauher, J. W. Weak interactions dominating the supramolecular self-assembly in a salt: a designed single-crystal-to-single-crystal topochemical polymerization of a terminal aryldiacetylene. *J. Am. Chem. Soc.* **2009,** *131*, 634-643.

24. Naumov, P.; Chizhik, S.; Panda, M. K.; Nath, N. K.; Boldyreva, E. Mechanically Responsive Molecular Crystals. *Chem. Rev.* **2015,** *115*, 12440-12490.

25. Burgert, I.; Fratzl, P. Actuation systems in plants as prototypes for bioinspired devices. *Phil. Trans. R. Soc. A* **2009,** *367*, 1541-1557.

26. Balzani, V.; Credi, A.; Raymo, F. M.; Stoddart, J. F. Artificial Molecular Machines. *Angew. Chem.* **2000,** *39*, 3348-3391.

27. Morimoto, M.; Irie, M. A diarylethene cocrystal that converts light into mechanical work. *J. Am. Chem. Soc.* **2010,** *132*, 14172-14178.

28. Reczek, J. J.; Villazor, K. R.; Lynch, V.; Swager, T. M.; Iverson, B. L. Tunable columnar mesophases utilizing C2 symmetric aromatic donor-acceptor complexes. *J. Am. Chem. Soc.* **2006,** *128*, 7995-8002.

29. Yuan, T.; Vazquez, M.; Goldner, A. N.; Xu, Y.; Contrucci, R.; Firestone, M. A.; Olson, M. A.; Fang, L. Thermochromic Materials: Versatile Thermochromic Supramolecular Materials Based on Competing Charge Transfer Interactions. *Adv. Funct. Mater.* **2016,** *26*, 8566-8566.

30. Yuan, T.; Vazquez, M.; Goldner, A. N.; Xu, Y.; Contrucci, R.; Firestone, M. A.; Olson, M. A.; Fang, L. Versatile Thermochromic Supramolecular Materials Based on Competing Charge Transfer Interactions. *Adv. Funct. Mater.* **2016,** *26*, 8604-8612.

31. Hou, X.; Ke, C.; Bruns, C. J.; McGonigal, P. R.; Pettman, R. B.; Stoddart, J. F. Tunable solid-state fluorescent materials for supramolecular encryption. *Nat. Commun.* **2015,** *6*, 6884.

32. Rybakiewicz, R.; Tszydel, I.; Zapala, J.; Skorka, L.; Wamil, D.; Djurado, D.; Pecaut, J.; Ulanski, J.; Zagorska, M.; Pron, A. New semiconducting naphthalene bisimides N-substituted with alkoxyphenyl groups: spectroscopic, electrochemical, structural and electrical properties. *RSC Adv.* **2014,** *4*, 14089-14100.

33. Yin, J.; Chaitanya, K.; Ju, X.-H. Theoretical investigations of charge carrier transport in organic semiconductors of naphthalene bisimides N-substituted with alkoxyphenyl groups. *Can. J. Chem.* **2015,** *93*, 740-748.

34. He, T.; Stolte, M.; Burschka, C.; Hansen, N. H.; Musiol, T.; Kalblein, D.; Pflaum, J.; Tao, X.; Brill, J.; Wurthner, F. Single-crystal field-effect transistors of new Cl(2)-NDI polymorph processed by sublimation in air. *Nat. Commun.* **2015,** *6*, 5954.

35. Pisula, W.; Kastler, M.; Wasserfallen, D.; Robertson, J. W.; Nolde, F.; Kohl, C.; Mullen, K. Pronounced supramolecular order in discotic donor-acceptor mixtures. *Angew. Chem.* **2006,** *45*, 819-823.

36. Schab-Balcerzak, E.; Iwan, A.; Grucela-Zajac, M.; Krompiec, M.; Podgorna, M.; Domanski, M.; Siwy, M.; Janeczek, H. Characterization, liquid crystalline behavior, optical and electrochemical study of new aliphatic–aromatic polyimide with naphthalene and perylene subunits. *Synth. Met.* **2011,** *161*, 1660-1670.

37. Würthner, F.; Thalacker, C.; Diele, S.; Tschierske, C. FluorescentJ-type Aggregates and Thermotropic Columnar Mesophases of Perylene Bisimide Dyes. *Chem. Eur. J.* **2001,** *7*, 2245-2253.

38. Stempfle, B.; Grosse, A.; Ferse, B.; Arndt, K. F.; Woll, D. Anomalous diffusion in thermoresponsive polymer-clay composite hydrogels probed by wide-field fluorescence microscopy. *Langmuir* **2014,** *30*, 14056-14061.

39. This claim is made to the best of our knowledge and a good-faith effort was put forward to identify reports to this effect. To establish this claim, we conducted a series of searches between (1st of August 2016 to 5th of June 2017). The search terms and parameters used to define novelty are outlined in the supporting information.

40. Sheldrick, G. M. SHELXT – Integrated space-group and crystal-structure determination. Acta Crystallogr., Sect. A: Found. Adv., 2015, 71, 3-8.

41. Sheldrick, G. M. Crystal structure refinement with SHELXL. Acta Crystallogr., Sect. C: Struct. Chem., 2015, 71, 3-8.

42. Nauha, E.; Naumov, P.; Lusi, M. Fine-tuning of a thermosalient phase transition by solid solutions. *CrystEngComm* **2016,** *18*, 4699-4703.

43. Skoko, Z.; Zamir, S.; Naumov, P.; Bernstein, J. The thermosalient phenomenon. "Jumping crystals" and crystal chemistry of the anticholinergic agent oxitropium bromide. *J. Am. Chem. Soc.* **2010,** *132*, 14191-14202.

44. Chandra Sahoo, S.; Nath, N. K.; Zhang, L.; Semreen, M. H.; Al-Tel, T. H.; Naumov, P. Actuation based on thermo/photosalient effect: a biogenic smart hybrid driven by light and heat. *RSC Adv.* **2014,** *4*, 7640.

45. Shima, T.; Muraoka, T.; Hoshino, N.; Akutagawa, T.; Kobayashi, Y.; Kinbara, K. Thermally Driven Polymorphic Transition Prompting a Naked-Eye-Detectable Bending and Straightening Motion of Single Crystals. *Angew. Chem.* **2014,** *126*, 7301-7306.

46. Siegrist, T.; Besnard, C.; Haas, S.; Schiltz, M.; Pattison, P.; Chernyshov, D.; Batlogg, B.; Kloc, C. A Polymorph Lost and Found: The High-Temperature Crystal Structure of Pentacene. *Adv. Mater.* **2007,** *19*, 2079-2082.

47. Ghosh, S.; Mishra, M. K.; Ganguly, S.; Desiraju, G. R. Dual Stress and Thermally Driven Mechanical Properties of the Same Organic Crystal: 2,6-Dichlorobenzylidene-4-fluoro-3-nitroaniline. *J. Am. Chem. Soc.* **2015,** *137*, 9912-9921.

48. Horie, M.; Suzaki, Y.; Hashizume, D.; Abe, T.; Wu, T.; Sassa, T.; Hosokai, T.; Osakada, K. Thermally-induced phase transition of pseudorotaxane crystals: changes in conformation and interaction of the molecules and optical properties of the crystals. *J. Am. Chem. Soc.* **2012,** *134*, 17932-17944.

49. Commins, P.; Desta, I. T.; Karothu, D. P.; Panda, M. K.; Naumov, P. Crystals on the move: mechanical effects in dynamic solids. *Chem Commun.* **2016,** *52*, 13941-13954.

50. Ng, W. K.; Kwek, J. W.; Yuen, A.; Tan, C. L.; Tan, R. Effect of milling on DSC thermogram of excipient adipic acid. *AAPS PharmSciTech* **2010,** *11*, 159-167.

51. Van Dooren, A. A.; Müller, B. W. Effects of heating rate and particle size on temperatures and specific enthalpies in quantitative differential scanning calorimetry. *Thermochim. Acta* **1982,** *54*, 115-129.

52. Color changes in response to temperature in BNDI are clear indications of bandgap changes within this semiconducting material. This is quite curious and this behavior, and a full solid-state and computational analysis of it will be followed up in a subsequent publication

CHAPTER 3

THE THERMO-RESPONSIVE BEHAVIOR IN MOLECULAR CRYSTALS OF

NAPHTHALENE DIIMIDES AND THEIR 3D PRINTED

THERMOCHROMIC COMPOSITES[1]

Authors – Madushani Dharmarwardana, Bhargav S. Arimilli, Michael A. Luzuriaga, Hamilton Lee, Gayan A. Appuhamillage, Gregory T. McCandless, Ronald A. Smaldone, Jeremiah J. Gassensmith

The Department of Chemistry, BE26

The University of Texas at Dallas

800 West Campbell Road

Richardson, Texas 75080-3021

[1]Dharmarwardana, M.; Bhargav, A. S.; Luzuriaga, M. A.; Lee, H.; McCandless, G. T.; Appuhamillage, G. A.; Smaldone, R. A.; Gassensmith, J.J. *Submitted.*

3.1 Summary

Herein, we communicate that altering the number of carbon atoms on the alkoxyphenyl substituent in naphthalene diimides results in tunable thermo-salient behavior across a variety of temperatures. Additionally, these compounds were found to display reversible thermochromic behavior in the single crystalline state. We analyzed this behavior using differential scanning calorimetry (DSC), single crystal X-ray diffraction (SXRD), powder XRD (PXRD), and hot-stage microscopy. The heptoxyphenyl-, octoxyphenyl-, and nonoxyphenyl- derivatives exhibited "acrobatic" behavior—namely, bending, jumping, and splitting—upon an irreversible phase transition. This study contributes to a developing paradigm in the understanding of certain naphthalene diimide single crystals that the energy associated with irreversible phase transitions has the potential to perform mechanical work, and that the temperature at which this energy can be fine-tuned by selecting an appropriate alkoxyphenyl substituent. Furthermore, we show that these thermochromic NDI derivatives can be incorporated into commercially-available, polymeric 3D printing materials and the resulting printed mixed polymer-crystalline objects still exhibit thermochromic behavior after incorporation.

3.2 Introduction

Mechanically responsive materials have gained much attention as they have potential applications in sensors, actuators, artificial muscles, and soft robots.[1-3] Polymers that exhibit mechanical motion upon exposure to external stimuli are very common.[3-5] These easily-fabricated materials have been shown to exhibit favorable elastic properties and high degrees of reversibility.[5,6] Mechanically responsive single crystals, however, have potential advantages relative to polymeric materials as

they can rapidly convert energy owing to the former's highly ordered periodic structure.[7] Recently, several studies on photo-mechanically responsive molecular crystals have appeared in literature.[1, 8-14] To date, only a handful of thermo-mechanically responsive—also known as thermo-salient—organic single crystals have been reported.[7, 14-24] These thermo-salient materials can be utilized as fuses,[25] switches, and sensors; however, thermo-mechanical behavior in molecular single crystals and the mechanism behind this motion are still areas of active research with few comprehensive structure-function studies.

Another type of stimuli-responsive behavior of interest is thermochromism, which refers to a change in color in response to a change in temperature.[26,27] Thermochromic materials have potential commercial applications as they can be fabricated into temperature sensors.[28] Most thermochromic compounds exhibit positive thermochromism, in which the material's high-temperature phase absorbs energy at a higher wavelength in comparison to its low-temperature phase. The opposite of this phenomenon is negative—or inverse—thermochromism, in which the high-temperature phase absorbs higher energy compare to the lower temperature phase. Compounds exhibiting inverse thermochromism are rare and have not been extensively reported in literature.[27,29-41] Organic single crystalline thermochromic materials are particularly interesting but are uncommon. In addition, efforts have been taken to expand the applicability of thermochromic materials in industrial settings. One such effort is the incorporation of thermochromic solids to polymeric matrices to fabricate thin films,[42-44] which has been done for many years. More advanced and contemporaneous methods of fabrication have come into vogue—in particular, additive manufacturing or 3D printing—a method to fabricate specific shapes by

adding material in a layer-by-layer fashion using CAD software.[45] 3D printing has become a major industry that is in search of materials and methods for integrating new and existing chemistry.[46-48] We recently reported[49] that a butoxyphenyl N-substituted derivative (BNDI) of naphthalene diimides—a class[50, 51] of highly electron-deficient aromatic compounds—exhibits thermo-mechanical properties followed by thermochromism. Thermo-mechanical properties of BNDI were found to be derived from an irreversible phase transition of a non-thermochromic monoclinic polymorph (BNDI-M) to a thermochromic triclinic polymorph (BNDI-T). Upon heating, the BNDI crystals underwent a complete rearrangement of the constituent molecules, releasing the accumulated stress in the form of mechanical motion which was sufficiently powerful to lift a metal ball ~100 times the mass of the crystal itself. We showed that a majority of BNDI crystals become bent during this irreversible phase transition. However, the temperature at which this transition occurs was quite high, restricting the self-actuating behavior to only high-temperature sensing applications. Further, our study left open the possibility that BNDI was unique in its behavior. We wondered whether other derivatives in this family would also actuate and if they would do so at lower-transition temperatures, making them useful in lower-temperature sensing applications.

To investigate this question, we synthesized a library of alkoxyphenyl N-substituted NDIs (ANDIs) by modifying the alkane chain emanating from the phenol group. Specifically, we synthesized pentyl- (PNDI), hexyl- (HxNDI), heptyl- (HNDI), octyl- (ONDI), and nonyl- (NNDI) derivatives. After extensive crystallographic, thermal, and optical analysis of ANDI single crystals, it is clear that the majority of ANDIs exhibit thermo-mechanical and thermochromic behavior. All of these thermochromic derivatives exhibit reversible thermochromism in the solid state and have

proven to be extremely robust at ambient conditions. Thus, this emerging class of thermochromic single crystals can be appropriated into thermally sensing materials. To demonstrate this concept, we were easily able to incorporate the non-thermo-salient crystals of the inversely thermochromic BNDI-T and positively thermochromic HxNDI derivatives into the thermoplastic polylactic acid (PLA) and hot extrude these mixtures into a filament. We then 3D printed different objects using these filaments *via* fused deposition modeling (FDM). These 3D printed objects then exhibited the reversible thermochromic properties of the parent crystals.

3.3   Experimental

3.3.1   Instrumentation

Nuclear Magnetic Resonance (NMR)

NMR spectra were measured using a Bruker ASCEND 600 MHz spectrometer in $CDCl_3$ and DMSO-d_6 using $Si(CH_3)_4$ as a reference standard.

Single Crystal X-Ray Diffraction (SXRD)

SXRD data were collected for ANDI derivatives using a Bruker Kappa D8 Quest diffractometer. Bruker Kappa D8 Quest diffractometer is equipped with an Incoatec microfocus Mo Kα radiation source, HELIOS multilayer optics, Oxford Cryosystems cryostream, and a Photon 100 CMOS detector. Bruker SAINT was used for all data sets for integration and scaling, SADABS was used for absorption correction (multi-scan) and analysis of systematic absences of hkl reflections and XPREP was used for space group selection. All initial triclinic and monoclinic models of the two polymorphs were generated with SHELXT (intrinsic phasing method)[1] and least-squares refinement was carried out with SHELXL2014.[2]

Powder X-Ray Diffraction (PXRD)

PXRD were collected using a Rigaku Ultima III XRD equipped with Cu Kα radiation.

Thermal Analysis

Thermal properties of BNDI samples were analyzed with differential scanning calorimetry (DSC) using a TA Instruments Q2000. The samples were heated from 0 °C to 240 °C at a heating rate of 10 K/min, under a flow of nitrogen (50 mL/min).

Hot-Stage Polarized Optical Microscopy

Thermo-mechanical behavior was analyzed using a MEIJI TECHNO ML9000 series polarizing microscope equipped with an Instech hot stage. The maximum temperature that the sample can be heated on this stage is 200 °C. The sample was placed on a 1 mm thick glass slide and the sample was cooled 0 °C by sending cooled nitrogen gas through the stage. Then the sample was heated to 200 °C. The actual temperature of the stage was determined by a Phidget Temperature Sensor (P/N 1051_2).

3D Printed BNDI/PLA Filament

BNDI-T was mixed at 150°C with polylactic acid (PLA) at 1:19 and 1:9 w/w% until homogenous. Approximately ten grams of BNDI-T:PLA at 1:19 were cut into small pieces to be inserted into a Filabot original benchtop extruder (Filabot, Barre, VT). The extruder was run at 170°C with pure PLA for 10 min. At the same temperature, the BNDI-T@PLA blend was added and extruded to obtain an average filament diameter of 2.35 mm. Dog bones were designed using the open source Blender software package (https://www.blender.org) and printed with a LulzBot TAZ 5 3D printer (Figure 6, Aleph Object, Inc., Loveland, CO). The printer was operated using the open source Cura software package for LulzBot. The printing parameters used to fabricate the thermochromic 3D printed objects are as such: print speed: 50 mm/s, layer height: 0.25 mm, shell thickness: 0.50 mm,

retraction speed: 10 mm/s, travel speed: 175 mm/s, bottom layer speed: 15 mm/s, infill speed: 30 mm/s, top/bottom speed: 35 mm/s, outer shell speed: 35 mm/s, and inner shell speed: 35 mm/s. The temperature of the hot end was set at 190°C, and the temperature of the print bed was set to 65 °C. A print head with a 0.50 mm nozzle diameter was used. Filaments were also extruded with BNDI-T@PLA at 1:19 w/w% and with HxNDI@PLA at 1:9 w/w %. to print thermochromic dog bones (Figure 7).

3.3.2   Synthesis and Characterization

Synthesis of NDI-Ph

Phenyl N-substituted naphthalene diimide (NDI-Ph) was prepared as shown in Scheme 3.1. A mixture of 1,4,5,8-naphthalenetetracarboxylic dianhydride (4.582 g, 2.119 mmol and 4-aminophenol (4.627 g, 4.240 mmol) was heated under reflux at 130 °C for 24 h. The reaction product was then collected under filtration and washed with dimethylformamide. ^{1}H-NMR (600 MHz, DMSO-D$_6$, ppm) (Figure S1): 6.90 (d, 8.6 Hz, 4H), 7.22 (d, 8.3 Hz, 4 H), 8.85 (s, 4 H).

Synthesis of BNDI

Butoxyphenyl N-substituted naphthalene diimide (BNDI) was prepared using a previously described method.[49]

Synthesis of PNDI

Pentoxyphenyl N-substituted naphthalene diimide (PNDI) was prepared as shown in Scheme 3.1. NDI-Phenol (1.980 g, 4.400 mmol) was mixed with 1-bromopentane (1.330 g, 8.800 mmol) in 1-methyl-2-pyrrolidinone (80.00 mL) and heated to 70 °C for 6 h. The reaction mixture was poured into diluted hydrochloric acid and a precipitate was observed, filtered under vacuum, and purified using column chromatography (hexane-DCM) with a 60.11% yield. ^{1}H-NMR (600 MHz, CDCl$_3$,

ppm): 0.94 (t, 7.3 Hz, 6 H), 1.40 (s, 7.3 Hz, 4 H), 1.46 (q, 7.8 Hz, 4 H), 1.82 (q, 7.1 Hz, 4 H), 4.01 (t, 6.5 Hz, 4 H), 7.06 (d, 8.4 Hz, 4 H), 7.22 (d, 8.4 Hz, 4 H), 8.81 (s, 4H).

Synthesis of HxNDI

Hexoxyphenyl N-substituted naphthalene diimide (HxNDI) was prepared according to our previously published literature[49] with a 63.02% yield. ^{1}H-NMR (600 MHz, CDCl$_3$, ppm): 0.93 (t, 6.3 Hz, 6 H), 1.37 (m, 3.7 Hz, 8 H), 1.50 (q, 7.9 Hz, 4 H), 1.83 (q, 7.5 Hz, 4 H), 4.03 (t, 7.6 Hz, 4 H), 7.08 (d, 8.6 Hz, 4 H), 7.24 (d, 8.5 Hz, 4 H), 8.83 (s, 4H).

Synthesis of HNDI

Heptoxyphenyl N-substituted naphthalene diimide (HNDI) was prepared as shown in Scheme 3.1. NDI-Phenol (1.980 g, 4.400 mmol) was mixed with 1-bromoheptane (1.576 g, 8.800 mmol) in 1-methyl-2-pyrrolidinone (80.00 mL) and heated to 70 °C for 6 hours. The reaction mixture was poured into diluted hydrochloric acid and a precipitate was observed, filtered under vacuum, and purified using column chromatography (hexane-DCM) with a 63.02% yield. ^{1}H-NMR (600 MHz, CDCl$_3$, ppm): 0.89 (t, 6.9 Hz, 6 H), 1.32 (m, 7.7 Hz, 8 H), 1.37 (m, 7.7 Hz, 4 H), 1.47 (q, 7.6 Hz, 4 H), 1.81 (q, 7.4 Hz, 4 H), 4.01 (t, 6.6 Hz, 4 H), 7.06 (d, 8.4 Hz, 4 H), 7.22 (d, 8.3 Hz, 4 H), 8.81 (s, 4H).

Synthesis of ONDI

Octoxyphenyl N-substituted naphthalene diimide (ONDI) was prepared as shown in Scheme 3.1. NDI-Phenol (1.980 g, 4.400 mmol) was mixed with 1-bromooctane (1.699 g, 8.800 mmol) in 1-methyl-2-pyrrolidinone (80.00 mL) and heated to 70 °C for 6 hours. The reaction mixture was poured into diluted hydrochloric acid and a precipitate was observed, filtered under vacuum, and purified using column chromatography (hexane-DCM) with a 62.75% yield. 1H-NMR (600 MHz,

CDCl3, ppm) (Figure S5): 0.91 (t, 6.9 Hz, 6H), 1.33 (m, 6.5 Hz, 16 H), 1.49 (q, 7.7 HZ, 4 H), 1.83 (q, 7.6 Hz, 4 H), 4.03 (t, 6.6 Hz, 4 H), 7.08 (d, 8.8 HZ, 4 H), 7.24 (d, 8.6 Hz, 4 H), 8.84 (s, 4 H).

Synthesis of NNDI

Nonoxyphenyl N-substituted naphthalene diimide (NNDI) was prepared as shown in Scheme 3.1. NDI-Phenol (1.980 g, 4.400 mmol) was mixed with 1-bromononane (1.820 g, 8.800 mmol) in 1-methyl-2-pyrrolidinone (80.00 mL) and heated to 70 °C for 6 hours. The reaction mixture was poured into diluted hydrochloric acid and a precipitate was observed, filtered under vacuum, and purified using column chromatography (hexane-DCM) with a 69.57% yield. ^{1}H-NMR (600 MHz, CDCl$_3$, ppm): 0.90 (t, 7.0 Hz, 6 H), 1.33 (m, 6.1 Hz, 20 H), 1.49 (q, 7.3 Hz, 4 H), 1.83 (q, 7.3 Hz, 4 H), 4.03 (t, 6.2 Hz, 4 H), 7.08 (d, 8.4 Hz, 4 H), 7.24 (d, 8.4 Hz, 4 H), 8.83 (s, 4 H).

3.3.3 Crystal data

Crystal data for HxNDI. C$_{38}$H$_{38}$N$_2$O$_6$, M$_r$ = 618.7, monoclinic, a = 8.395(3), b = 8.853(3), c = 23.938(9) Å, α = 89.528(11), β = 80.712(14), γ = 62.60(2)°, V = 1554.3(10) Å^3, T = 100 K, space group P$\bar{1}$, Z = 2, μ = 0.09 mm^{-1}, 20000 reflections measured, 7191 unique (R$_{int}$ = 0.044) which were used in all calculations. The final wR(2) was 0.133 (all data) and R(1) was 0.055 (>2σ(I)). CCDC deposition number 1839983.

Crystal data for HNDI. C$_{40}$H$_{42}$N$_2$O$_6$, M$_r$ = 646.75, monoclinic, a = 4.1696(15), b = 46.595(14), c = 8.214(3) Å, α = 90, β = 93.529(10), γ = 90°, V = 1592.7(9) Å^3, T = 100 K, space group P2$_1$, Z = 2, μ = 0.09 mm^{-1}, 40965 reflections measured, 3672 unique (R$_{int}$ = 0.060) which were used in all calculations. The final wR(2) was 0.104 (all data) and R(1) was 0.046 (>2σ(I)). CCDC deposition number 1839985.

Crystal data for ONDI, polymorph 1. $C_{42}H_{46}N_2O_6$, $M_r = 674.81$, triclinic, $a = 4.1680(14)$, $b = 8.217(3)$, $c = 24.901(7)$ Å, $\alpha = 97.81(1)$, $\beta = 93.453(7)$, $\gamma = 90°$, $V = 841.0(5)$ Å^3, T = 100 K, space group P$\bar{1}$, Z = 1, $\mu = 0.09$ mm^{-1}, 25306 reflections measured, 3887 unique ($R_{int} = 0.076$) which were used in all calculations. The final wR(2) was 0.120 (all data) and R(1) was 0.054 (>2σ(I)). CCDC deposition number 1839986.

Crystal data for NNDI. $C_{44}H_{50}N_2O_6$, $M_r = 702.86$, monoclinic, $a = 4.154(2)$, $b = 51.72(2)$, $c = 8.253(3)$ Å, $\alpha = 90(1)$, $\beta = 93.663(12)$, $\gamma = 90°$, $V = 1769.6(14)$ Å^3, T = 100 K, space group P2$_1$, Z = 2, $\mu = 0.09$ mm^{-1}, 36862 reflections measured, 4080 unique ($R_{int} = 0.095$) which were used in all calculations. The final wR(2) was 0.118 (all data) and R(1) was 0.055 (>2σ(I)). CCDC deposition number 1839987.

3.4   Results and Discussion

3.4.1   Synthesis and Crystallization of ANDI Derivatives
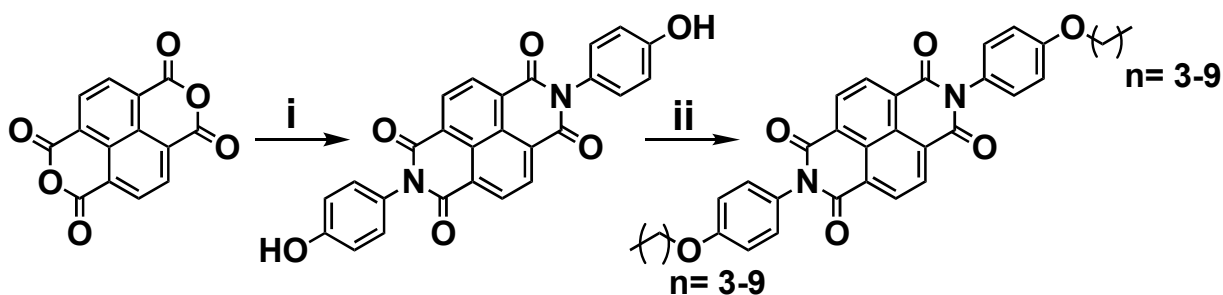
Figure 3.1. Synthesis of alkoxyphenyl N-substituted naphthalene diimides discussed in this study. (i) 4-aminophenol, 24 h in DMF. (ii) 1-bromoalkane of appropriate chain length, 24 h DMF 140 °C

All NDI derivatives used in this study were synthesized using naphthalene tetracarboxylic acid dianhydride (NDA). NDA was initially combined with 4-aminophenol to obtain phenyl N-substituted NDI. This compound was then subjected to nucleophilic substitution of different bromoalkenes to yield a library of ANDI derivatives (Figure 3.1).[52] In our previous study, we

discovered that BNDI can be crystallized into two stable polymorphs—a thermochromic triclinic phase and a mechanically responsive monoclinic phase.[49] When we tried these same methods to generate single crystal polymorphs for each ANDI derivative, we found that none of them produced high-quality single crystals suitable for single crystal X-ray diffraction (SXRD) analysis.

Table 3.1. Crystallographic parameters for ANDI derivatives.

		BNDI-M	BNDI-T	HxNDI	HNDI	ONDI	NNDI
Temperature/ K		100	100	100	100	100	100
Crystal system		monoclinic	triclinic	triclinic	monoclinic	triclinic	monoclinic
Space group		P2$_1$/c	P$\bar{1}$	P$\bar{1}$	P2$_1$/n	P$\bar{1}$	P2$_1$/n
Unit cell/Å	$a =$	5.026(2)	4.1636(8)	8.395(3)	4.1696(15)	4.1680(14)	4.154(2)
	$b =$	33.756(5)	8.1371(18)	8.853(3)	46.595(14)	8.217(3)	51.72(2)
	$c =$	7.9533(14)	20.104(5)	23.938(9)	8.214(3)	24.901(7)	8.253(3)
	$\alpha =$	90°	100.182(11)°	89.528(11)°	90°	97.81(1)°	90°
	$\beta =$	99.997(10)°	93.124(14)°	80.712(14)°	93.529(10)°	93.453(7)°	93.663(12)°
	$\gamma =$	90°	94.102(14)°	62.60(2)°	90°	93.834(6)°	90°
Volume/ Å^3		1328.8(6)	667.1(3)	1554.3(10)	1592.7(9)	841.0(5)	1769.6(14)
Crystal color		yellow	red/orange	orange	orange	orange	orange
Z		2	1	2	2	1	2
Interplanar distance(s)/ Å		3.344	3.369	3.413 3.189	3.392	3.402	3.403

To grow single crystals, we used our automated flash chromatography system to create gradients of solvent concentrations for each sample. Following chromatographic separation of the crude ANDI derivatives, the resulting solutions sat undisturbed until fully evaporated and each vial was scanned for suitable single crystals. All the ANDI derivatives we report in this manuscript yielded single crystals using this modified slow evaporation technique and we were able to collect SXRD data for each derivative (Table 3.1). While we were able to obtain single crystals for the PNDI compound, the data set was low-resolution and the refined and converged structure still had high

R-factors. Consequently, we omit this system from the crystallographic discussion, but we elaborate upon it in the thermally responsive sections.

Table 3.2. Summary of properties of ANDI derivatives studied in this manuscript.

n	Material	Crystal system	Thermochromic	Thermo-salient	Molecular arrangement	Irreversible phase transition/ K
3	BNDI-M	Monoclinic	✘	✔	herringbone	113.46
4	BNDI-T	Triclinic	✔	✘	infinite 1D chains	NA
4	PNDI	NA	✔	✘	NA	NA
5	HxNDI	Triclinic	✔	✘	infinite 1D chains	NA
6	HNDI	Monoclinic	✔	✔	herringbone	105.90
7	ONDI	Triclinic	✔	✔	lamellar	72.09
8	NNDI	Monoclinic	✔	✔	herringbone	100.69

3.4.2 Thermo-mechanical and Thermochromic Behavior of ANDI family
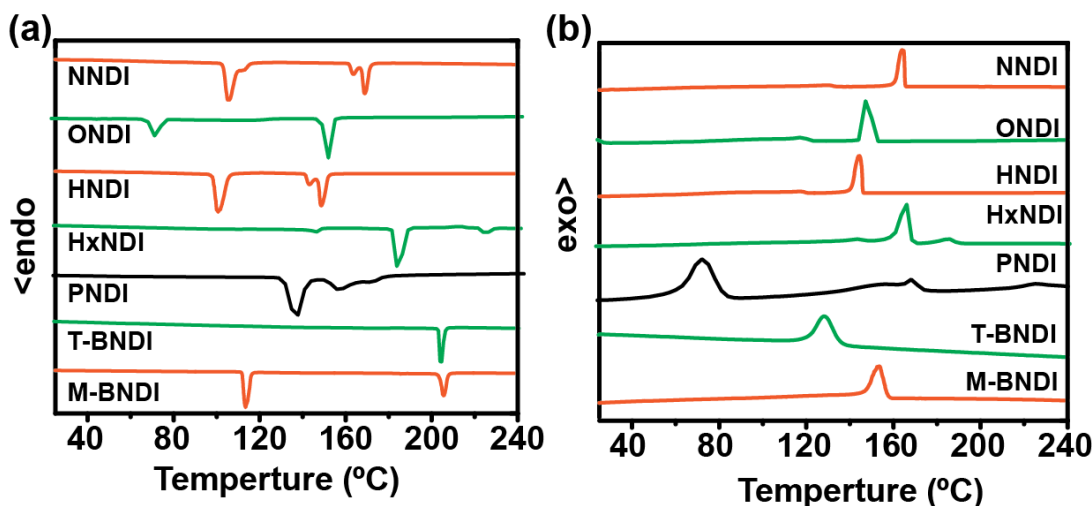
Figure 3.2. (a) Heating curves of ANDI derivatives and their corresponding (b) cooling curves. Orange lines correspond to monoclinic crystal systems and green lines correspond to triclinic crystal systems.

As demonstrated in our previous work, BNDI's irreversible phase transition was found to be associated with the presence of thermo-salient behavior. Thermo-salient behavior includes jumping, splitting, coiling, or other motion in response to heat and so far, the only ANDI derivative

it has been observed in is BNDI-M.[49] We thus decided to investigate whether other ANDI

derivatives possessing irreversible phase transitions would exhibit the same behaviour.
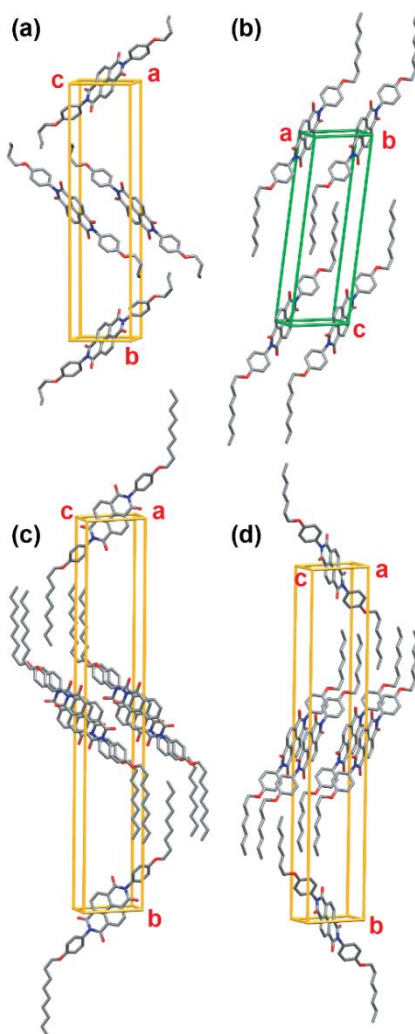
Figure 3.3. Comparison of thermo-salient derivative unit cells: (a) BNDI-M (b) ONDI and (c) NNDI (d) HNDI. Orange unit cell axes correspond to monoclinic crystal systems and green unit cell axes correspond to triclinic crystal systems.

The thermo-salient behaviour of ANDIs was characterized by DSC, SXRD, and hot-stage

microscopy. We first conducted DSC for all the derivatives within the temperature range of 25 °C

to 240 °C. As shown in Figure 3.2, all the compounds undergo phase transitions within this

temperature range; however, we have found that the thermo-salient properties occur only at the

irreversible phase transitions, which is what we are focusing on here as any thermo-responsive behaviour at temperatures higher than 200 °C could not be analysed due to constraints of our hot stage microscope.
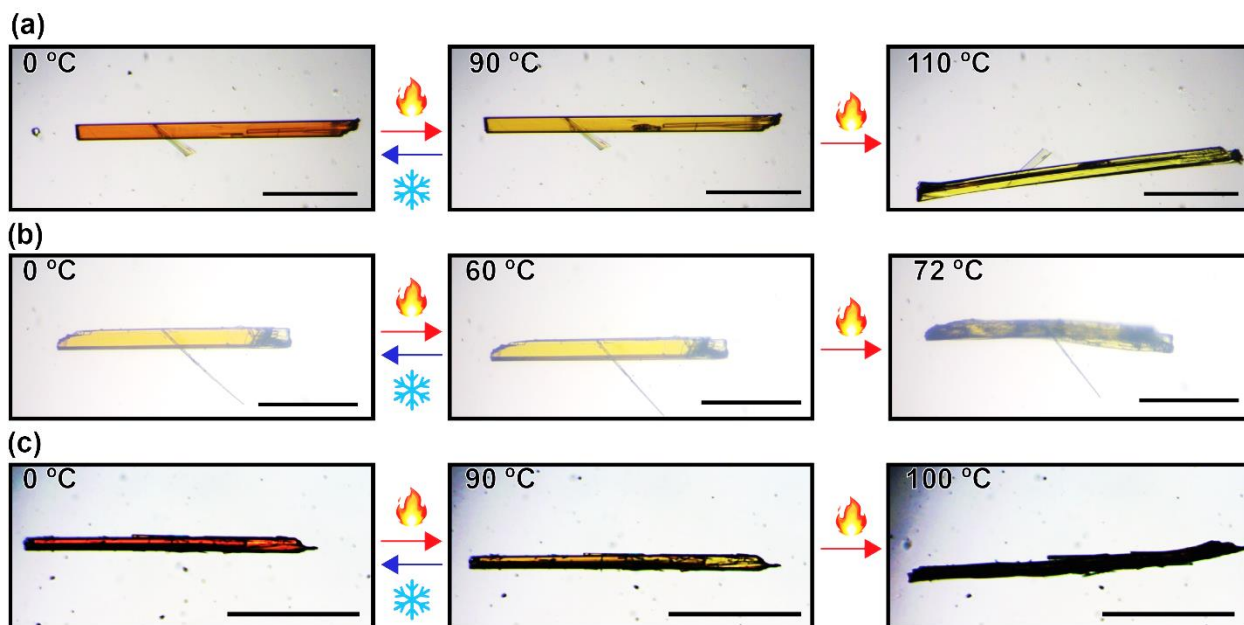
Figure 3.4. Thermochromic and thermo-mechanical properties of (a) HNDI, (b) ONDI, and (c) NNDI. First two images in a sequence show thermochromic behaviour (if any) and the final, irreversible step shows the product of the thermo-salient behaviour—typically the crystal splits. Scale bar is 500 μm

DSC analysis of each derivative yielded surprising results and showed that thermo-responsive behaviour in ANDI derivatives is dependent on the alkoxyphenyl substituent and solid-state packing. As shown in Figure 3.2a and Table 3.2, compounds BNDI-M, HNDI, ONDI, and NNDI each undergo an irreversible phase transition followed by a reversible phase transition at an even higher temperature. The temperature at which the irreversible phase transition occurs for three derivatives—BNDI-M (4 carbons, 113.46 °C), HNDI (7 carbons, 105.90 °C), and NNDI (9 carbons, 100.69 °C)—decreases as the chain length of the alkane group increases. This similarity in thermal behaviour can also be explained via SXRD analysis of BNDI-M, HNDI and NNDI. All

three derivatives show similar herringbone molecular packing and belong to the monoclinic crystal system (Table 3.1 and Figure 3.3). Curiously, ONDI exhibits a lower transition temperature (8 carbons, 72.09 °C) compared to these three derivatives. Unlike the previous three derivatives, ONDI was solved as a triclinic crystal system and its packing is also slightly different, as it packs in a lamellar array instead of a herringbone arrangement. HxNDI exhibited no irreversible phase transitions and its packing, which is significantly different than the other derivatives, will be discussed later. Finally, PNDI crystals diffracted poorly, limiting SXRD data analysis. However, according to our thermal analysis of PNDI, no irreversible phase transitions were observed (black line, Figure 3.1).
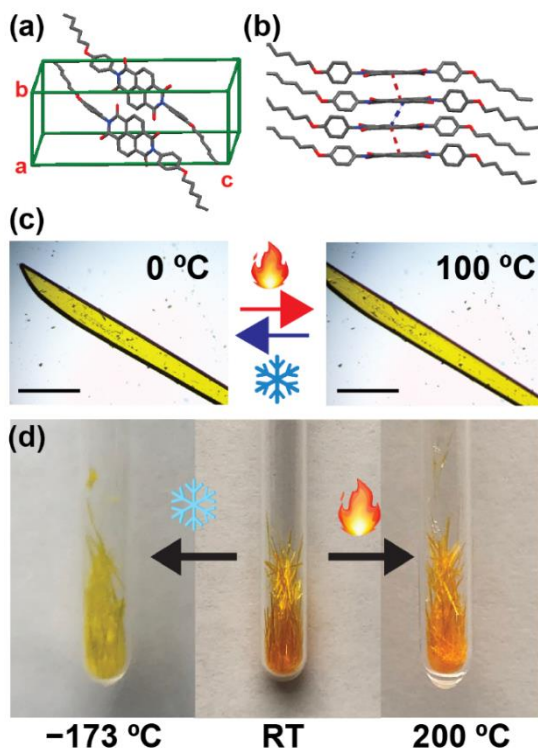
Figure 3.5. (a) Unit cell packing structure of HxNDI, (b) alternating interplanar distances of HxNDI (c) POM images showing HxNDI single crystal expansion during heating from 0 °C to 100 °C (Scale Bar is 500 µm), and (d) thermochromic behaviour of HxNDI.

We characterized the thermo-responsive behavior of the ANDI single crystals using hot-stage microscopy and SXRD. We first placed each derivative on a polarized optical microscope (POM) heating stage that was cooled under cold nitrogen gas to 0 °C. The samples were then heated, during which we observed thermo-mechanical motion at temperatures beyond the phase transition (Figure 3.4). As shown in Figure 3.4a, HNDI single crystals exhibited reversible thermochromism until they reached 105.90 °C. At this temperature, a wave front began at one end of the crystal and moved to the other end, followed by a change in color from orange/yellow to bright yellow (Figure 3.4a) At this point, crystals began to exhibit motions including bending, jumping, and splitting. After this irreversible phase transition, HNDI crystals were no longer thermochromic and were not suitable for SXRD analysis, as they were no longer single crystalline in nature. Thus, we performed PXRD analysis to confirm that the phase transition occurred fully (Appendix B).
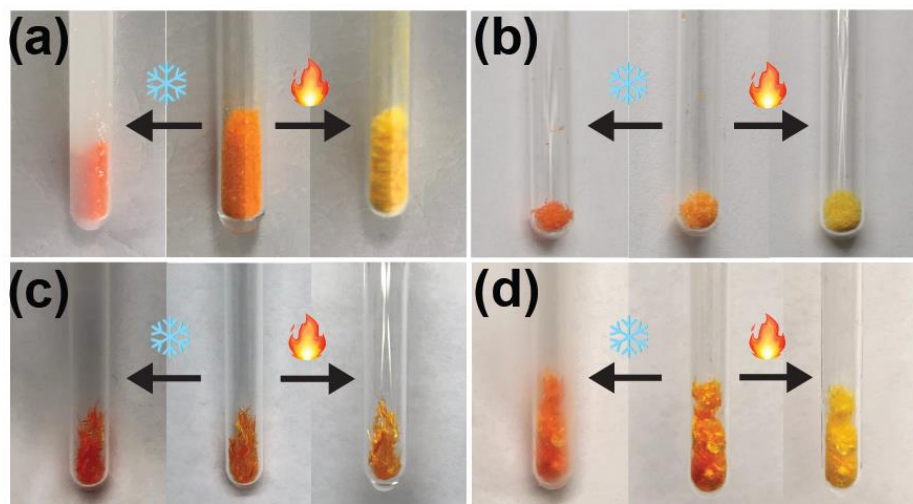
Figure 3.6. Thermochromic behavior of (a) PNDI, (b) HNDI, (c) ONDI, and (d) NNDI. All the samples were heated to 100 °C and cooled to −173 °C for the visualization of thermochromic behavior.

Similarly, we conducted hot-stage microscopy for NNDI and ONDI, which exhibited similar thermochromic and thermo-mechanical behavior as HNDI (Figure 3.4b and 3.4c). Finally, we

analyzed the thermo-responsive behavior of HxNDI using hot stage microscopy. As shown in Figure 3.5b, we found that HxNDI crystals showed anomalous expansion during heating, with a slight change in the crystal color. However, the crystals returned back to their original size and color as we cooled the crystals back to room temperature. More importantly, we did not observe any thermo-salient behavior.
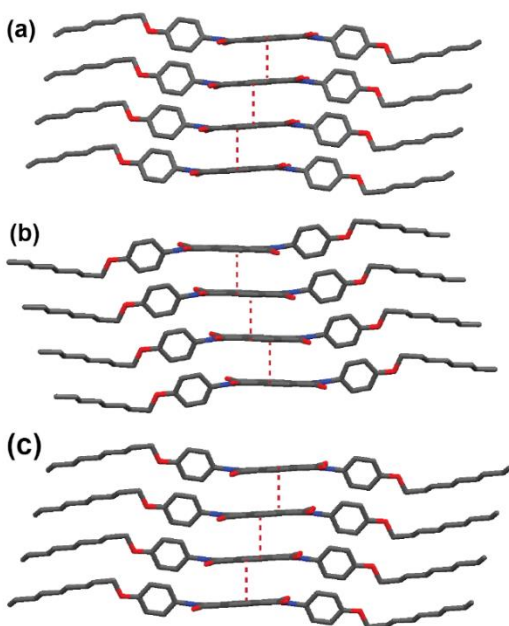
Figure 3.7. Comparison of interplanar distances of ANDI derivatives; (a) HNDI, (b) ONDI, and (c) NNDI.

In contrast to thermo-salience, we observed that all derivatives studied in this manuscript exhibited some type of thermochromism. Typically, crystals showed red/orange (low temperature) to yellow (high temperature) inverse thermochromic behavior, with the exception of HxNDI, which exhibited yellow (low temperature) to orange (high temperature) positive thermochromic behavior (Table 3.2, Figure 3.6, and Figure 3.5d). Of all the compounds we analyzed in this study, HxNDI exhibited anomalous behavior in the solid state. After careful analysis of its crystal structure, we found that the dihedral angles of HxNDI's two phenyl rings with respect to its NDI core were not

the same and measured 55.25(6)° and 74.18(5)°. In contrast, the other ANDI derivatives are symmetric at both ends and thus have matching dihedral angles. Furthermore, BNDI, HNDI, and NNDI each possessed a single interplanar π-π stacking distance (Figure 3.7). HxNDI, however, possessed two interplanar π-π stacking distances—3.413 Å and 3.189 Å—that alternated throughout its crystal structure (Figure 3.5b).

3.4.3 3D Printing with BNDI-T and HxNDI
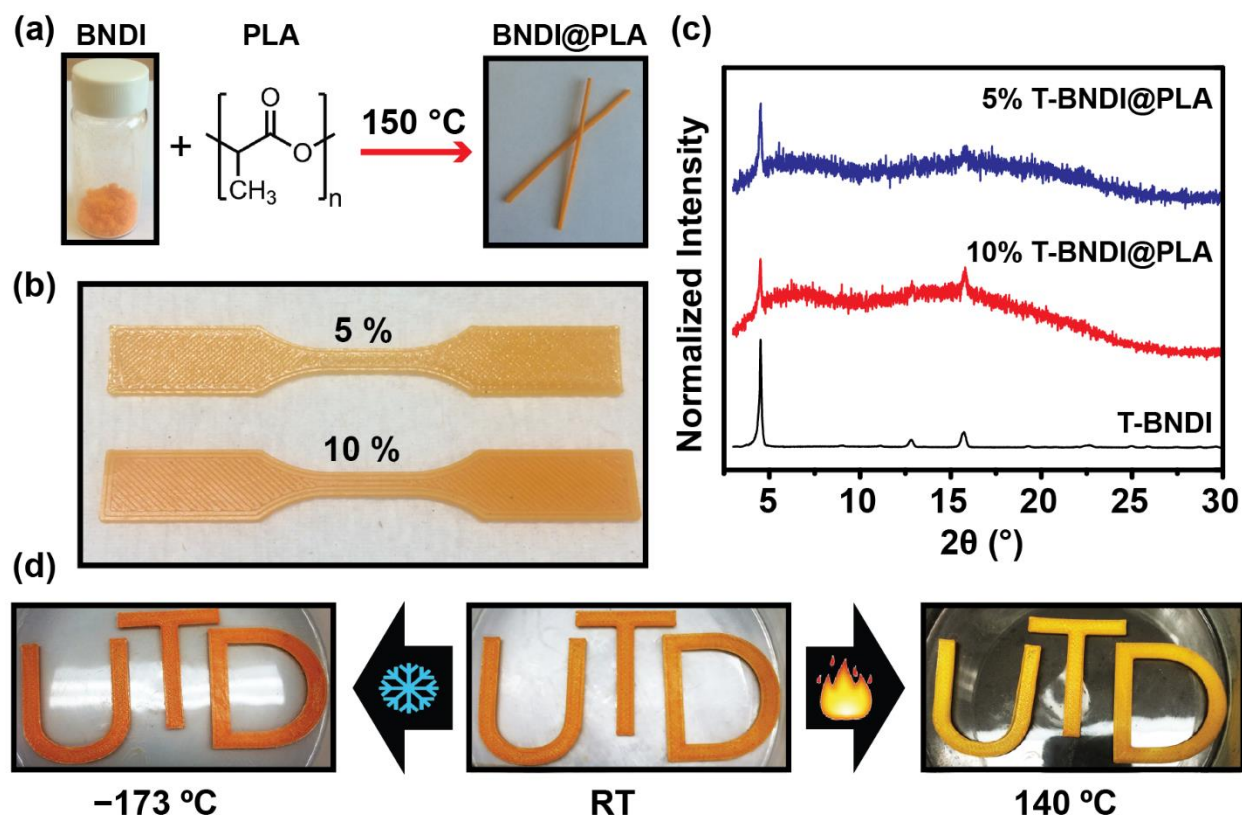
Figure 3.8. (a) Schematic diagram of the fabrication of BNDI-T@PLA filaments, (b) varying ratios of BNDI-T incorporated into PLA, (c) PXRD data for BNDI-T@PLA composites, and (d) negative thermochromic behavior of BNDI-T@PLA.

The robustness and practical temperature range of the thermochromism of these samples inspired us to attempt to integrate them into thermoplastic matrices to produce thermally responsive

polymers. Thermochromic materials have long been used as a visual indicator of surface temperature. With the emergence of 3D printing using thermoplastics, new technologies that can exploit the robust nature of solid-state materials would be a benefit. Since we have identified both positive and negative thermochromic materials, we decided to see if we could make 3D printed composites of each.
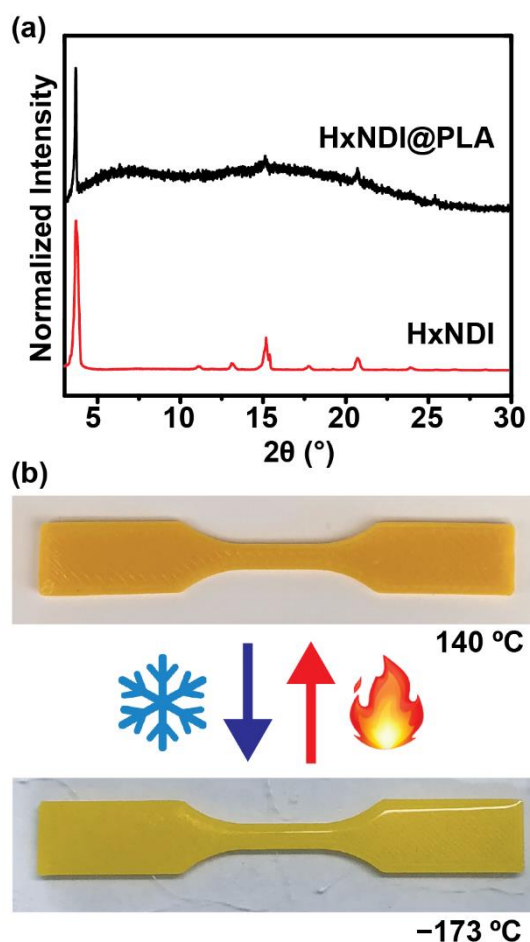
Figure 3.9. (a) PXRD data for HxNDI@PLA composites and (b) positive thermochromic behavior of HxNDI @PLA.

Mixtures of PLA beads—an inexpensive, biodegradable polymeric material commonly used in 3D printing—and crystals of either BNDI-T or HxNDI were added to a filament extruder, which produced long, single wires of ANDI@PLA. We first melted PLA with BNDI-T in 1:19 and 1:9

ratios at 200 ℃ (Figure 3.7b). The BNDI-T@PLA composite was characterized using PXRD (Figure 3.8c). This result demonstrate that the crystalline morphology of BNDI-T does not undergo degradation when incorporated into PLA at elevated temperatures and the resulting plastics appear smooth and the color homogenously distributed. We then tested the thermochromic properties of the BNDI-T@PLA composite. As shown in Figure 3.7d, the composite exhibited clear reversible thermochromic behavior. Higher concentrations of BNDI-T showed a more pronounced color change (Figure 3.8d).

To visualize positive thermochromism in a polymeric system, HxNDI single crystals were combined with PLA in a 1:9 ratio. As seen in Figure 3.9a 3D printed PLA dog bone featuring HxNDI did exhibit modest positive thermochromic behavior, with the low temperature plastic being bright yellow and the high temperature plastic being orange. Again, the 3D printing and hot extrusion did not appear to degrade the crystals inside the filament.

3.5   Conclusions

We have shown thermally-induced, irreversible phase transitions are a common property of alkoxyphenyl N-substituted naphthalene diimides. Some of these single crystals exhibit thermo-salient behavior, such as bending, jumping, and splitting. The temperature at which this behavior occurs can be modulated based on the length of the alkoxyphenyl chain, as observed in our family of derivatives. In general, the temperatures at which the thermo-salience occur decrease with increasing alkyl chain length. In all cases, compounds exhibited thermochromic behavior and this behavior could be reproduced with the 6- and 4-carbon chained ANDI derivatives inside a 3D printed polymeric matrix. Negatively and positively thermochromic 3D printed composites were created using BNDI-T and HxNDI, respectively. With the emergence of 3D printing, temperature

responsive organic single crystals may serve as dopants with the organic thermo-polymeric filaments to enhance their use and utility. Finally, it should be mentioned that alkoxyphenyl NDI derivatives have been used in organic electronics as n-type semiconducting materials.[53, 54] Even when combined in polymeric systems, it is quite clear a color change (and presumably a band-gap change) occurs based on temperature.

3.6   References

1. Naumov, P.; Chizhik, S.; Panda, M. K.; Nath, N. K.; Boldyreva, E. Mechanically Responsive Molecular Crystals. *Chem. Rev.* **2015,** *115*, 12440-12490.

2. Yamada, M.; Kondo, M.; Mamiya, J.; Yu, Y.; Kinoshita, M.; Barrett, C. J.; Ikeda, T. Photomobile polymer materials: towards light-driven plastic motors. *Angew. Chem.* **2008,** *47*, 4986-4988.

3. White, T. J.; Tabiryan, N. V.; Serak, S. V.; Hrozhyk, U. A.; Tondiglia, V. P.; Koerner, H.; Vaia, R. A.; Bunning, T. J. A high frequency photodriven polymer oscillator. *Soft Mat.* **2008,** *4*, 1796.

4. Natansohn, A.; Rochon, P. Photoinduced Motions in Azo-Containing Polymers. *Chem. Rev.* **2002,** *102*, 4139-4176.

5. Yu, Y.; Nakano, M.; Ikeda, T. Photomechanics: directed bending of a polymer film by light. *Nature* **2003,** *425*, 145.

6. Pelrine, R. High-Speed Electrically Actuated Elastomers with Strain Greater Than 100%. *Science* **2000,** *287*, 836-839.

7. Nath, N. K.; Panda, M. K.; Sahoo, S. C.; Naumov, P. Thermally induced and photoinduced mechanical effects in molecular single crystals—a revival. *CrystEngComm* **2014,** *16*, 1850.

8. Krishna, G. R.; Devarapalli, R.; Lal, G.; Reddy, C. M. Mechanically Flexible Organic Crystals Achieved by Introducing Weak Interactions in Structure: Supramolecular Shape Synthons. *J. Am. Chem. Soc.* **2016**.

9. Kobatake, S.; Takami, S.; Muto, H.; Ishikawa, T.; Irie, M. Rapid and reversible shape changes of molecular crystals on photoirradiation. *Nature* **2007,** *446*, 778-781.

10. Kitagawa, D.; Tsujioka, H.; Tong, F.; Dong, X.; Bardeen, C. J.; Kobatake, S. Control of Photomechanical Crystal Twisting by Illumination Direction. *J. Am. Chem. Soc.* **2018,** *140*, 4208-4212.

11. Kitagawa, D.; Kawasaki, K.; Tanaka, R.; Kobatake, S. Mechanical Behavior of Molecular Crystals Induced by Combination of Photochromic Reaction and Reversible Single-Crystal-to-Single-Crystal Phase Transition. *Chem. Materials* **2017,** *29*, 7524-7532.

12. Takanabe, A.; Tanaka, M.; Johmoto, K.; Uekusa, H.; Mori, T.; Koshima, H.; Asahi, T. Optical Activity and Optical Anisotropy in Photomechanical Crystals of Chiral Salicylidenephenylethylamines. *J. Am. Chem. Soc.* **2016,** *138*, 15066-15077.

13. Medishetty, R.; Sahoo, S. C.; Mulijanto, C. E.; Naumov, P.; Vittal, J. J. Photosalient Behavior of Photoreactive Crystals. *Chem. Mater.* **2015,** *27*, 1821-1829.

14. Chandra Sahoo, S.; Nath, N. K.; Zhang, L.; Semreen, M. H.; Al-Tel, T. H.; Naumov, P. Actuation based on thermo/photosalient effect: a biogenic smart hybrid driven by light and heat. *RSC Adv.* **2014,** *4*, 7640.

15. Commins, P.; Desta, I. T.; Karothu, D. P.; Panda, M. K.; Naumov, P. Crystals on the move: mechanical effects in dynamic solids. *Chem. Commun.* **2016,** *52*, 13941-13954.

16. Skoko, Z.; Zamir, S.; Naumov, P.; Bernstein, J. The thermosalient phenomenon. "Jumping crystals" and crystal chemistry of the anticholinergic agent oxitropium bromide. *J. Am. Chem. Soc.* **2010,** *132*, 14191-14202.

17. Sahoo, S. C.; Sinha, S. B.; Kiran, M. S.; Ramamurty, U.; Dericioglu, A. F.; Reddy, C. M.; Naumov, P. Kinematic and mechanical profile of the self-actuation of thermosalient crystal twins of 1,2,4,5-tetrabromobenzene: a molecular crystalline analogue of a bimetallic strip. *J. Am. Chem. Soc.* **2013,** *135*, 13843-13850.

18. Panda, M. K.; Runcevski, T.; Husain, A.; Dinnebier, R. E.; Naumov, P. Perpetually self-propelling chiral single crystals. *J. Am. Chem. Soc.* **2015,** *137*, 1895-1902.

19. Panda, M. K.; Runcevski, T.; Sahoo, S. C.; Belik, A. A.; Nath, N. K.; Dinnebier, R. E.; Naumov, P. Colossal positive and negative thermal expansion and thermosalient effect in a pentamorphic organometallic martensite. *Nat. Commun* **2014,** *5*, 4811.

20. Nauha, E.; Naumov, P.; Lusi, M. Fine-tuning of a thermosalient phase transition by solid solutions. *CrystEngComm* **2016,** *18*, 4699-4703.

21. Panda, M. K.; Centore, R.; Causa, M.; Tuzi, A.; Borbone, F.; Naumov, P. Strong and Anomalous Thermal Expansion Precedes the Thermosalient Effect in Dynamic Molecular Crystals. *Sci. Rep.* **2016,** *6*, 29610.

22. Takeda, T.; Akutagawa, T. Anisotropic Dissociation of pi-pi Stacking and Flipping-Motion-Induced Crystal Jumping in Alkylacridones and Their Dicyanomethylene Derivatives. *Chem. Eur. J.* **2016,** *22*, 7763-7770.

23. Ghosh, S.; Mishra, M. K.; Ganguly, S.; Desiraju, G. R. Dual Stress and Thermally Driven Mechanical Properties of the Same Organic Crystal: 2,6-Dichlorobenzylidene-4-fluoro-3-nitroaniline. *J. Am. Chem. Soc.* **2015,** *137*, 9912-9921.

24. Sahoo, S. C.; Panda, M. K.; Nath, N. K.; Naumov, P. Biomimetic crystalline actuators: structure-kinematic aspects of the self-actuation and motility of thermosalient crystals. *Journal of the American Chemical Society* **2013,** *135*, 12241-12251.

25. Khalil, A.; Ahmed, E.; Naumov, P. Metal-coated thermosalient crystals as electrical fuses. *Chem. Commun* **2017,** *53*, 8470-8473.

26. Seeboth, A.; Lotzsch, D.; Ruhmann, R.; Muehling, O. Thermochromic polymers--function by design. *Chem. Rev.* **2014,** *114*, 3037-3068.

27. Day, J. H. Thermochromism. *Chem. Rev.* **1963,** *63*, 65-80.

28. White, M. A.; LeBlanc, M. Thermochromism in commercial products. *J. Chem. Educ.* **1999,** *76*, 1201-1205.

29. Xiong, Y.; Ma, Y.; Yan, X.; Yin, G.; Chen, L. Significant effect of alkyl chain length on fluorescent thermochromism of 9,10-bis(p-alkoxystyryl)anthracenes. *RSC Adv.* **2015,** *5*, 53255-53258.

30. Avadanei, M.; Cozan, V.; Shova, S.; Paixão, J. A. Solid state photochromism and thermochromism of two related N-salicylidene anilines. *Chem. Phy.* **2014,** *444*, 43-51.

31. Langhals, H.; Kinzel, S. Thermochromism of perylenes: dynamics in aromatics. *Spectrochimica acta. Part A, Molecular and biomolecular spectroscopy* **2011,** *78*, (3), 1212-4.

32. Naumov, P.; Lee, S. C.; Ishizawa, N.; Jeong, Y. G.; Chung, I. H.; Fukuzumi, S. New type of dual solid-state thermochromism: modulation of intramolecular charge transfer by intermolecular pi-pi interactions, kinetic trapping of the aci-nitro group, and reversible molecular locking. *J. Phys. Chem. A* **2009,** *113*, 11354-11366.

33. Sliwa, M.; Spangenberg, A.; Malfant, I.; Lacroix, P. G.; Metivier, R.; Pansu, R. B.; Nakatani, K. Structural, optical, and theoretical studies of a thermochromic organic crystal with reversibly variable second harmonic generation. *Chem. Mater.* **2008,** *20*, 4062-4068.

34. Morita, Y.; Suzuki, S.; Fukui, K.; Nakazawa, S.; Kitagawa, H.; Kishida, H.; Okamoto, H.; Naito, A.; Sekine, A.; Ohashi, Y.; Shiro, M.; Sasaki, K.; Shiomi, D.; Sato, K.; Takui, T.; Nakasuji, K. Thermochromism in an organic crystal based on the coexistence of sigma- and pi-dimers. *Nat. Mater* **2008**, *7*, 48-51.

35. Yu, X.; Luo, Y.; Wu, W.; Yan, Q.; Zou, G.; Zhang, Q. Synthesis and reversible thermochromism of azobenzene-containing polydiacetylenes. *Eur. Polymer Journal* **2008**, *44*, 3015-3021.

36. Levy, A.; Pogodin, S.; Cohen, S.; Agranat, I. Thermochromism at Room Temperature in Overcrowded Bistricyclic Aromatic Enes: Closely Populated Twisted and Folded Conformations. *Eur. J. Org. Chem.* **2007**, *2007*, 5198-5211.

37. Lee, S. C.; Jeong, Y. G.; Jo, W. H.; Kim, H.-J.; Jang, J.; Park, K.-M.; Chung, I. H. Thermochromism of a novel organic compound in the solid state via crystal-to-crystal transformation. *J Mol Struct* **2006**, *825*, 70-78.

38. Biedermann, P. U.; Stezowski, J. J.; Agranat, I. Polymorphism versus thermochromism: interrelation of color and conformation in overcrowded bistricyclic aromatic enes. *Chemistry* **2006**, *12*, 3345-3354.

39. Suh, H.-J.; Lim, W.-T.; Cui, J.-Z.; Lee, H.-S.; Kim, G.-H.; Heo, N.-H.; Kim, S.-H. The crystalline-state photochromism, thermochromism and X-ray structural characterization of a new spiroxazine. *Dyes Pigments* **2003**, *57*, 149-159.

40. Lambi, E.; Gegiou, D.; Hadjoudis, E. Thermochromism and photochromism of N-salicylidenebenzylamines and N-salicylidene-2-aminomethylpyridine. *J. Photochem. Photobiol. A* **1995**, *86*, 241-246.

41. Mills, J. F. D.; Nyburg, S. C. 49. Thermochromism and related effects in bixanthenylidenes and bianthronylidenes. Part I. Crystal structure analyses. *J. Am. Chem. Soc.* **1963**, 308.

42. Troyano, J.; Castillo, O.; Martínez, J. I.; Fernández-Moreira, V.; Ballesteros, Y.; Maspoch, D.; Zamora, F.; Delgado, S. Reversible Thermochromic Polymeric Thin Films Made of Ultrathin 2D Crystals of Coordination Polymers Based on Copper(I)-Thiophenolates. *Adv. Func. Mater.* **2018**, *28*, 1704040.

43. Zhai, L.; Zhang, W. W.; Zuo, J. L.; Ren, X. M. A simple but efficient strategy to enhance hydrostability of intensely fluorescent Mg-based coordination polymer (CP) via forming a composite of CP with hydrophobic PVDF. *Dalton transactions* **2016**, *45*, 3372-3379.

44. Denny, M. S.; Cohen, S. M. In Situ Modification of Metal-Organic Frameworks in Mixed-Matrix Membranes. *Angew. Chem.* **2015**, *127*, 9157-9160.

45. Guo, N.; Leu, M. C. Additive manufacturing: technology, applications and research needs. *Frontiers of Mechanical Engineering* **2013,** *8*, 215-243.

46. Luzuriaga, M. A.; Berry, D. R.; Reagan, J. C.; Smaldone, R. A.; Gassensmith, J. J. Biodegradable 3D printed polymer microneedles for transdermal drug delivery. *Lab on a chip* **2018,** *18*, 1223-1230.

47. Appuhamillage, G. A.; Reagan, J. C.; Khorsandi, S.; Davidson, J. R.; Voit, W.; Smaldone, R. A. 3D printed remendable polylactic acid blends with uniform mechanical strength enabled by a dynamic Diels–Alder reaction. *Polymer Chemistry* **2017,** *8*, 2087-2092.

48. Davidson, J. R.; Appuhamillage, G. A.; Thompson, C. M.; Voit, W.; Smaldone, R. A. Design Paradigm Utilizing Reversible Diels-Alder Reactions to Enhance the Mechanical Properties of 3D Printed Materials. *ACS Appl Mater Interfaces* **2016,** *8*, 16961-16966.

49. Dharmarwardana, M.; Welch, R. P.; Kwon, S.; Nguyen, V. K.; McCandless, G. T.; Omary, M. A.; Gassensmith, J. J. Thermo-mechanically responsive crystalline organic cantilever. *Chem. Commun* **2017,** *53*, 9890-9893.

50. Kobaisi, M. A.; Bhosale, S. V.; Latham, K.; Raynor, A. M.; Bhosale, S. V. Functional Naphthalene Diimides: Synthesis, Properties, and Applications. *Chem. Rev.* **2016**.

51. Bhosale, S. V.; Jani, C. H.; Langford, S. J. Chemistry of naphthalene diimides. *Chem. Soc. Rev.* **2008,** *37*, 331-342.

52. Fomine, S.; Fomina, L.; Arreola, R.; Alonso, J. C. Bisimide-lactamimide ring contraction in six-membered polyimides. *Polymer* **1999,** *40*, 2051-2058.

53. Rybakiewicz, R.; Tszydel, I.; Zapala, J.; Skorka, L.; Wamil, D.; Djurado, D.; Pecaut, J.; Ulanski, J.; Zagorska, M.; Pron, A. New semiconducting naphthalene bisimides N-substituted with alkoxyphenyl groups: spectroscopic, electrochemical, structural and electrical properties. *RSC Adv.* **2014,** *4*, 4089-14100.

54. Yin, J.; Chaitanya, K.; Ju, X.-H. Theoretical investigations of charge carrier transport in organic semiconductors of naphthalene bisimides N-substituted with alkoxyphenyl groups. *Can. J. Chem.* **2015,** *93*, (7), 740-748.

CHAPTER 4

COLOSSAL ANISOTROPIC THERMAL EXPANSION AND THERMOCHROMISM VIA SUPRAMOLECULAR GROUND-STATE COVALENT II-BONDING IN NAPHTHALENE DIIMIDE POLYMORPHS VS PYRENE[1]

Authors: Madushani Dharmarwardana, Mukunda M. Ghimire, Brooke M. Otten, Usharee Kapia, Bhargav S. Arimilli, Christopher M. Williams, Stephen Boateng, Gregory T. McCandless, Mohammad A. Omary, Jeremiah J. Gassensmith

The Department of Chemistry, BE26

The University of Texas at Dallas

800 West Campbell Road

Richardson, Texas 75080-3021

[1]Manuscript is in preparation.

4.1   Summary

We report colossal anisotropic thermal expansion, reversible thermochromism, polymorphism, solid-state and solution supramolecular π-bonds with covalent bonding strength, and ambipolar organic semiconductor characteristics of N-butoxyphenyl(naphthalene)diimide, BNDI. Linear thermal expansion coefficients (αa, αb, αc, β) of (452, -16.8, -154, 273) $\times$ 10^{-6} K^{-1} and (70.1, -44.7, 163, 177) $\times$ 10^{-6} K^{-1} were observed in the triclinic (BNDI-T) and monoclinic (BNDI-M) polymorphs, respectively, exceeding the 100 $\times$ 10^{-6} K^{-1} established threshold needed for anisotropic thermal expansions to be deemed "colossal." Further, the triclinic system (BNDI-T) exhibits highly-reversible thermochromism in the solid state over a 300 K range without observable hysteresis. Single crystals of BNDI exhibit gradual color changes from orange at room temperature toward red at cryogenic temperatures or yellow at 375 K. Using a combined experimental/computational approach, we show that the anisotropic thermal expansion and color change arise from a temperature-dependent attenuation in the distance between the naphthalene diimide cores. These materials manifested remarkable robustness such that reliable single crystal data were collected after repeated thermal cycling in open atmosphere over a two-year period. The intermolecular interaction is detectable in solution by absorption spectroscopy for oligomeric units, whereas in the solid state it occurs cooperatively in infinite stacks. The pertinent bonding strength is 49.7 kcal.mol-1 in a BNDI-T dimer model, suggesting a ground-state supramolecular-covalent π bond, which forms by virtue of a combined electrostatic and molecular orbital overlap. This behavior contrasts that for the prototypical π-stacking system of pyrene, whose supramolecular-covalent bonding is supposed to occur only in the excited state. Yet, the pyrene excimer π-bond strength is weaker (29.1 kcal.mol^{-1} by the same method/basis set) than the [BNDI-

T]$_2$ ground-state bonding and does not exhibit solid-state cooperativity. Surprisingly, the ground-state bonding in pyrene is found stronger than expected both experimentally and computationally, as we show that its yellow color in the solid state and nearly-saturated solutions is due to a supramolecular π-bond as strong as ~20 kcal/mol, and that its visible excitation leads to a vibronically-resolved excimer emission with no detectable risetime! On the other hand, the sensitized supramolecular π-bonding in the BNDI excimer leads to an additional (up to 10 kcal/mol and 25% excess binding energy) and calculated red shifts in electronic transition energies to the near-IR, which may explain the absence of luminescence experimentally. Finally, DFT simulations suggest interesting ambipolar organic semiconductor characteristics with both π-acidic and π-basic regions in BNDI oligomers, which explains the electrostatic (quadrupolar) component of the strong supramolecular bonding besides being promising toward novel molecular optoelectronic devices.

4.2   Introduction

Temperature-dependent expansion in crystalline materials is typically very small and on the order of 10^{-6} K^{-1}, resulting in very little lattice change. Colossal thermal expansion, which has been defined as change on the 10^{-4} K^{-1} order of magnitude,[1] is very rare though potentially quite desirable as large changes in solid-state packing, when they can be rationally designed and controlled, can give rise to useful electrochemical and magnetic properties for molecular organic, inorganic or organometallic materials. For instance, colossal positive and negative thermal expansion in metal-organic frameworks (MOFs) has been explored as a way to dynamically address intraframework pore dimensions.[2-5] While examples of colossal thermal expansion of inorganic1, [6-8] some organic salts[9] or MOF systems have become more common, examples involving metal-free organic semiconductor systems remain almost non-existent.[10] Demonstrating

69

positive and negative thermal expansion properties in certain types of organic molecules could be very useful. It has been known for some time that polymeric[11-14] and liquid crystalline systems[15-27] composed of the n-type semiconducting[28-29] naphthalene diimide[30-31] and the analogous perylene derivatives exhibit temperature dependent color changes—a material property called thermochromism—that arise from changes in intermolecular packing. While attempts to mechanistically describe these changes in packing have been made using optical spectroscopy and computational analysis, no temperature-dependent single crystal studies have been done on any of these compounds.[32-34] Recently,[35] we described a single crystal NDI system that had the uncanny ability to undergo a single-crystal to single-crystal transition and, in doing so, underwent drastic physical motion. This motion thermally induced motion—called thermo-salience—could be harnessed to lift steel balls over 100 times heavier than the crystal itself. Strikingly, after the thermo-salient motion ended, the resulting polymorph was conspicuously thermochromic. Herein we report that this system not only shows profound temperature-dependent structural changes but also colossal expansion rates on the same order of magnitude as that for purely inorganic systems. Furthermore, the expansion induces a large change in the optical bandgap, demonstrating that such expansion behaviors in organic systems can also give rise to optoelectronic phenomena in purely organic single crystal compounds.

4.3   Experimental

4.3.1   Synthesis

BNDI was synthesized according to a modified literature procedure.[30] A mixture of 1,4,5,8-naphthalene-tetracarboxylic dianhydride (NDA) (0.805 g, 3.00 mmol) and p-butoxyaniline (0.991

g, 6.00 mmol) in DMF (20.0 mL) was refluxed for 8 h and the reaction mixture was cooled to room temperature. The resultant red/orange crystalline precipitate was collected by vacuum filtration and purified by recrystallization with chloroform (Yield: 70 %). ^{1}H-NMR (500 MHz, CDCl$_3$, ppm): 1.04 (t, J=7.41 Hz, 6 H) 1.52 – 1.62 (m, 4 H), 1.81 – 1.91 (m, 4 H) 4.05 - 4.14 (t, 4 H) 7.07 – 7.15 (m, 4 H) 7.23 - 7.33 (m, 4 H) 8.86 (s, 4 H). ^{13}C-NMR (125 MHz, CDCl$_3$, ppm): 13.87, 19.29, 31.30, 67.99, 115.40, 127.07, 129.36, 129.38, 131.44, 159.59, 163.24.

4.3.2   Instrumentation

1H and 13C NMR spectra were obtained using a Bruker Ascend 500 MHz Spectrometer. Solution and solid-state UV-vis-NIR absorption spectra and diffuse reflectance spectral measurements were carried out using a PerkinElmer Lambda 900 spectrophotometer in Suprasil quartz cuvettes with 1-mm, 1-cm, and/or 10-cm path lengths. The solid-state absorption (via diffuse reflectance) data were collected using the LabSphere integrating sphere accessory to the Lambda 900 spectrophotometer which is connected to a Peltier system for temperature dependent experiments. Thermal properties of BNDI were analyzed with differential scanning calorimetry (TA Instruments Q2000) at a heating rate of 5 K/ min.

4.3.3   Crystallography

The temperature dependent single crystal X-ray diffraction (SXRD) data were collected for the two BNDI polymorphs, BNDI-T and the monoclinic polymorph of BNDI (BNDI-M), using a Bruker Kappa D8 Quest diffractometer (SI). Bruker D8 Advance Powder Diffractometer was used to obtain PXRD of BNDI before and after heating beyond the phase transition observed by DSC (Figure 11). Powder diffraction data were collected for a 2-theta range from 2° to 40°. Bruker

Kappa D8 Quest diffractometer is equipped with an Incoatec microfocus Mo Kα radiation source, HELIOS multilayer optics, Oxford Cryosystems cryostream, and a Photon 100 CMOS detector. Bruker SAINT was used for all data sets for integration and scaling, SADABS was used for absorption correction (multi-scan) and analysis of systematic absences of hkl reflections and XPREP was used for space group selection. All initial triclinic and monoclinic models of the two polymorphs were generated with SHELXT (intrinsic phasing method) and least-squares refinement was carried out with SHELXL2014.

All the structural information reported in this publication for the thermochromic polymorph, BNDI-T, are from the same single crystal. Confirmation of the temperature dependent thermochromic behaviour and structural changes were repeated across different batches, demonstrating the reproducibility of the thermochromism of BNDI-T.

Likewise, data collected on BNDI-M are also based on one single crystal, no thermochromic behaviour was observed over the operating temperature of our cryostream. The reproducibility of this observation was confirmed using other single crystals.

4.3.4   Computational Studies

Two functionals were evaluated based on literature precedent: N12SX and HSEH1PBE. The following keywords were employed: Int(Grid=SuperFineGrid), Iop(5/13=1,5/33=1,5/181=10), SCF=(NoVarAcc,NoIncFock,Tight) and NoSymm. These two functionals were utilized with several different pseudopotential basis sets, although little sensitivity in the computed band gaps was found; hence, the description below focuses on those results obtained with the largest basis set evaluated in this research, CEP-121G(d). The C–H distances were normalized (C–H = 1.089 Å) using the Mercury 3.5.1 package.

4.4   Results and Discussion

4.4.1   Polymorphism
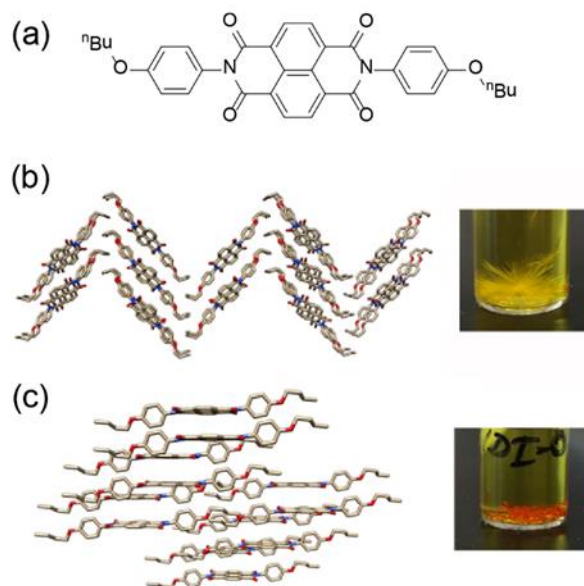
Figure 4.1. (a) Molecular structure of BNDI, two polymorphs of BNDI are shown. In both instances, BNDI molecules form infinite 1D chains along their π surfaces. (b) herringbone arrayed monoclinic polymorph (yellow crystals, or BNDI-M). (c) triclinic polymorph (red/orange crystals, or BNDI-T)

During our systematic solid-state investigation of NDI complexes, a triclinic polymorph of BNDI

(BNDI-T, Figure 4.1a and Figure 4.1c) was isolated, which we found underwent a readily apparent

change in color when the sample was cooled below room temperature. This polymorph was easily

distinguished from the well-known[30] monoclinic system as it forms red/orange rod-shaped crystals

at room temperature, while the monoclinic form of BNDI (BNDI-M, Figure 4.1b) forms yellow

needles. Furthermore, unlike our newly isolated triclinic system, the BNDI-M polymorph

demonstrated no variation in color at any of our tested temperatures. This is intriguing since the

origin of the well-known thermochromic behavior found in polymeric[11-14] and liquid crystal

samples[15-27] of NDI or perylene system has never adequately been elucidated. Temperature

dependent single crystal X-ray diffraction analyses (SXRD) were thus conducted on both polymorphs and it was found that, across the temperature range studied, BNDI-T forms cofacial slipped stacked sheets in the solid state (Figure 4.1c) while a herringbone configuration is observed in non-thermochromic BDNI-M system (Figure 4.1b). A comparison of the crystallographic parameters and PXRD of the two polymorphs are given in Table 4.1.

Table 4.1. Crystallographic parameters for BNDI polymorphs

		BNDI-T	BNDI-M
Formula		$C_{34}H_{30}N_2O_6$	$C_{34}H_{30}N_2O_6$
Formula weight		562.60	562.60
Temperature/ K		100	100
Crystal System		triclinic	monoclinic
Space group		$P\bar{1}$	$P2_1/c$
Unit cell parameters/ Å	a =	4.1636(8)	5.026(2)
	b =	8.1371(18)	33.756(5)
	c =	20.104(5)	7.9533(14)
Angles/ °	α =	100.182(11)	90
	β =	93.124(14)	99.997(10)
	γ =	94.102(14)	90
Volume/ Å³		667.1(3)	1328.8(6)
Crystal description		blade	blade
Crystal color		red/orange	yellow
$R[F^2 > 2\sigma(F^2)]$		0.045	0.050

4.5 Anisotropic Thermal Expansion and Thermochromism of BNDI
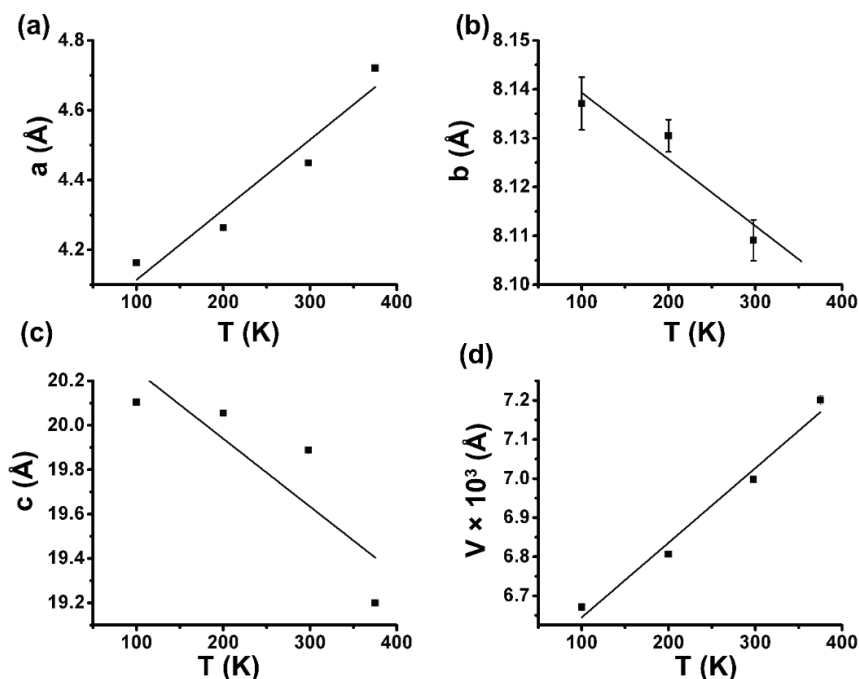
Figure 4.2. Analysis of unit cell parameters (Å) of BNDI-T versus temperature (K); where (a) a-axis (b) b-axis (c) c-axis and (d) unit cell volume (V), respectively.

Startlingly, further analysis of the SXRD data of both polymorphs show unprecedented expansion in unit cell sizes for these organic single crystals (Table 4.2). From these data, it is seen that single crystals of both BNDI-T and BNDI-M exhibit anisotropic thermal expansion behavior. The cell parameters are plotted versus temperature in Figure 4.2 and Figure 4.3 for BNDI-T and BNDI-M, respectively, and are summarized in Table 4.3 and Table 4.4. From these data, it was determined that single crystals of BNDI-T and BNDI-M exhibit linear thermal expansion rates of $(\partial V/\partial T)_P = +0.191$ and $+0.247$ $Å^3 \cdot K^{-1}$, respectively, describing an overall positive thermal expansion (PTE) upon cooling from 375 to 100 K — Figure 4.2d and Figure 4.3d, respectively.

Table S2. Intramolecular and intermolecular structural parameters of BNDI-T
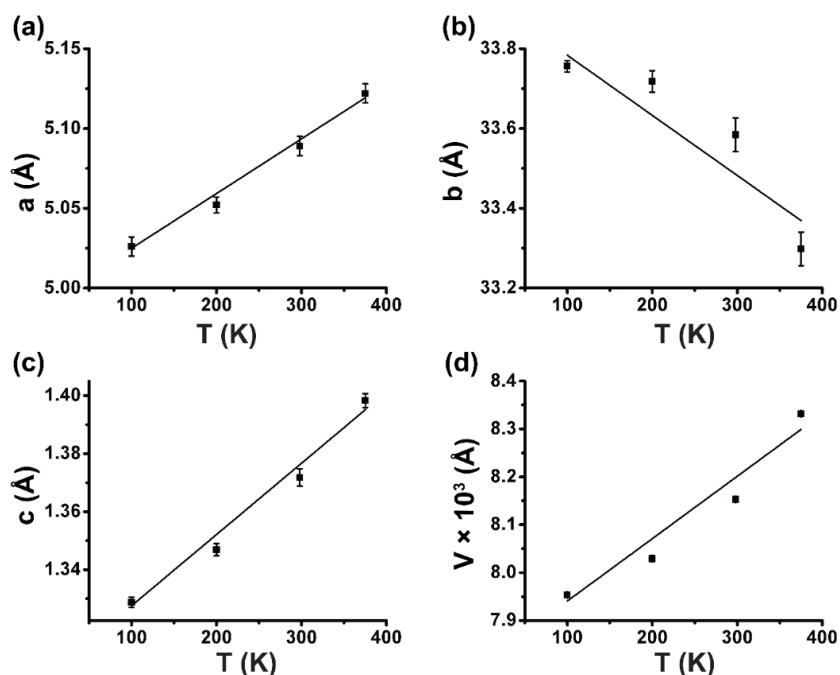
Figure 4.3. Analysis of unit cell parameters (Å) of BNDI-M versus temperature (K); where (a) a-axis (b) b-axis (c) c-axis and (d) unit cell volume (V), respectively.

Table 4.2. Intramolecular and intermolecular structural parameters of BNDI-T

T/ K	a/ Å	b/ Å	c/ Å	V/ Å3	Dihedral angle/ °	Interplanar distance/ Å
100	4.1636(8)	8.1371(18)	20.104(5)	667.1(3)	65.57(3)	3.360
200	4.2634(10)	8.1305(11)	20.055(5)	680.6(2)	68.30(4)	3.401
298	4.4494(10)	8.1091(14)	19.887(4)	699.8(2)	73.82(5)	3.437
375	4.7207(18)	8.132(2)	19.200(6)	720.1(4)	82.72(7)	3.466

Table 4.3. Intramolecular and intermolecular structural parameters of BNDI-M

T/ K	a/ Å	b/ Å	c/ Å	V/ Å^3	Dihedral angle/ °	Interplanar distance/ Å
100	5.026(2)	33.756(5)	7.9533(14)	1328.8(6)	79.30(4)	3.344
200	5.052(16)	33.718(9)	8.0290(2)	1346.8(7)	79.68(6)	3.376
298	5.089(2)	33.584(14)	8.1530(4)	1371.8(10)	79.97(5)	3.409
375	5.122(2)	33.298(14)	8.3320(4)	1398.3(8)	80.75(7)	3.452

Though the overall behavior is PTE, thermal expansion within both crystals is anisotropic. Thus,

upon cooling BNDI-T crystals from 375 to 90 K, the unit cell parameters *b* and *c* expand with a

rate of $(\partial b/\partial T)_P$ and $(\partial c/\partial T)_P = -1.36 \times 10^{-4}$ and -3.06×10^{-3} Å·K^{-1} as illustrated in Figure 4.2b and Figure 4.2c, respectively, representing *two* orthogonal uniaxial negative thermal expansion (NTE) processes, whereas the *a* parameter shrinks with a rate of $(\partial a/\partial T)_P = +2.01 \times 10^{-3}$ Å·K^{-1}— a uniaxial positive thermal expansion (PTE). A noteworthy difference in the monoclinic system is observed when cooling from 375 to 90 K, which leads to only the unit cell parameter *b* undergoing a *single* uniaxial NTE by expanding with a rate of $(\partial b/\partial T)_P = -1.51 \times 10^{-3}$ Å·K^{-1} as illustrated in Figure 4.3b, whereas the *a* and *c* parameters shrink with rates of $(\partial a/\partial T)_P$ and $(\partial c/\partial T)_P = +3.52 \times 10^{-4}$ and $+1.63 \times 10^{-3}$ Å·K^{-1}, Figures 4.3a and 4.3c, respectively, representing two orthogonal uniaxial PTE processes, respectively. The aforementioned anisotropic NTE/PTE rates translate into (α_a, α_b, α_c, β) of (452, -16.8, -154, 273) $\times 10^{-6}$ K^{-1} and (70.1, -44.7, 163, 177) $\times 10^{-6}$ K^{-1} in BNDI-T and BNDI-M polymorphs, respectively. The anisotropic NTE/PTE parameters for BNDI-T and BNDI-M compare favorably with the literature (Table 4.4).

For example, the highest coefficients are indeed higher than the coefficients characterizing the thermal expansion behavior deemed "colossal" for $Ag_3[Co(CN)_6]$ as reported recently by Goodwin *et al.*,[1] who defined colossal as one that produces α values that surpass a threshold of 100×10^{-6} K^{-1}. These uniaxial NTE/PTE coefficients are also significantly higher by orders of magnitude than those reported for the prototypical NTE inorganic oxide material, ZrW_2O_8,[6] and are only exceeded by those for the pure NTE/PTE behavior of the porous metal-organic framework FMOF-1.[2] The anisotropic NTE/PTE behavior of BNDI-T and BNDI-M merits additional discussion. First, from a phenomenological standpoint, BNDI-T and BNDI-M manifest *bona fide*, pure NTE/PTE phenomena—as opposed to the gas adsorption-assisted/mediated NTE or PTE manifestation of the sort invoked in the literature for MOFs (*e.g.*, MOF-5 and FMOF-1). The

current observations are especially noteworthy given that the materials herein are not porous and do not exhibit any detectable guest-accessible surface area.[2, 5] Second, we ascribe the colossal thermal expansion in materials of this type to the weakness of π-stacking interactions on a per-mole basis. Noble gas matrices such as those of Xe[37] as well as ionic solids[1, 6, 8] are among prototypical materials that exhibit this phenomenon. Third, that the intermolecular π-stacking interactions occur as long-range interactions in long chains of organic NDI chromophores, as opposed to the simple, dimeric interactions in more conventional organic chromophores such as those of pyrene,[38] should facilitate the manifestation of the phenomenon, as it is easier to compress a linear chain of weakly-interacting lattice motifs versus dimeric or oligomeric units of more strongly-bonded analogues.

Table 4.4. Anisotropic thermal expansion parameters for BNDI-T and BNDI-M versus literature precedents.

Material	α_a/K^{-1}	α_b/K^{-1}	α_c/K^{-1}	β/K^{-1}	Reference
BNDI-T	4.52×10^{-4}	-1.68×10^{-5}	-1.54×10^{-4}	2.73×10^{-4}	This work
BNDI-M	7.01×10^{-4}	-4.47×10^{-5}	1.63×10^{-4}	1.77×10^{-4}	This work
ZrW_2O_8	-9.10×10^{-6}	-9.10×10^{-6}	-9.10×10^{-6}	-2.70×10^{-5}	6
$Cd(CN)_2$	-2.00×10^{-6}	-2.00×10^{-6}	-2.00×10^{-6}	–	8
$AlPO_4$-17	-1.20×10^{-5}	-1.20×10^{-5}	-1.20×10^{-5}	-3.50×10^{-5}	7
$Ag_3[Co(CN)_6]$	1.50×10^{-4}	1.50×10^{-4}	-1.30×10^{-4}	1.60×10^{-4}	1
FMOF-1	2.30×10^{-4}	2.30×10^{-4}	-1.70×10^{-4}	3.00×10^{-4}	2
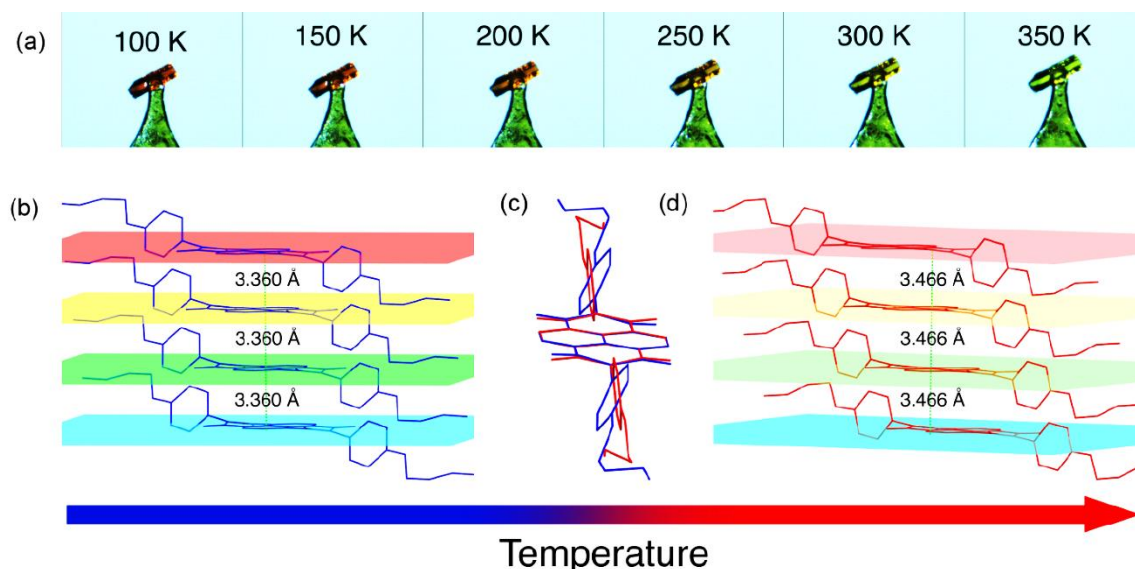
Figure 4.4. (a) Images of a single crystal situated on a loop as viewed through the mounting camera at different temperatures. The temperatures were controlled via cryostat. The background behind the crystal is blue, which causes the yellows to appear green. The distance, as measured from the plane of the NDI, is (b) 3.360 Å at 100 K and increases to (d) 3.466 Å at 375 K. This change of the intermolecular spacing allows the butoxyphenyl substituents to twist to maximize the interplanar distance. When the planes are far apart, the phenyl rings are nearly perpendicular to the NDI plane (red structure) in (c) whereas when the planes are close together, the phenyl rings rotate (blue structure) to accommodate the decrease in free volume.

Curiously, the dramatic changes in unit cell parameters as a function of temperature accompanied a bathochromic shift in BNDI-T yet not in BNDI-M. Qualitatively, the orange crystals of the triclinic polymorph gradually become dark red when the temperature is lowered to 100 K and then yellow upon heating to 375 K (Figure 4.4 and Figure 4.5). Moreover, this color change is reversible for many cycles of cooling and heating. In our laboratory, we were able to cycle the same sample—stored out on an open benchtop—over the course of 24 months. From the analysis of SXRD data, changes of molecular structure and packing could be quantified at both low and high temperatures (Figures 4.4b – 4.4d).
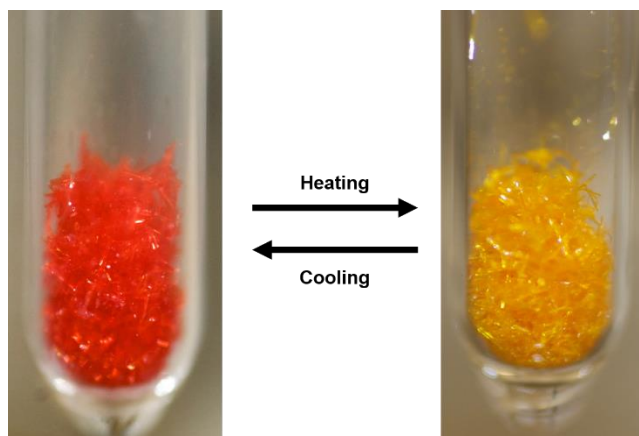
Figure 4.5. Reversible color change of BNDI-T upon cooling to ~100 K and heating to 375 K. The color change is reversible for any number of cooling and heating cycles.

The most noticeable differences between the low and high temperature structures are a shortening of the interplanar distances of the NDI core and a rotation of the butoxyphenyl substituent (Figure 4c). At 100 K, the rotation of the butoxyphenyl substituent is 65.57(3)° and at 375 K the butoxyphenyl substituent is rotated 82.72(7)° relative to the plane of the NDI core and thus approaches a perpendicular orientation relative to the NDI core. As a reference, the non-thermochromic BNDI-M has an average rotation of ~80°, which varies by ± 1.4° between the 100 and 375 K structures (compare Table 4.2 and Table 4.3). This rotation is tentatively attributed to the tighter packing arrangement in the low temperature structure. At 100 K, the π-π stacking distances are relatively close at 3.360 Å, Figure 4.4b. When the planes of the NDI core are close together as such, the butoxyphenyl rings must twist to be less perpendicular than at higher temperatures to facilitate a closer packing arrangement. As the temperature increases, the π-π stacking distances increase to 3.466 Å, which allows the butoxyphenyl substituent to twist to a more perpendicular conformation (Figure 4.4d). This phenomenon is reflected in colossal changes of the unit cell parameters upon heating or cooling. Heating from 100 to 375 K results in a ~8%

increase in the unit cell volume because of cell expansion along the π-π stacking direction, which

corresponds to the crystallographic a-axis stretching by approximately +13% (Table 4.2).
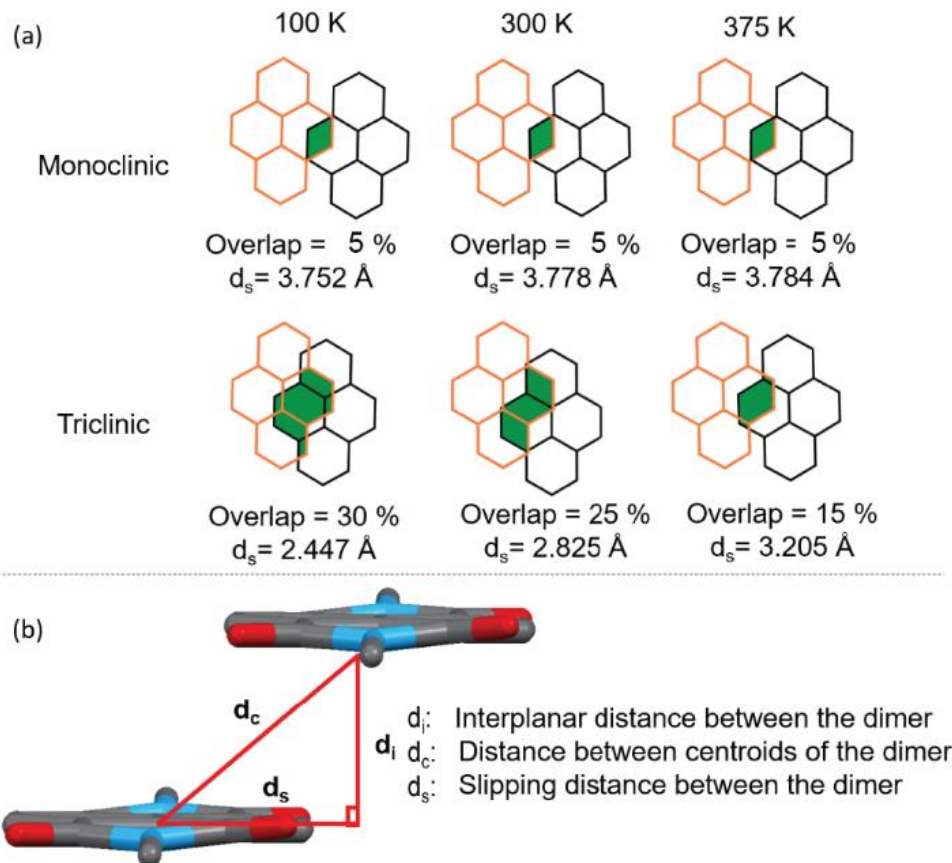
Figure 4.6. π-slippage distances and percent π-overlapping between NDI cores; (a) comparison between percent π-overlap and slipping distance for two polymorphs at 100, 298, and 375 K; (b) three different distances between an isolated dimer of BNDI: d_i and d_c could be obtained directly from the crystal structure and d_s was determined from the hypotenuse of d_i and d_c values.

In addition to changes in π-π stacking distances, there are changes in the slippage distance between

vicinal NDI cores. Three different distances are illustrated in Figure 4.6 between an isolated dimer

of BNDI, which are defined as the interplanar distance or π-stacking within the dimer (d_i), the

distance between centroids of the dimer (d_c), and the slippage distance[39-41] within the dimer (d_s).

According to Figure 4.7, d_i changes in a similar fashion in both polymorphs. The d_c and d_s values

are notably different in BNDI-T, while changing only modestly in BNDI-M. For instance, at 100

K, the calculated π-overlap is double that of the monoclinic system and the slippage distance is nearly 1.3 Å less (Figure 4.6a). As the temperature increases the percentage of π-overlap tends to decrease for both polymorphs, but larger changes are observed in the case of BNDI-T. From these observations, it can be seen that the triclinic polymorph shows a closer packing arrangement with a higher percentage of π-overlap.
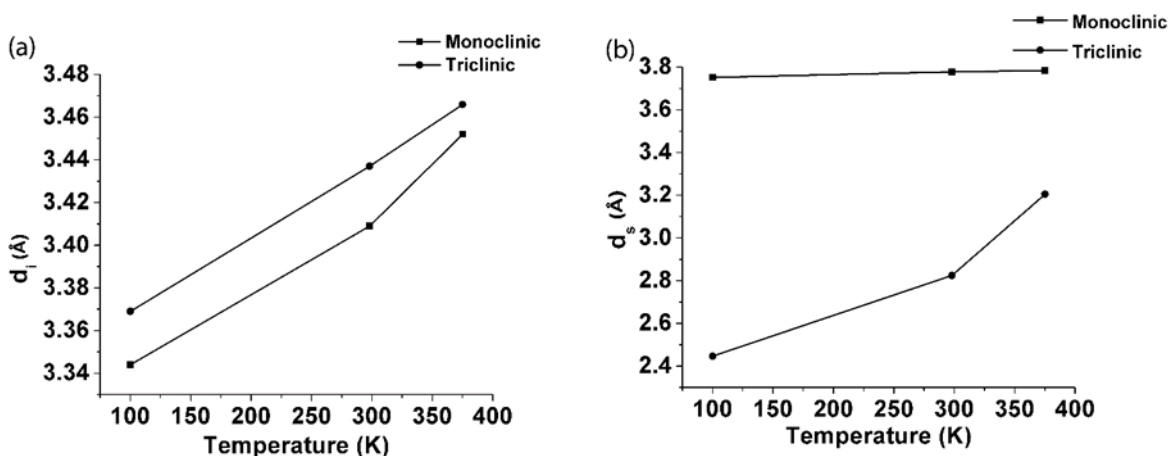
Figure 4.7. Comparison between (a) interplanar distance (d_i) and (b) slippage distance (d_s) for both polymorphs.

4.5.1 Spectroscopic Results for BNDI and Pyrene Solids and Solutions.

From our solid-state experimental results, it is clear that there is dynamic behavior in both polymorphs of NDI with the triclinic system exhibiting measurably more translational motion. From these data, it seems plausible that greater π-overlap between NDI cores results in a greater impact on thermochromism in BNDI-T.[42] While this strongly implicates solid state phenomenon as opposed to single molecule dynamics, we sought to ascertain if the color change was a result of single molecule behavior or oligomerization of BNDI molecules. To that end, UV-Vis electronic absorption spectroscopy was used to confirm if the change in the physical color of BNDI arises from oligomerization of BNDI molecules in both solution (transmission mode) and the solid state

82

(diffuse reflectance mode). Figure 4.8 shows polymorph- and concentration-dependent absorption spectra at room temperature for BNDI. At micromolar concentrations (green line, Figure 4.8i; trace f), the spectrum shows the typical discrete absorption lines corresponding to vibronically-resolved π-π^* electronic transitions within BNDI monomers. Notably, there is an abrupt loss of optical absorption at 400 nm, which justifies the colorless appearance and lack of visible absorption in monomeric units of BNDI. If the BNDI molecules did not interact with each other in solution, one would expect to see only an increase in the absorption intensities at higher concentrations; however, a bathochromic shift of the cut-off wavelengths at higher concentrations in solution is clearly observed. In Figure 4.8ii the absorption spectra of dilute solutions of BNDI molecules in chloroform at ambient temperature are shown. The large bathochromic shift in the solid state is a reflection of extended-chain association of BNDI molecules in solution, indicating that oligomerization indeed takes place as concentration increases.[43] From the concentration-dependent and temperature-dependent studies for the data set shown in the Figure 4.8iii inset, extinction coefficients, formation constants, free energies, enthalpies and entropies were quantified as 800 $M^{-1}cm^{-1}$, $3.13 \times 10^4\,M^{-1}$, -25.6 kJ/mol, -444 kJ/mol, and -1.65 kJ/mol, respectively, for the $[BNDI]_2$ dimer in chloroform solution. Further manipulations at different concentration ranges give rise to larger $[BNDI]_n$ oligomers beyond a dimer, which are accompanied by further red-shifting of the absorption cut-off at the higher concentrations (progressively converging toward the solid-state absorption). The monomer, dimer, and larger $[BNDI]_n$ oligomers likely exist in an equilibrium, which complicates the quantitative analysis for the thermodynamic parameters of each oligomer. The qualitative trend, however, is unmistakable for the red-shifting of absorption cut-off at higher concentrations based upon the data in Figure 7i – beyond the dimer band in Figure 4.8ii – so as to

suggest the formation of larger oligomers in equilibrium with one another and with the dimer and monomer at such higher concentrations.
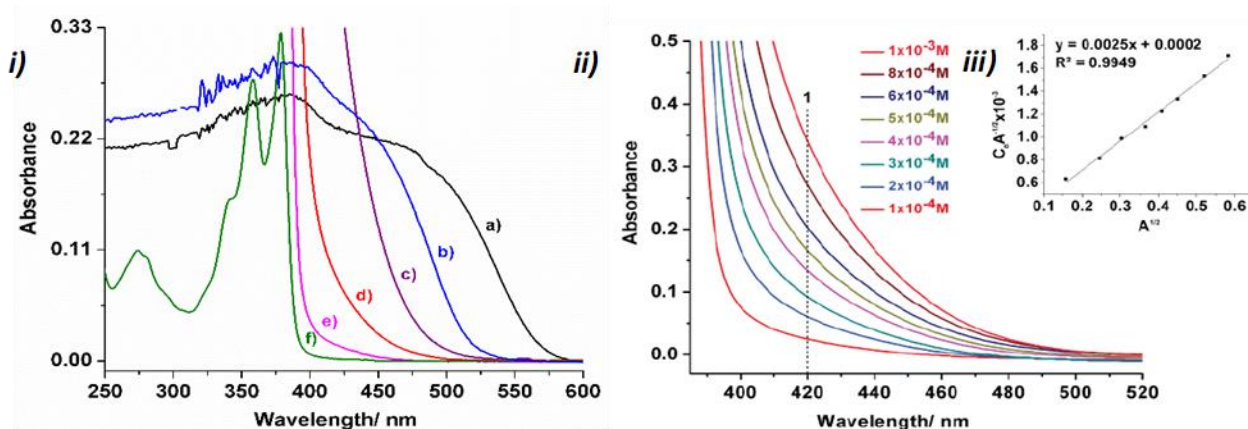
Figure 4.8. *i)* Comparison between solid-state UV-Vis spectra of BNDI-T versus solution absorption spectra as a function of concentration at ambient temperature. Spectra labeled a) and b) are diffuse reflectance spectra for solid samples of BNDI-T and BNDI-M, respectively, whereas spectra c), d), e) and f) are for 1.0 mM, 0.1 mM, 0.01 mM and 1.0 µM solutions, respectively, of BNDI in chloroform. A bathochromic shift occurs with increasing BNDI concentration approaching the solid-state absorption cut-off for BNDI-T. *ii)* Absorption spectra versus concentration of BNDI-T 10^{-4} M chloroform solutions at ambient temperature. *iii)* A plot of $C_0A^{-1/2}$ vs $A^{1/2}$ (Inset). Data was collected by Dr.Omary's group at University of North Texas.

The trends seen for BNDI aggregates are also seen for pyrene solids and solutions at high concentration, as shown in Figure 4.9i. Indeed, we show that the yellow color of the crystalline solid of pyrene is due to visible absorption bands, which are bleached upon grinding the solid or drop-casting a thin film (Figure 4.9ii). The visible absorption peaks appear with a surprisingly high resolution at ca. 410, 425, and 450 nm in both the crystalline solid-state and solutions in the 0.01-0.1 M range in cyclohexane.
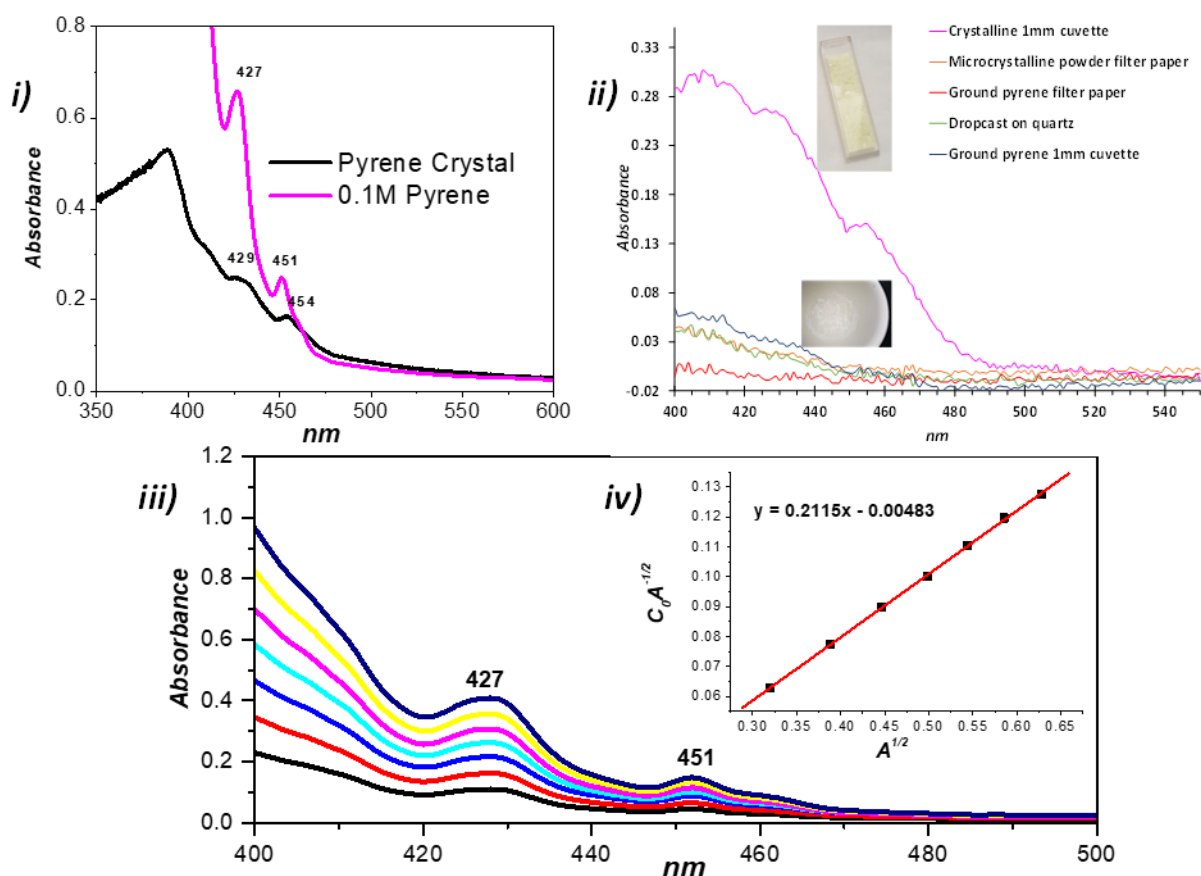
Figure 4.9. *i)* UV-Vis spectra of pyrene in the crystalline solid-state and 0.1 M solution in cyclohexane showing visible absorption peaks. *ii)* Disappearance of visible absorption peaks of pyrene solid upon disruption of crystallinity (by gentle grinding via a spatula on a filter paper and/or strong mechanical grinding via mortar and pestle, or dropcasting a thin film on a glass substrate). *iii)* UV-Vis spectra of pyrene solutions vs concentration in cyclohexane. *iv)* A plot of $C_0A^{-1/2}$ vs $A^{1/2}$. Data was collected by Dr.Omary's group at University of North Texas

Temperature-dependent absorption studies of the thermochromic crystalline solid sample were also performed and these data are shown in Figure 4.10. Only the absorption edge showing the absorption cutoff is needed to draw conclusions from such solid-state spectra; this cutoff corresponds to the bandgap (E_g) of the sample. The data clearly demonstrate temperature dependent E_g values, tabulated in Table 4.5, whereby a bathochromic shift is revealed upon cooling. These data are in excellent qualitative correlation to the reduction in the interplanar π-stacking distances shown in the temperature-dependent crystallographic data for this polymorph.

85

To the best of our knowledge, there are no organic n-type crystalline solids that show such a reversible thermal response, despite the discovery of semiconducting crystalline derivatives of NDI more than 16 years ago.[28]
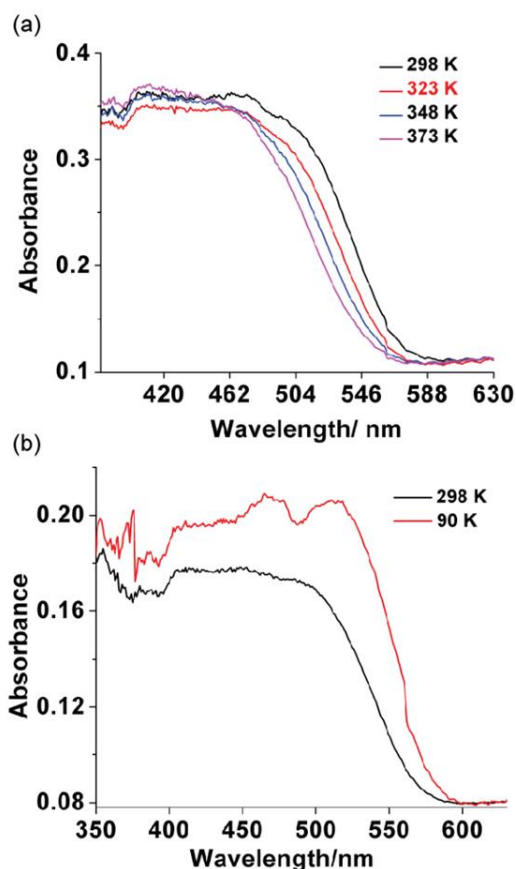
Figure 4.10. Comparison of solid-state absorption spectra for BNDI-T crystals versus temperature, showing (a) the hypsochromic shifts when heated from room temperature to higher temperature and (b) the bathochromic shifts when cooled from room temperature to cryogenic temperatures. Data was collected by Dr.Omary's group at University of North Texas

Based on the solid-state absorption measurements, an E_g that decreases by ~0.10–0.15 eV was found upon cooling from 373 to ~90 K. While the numerical values of E_g are rough estimates due to the experimental limitations of the temperature-dependent solid-state absorption experiment, the qualitative trend is unmistakable in terms of correlating the red shift clearly observed upon

cooling to the concomitant increase in π-stacking observed crystallographically for the triclinic polymorph.

Table 4.4. Band Gap Versus Temperature for the BNDI-T Solid Polymorph.[a,b]

Temperature (K)	E_g^a (eV)	E_g^b (eV)
90	2.07	2.39
298	2.11	2.46
323	2.15	2.50
348	2.16	2.52
373	2.17	2.54

[a]Notation: E_g^a = Estimated band gap at the absorption edge values. E_g^b = Estimated band gap at the absorption decline values. [b]These E_g estimates are qualitative given the uncertainties in measuring the temperature; see the experimental section. Data was collected by Dr.Omary's group at University of North Texas

Finally, luminescence experiments were attempted for the crystalline samples of BNDI-T and BNDI-M. The samples did not exhibit any detectable luminescence even at cryogenic temperatures; attempts were made using both liquid nitrogen and liquid helium. Direct conjugation of an amide functionality to the chromophoric aromatic naphthalene moiety, which induces electron transfer quenching and intersystem crossing, as well as the two large alkoxy chains, which increase thermal motion and consequently non-radiative decay to the ground state *via* multi-phonon relaxation, are the likely culprits for the lack of observation of detectable luminescence. On the other hand, this finding emphasizes that the association in BNDI is a *ground state phenomenon* detectable by *absorption* spectral changes *vis–à–vis* the *excited state* changes that are detectable only by *fluorescence* spectral changes in conventional organic chromophores such as those of pyrene.[38] The pyrene solid, on the other hand, can be excited directly at the visible dimer

absorption peaks, leading to a structured emission and disappearance of a risetime component in the time-resolved spectra for the resulting static excimer band, whereas monomer excitation leads to the dynamic excimer with an unstructured emission and detectable risetime. These results for pyrene solid luminescence challenge yet another common myth in the photophysics of this classical compound -- besides the above ones about its visible absorption bands in the crystalline solid state. In the foremost review on preassociated pyrenes by Winnik,[50] it was concluded that: "*The selection of the excitation wavelength merits consideration. If it were possible to excite preassociated pyrenes to the exclusion of isolated pyrenes (or vice versa), the profile of the excimer emission would vary with excitation wavelength.*[50]" We showed that this is true, result in differences in preassociated *vs*. predissociated pyrene excimer fluorescence bands in the emission profile, excitation profiles, time, and temperatures.

4.5.2   Thermal Analysis of BNDI-T

Thermal properties of BNDI-T were analyzed by DSC measurements and the plotted data in Figure 4.11a reveal no phase transitions over the range of temperatures for which our single crystal and solution state experiments were conducted. We do observe two endothermic peaks, however, both of which occur above the temperature limits of our single crystal diffraction system. The first endothermic peak at 477.8 K corresponds to a phase transition and the second peak at 634.8 K is the melting of BNDI-T. In the cooling process, two exothermic peaks were observed; the peak at 625.8 K corresponds to the solidification of the melted crystals whereas the other peak at 401.9 K represents another phase transition.
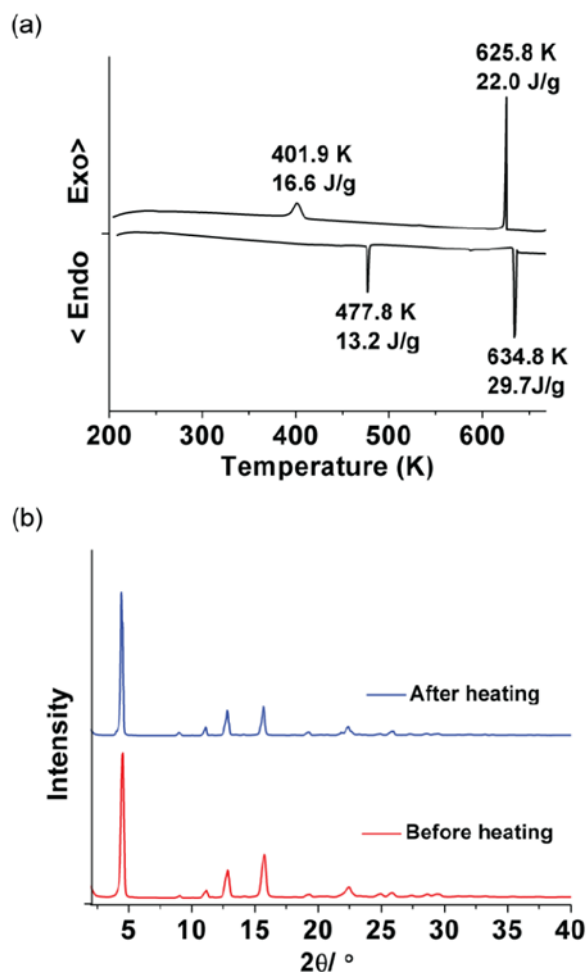
Figure 4.11. (a) DSC curve for BNDI-T recorded by heating at 5 K/min (b) PXRD data for BNDI-T (bottom) before heating beyond phase transition at 477.8 K and (top) after heating beyond the phase transition at 477.8 K.

The physical limitations of the experimental setup employed prevent the SXRD instrument from collecting data at or above 400 K. However, it was confirmed that thermally cycling samples above the first endothermic transition and then back to room temperature results in no difference in the PXRD spectrum (Figure 4.11b). This suggests that the transition occurring is fully reversible and has no impact on the behavior of the sample after a full cycle above 500 K.

4.6   Computational Analysis of the Bonding, Spectral, and Semiconducting Properties.

In light of the intriguing properties of these polymorphs, a computational study was launched in order to investigate the experimental phenomena described herein. This study was completed using Grimme's semi-empirical GGA-type density functional, which includes a long-range dispersion correction (B97D). This functional was employed based on its performance modeling noncovalent interactions, such as those seen in larger aromatic dimer systems. The study showed that this functional is capable of modeling the π-π stacking seen in these larger aromatic complexes, such as naphthalene and pyrene.[44] This functional was used in conjunction with the CEP-121G basis set[45-47] with d functions added to the heavy element.[48] These calculations were completed using the Gaussian09[36] suite of programs. The binding energies of the two polymorphs were determined from the geometry at the crystal structure at room temperature as well as from the optimized geometries of the dimer and the BNDI monomer. In order to accurately model the photophysical phenomena observed experimentally, the crystal structures were used to perform a TD-DFT analysis. These results were then compared against the known pyrene dimer, which is non-bonded in the ground state but when excited produces an excimer to determine the differences in bonding character.

The NDI monomer shows ambipolar character while the pyrene doesn't show this delocalization of charge, as is demonstrated by Figure 4.12a, which shows the separation and localization of charge as indicated by the color gradient. In Figure 4.12a, the red regions denote areas of partial negative charge, which as expected is localized over the more electron withdrawing portions of the molecule (i.e. – the location of the oxygen). The green regions represent areas of neutral charge, which is most evident in the area of the naphthalene rings and the light blue regions show areas of

slightly positive charge and as expected, these areas are localized over the nitrogens of the imide groups as well as the peripherals of the naphthalene rings that contain hydrogens. However, this separation of charge is not seen with the pyrene (Figure 4.12b). Also shown in Figure 4.12 is the same molecular electrostatic potential mapped on the molecule surface, however, the charge distribution has been exaggerated, so each section is shown possessing a positive or negative charge distribution.
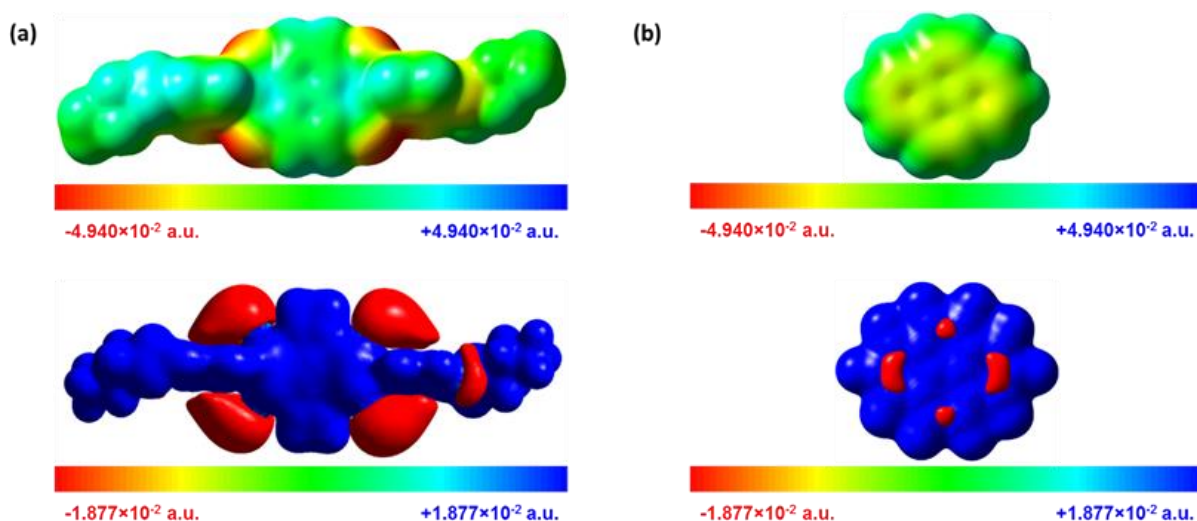
Figure 4.12. Molecular electrostatic potential plots of (a) NDI and (b) pyrene monomer. Data was collected by Dr.Omary's group at University of North Texas

Table 4.5. Calculated Binding Energies of [BNDI]$_2$ and [Pyrene]$_2$ Based on Optimized Geometries (kcal mol^{-1} Units) or Single-Point Calculations for the Crystal Structures of Polymorphs. Data was collected by Dr.Omary's group at University of North Texas.

	[BNDI]$_2$				[Pyrene]$_2$			
	ΔE	ΔG	ΔH	ΔS	ΔE	ΔG	ΔH	ΔS
Ground State (S$_0$)	-41.6	-15.9	-39.9	-0.081	-15.0	-3.09	-14.8	-0.039
Excited State (T$_1$)	-52.2	-26.6	-50.0	-0.079	-24.1	-10.1	-24.3	-0.047
	[BNDI-M]$_2$				[BNDI-T]$_2$			
	ΔE				ΔE			
298K Crystal Structure	-33.3				-41.2			

The binding energies of [BNDI]$_2$ and [Pyrene]$_2$ were calculated via two different methods. The first method is represented in Table 4.5. In this method, the binding energies were determined through the optimization of the dimer units and monomer units. With this method, the binding energy of the pyrene is predicted to be -15.0 kcal mol^{-1} in the ground state which is similar to the value of -13.0 kcal mol^{-1} Grimme's calculated in the initial studies of the B97D functional.[44] When this molecule is excited, there is an increase of the binding energies (-15.0 to -24.1 kcal mol^{-1}). This increase is also seen seen for [BNDI]$_2$, where the calculated binding energy in the ground state is -42.6 kcal mol^{-1} and upon excitation this increases to -52.2 kcal mol^{-1}. These high binding energies were also found when calculated based on the 298K crystal structures.
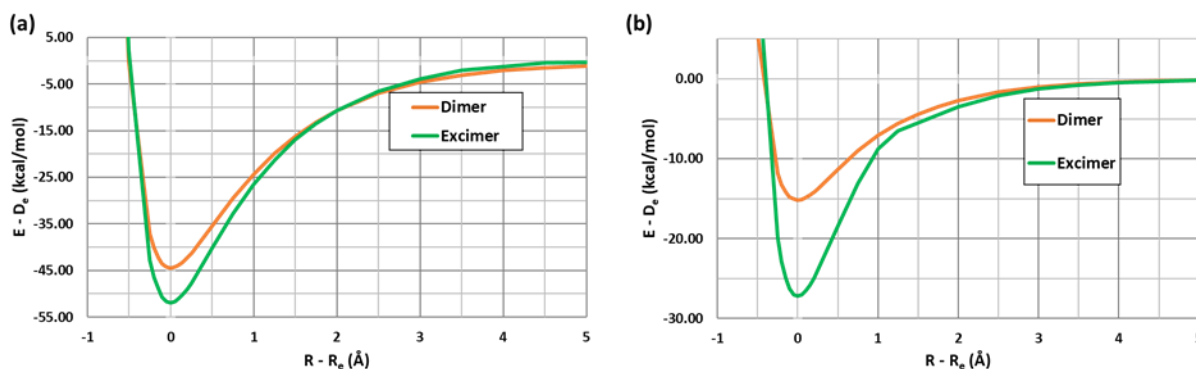
Figure 4.13. One-dimensional potential energy surfaces of a) [BNDI]$_2$ and (b) [Pyrene]$_2$ in the ground (orange) and excited (green) state. Data was collected by Dr.Omary's group at University of North Texas

The second method comes from the derivation of a rigid one-dimensional potential energy surface (PES), which monitors the energy change of the system as the distance between the two monomer units is modified (Figure 4.13). In this type of PES the geometry of each monomer is frozen and the only thing that changes is the distance between the two monomer units. This removes contributions of rearrangement energy from the calculated binding energies. As in method one, the binding energies are of the same magnitude, with the ground state binding energies being lower

than excited state binding energies. These PES were then used to complete an analysis for the vibrational frequency corresponding to the movement of the monomers through the use of a Dunham analysis.[49] This analysis is a polynomial fitting of the potential well around the equilibrium bond length (R_e) to determine the vibrational frequency (cm^{-1}) and the anharmonicity constant (cm^{-1}) (Table 4.6). For both complexes there was a decrease in the inter-planar distance with a corresponding increase in the vibrational frequency which supports the conclusion that the interaction is stronger in the excited state.

Table 4.6. Equilibrium distances between monomer planes (R_e), vibrational frequencies (ω_e) and anharmonicity constants ($\chi_e\omega_e$) reported in Å and cm^{-1}, respectively. Data was collected by Dr.Omary's group at University of North Texas

Complex	R_e	ω_e	$\chi_e\omega_e$
$^1[BNDI]_2$	3.239	79.9	0.25
$^3[BNDI]_2$	3.143	90.2	0.06
$^1[Pyrene]_2$	3.272	88.6	0.56
$^3[Pyrene]_2$	3.136	134.9	0.51
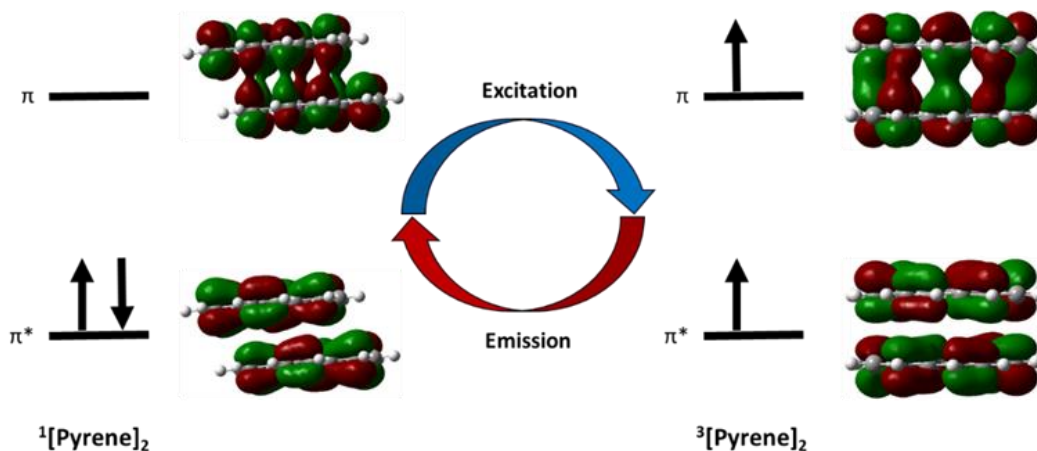
Figure 4.14. [Pyrene]$_2$ frontier orbitals in the (left) ground and (right) excited state (isovalue=0.02). Data was collected by Dr.Omary's group at University of North Texas

In the case of the pyrene dimer, this stronger interaction in the excited state is known to be due to formation of an excimer. Further support for the excimer formation comes from the analysis of the orbitals involved in the singlet to triplet transition for the pyrene dimer (Figure 4.14). The HOMO and LUMO plotted on the left show that the HOMO is a π-π anti-bonding orbital and the LUMO is shown to be a π-π bonding orbital. Upon excitation, there is a shift in the geometry which leads to better π overlap and the promotion of an electron from an anti-bonding orbital to a bonding orbital. This leads to a system where the bond order is no longer zero, as it is in the ground state. This orbital analysis lends credence to the conclusion by offering more support for the increase in the binding energy and the decrease in the inter-planar distances.
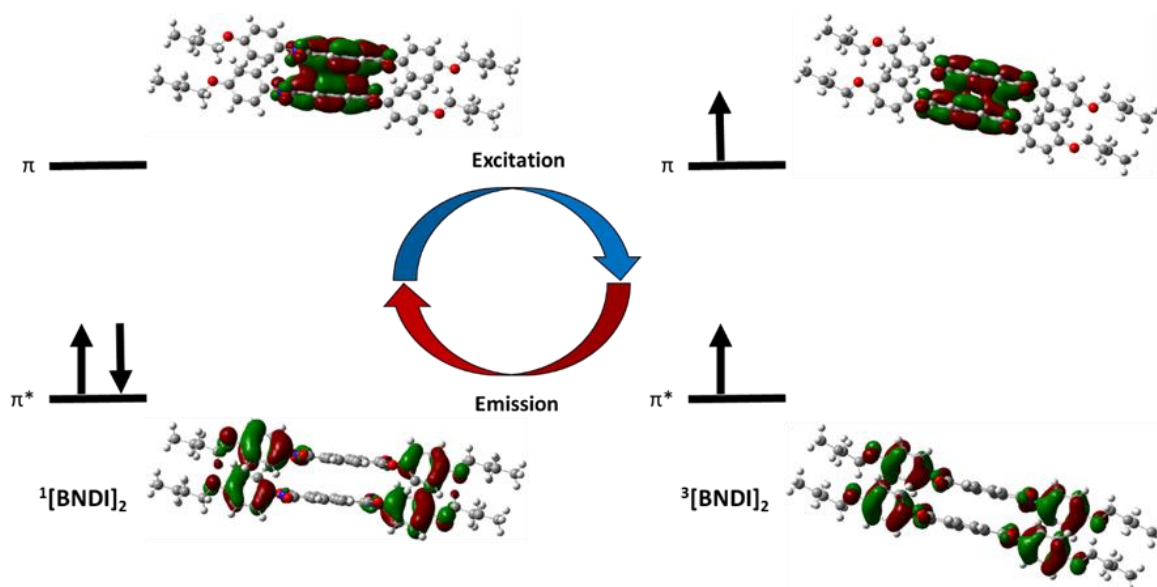
Figure 4.15. [BNDI]$_2$ frontier orbitals in the (left) ground and (right) excited state (isovalue=0.02). Data was collected by Dr.Omary's group at University of North Texas.

A similar orbital analysis can be reached for [BNDI]$_2$ (Figure 4.15) whereby, upon excitation there is the promotion of an electron from a π-π anti-bonding orbital to a π-π bonding orbital. However, unlike the pyrene, BNDI has substituents that also contain aromatic groups, which are capable of having their own π-π interactions, both attractive and repulsive. With the BNDI, the HOMO is

based on the benzyl ring of the substituent of the central naphthalene unit, while the LUMO is located on the naphthalene unit. Upon excitation there is still a change in the geometry leading to better π overlap upon the promotion of an electron (Figure 4.16). This points to a similar conclusion as with [Pyrene]$_2$ where there is an increase in the binding energy due to stronger π-π interactions in the excited state which leads to the decreased inter-planar distance.
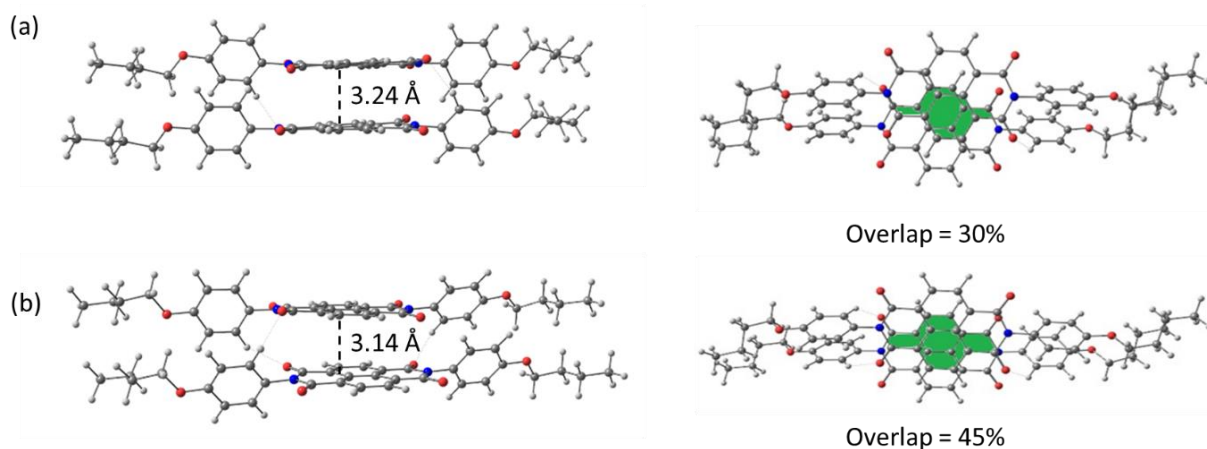
Figure 4.16. Comparison of inter-planar distance (left) and degree of π overlap (right) for ^{1}[BNDI]$_2$ (a) and ^{3}[BNDI]$_2$ (b) (isovalue=0.02). Data was collected by Dr.Omary's group at University of North Texas.

While [Pyrene]$_2$ and [BNDI]$_2$ leads to similar conclusions about the excited state *vs* the ground state, there remains the question of magnitude for the ground state binding energies. The ground state binding energy of [Pyrene]$_2$ is calculated to be less than half the binding energy for the [BNDI]$_2$. In order to elucidate a reasoning behind this, the Kohn-Sham (KS) orbitals were analyzed for both of these complexes. The orbital analysis of [Pyrene]$_2$ shows an equal number of π-π attractive and repulsive interactions in the ground state (Figure 4.17a), this supports the conclusion that the [Pyrene]$_2$ system is not covalently bound in the ground state. However, for [BNDI]$_2$ there are 6 π-π attractive interactions and only 5 π-π repulsive interactions identified (Figure 4.17b). If there is an overall attractive interaction between the π systems of the BNDI monomers, this would

lead to a higher binding energy in the ground state than seen for the [Pyrene]$_2$ where there is an overall bond order of zero.
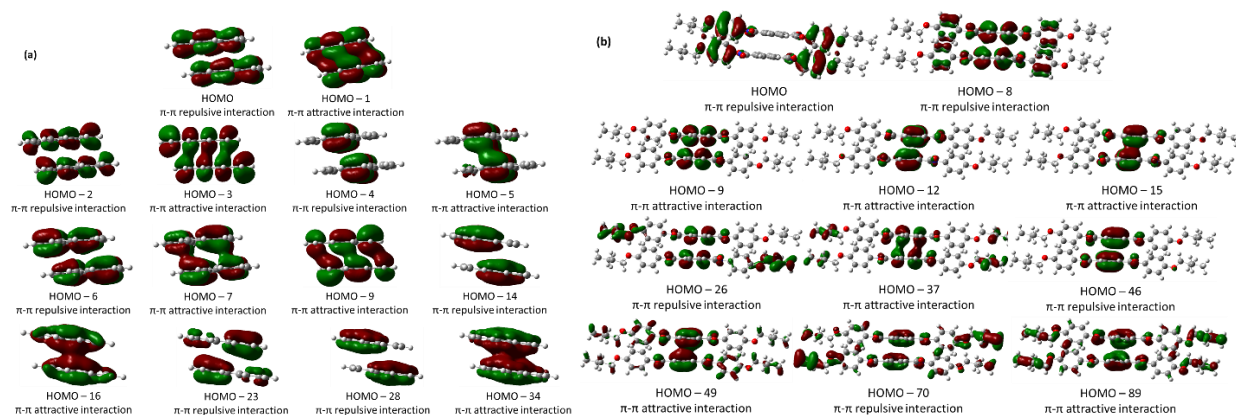
Figure 4.17. Orbital contours showing π-π attractive and repulsive interactions for (a) [Pyrene]$_2$ and (b) [BNDI]$_2$ (isovalue=0.02). Data was collected by Dr.Omary's group at University of North Texas.
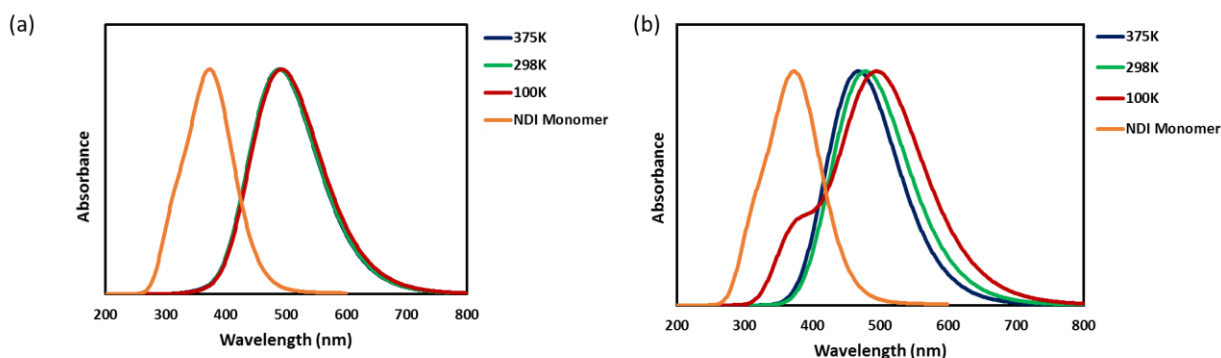
Figure 4.18. Comparison of calculated absorption spectra of (a) BNDI-M and (b) BNDI-T at various temperatures and versus the BNDI monomer. Data was collected by Dr.Omary's group at University of North Texas.

To understand the photophysical phenomena seen for the BNDI-T polymorph that is absent for the BNDI-M polymorph, the absorption spectra was calculated for each polymorph at 100K, 298K and 375K. This was done using the crystal structures at these temperatures as the singlet geometry (^{1}S$_0$). It was found for both of the polymorphs there was a red shift in the absorption band. However, for the BNDI-M polymorph the structural differences at each temperature were not

enough to change the absorption spectra appreciably (Figure 4.18a). However, the absorption spectra for the BNDI-T polymorph revealed that as the structure of the polymorph changes, there is a red shift in the absorbance band as the temperature is decreased (Figure 4.18b), which is consistent with the experimental data. This change in the λ_{max} is attributed to the change in the percent overlap of the naphthalene rings, as shown in Figure 4.6. At 100K, there is a larger overlap of the naphthalene rings leading to a λ_{max} around 495 nm, and at 375K the band is shifted to 468 nm at 375K. The overall thermochromatic shifting of the bands is 10 times larger for the BNDI-T polymorph (117 cm^{-1} vs 1166 cm^{-1}).

4.7   Conclusions

Unprecedented thermal expansion has been uncovered in two different polymorphs of naphthalene diimide containing systems that causes very different changes in the optoelectronic properties for each polymorph. The root cause of this difference was comprehensively investigated across a wide range of temperatures. The experimental data confirm that the anisotropic thermal expansion and thermochromic changes observed in the BNDI-T polymorph arise from solid state oligomerization and not from simple intramolecular dynamics. Computational modeling further confirms that these changes arise from changes in the overlap of the aromatic cores rather than the the π-π stacking distance, which corroborates the experimental data and further confirms that the crystallographic expansion/contraction and color change process occur as a result of orbital mixing as opposed to charge transfer or intramolecular dynamics. The data reveal a hitherto unreported mechanism of thermochromism in the solid state and it occurs in one of the most well-studied organic n-type semiconducting materials reported in the literature. Furthermore, these materials undergo the most

dramatic anisotropic thermal expansion behavior known for organic single crystals of relevance for next-generation organic optoelectronic devices.

4.8   References

1. Goodwin, A. L.; Calleja, M.; Conterio, M. J.; Dove, M. T.; Evans, J. S.; Keen, D. A.; Peters, L.; Tucker, M. G., Colossal Positive and Negative Thermal Expansion in the Framework Material $Ag_3[Co(CN)_6]$. *Science* **2008**, *319*, 794-797.

2. Yang, C.; Wang, X.; Omary, M. A., Crystallographic Observation of Dynamic Gas Adsorption Sites and Thermal Expansion in a Breathable Fluorous Metal-Organic Framework. *Angew. Chem.* **2009**, *48*, 2500-2505.

3. Dubbeldam, D.; Walton, K. S.; Ellis, D. E.; Snurr, R. Q., Exceptional Negative Thermal Expansion in Isoreticular Metal-Organic Frameworks. *Angew. Chem.* **2007**, *46*, 4496-9.

4. Han, S. S.; Goddard, W. A., Metal−Organic Frameworks Provide Large Negative Thermal Expansion Behavior. *J. Phys. Chem. C* **2007**, *111*, 15185-15191.

5. Rowsell, J. L.; Spencer, E. C.; Eckert, J.; Howard, J. A.; Yaghi, O. M., Gas Adsorption Sites in a Large-Pore Metal-Organic Framework. *Science* **2005**, *309*, 1350-1354.

6. Mary, T. A.; Evans, J. S. O.; Vogt, T.; Sleight, A. W., Negative Thermal Expansion from 0.3 to 1050 Kelvin in ZrW_2O_8. *Science* **1996**, *272*, 90-92.

7. Attfield, M. P.; Sleight, A. W., Exceptional Negative Thermal Expansion in Alpo4-17. *Chem. Mater.* **1998**, *10*, 2013-2019.

8. Goodwin, A. L.; Kepert, C. J., Negative Thermal Expansion and Low-Frequency Modes in Cyanide-Bridged Framework Materials. *Phy. Rev. B* **2005**, *71*.

9. de Pedro, I.; García-Saiz, A.; Dupont, J.; Migowski, P.; Vallcorba, O.; Junquera, J.; Rius, J.; Rodríguez Fernández, J., On the Colossal and Highly Anisotropic Thermal Expansion Exhibited by Imidazolium Salts. *Cryst Growth Des.* **2015**, *15*, 5207-5212.

10. He, T.; Stolte, M.; Burschka, C.; Hansen, N. H.; Musiol, T.; Kalblein, D.; Pflaum, J.; Tao, X.; Brill, J.; Wurthner, F., Single-Crystal Field-Effect Transistors of New Cl(2)-NDI Polymorph Processed by Sublimation in Air. *Nat. Commun.* **2015**, *6*, 5954-5963.

11. Carlotti, M.; Gullo, G.; Battisti, A.; Martini, F.; Borsacchi, S.; Geppi, M.; Ruggeri, G.; Pucci, A., Thermochromic Polyethylene Films Doped with Perylene Chromophores: Experimental Evidence and Methods for Characterization of Their Phase Behaviour. *Poly. Chem,* **2015**, *6*, 4003-4012.

12. Seeboth, A.; Lotzsch, D.; Ruhmann, R.; Muehling, O., Thermochromic Polymers--Function by Design. *Chem. Rev.* **2014**, *114*, 3037-68.

13. Bohm, A.; Krieger, M.; Becker, S.; Mullen, K. Thermochromic Rylene Dyes. US 6,890,377 B2, 2005.

14. Becker, S.; Bohm, A.; Mullen, K., New Thermotropic Dyes Based on Amino-Substituted Perylendicarboximides. *Chem. Eur. J* **2000**, *6*, 3984-3990.

15. Chen, Z.; Stepanenko, V.; Dehm, V.; Prins, P.; Siebbeles, L. D.; Seibt, J.; Marquetand, P.; Engel, V.; Wurthner, F., Photoluminescence and Conductivity of Self-Assembled Pi-Pi Stacks of Perylene Bisimide Dyes. *Chem. Eur. J* **2007**, *13*, 436-449.

16. van Herrikhuyzen, J.; Syamakumari, A.; Schenning, A. P.; Meijer, E. W., Synthesis of N-Type Perylene Bisimide Derivatives and Their Orthogonal Self-Assembly with P-Type Oligo(P-Phenylene Vinylene)S. *J. Am. Chem. Soc* **2004**, *126*, 10021-10027.

17. Percec, V.; Sun, H. J.; Leowanawat, P.; Peterca, M.; Graf, R.; Spiess, H. W.; Zeng, X.; Ungar, G.; Heiney, P. A., Transformation from Kinetically into Thermodynamically Controlled Self-Organization of Complex Helical Columns with 3d Periodicity Assembled from Dendronized Perylene Bisimides. *J. Am. Chem. Soc.* **2013**, *135*, 4129-4148.

18. Iverson, I. K.; Casey, S. M.; Seo, W.; Tam-Chang, S.-W.; Pindzola, B. A., Controlling Molecular Orientation in Solid Films Via Self-Organization in the Liquid-Crystalline Phase. *Langmuir* **2002**, *18*, 3510-3516.

19. Wurthner, F.; Thalacker, C.; Diele, S.; Tschierske, C., Fluorescent J-Type Aggregates and Thermotropic Columnar Mesophases of Perylene Bisimide Dyes. *Chem. Eur. J.* **2001**, *7*, 2245-2253.

20. Gregg, B. A.; Cormier, R. A., Liquid Crystal Perylene Diimide Films Characterized by Electrochemical, Spectroelectrochemical, and Conductivity Versus Potential Measurements. *J Phys Chem B.* **1998**, *102*, 9952-9957.

21. Cormier, R. A.; Gregg, B. A., Self-Organization in Thin Films of Liquid Crystalline Perylene Diimides. *J Phys Chem B.* **1997**, *101*, 11004-11006.

22. Gregg, B. A.; Cormier, R. A., Doping Molecular Semiconductors: N-Type Doping of a Liquid Crystal Perylene Diimide. *J. Am. Chem. Soc.* **2001**, *123*, 7959-7960.

23. Würthner, F.; Thalacker, C.; Diele, S.; Tschierske, C., Fluorescent J-Type Aggregates and Thermotropic Columnar Mesophases of Perylene Bisimide Dyes. *Chem. Eur. J.* **2001**, *7*, 2245-2253.

24. Wurthner, F.; Saha-Moller, C. R.; Fimmel, B.; Ogi, S.; Leowanawat, P.; Schmidt, D., Perylene Bisimide Dye Assemblies as Archetype Functional Supramolecular Materials. *Chem. Rev.* **2016**, *116*, 962-1052.

25. Gsanger, M.; Oh, J. H.; Konemann, M.; Hoffken, H. W.; Krause, A. M.; Bao, Z.; Wurthner, F., A Crystal-Engineered Hydrogen-Bonded Octachloroperylene Diimide with a Twisted Core: An N-Channel Organic Semiconductor. *Angew. Chem.* **2010**, *49*, 740-743.

26. Schmidt-Mende, L.; Fechtenkotter, A.; Mullen, K.; Moons, E.; Friend, R. H.; MacKenzie, J. D., Self-Organized Discotic Liquid Crystals for High-Efficiency Organic Photovoltaics. *Science* **2001**, *293*, 1119-1122.

27. Wurthner, F.; Chen, Z.; Dehm, V.; Stepanenko, V., One-Dimensional Luminescent Nanoaggregates of Perylene Bisimides. *Chem. Commun.* **2006**, 1188-1190.

28. Katz, H. E.; Lovinger, A. J.; Johnson, J.; Kloc, C.; Siegrist, T.; Li, W.; Lin, Y. Y.; Dodabalapur, A., A Soluble and Air-Stable Organic Semiconductor with High Electron Mobility. *Nature* **2000**, *404*, 478-481.

29. Zhan, X.; Facchetti, A.; Barlow, S.; Marks, T. J.; Ratner, M. A.; Wasielewski, M. R.; Marder, S. R., Rylene and Related Diimides for Organic Electronics. *Adv. Mater.* **2011**, *23*, 268-284.

30. Rybakiewicz, R.; Tszydel, I.; Zapala, J.; Skorka, L.; Wamil, D.; Djurado, D.; Pecaut, J.; Ulanski, J.; Zagorska, M.; Pron, A., New Semiconducting Naphthalene Bisimides N-Substituted with Alkoxyphenyl Groups: Spectroscopic, Electrochemical, Structural and Electrical Properties. *RSC Adv.* **2014**, *4*, 14089-14100.

31. Kobaisi, M. A.; Bhosale, S. V.; Latham, K.; Raynor, A. M.; Bhosale, S. V., Functional Naphthalene Diimides: Synthesis, Properties, and Applications. *Chem. Rev.* **2016**.

32. Bell, T. D.; Bhosale, S. V.; Forsyth, C. M.; Hayne, D.; Ghiggino, K. P.; Hutchison, J. A.; Jani, C. H.; Langford, S. J.; Lee, M. A.; Woodward, C. P., Melt-Induced Fluorescent Signature in a Simple Naphthalenediimide. *Chem. Commun.* **2010**, *46*, 4881-4883.

33. Mizoshita, N.; Tani, T.; Inagaki, S., Isothermally Reversible Fluorescence Switching of a Mechanochromic Perylene Bisimide Dye. *Adv. Mater.* **2012**, *24*, 3350-5.

34. Mizuguchi, J., Electronic Characterization of N,N[Sup ′]-Bis(2-Phenylethyl)Perylene-3,4:9, 10-Bis(Dicarboximide) and Its Application to Optical Disks. *J. Appl. Phys.* **1998**, *84*, 4479.

35. Dharmarwardana, M.; Welch, R. P.; Kwon, S.; Nguyen, V. K.; McCandless, G. T.; Omary, M. A.; Gassensmith, J. J., Thermo-Mechanically Responsive Crystalline Organic Cantilever. *Chem. Commun.* **2017**, *53*, 9890-9893.

36. Gaussian 09, R. E., M. J. Frisch, G. W. Trucks, H. B. Schlegel, G. E. Scuseria, M. A. Robb, J. R. Cheeseman, G. Scalmani, V. Barone, B. Mennucci, G. A. Petersson, H. Nakatsuji, M. Caricato, X. Li, H. P. Hratchian, A. F. Izmaylov, J. Bloino, G. Zheng, J. L. Sonnenberg, M. Hada, M. Ehara, K. Toyota, R. Fukuda, J. Hasegawa, M. Ishida, T. Nakajima, Y. Honda, O. Kitao, H. Nakai, T. Vreven, J. A. Montgomery, Jr., J. E. Peralta, F. Ogliaro, M. Bearpark, J. J. Heyd, E. Brothers, K. N. Kudin, V. N. Staroverov, R. Kobayashi, J. Normand, K. Raghavachari, A. Rendell, J. C. Burant, S. S. Iyengar, J. Tomasi, M. Cossi, N. Rega, J. M. Millam, M. Klene, J. E. Knox, J. B. Cross, V. Bakken, C. Adamo, J. Jaramillo, R. Gomperts, R. E. Stratmann, O. Yazyev, A. J. Austin, R. Cammi, C. Pomelli, J. W. Ochterski, R. L. Martin, K. Morokuma, V. G. Zakrzewski, G. A. Voth, P. Salvador, J. J. Dannenberg, S. Dapprich, A. D. Daniels, Ö. Farkas, J. B. Foresman, J. V. Ortiz, J. Cioslowski, and D. J. Fox, Gaussian, Inc., Wallingford CT, 2009.

37. Sears, D. R.; Klug, H. P., Density and Expansivity of Solid Xenon. *J. Chem. Phy.* **1962**, *37*, 3002.

38. Safin, D. A.; Bolte, M.; Garcia, Y., Solid-State Photochromism and Thermochromism of N-Salicylidene Pyrene Derivatives. *CrystEngComm* **2014**, *16*, 8786.

39. Karabiyik, H.; Karabiyik, H.; Ocak Iskeleli, N., Hydrogen-Bridged Chelate Ring-Assisted π-Stacking Interactions. *Acta Cryst. A* **2012**, *B68*, 71-9.

40. Wurthner, F., Perylene Bisimide Dyes as Versatile Building Blocks for Functional Supramolecular Architectures. *Chem. Commun.* **2004**, 1564-1579.

41. Naito, H.; Morisaki, Y.; Chujo, Y., *O*-Carborane-Based Anthracene: A Variety of Emission Behaviors. *Angew. Chem.* **2015**, *54*, 5084-7.

42. Graser, F.; Hädike, E., Kristallstruktur Und Farbe Bei Perylen-3,4:9,10-Bis(Dicarboximid)-Pigmenten,2. *Liebigs Ann.* **1984**, *1984*, 483-494.

43. Rawashdeh-Omary, M. A.; Omary, M. A.; Patterson, H. H., Oligomerization of Au(Cn)2-and Ag(Cn)2-Ions in Solution Via Ground-State Aurophilic and Argentophilic Bonding. *J. Am. Chem. Soc.* **2000**, *122*, 10371-10380.

44. Grimme, S., Semiempirical Gga-Type Density Functional Constructed with a Long-Range Dispersion Correction. *J. Comput. Chem.* **2006**, *27*, 1787-1799.

45. Cundari, T. R.; Stevens, W. J., Effective Core Potential Methods for the Lanthanides. *J. Chem. Phy.* **1993**, *98*, 5555-5565.

46. Stevens, W. J.; Basch, H.; Krauss, M., Compact Effective Potentials and Efficient Shared-Exponent Basis Sets for the First- and Second-Row Atoms. *J. Chem. Phy.* **1984**, *81*, 6026-6033.

47. Stevens, W. J.; Krauss, M.; Basch, H.; Jasien, P. G., Relativistic Compact Effective Potentials and Efficient, Shared-Exponent Basis Sets for the Third-, Fourth-, and Fifth-Row Atoms. *Can. J. Chem.* **1992**, *70*, 612-630.

48. Pietro, W. J.; Francl, M. M.; Hehre, W. J.; DeFrees, D. J.; Pople, J. A.; Binkley, J. S., Self-Consistent Molecular Orbital Methods. 24. Supplemented Small Split-Valence Basis Sets for Second-Row Elements. *J. Am. Chem. Soc.* **1982**, *104*, 5039-5048.

49. Dunham, J. L., The Energy Levels of a Rotating Vibrator. *Phy. Rev.* **1932**, *41*, 721-731.

50. Winnik, F. M. Photophysics of Preassociated Pyrenes in Aqueous Polymer Solutions and in Other Organized Media. *Chem. Rev.* **1993**, *93*, 587-614.

CHAPTER 5

NITROXYL MODIFIED TOBACCO MOSAIC VIRUS AS A METAL-FREE HIGH-RELAXIVITY MRI AND EPR ACTIVE SUPEROXIDE SENSOR[1]

Authors – Madushani Dharmarwardana, André F. Martins, Zhuo Chen, Philip M. Palacios,

Chance M. Nowak, Raymond P. Welch, Shaobo Li, Michael A. Luzuriaga, Leonidas Bleris,

Brad S. Pierce, A. Dean Sherry, Jeremiah J. Gassensmith

The Department of Chemistry, BE26

The University of Texas at Dallas

800 West Campbell Road

Richardson, Texas 75080-3021

5.1 Summary

Superoxide overproduction is known to occur in multiple disease states requiring critical care yet non-invasive detection of superoxide in deep tissue remains a challenge. Herein, we report a metal-free magnetic resonance imaging (MRI) and electron paramagnetic resonance (EPR) active contrast agent prepared by "click conjugating" paramagnetic organic radical contrast agents (ORCAs) to the surface of tobacco mosaic virus (TMV). While ORCAs are known to be reduced *in vivo* to an MRI/EPR silent state, their oxidation is facilitated specifically by reactive oxygen species—in particular superoxide—and are largely unaffected by peroxides and molecular oxygen. Unfortunately, single molecule ORCAs typically offer weak MRI contrast. In contrast, our data confirm that the macromolecular ORCA-TMV conjugates show marked enhancement for T_1 contrast at low field (<3.0 T), and T_2 contrast at high field (9.4 T). Additionally, we demonstrated that the unique topology of TMV allows for "quenchless fluorescent" bimodal probe for concurrent fluorescence and MRI/EPR imaging, which was made possible by exploiting the unique inner and outer surface of the TMV nanoparticle. Finally, we show TMV-ORCAs do not respond to normal cellular respiration, minimizing the likelihood for background, yet still respond to enzymatically produced superoxide in complicated biological fluids like serum.

5.2 Introduction

The upregulation of reactive oxygen species (ROS), in particular superoxide, is associated with certain cancers,[1,2] neurodegenerative disorders[1,3,4] such as Parkinson's disease,[5] diabetes,[6,7] mitochondrial diseases such as Friedreich ataxia,[8] Leber's hereditary optic neuropathy (LHON),[9] mitochondrial encephalomyopathy, lactic acidosis, stroke-like episodes (MELAS),[10] myoclonic

epilepsy with ragged red fibers (MERRF),[11] and Leigh syndrome (LS).[3,4,12,13] The detection of superoxides, both extra- and intracellularly, has consequently become an area of research interest in efforts to study and target diseased tissues.[14,15] Superoxide sensing in biological tissues has largely focused on fluorescent imaging, as many dyes are easily quenched in the presence of ROS,[16,17] and superoxide in particular.[18] Moreover, the superoxides produced by diabetics can cause serious health complications such as heart injuries and sensing of superoxide overproduction in these situations is also done using fluorescence imaging.[19,20] An unavoidable issue with fluorescence imaging in general, however, is limited tissue penetration, making it problematic for tissue imaging but ideal in guided surgery applications. Consequently, the need to detect cellular and biological events in deep tissue non-invasively has driven the development of "smart" probes for magnetic resonance imaging (MRI)[21-23] or electron paramagnetic resonance (EPR) modalities.[14,24]

On the MRI front, paramagnetic chemical exchange saturation transfer (paraCEST) and other stimuli responsive contrast agents have begun to generate considerable interest for their ability to detect changes in extracellular pH or production of specific biological markers like lactate.[25-27] While redox active paraCEST agents based on lanthanides have emerged as potential sensors of singlet oxygen[28] and peroxide,[29] none have clearly emerged as candidates for superoxide.[25] Paramagnetic nitroxide organic radical contrast agents (ORCAs), on the other hand, have been making inroads toward superoxide detection *in vivo* and *in vitro*.[14,30-32] While sterically unencumbered nitroxide radicals like TEMPO (Figure 5.1b) are easily reduced to diamagnetic hydroxylamines in biological media, making their use as long-lived MRI contrast agents problematic, this property has been utilized to map redox activity in tumors *ex vivo* and *in vivo*.[33]

On the other hand, re-oxidation is kinetically favored by superoxide while less reactive ROS, and in particular hydrogen peroxide, do not significantly oxidize hydroxylamines back.[1] Consequently, TEMPO can serve as a "turn-on" MRI sensor for superoxide. The benefit of "turn-on" over "turn-off" sensors is that they can have nearly infinite contrast against background.[34]
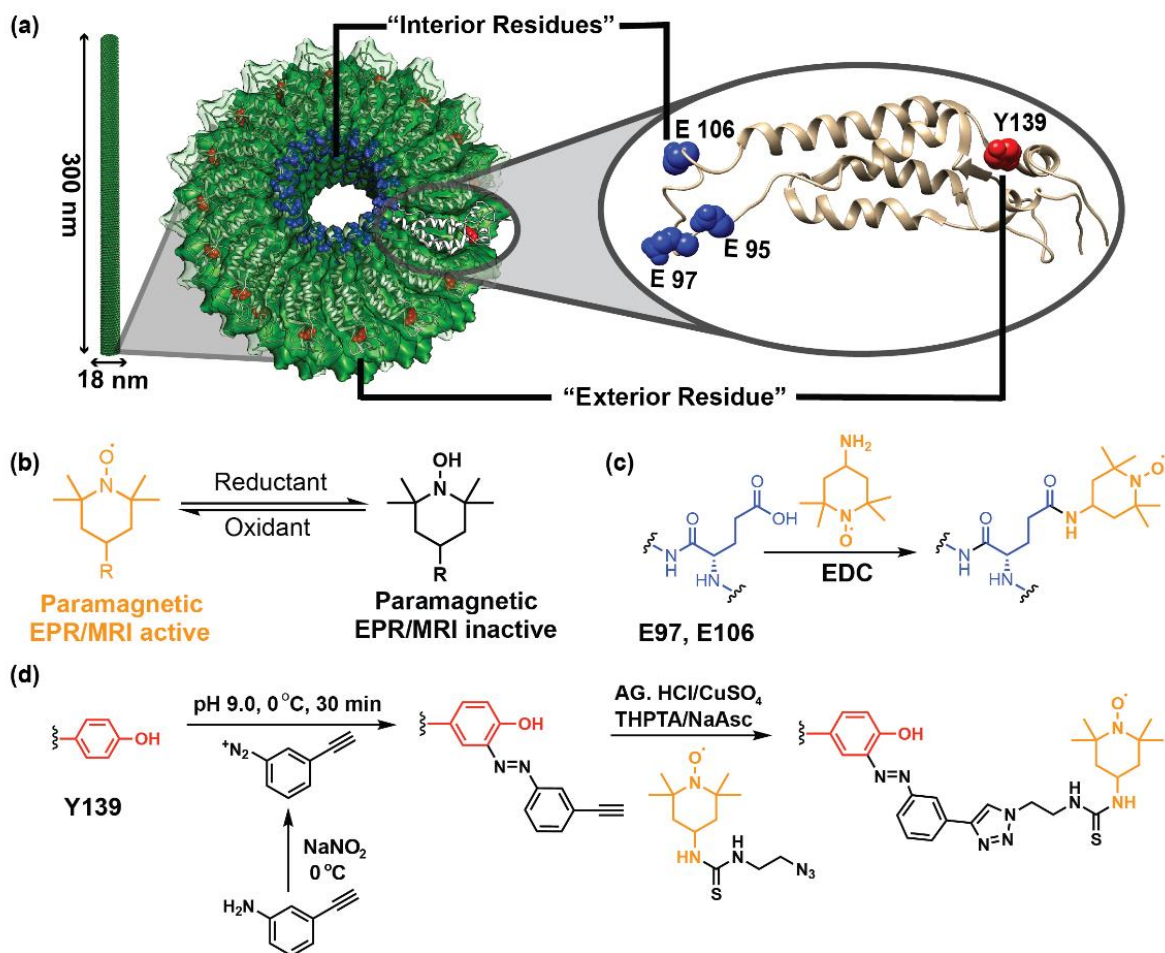
Figure 5.1. (a) Representations of a single TMV nanoparticle (created in Chimera using PDB ID is 2tmv) and a single TMV coat protein highlighting solvent exposed amino acid residues available for bio-conjugation reactions. (b) Oxidation states of nitroxide radicals. Paramagnetic radical species can be detected by both EPR and MRI whereas the reduced diamagnetic species is neither MRI nor EPR active. (c) Bioconjugation to the interior surface of TMV via EDC coupling reaction to make inTEMPO-TMV. (d) TMV bioconjugation on the exterior via stepwise diazonium coupling followed by a CuAAC reaction to make exTEMPO-TMV.

Nevertheless, ORCAs, have historically suffered from low proton relaxation rates compared to metal-based contrast agents. These poor relaxivities have been cleverly addressed using polymeric systems[33,35-39] as these multivalent scaffolds allow for high local concentrations of paramagnetic ORCAs. While such multimeric polymeric scaffolds allow for attachment of both MRI and fluorescence agents on the same platform, ORCAs are well-known and potent quenchers of adjacent fluorophores.[33] This quenching process means that when an ORCA is MRI/EPR active, adjacent fluorophores are typically quenched. While this has been elegantly exploited,[32,33,40,41] a true ratiometric sensor capable of assessing the probe concentration by fluorescence and the relative ROS levels by EPR/MRI signal would require a constant fluorescence emission regardless of the oxidation state of the ORCA. Viral nanoparticles (VNPs) provide distinct structural features that make them well suited to resolving some of these issues. For instance, they contain spatially well-defined functionalities, are rigid and monodisperse, and contain discrete topological surfaces that provide a distinct "outer" and "inner" surface.[42] These distinctions are well suited for EPR active spin systems prone to spin pairing and relaxation when in close contact with other radical species.[25] Tobacco Mosaic Virus (TMV) is a 300 nm × 18 nm rod-shaped RNA virus that contains 2130 individual coat proteins.[43-45]

Each of these coat proteins contains an easily functionalizable tyrosine residue (Y139) on the exterior surface, which is spatially separated from the next closest accessible tyrosine[46] by 2.3 – 2.6 nm.[47,48] Furthermore, TMV contains a 4 nm narrow pore lined with glutamic acid residues (E97 and E106), likewise easily functionalized, and electronically inaccessible to the exterior surface.[49-51] These features provide two distinct advantages over existing polymeric nanostructures containing nitroxide radicals: (i) radical systems on the surface are spaced far enough apart so that

spin-spin coupling is minimized even if 100% of the available functional groups are utilized and, (ii) fluorophores placed on the interior of the capsid will not be quenched by electron transfer processes from radical TEMPO moieties placed on the exterior surface. Previous studies have shown that VNPs and virus-like particles (VLPs) decrease the T_1 and T_2 relaxation times of attached metal-based MRI contrast agents.[41,48,52-63] The increase in r_1 ($1/T_{1p}$, p = paramagnetic contribution; $mM^{-1} \cdot s^{-1}$) relaxivity in these systems has been attributed to an increase in molecular diffusion and translation correlation times brought about by attachment to the surface of relatively massive, rigid, and slowly diffusing protein ensembles.

Here we present a method to create a sensitive EPR/MRI probe for superoxide detection *in vitro* with enhanced r_1 and r_2 relaxivities that rival clinically used molecular lanthanide-based MRI probes. The observed r_2/r_1 ratio allows TEMPO-conjugated TMV probes to operate as both a T_1 and T_2 contrast agent, making these probes valuable for both clinical (<3 T) and pre-clinical (>3 T) MRI scanners. We have also designed a bimodal TEMPO-TMV probe for ratiometric fluorescence experiments that is functionalized with a fluorescent dye on the interior and with an ORCA for MRI/EPR imaging on the exterior. The unique topology of the VNP scaffold allows for the insertion of an internal fluorescent probe as a concentration marker that is insensitive to the oxidation state of the ORCA probe. Finally, we present the evaluation of these probes in both cells and serum.

5.3 Experimental

5.3.1 Materials

All the solvents and reagents for buffers were purchased from Fisher Scientific. 4-Amino-2,2,6,6-tetramethylpiperidine 1-oxyl free radical (TEMPO-NH$_2$), 4-isothiocyanato-2,2,6,6-tetramethylpiperidine 1-oxyl free radical (TEMPO-NCS), 2-bromoethylamine hydrobromide, sodium nitrite, *p*-toluenesulfonic acid monohydrate, 3-ethynylaniline, cupric sulfate pentahydrate, sodium ascorbate, aminoguanidine hydrochloride, 1-(3-dimethylaminopropyl)-3-ethylcarbodiimide hydrochloride (EDC), 1-hydroxybenzotriazole hydrate (HOBt), propargylamine, triethylamine, fluorescein isothiocyanate isomer I (FITC), sodium azide, β-mercaptoethanol, polyethylene glycol 8000 (PEG 8000), triton X-100 surfactant, Hydrazinobenzene sulfonic acid hydrates, 3-methyl-2-butanone, potassium hydroxide, o-dichlorobenzene, 6-bromohexanoic acid, malonaldehyde bis(phenylimine) monohydrochloride, and pyridine were purchased from Alfa Aesar, Acros Organics, Fisher Scientific, Oakwood Chemical, TCI Chemicals, or Sigma Aldrich, and used without further purification. Protein concentration was measured using a Pierce™ Modified Lowry Protein Assay Kit (Thermal Fisher Scientific, Waltham, MA).

5.3.2 Propagation and Isolation of TMV

TMV particles were isolated from *N. benthamiana* plants from a published method.[50] The tobacco plants were grown, infected, and collected after 10 d of infection and stored at -80 °C until needed. Approximately 100 g of leaves were blended in pulses with ice cold extraction buffer (0.1 M pH 7.4 potassium phosphate (KP) buffer, 0.2% (v/v) β-mercaptoethanol) followed by being pulverized

with a mortar and pestle. The mixture was filtered through cheesecloth to remove the plant solids, and the filtrate centrifuged at 11,000 $\times g$ for 20 min at 4°C. The supernatant was filtered through cheesecloth again, and an equal volume of 1:1 chloroform/1-butanol mixture was added and stirred on ice for 30 min. The mixture was centrifuged at 4500 $\times g$ for 10 min. The supernatant was collected, and the aqueous phase separated. To the aqueous phase was added NaCl to 0.2 M, 8% (w/w) PEG 8000, and 1% (w/w) Triton X-100 surfactant. The mixture was stirred on ice for 30 min and stored at 4 °C for 1 h. The solution was centrifuged at 22,000 $\times g$ for 15 min at 4 °C. The supernatant was discarded, and the pellet resuspended in 0.1 M pH 7.4 KP buffer at 4 °C overnight. The supernatant was carefully layered on a 40% (w/v) sucrose gradient in 0.01 M KP buffer (with at least 1 freeze-thaw cycle) in ultraclear tubes and centrifuged in a swing bucket rotor for 2 h at 96,000 $\times g$. The light-scattering region was collected and centrifuged at 360,562 $\times g$ for 1.5 h. The supernatant was discarded, and the pellet resuspended in 0.01 M pH 7.4 KP buffer overnight. The solution was portioned equally into microcentrifuge tubes and centrifuged at 15,513 $\times g$ for 15 min. The supernatant was collected as the final TMV solution. UV-Vis measurements were taken with NanoDrop at 260 nm (RNA) and 280 nm (protein). A ratio of A_{260}/A_{280} around 1.26 indicates intact TMV. Using the Beer-Lambert Law with $\varepsilon = 3$ as reported,[64] the solution concentration was determined.

5.3.3 Bioconjugations

<u>Exterior surface modification of TMV with TEMPO-N$_3$ (exTEMPO-TMV)</u>

First, 3-ethynylaniline diazonium salt was prepared *in situ* by adding 400 µL of 0.3 M *p*-toluenesulfonic acid monohydrate, 75 µL of 0.68 M 3-ethynylaniline and 25 µL of 3.0 M sodium nitrite. The resultant mixture was coved with an aluminum foil and cooled on ice for 1 h. Then,

100 µL of stock TMV solution (20 mg/mL) was diluted to 2 mg/mL with 850 µL of 0.1 M pH 8.8 borate buffer and cooled on ice at least 10 min. To this solution, 50 µL of *in situ* prepared 3-ethynylaniline diazonium salt was added and kept on ice for 1 h. Finally, the resultant solution (TMV-Alkyne) was purified with a PD MidiTrap G-25 column and the solution was washed three times with 0.1 KP buffer and concentrated to 10 mg/mL with a 10K MWCO Pierce™ Protein Concentrator.

200 µL of TMV-Alkyne (10 mg/mL) was mixed with 730 µL of 0.1 M pH 7.4 KP buffer. Then, 10 µL of 0.05 M TEMPO-N_3 (50 eq per coat protein) and 10 µL of 0.1 M aminoguanidine hydrochloride were added to the TMV solution. Copper(I) was prepared *in situ* by adding 20 µL of 0.1 M $CuSO_4$, 20 µL of 0.5 M Tris(3-hydroxypropyltriazolylmethyl)amine (THPTA) and 10 µL of sodium ascorbate and this solution was then added to the above TMV solution. The reaction mixture was incubated at room temperature for 3 h and 20 µL of 0.5 M EDTA was added to the reaction and incubated another 10 min at room temperature. The reaction mixture was then purified with a PD MidiTrap G-25 column and the solution was washed three times with 0.1 KP buffer and concentrated to 10 mg/mL with a 10K MWCO Pierce™ Protein Concentrator.

Interior surface modification of TMV with TEMPO-NH_2 (inTEMPO-TMV)

First, 100 µL of stock TMV solution (20 mg/mL) was diluted to 2 mg/mL with 674 µL of 0.1 M pH 7.4 HEPES buffer at room temperature followed by the addition of 130 µL of 0.1 M TEMPO-NH_2, 3 mg of HOBt and 96 µL of 0.1 M EDC. The reaction mixture was incubated at room temperature for 24 h and then purified with a PD MidiTrap G-25 column and the solution was washed three times with 0.1 KP buffer and concentrated to 10 mg/mL with a 10K MWCO Pierce™ Protein Concentrator.

Dual surface modification with TEMPO and FITC (inFITC-exTEMPO-TMV)

The exterior surface of *in*FITC-TMV was modified with TEMPO-N$_3$ as described in the "*Exterior surface modification of TMV with TEMPO-N$_3$ (ex*TEMPO-TMV)*" section to yield *ex*TEMPO-TMV. Then the interior surface was modified with propargyl amine using an EDC coupling reaction. 200 µL of *ex*TEMPO-TMV solution (10 mg/mL) was diluted to 2 mg/mL with 574 µL of 0.1 M pH 7.4 HEPES buffer at room temperature followed by the addition of 130 µL of 0.1 M propargyl amine, 3 mg of HOBt, and 96 µL of 0.1 M EDC. The reaction mixture was incubated at room temperature for 24 h, purified with a PD MidiTrap G-25 column, and the solution was washed three times with 0.1 KP buffer and concentrated to 10 mg/mL with a 10K MWCO Pierce™ Protein Concentrator to yield *in*PA-*ex*TEMPO-TMV. FITC-azide was then attached by the CuAAC reaction. 200 µL of *in*PA-*ex*TEMPO-TMV (10 mg/mL) was mixed with 750 µL of 0.1 M pH 7.4 KP buffer. Then, 10 µL of 0.01 M FITC-azide (10 eq per coat protein) and 10 µL of 0.1 M aminoguanidine hydrochloride were added to the *in*PA-*ex*TEMPO-TMV solution. Copper(I) was prepared *in situ* by adding 20 µL of 0.1 M CuSO$_4$, 20 µL of 0.5 M Tris(3-hydroxypropyltriazolylmethyl)amine (THPTA) and 10 µL of sodium ascorbate and this solution was then added to the above TMV solution. The reaction mixture was incubated at room temperature for 3 h and 20 µL of 0.5 M EDTA was added to the reaction and incubated another 10 min at room temperature. The reaction mixture was then purified with a PD MidiTrap G-25 column and the solutions were concentrated to 10 mg/mL with a 10K MWCO Pierce™ Protein Concentrator.

Dual surface modification with TEMPO and Cy5 (inCy5-exTEMPO-TMV)

The exterior surface of *in*FITC-TMV was modified with TEMPO-N$_3$ as described in the "*Exterior surface modification of TMV with TEMPO-N$_3$ (ex*TEMPO-TMV)*" section to yield *ex*TEMPO-TMV. Then the interior surface was modified with propargyl amine using an EDC coupling reaction. 200 µL of *ex*TEMPO-TMV solution (10 mg/mL) was diluted to 2 mg/mL with 574 µL of 0.1 M pH 7.4 HEPES buffer at room temperature followed by the addition of 130 µL of 0.1 M ethylenediamine (EA), 3 mg of HOBt, and 96 µL of 0.1 M EDC. The reaction mixture was incubated at room temperature for 24 h, purified with a PD MidiTrap G-25 column, and the solution was washed three times with 0.1 KP buffer and concentrated to 10 mg/mL with a 10K MWCO Pierce™ Protein Concentrator to yield *in*EA-*ex*TEMPO-TMV. Cy5-COOH was then attached by the EDC reaction. 200 µL of *in*EA-*ex*TEMPO-TMV solution (10 mg/mL) was diluted to 2 mg/mL with 574 µL of 0.1 M pH 7.4 HEPES buffer at room temperature followed by the addition of 130 µL of 0.1 M Cy5-COOH, 3 mg of HOBt, and 96 µL of 0.1 M EDC. The reaction mixture was incubated at room temperature for 24 h, purified with a PD MidiTrap G-25 column, and the solution was washed three times with 0.1 KP buffer and concentrated to 10 mg/mL with a 10K MWCO Pierce™ Protein Concentrator to yield *inCy5-ex*TEMPO-TMV.

5.3.4   Instrumentation

Nuclear Magnetic Resonance (NMR)

NMR spectra were measured using a Bruker AVANCE III 500 MHz spectrometer with Si(CH$_3$)$_4$ used as a reference standard.

Transmission Electron Microscopy (TEM)

Transmission electron micrographs were taken on a JEOL JEM-1400+ at 120 kV with a Gatan 4k × 4k CCD camera. 5 µL of the ~0.1 mg/mL desalted sample was placed on a 300 mesh Formvar/carbon-coated copper grid (Electron Microscopy Sciences, Hatfield, PA, USA), allowed to stand for 30 seconds, and wicked off with Whatman #1 filter paper. 5 µL of 2% uranyl acetate (SPI Supplies, West Chester, PA, USA) was placed on the grid, allowed to stand for 30 seconds, wicked off as before, and the grid allowed to dry completely in air.

Electrospray Ionization Mass Spectrometry (ESI-MS)

Modified TMV samples were characterized by an LC/ESI-MS system composed of an Agilent 1100 series HPLC system followed by a 4000 QTRAP mass spectrometer. HPLC was performed using a reverse-phase Agilent Zorbax® C_{18} (150 mm) column with acetonitrile:18.2 MΩ DI H_2O gradient (1 mL/min) mobile phase containing 0.1% formic acid. Spectra obtained with Analyst software (4000 QTRAP) were deconvoluted using Peakview 2.1 software from AB SCIEX.

Size exclusion chromatography (SEC)

Analytical SEC was performed using an Agilent 1100 series HPLC system on a GS400SWXL (7.8 mm × 300 cm) column with 100 mM pH 7.4 KP buffer with 0.05% NaN_3.

Fluorescence Measurements

Fluorescence spectra were measured with a a Horiba Fluorolog fluorimeter (Horiba, Kyoto, Japan). The dye modified *ex*TEMPO-TMV (1 mg/mL) and control samples were prepared in pH 7.4 100 mM KP buffer. 1.5 mL of the TMV sample was mixed with 57 µL of either 100 mM KP buffer (control) or 100 mM sodium ascorbate. Emission spectra were recorded for 1 h at 10 min time intervals.

<u>UV-Vis spectroscopy</u>

UV-Vis spectra were taken using a UV-1601PC UV-Vis-NIR Spectrophotometer (Shimadzu, Kyoto, Japan), Tecan Spark 20M plate reader, or Biotek Synergy H4 hybrid reader (Biotek, Winooski, VT). NanoDrop UV-Vis measurements were performed on a Thermo Scientific NanoDrop 2000 Spectrophotometer.

<u>Electron Paramagnetic Resonance (EPR) spectroscopy</u>

In this manuscript we used two types of X-band EPR spectrometers.

X-band (9 GHz) electron paramagnetic resonance (EPR) spectra were recorded on a Bruker (Billerica, MA) EMX Plus spectrometer equipped with a bimodal resonator (Bruker model 4116DM). A modulation frequency and amplitude of 100 kHz and 0.1 mT was used for all EPR measurements. All experimental data used for spin-quantification were collected under non-saturating conditions. EPR spectra were calculated by diagonalization of the general spin Hamiltonian[65-67] for a single electron wavefunction using the software SpinCount (ver. 6.0.6325.21642), written by Professor M. P. Hendrich at Carnegie Mellon University.[68] Nuclear hyperfine interactions (A) are treated with second order perturbation theory. The simulations were generated with consideration of all intensity factors, both theoretical and experimental, to allow for determination of species concentration. The only unknown factor relating the spin concentration to signal intensity was an instrumental factor that is specific to the microwave detection system. However, this was determined by a spin standard, Cu(EDTA), prepared from a copper atomic absorption standard solution purchased from Sigma-Aldrich.

All the *ex*TEMPO-TMV and *in*TEMPO-TMV samples were prepared in 100 mM pH 7.4 KP buffer for the EPR measurements. Each sample were placed in a 1 mm glass capillary tube, and X-band

EPR spectra were recorded using a Bruker ER041XG microwave bridge X-band EPR instrument with a TE102 rectangular cavity. All the EPR measurements were taken using the following instrumental conditions: microwave frequency: 9.38 GHz, microwave power: 1 mW, modulation amplitude: 0.1 mT, temperature: 293 K.

Radical quenching by EPR spectroscopy

First, 10 mM sodium ascorbate solution was made with 0.1 M of pH 7.4 KP. Then, 5 µL of 10 mg/mL of dye modified *ex*TEMPO-TMV was diluted with 44 µL of 0.1 M pH 7.4 KP. To this solution, 0.7 µL of prepared 10 mM sodium ascorbate solution was added and mixed well. The resulting solution was drawn into the 1-mm glass capillary tube and placed in a 4-mm quartz EPR tube and sealed with a lid. EPR spectra recorded as a function of time with 2 mW microwave power at 298 K.

Ex vivo EPR spectroscopy

HeLa cells were incubated in DMEM (Sigma-Aldrich, supplemented with 10% FBS, 4500 mg/L glucose and 1% Pen- Strep) cell culture media with 5% CO_2 at 37 ºC for 24 h. 1 x 10^6 of the cells were incubated with 500 ng/mL of PMA an hour. Then the reduced *ex*TEMPO-TMV samples was added (final concentration of 1 mg/mL) to the PMA simulated cells in serum-free DMEM and incubated with 5% CO_2 at 37 ºC for 1 hour. Then, the cell sample was drawn into 1 mm diameter capillary tube and placed in a 4-mm quartz EPR tube and capped, sealed with a parafilm and placed on ice until the measurements are taken. The reference for the cell experiment was prepared using 2.52 $mgmL^{-1}$ exTEMPO-TMV in $1\times$ PBS and the instrument was calibrated with 0.1 mM TEMPO-NH_2 in $1\times$ PBS.

116

Magnetic Resonance Imaging (MRI)

Longitudinal and transversal relaxation times were measured on a MRS-6 NMR analyzer from the Institute Jožef Stefan (Ljubljana, Slovenija) operating at 20 MHz, Brucker mq60 series, operating at 60MHz, and Bruker AVANCE III operating at 500 MHz. Relaxivity was determined by linear regression analysis of the relaxation rates of five solutions (0 – 0.14 mM). All samples were measured at 310 K using temperature control units.

Phantom images with *ex*TEMPO-TMV and *in*TEMPO-TMV samples, along with 18.2 MΩ DI H_2O, PBS buffer, sodium ascorbate, KO_2, and TEMPO-NH_2 standard solutions were acquired simultaneously on an Agilent (Santa Clara, CA) 9.4 T (500 MHz) small animal MRI system using standard 5-mm diameter cell culture glass tubes and a 38-mm diameter ^1H birdcage volume coil. Each sample was approximately 200 mL with a concentration of 0.14 mM per TEMPO in PBS buffer at a pH of 7.0. The sample temperature was monitored with a thermocouple and held constant by a heated air system from Small Animal Instruments (Stony Brook, NY). The fast spin-echo settings were: TE/TR = 200/2000 ms, averages = 6, field of view = $40 \times 40 \times 40$ mm, Matrix = $128 \times 128 \times 128$. The T_1-weighted gradient echo scans were: TE/TR = 1.69/3.34 ms, averages = 8, field of view = $40 \times 40 \times 40$ mm, Matrix = $128 \times 128 \times 128$.

Confocal Microscopy

4.0×10^4 of cells were seeded on 35 mm glass bottom petri dish with DMEM (Sigma-Aldrich, supplemented with 10% FBS, 4500 mg/L glucose and 1% Pen-Strep) cell culture media under 5% CO_2 at 37 ℃ for 24 h. Cells were incubated with 0.5 mg/mL of TMV samples in serum-free DMEM under 5% CO_2 at 37 °C for 4 h. Cells were then washed with DMEM three times, DPBS three times before stained using MitoTracker Deep Red at 37 °C for 30 min. Cells were then

washed with DPBS three times, followed by nucleus staining using Hoechst 33342 at RT for 5 min in dark. The cells were then washed using DPBS before DMEM was added. Live cells were imaged using an Olympus FV3000 confocal laser scanning microscope with 40× objective. Filter sets: Hoechst 33342 (nucleus), FITC (TMV conjugates) and Cy5 (MitoTracker Deep Red).

Reduced TMV-TEMPO for the detection of superoxide in serum using EPR and phantom imaging

Reduced exTEMPO-TMV (red-exTEMPO-TMV) probe for the superoxide detection was prepared using exTEMPO-TMV. The radical was quenched using 0.1 M sodium ascorbate solution, the sample was incubated at room temperature for 4 hours, excess reductant was removed by passing through a PD MidiTrap G-25 column, and the solutions were washed with 1× PBS treated with 25g/L Chelex-100 resin consisting of 1 mM DTPA and concentrated with a 10K MWCO Pierce™ Protein Concentrator. The concentration of TMV solution was determined by Lowry assay. (19.32 mgmL^{-1}). The solution was immediately purged with nitrogen gas, capped, and sealed with parafilm. 10 mM Xanthine (X) stock solution prepared solution was prepared using 1xPBS (with 1 mM DTPA) and a few drops of 1 M NaOH. Xanthine (final concentration 0.05 mM in 1× PBS with 50 µM DTPA) was added to the red-exTEMPO-TMV sample. The reaction was started by adding xanthine Oxidase (final concentration 0.1 U/mL). The reaction mixture contained 50% fetal bovine serum (FBS) by volume. EPR spectra were recorded as a function of time over 24 hours and phantom images were also obtained for the same samples.

Table 5.1. Table of reactant volume used in the serum study

Sample	V_{TMV}/ µL	V_X/ µL	V_{XO}/ µL	V_{FBS}/ µL	V_{1xPBS}/ µL
X/XO	125	25	50	250	50
Control	125	-	-	250	125

5.3.5 Synthesis

Synthesis of 2-azidoethylamine

The compound 2-azidoethylamine was synthesized according to a previously published procedure[50] ^{1}H-NMR (500 MHz, CDCl$_3$) δ ppm 1.456 (s, 2H), 2.788 (t, J=5.58, 2H), 3.273 (t, J=5.55, 2H) ^{13}C-NMR (125 MHz, CDCl$_3$) δ ppm 41.25, 54.52.

Synthesis of TEMPO-N$_3$
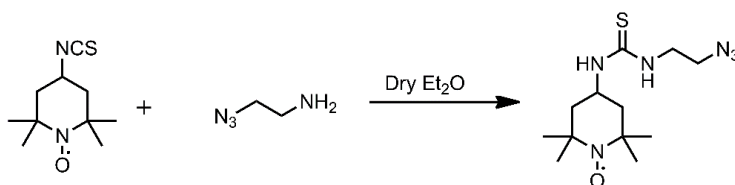
Figure 5.2. Synthesis of TEMPO-N$_3$

TEMPO-isothiocyanate (0.050 g, 0.23 mmol, 1.0 eq) in dry diethyl ether (1.0 mL) was added dropwise to a solution of 2-azidoethylamine (0.020 g, 0.23 mmol, 1.0 eq) in dry diethyl ether (1.0 mL). The reaction mixture was kept at room temperature until crystals appeared. (0.045 g, 0.15 mmol~ 90% yield). MALDI-TOF: Mass calculated for [M$^+$] 299.57, observed 299.14.

Synthesis of FITC-N$_3$
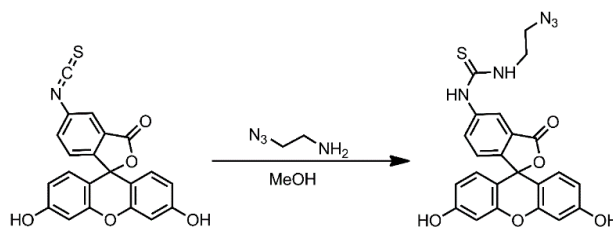
Figure 5.3. Synthesis of FITC-N$_3$

FITC-N$_3$ was synthesized according to a literature procedure.[50] A solution of fluorescein isothiocyanate (FITC) (0.152 g, 0.400 mmol) in 15.0 mL of MeOH was treated with 0.5 mL of Et$_3$N and 0.0738 g of 2-azidoethyl amine (0.900 mmol), stirred overnight, and evaporated to give FITC-N$_3$ as an orange colored solid (0.0700 g, 0.147 mmol, 46.0% yield).

Synthesis of THPTA
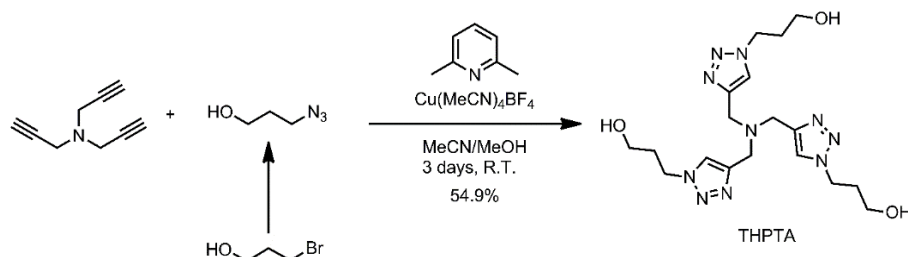
Figure 5.4. Synthesis of THPTA

Synthesis of 3-azido-1-propanol

3-azido-1-propanol was synthesized according to a literature procedure.[69] 3-Bromo-1-propanol (3.975 g, 28.60 mmol) and sodium azide (3.745 g, 57.60 mmol) were dissolved in 30.0 mL of water, the mixture was stirred at 90 °C overnight, and the mixture was extracted with (3×30 mL) of dichloromethane. The organic layers were combined and dried with anhydrous $MgSO_4$ and solvent was removed under reduced pressure to obtain 3-azido-1-propanol as a pale-yellow oil (2.541 g, 25.10 mmol, 87.90% yield). ^{1}H-NMR (500 MHz, $CDCl_3$) δ ppm 1.728 (5, J=6.40, 2H), 3.325 (t, J=6.75, 2H), 3.596 (t, J=6.10, 2H) ^{13}C-NMR (125 MHz, $CDCl_3$) δ ppm 31.27, 48.12, 59.45.

Synthesis of Tris(3-hydroxypropyltriazolylmethyl)amine (THPTA)

THPTA was synthesized according to a literature procedure.[69] Tripropargylamine (5.00 mmol, 0.707 mL), 3-azido-1-propanol (1.847 mL, 20.0 mmol), and 2,6-lutidine (0.58 mL, 5.0 mmol) were added to 10 mL of a 1:1 acetonitrile:MeOH mixture and cooled in an ice bath. Then, $Cu(CH_3CN)_4BF_4$ (0.0472 g, 0.150 mmol) was added and the reaction mixture stirred at room temperature for 3 d. The solvent was removed under vacuum, and the residue was dissolved in MeOH and precipitated in acetone. The product was crashed out of solution in the rotary evaporator in acetonitrile and a minimal amount of MeOH at 0 °C. The crystals were washed with

acetonitrile and dried under vacuum (1.192 g, 2.74 mmol, 55.0% yield). ^{1}H-NMR (500 MHz, CDCl$_3$) δ ppm 2.127 (5, J=6.51, 2H), 3.579 (t, J=6.18, 2H), 3.830 (s, 6H), 4.504 (t, J=6.95, 2H), 7.937 (s, 3H) ^{13}C-NMR (125 MHz, CDCl$_3$) δ ppm 31.78, 47.19, 47.53, 58.14, 125.26, 143.26.

Synthesis of Cy5-COOH[70]

Synthesis of 3H-Indole-2,3,3-trimethyl-5-sulfonic Acid, Potassium Salt (1)

Hydrazinobenzene sulfonic acid hydrates (1.50 g, 7.60 mmol) and 3-methyl-2-butanone (2.52 mL, 23.4 mmol) were dissolved in acetic acid (4.5 mL). The mixture was heated to reflux at 110 °C for 3 h and acetic acid was removed. A solution of crude sulfonic acid in methanol (10 mL) was added dropwise to a stirred solution of potassium hydroxide (0.500 g) in propanol (10 mL). The resulting mixture was stirred at 25 °C for 24 h and filtered through a paper filter. The residue was dried under reduced pressure to provide the crude compound (1.02 g, 4.49 mmol, 59.1% yield) (1). ^{1}H-NMR (600 MHz, D$_2$O) δ ppm 1.237 (s, 6H), 2.259 (s, 3H), 7.494 (d, J=8.02, 1H), 7.764 (d, J=8.09, 1H), 7.792 (s, 1H).
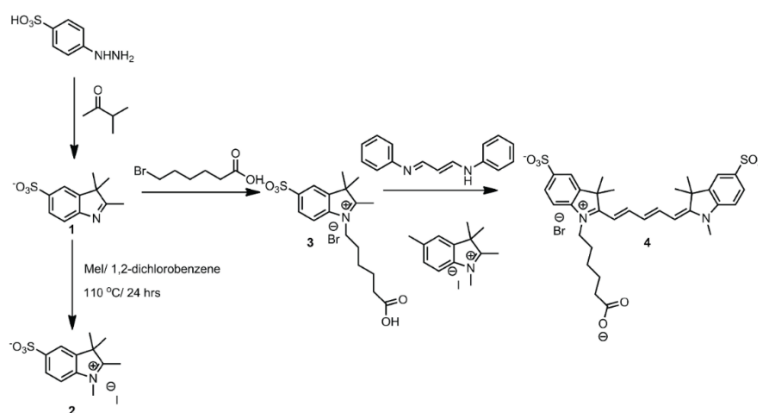
Figure 5.5. Synthesis of Cy5-COOH

Synthesis of 3H-Indolium, 1-Methyl-2,3,3-trimethyl-5-sulfonate (2)

A slurry of crude 1 (0.900 g, 3.24 mmol) in iodomethane (3.5 mL, 0.20 mol) under N$_2$ was heated to reflux for 24 h and cooled down to 25 °C. The liquid phase was decanted, and the residue was

washed with acetone (3 × 50 mL), filtered with a paper filter, and dried under reduced pressure at 40 °C to afford the crude compound (0.440 g, 1.25 mmol, 38.7% yield) (2). ^{1}H-NMR (600 MHz, D_2O) δ ppm 1.522 (s, 6H), 2.153 (s, 3H), 3.971 (s, 3H), 7.777 (d, J=8.25, 1H), 7.963 (d, J=8.80, 1H), 8.026 (s, 1H).

Synthesis of 3H-Indolium, 1-(5-Carboxypentyl)-2,3,3-trimethyl-5-sulfonate (3)

3H-Indole-2,3,3-trimethyl-5-sulfonic Acid, Potassium Salt (1.02 g, 3.70 mmol) and 6-bromohexanoic acid (0.827 g 4.33 mmol) were suspended in o-dichlorobenzene (5 mL). The suspension was stirred at 110 °C for 19 h, then allowed to cool to room temperature, and the supernatant was removed to afford 3H-Indolium, 1-(5-Carboxypentyl)-2,3,3-trimethyl-5-sulfonate (1.10 g, 2.73 mmol, 73.80% yield) (3). ^{1}H-NMR (600 MHz, D_2O) δ ppm 1.378 (m, 2H), 1.586 (s, 6H), 1.601 (m, 4H), 1.904 (t, J=7.65, 2H), 2.301 (t, J=7.14, 2H), 4.433 (t, J=7.41, 2H), 7.818 (d, J=8.58, 1H), 7.945 (d, J=8.64, 1H), 7.952 (s, 1H).

Synthesis of 3H-Indolium, 2-[5-[1-(5-Carboxypentyl)-1,3-dihydro-3,3- dimethyl-5-sulfo-2H-indol-ylidene]-1,3-pentadien-1-yl]-1-methyl-3,3-dimethyl-5-sulfonate (4)

A suspension of 1-methyl-2,3,3-trimethyl-3H-indol-1-ium-5-sulfonate (2) (0.253 g, 1.00 mmol) and malonaldehyde bis(phenylimine) monohydrochloride (0.235 g, 1.10 mmol) in acetic acid (5 mL) and acetic anhydride (5 mL) was refluxed at 110 °C for 4 h. Solvent was removed under reduced pressure and the resultant solid was dissolved in pyridine (10 mL) under N_2. The mixture was then treated with compound (3) (0.353 g, 1.00 mmol) at 25 °C. Reaction mixture was stirred at 60 °C for 4 h, cooled down to 25 °C, and agitated a heterogeneous mixture by addition of ethyl acetate (10 mL). Resulting mixture was filtered through a paper filter, and the residue was dried under reduced pressure and purified with reverse flash chromatography to yield (4) as a dark blue

solid (0.150 g, 0.234 mmol, 23.4% yield). ^{1}H-NMR (600 MHz, D$_2$O) δ ppm 1.372 (m, 2H), 1.539 (m, 14H), 1.716 (p, J=4.90, 4H), 2.294 (t, J=7.50, 2H), 3.518 (s, 3H), 3.964 (m, 2H), 6.0474 (t, J=14.03, 2H), 6.376 (t, J=12.19, 1H), 7.259 (t, J=6.78, 2H), 7.741-7.779 (m, 3H), 7.871 (t, J=12.72, 2H).

5.4   Results and discussion

5.4.1   Attaching ORCA to the Surfaces of TMV
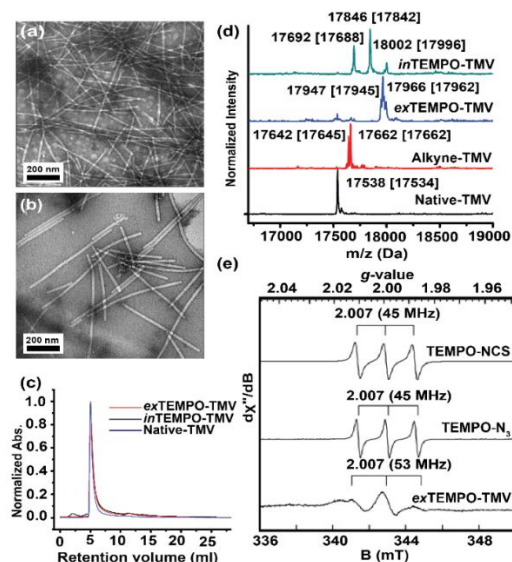
Figure 5.6. Characterization of TMV after bioconjugation reactions. The TEM images of (a) exTEMPO-TMV and (b) inTEMPO-TMV shows the expected rod-like morphology. (c) A single peak in the SEC chromatogram (at 260 nm) of modified TMV confirms the solution dispersity was unchanged. (d) Bioconjugation of the TEMPO radical to the TMV was characterized by ESI-MS. Native TMV has a peak at 17,538 m/z. The loss of this peak and emergence of a new peak at 17,662 m/z confirms that TMV was completely modified to alkyne-TMV. ESI-MS of exTEMPO-TMV shows that complete conjugation of TEMPO-N3 to the alkyne-TMV. The peak at 17,966 m/z represents the attachment of the TEMPO radical to the TMV coat protein. The interior surface of TMV consists of several glutamate residues, and three sites were modified via EDC coupling with TEMPO — one (17,692 m/z), two (17,846 m/z), or three (18,002 m/z) TEMPO molecules were installed. (e) X-band EPR spectra of exTEMPO-TMV. The exTEMPO-TMV sample was prepared in a capillary tube to minimize interaction between high dielectric aqueous solvent and the electric field of the incident microwave radiation.

As shown in Scheme 5.1a, TMV contains two distinct surfaces: (i) an outer surface with few charged functional groups and uninhibited access to bulk water and (ii) a 4-nm narrow inner channel with a net negative surface charge and less access to diffusing bulk water. We thus first set to determine if there would be any difference in measured relaxivities if ORCAs were placed on the inner vs the outer surface of TMV. The interior surface of TMV contains solvent exposed glutamic acid residues, which we functionalized *via* EDC coupling with TEMPO-NH$_2$ (Scheme 5.6c). High performance liquid chromatography/electron spray ionization mass spectroscopy (HPLC/ESI-MS) confirms that three sites were modified following the EDC coupling reaction to yield *in*TEMPO-TMV. As shown in Figure 5.6 d, peaks at 17,692 Da, 17,846 Da, and 18,002 Da represent the attachment of one, two, and three molecules of TEMPO respectively to the coat protein monomers of TMV. While only glutamate residues E97 and E106 have been identified as reactive sites,[49] the third peak at 18,002 Da likely corresponds to E95. Though three conjugations to this inner channel have been observed[55] before, the residue of the third modification site has never been identified. Separately, the exterior surface of TMV was functionalized initially using a diazonuim coupling reaction[49] (Alkyne-TMV) with *in situ* prepared 3-ethynyl phenyl diazonium salt. This quantitative reaction was followed by a copper-catalyzed azide-alkyne cycloaddition[64] (CuAAC) with TEMPO-N$_3$ to yield *ex*TEMPO-TMV (Figure 5.1d).

The TEMPO radical is known to be reduced in the presence of sodium ascorbate, so we modified a procedure initially described by Finn[69] by forming Cu^I(THPTA) separately by mixing a 1:5:1 molar ratio of Cu^{II} sulfate, the ligand THPTA, and sodium ascorbate in water. Starting with Cu^{II} sulfate as opposed to directly using a Cu^I source to form the Cu^I(THPTA) complex provided consistently high yields, likely because of the more favorable aqueous solubility of Cu^{II} sulfate.
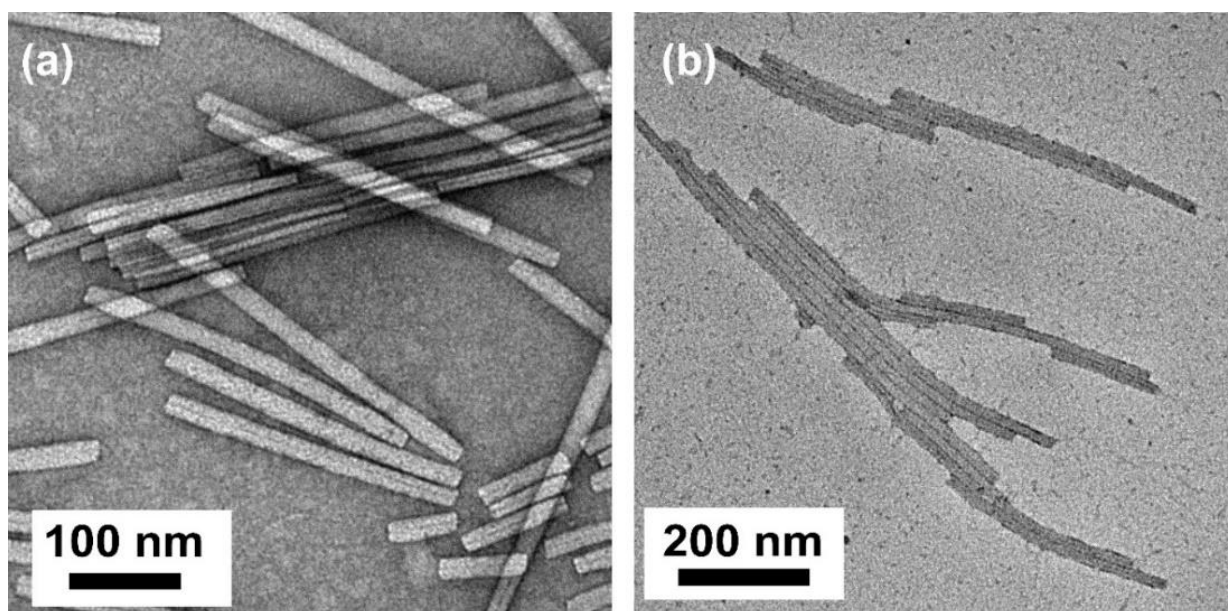
Figure 5.7. TEM image of (a) Native-TMV (b) Alkyne-TMV showing that the morphology has not changed after the diazonium coupling reaction to the native TMV.

This solution was transferred quickly in open air to an aqueous solution of TMV under N_2. Degassing of solutions were not necessary, and the successful attachment of the new functional groups was again confirmed by HPLC/ESI-MS. As shown in Figure 5.6 d, after the quantitative diazonium coupling reaction, all of the TMV coat protein monomers were modified to the azo adduct (17,666 Da) in line with previous literature reports.[71] The CuAAC reaction on the Alkyne-TMV with TEMPO-N_3 proceeded quantitatively, evidenced by the loss of the alkyne peak at 17,666 Da. The morphology and dispersity of TMV were checked after each bioconjugation reaction and were found unchanged by transmission electron microscopy (TEM) and size exclusion chromatography (SEC) respectively (Figure 5.6 a – c and Figure 5.7).

Finally, EPR spectroscopy was used to characterize the presence of paramagnetic species on the TMV surface. As shown in the Figure 5.6e, small molecule TEMPO radicals showed a characteristic ^{14}N-triplet (I = 1; A ~45 MHz) centered at a g-value of 2.007, which is typical of the nitrogen-centered radical. The sharp line width and isotropic g/A-values are consistent with

rotational averaging. By contrast, the *ex*TEMPO-TMV (Figure 5.6e) and *in*TEMPO-TMV (Figure 5.8) results in significantly broader and more anisotropic EPR spectra. The distributed g/A-values and attenuated signal intensity are attributed to decreased rotational and translational mobility of the radical. This significantly increases the observed line width of the mobilized radical. High density of radicals can also result in dipolar spin-spin exchange, which also contributes to the increased line width.
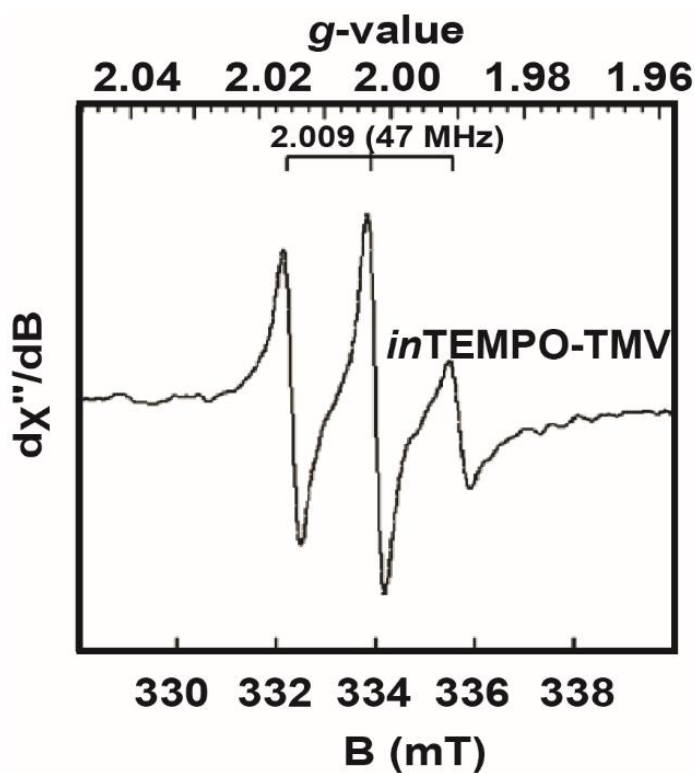
Figure 5.8. EPR spectrum of 2.52 mg/mL solution of *in*TEMPO-TMV in 0.1M pH 7.4 KP.

5.4.2 Proton Relaxation Properties of ORCA Loaded TMV Rods
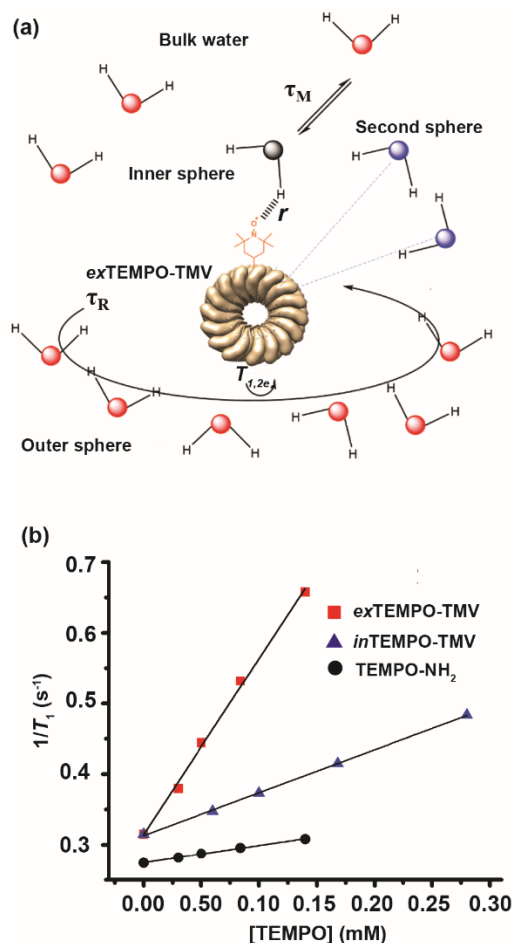
Figure 5.9. (a) Schematic representation of the *ex*TEMPO-TMV with one coordinated water molecule (*inner-sphere* water, its oxygen is colored black) in solution (*bulk water,* oxygens are red). *Second-sphere* water molecules (water oxygens are blue). The parameters that govern the relaxivity are also represented: NO–H distance (r), the mean lifetime (τ_m) of the water molecule (s) in the inner sphere, the rotational correlation time (τ_R) and the electronic spin relaxation times (T_{1e} and T_{2e}). (b) Plot of $1/T_1$ (s^{-1}) versus TEMPO concentration (mM) for *ex*TEMPO-TMV, *in*TEMPO-TMV and TEMPO-NH$_2$ at 23 MHz in 0.1 M pH 7.4 KP buffer and 310 K.

To characterize the relaxation behavior of the TEMPO-TMV particles, we performed proton

relaxometric measurements at different fields. It is worth noting that nitroxide radicals normally

bind non-covalently to at least one water molecule,[72] which is similar to that found with metal-

based complexes with one or more water molecules coordinated to the inner-sphere of the metal

centers.[34,73]The overall proton relaxation behavior is determined by the sum of the inner-sphere and outer-sphere contributions.[34] While the outer-sphere contributions cannot be neglected, the inner-sphere contributions are typically dominant.[74] For nitroxide radicals, under the extreme narrowing condition,[75,76] the primary inner-sphere relaxation mechanism is determined by dipolar and Curie dipolar contributions.[77,78] However, at higher magnetic fields, line broadening predominantly originates from Curie spin relaxation processes. The dipolar and Curie mechanisms from the inner- and outer-sphere contributions can be modeled as described in previous detailed reports.[78-80] Large macromolecules, like the TMV presented here, are characterized by slow rotation dynamics in solution[33,35] commonly represented by the rotational correlation time (τ_R). Other factors that have a high impact on the relaxation processes for T_1 and T_2 are the electronic relaxation rates ($1/T_{ei}$; $i = 1,2$) and solvent exchange lifetimes (τ_m) as defined by the correlation times (τ_{ci}; $i = 1,2$):

$$\tau_{ci} = \frac{1}{Tei} + \frac{1}{\tau_m} + \frac{1}{\tau_R}, i = 1,2 \tag{1}$$

We can make several simplifying assumptions. In systems where T_e is short, as is the case of TEMPO radicals ($T_{ei} \geq 20$ ns),[39] the molecular rotation and water exchange dominate τ_{ci}. The water exchange rate ($k_{ex} = 1/\tau_m$) for nitroxide radicals has been estimated to be quite slow ($k_{ex} \sim 2 \times 10^{-4}$ s)[39] and it is expected from theory[89] that the low-field total transverse relaxivity (T_2) will be small and similar to the longitudinal relaxivity, since it is modulated by T_e. At higher magnetic fields, the r_2 relaxivity is mostly affected by the square of the field (not r_1) and increases with field strength. As shown in Table 5.2, *ex*TEMPO-TMV, the most efficient system (Figure 5.9), shows a significant increase in r_2 at 9.4 T to 5.2 s^{-1} mM^{-1} per TEMPO compared to lower fields where r_1 and r_2 were similar.

Table 5.2. Determined r_1 and r_2 relaxivities for the agents *ex*TEMPO-TMV, *in*TEMPO-TMV, and TEMPO-NH$_2$ at 23 MHz, pH 7.4 KP buffer, and 310 K.

Agent	20 MHz (0.4 T)		60MHz (1.5 T)		500 MHz (9.4 T)	
	r_1 (s^{-1}mM^{-1})	r_2 (s^{-1}mM^{-1})	r_1 (s^{-1}mM^{-1})	r_2 (s^{-1}mM^{-1})	r_1 (s^{-1}mM^{-1})	r_2 (s^{-1}mM^{-1})
*ex*TEMPO-TMV	2.6 ± 0.1	2.7 ± 0.1	1.5 ± 0.1	4.7 ± 0.1	0.4 ± 0.1	5.2 ± 0.1
*in*TEMPO-TMV	0.6 ± 0.1	1.2 ± 0.1	0.4 ± 0.1	1.7 ± 0.1	0.2 ± 0.1	2.3 ± 0.1
TEMPO-NH$_2$	0.3 ± 0.1	0.2 ± 0.1	0.2 ± 0.1	0.2 ± 0.1	0.2 ± 0.1	0.3 ± 0.1
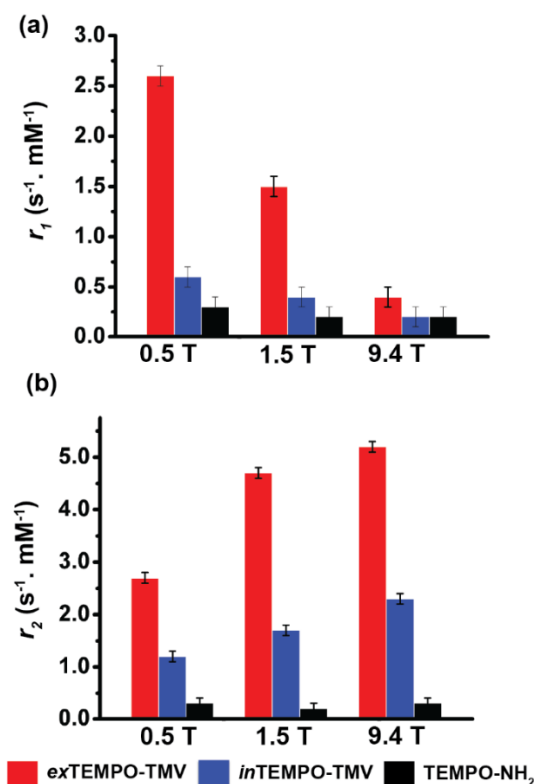
Figure 5.10. Determined (a) r_1 and (b) r_2 relaxivities for the agents exTEMPO-TMV, inTEMPO-TMV, and TEMPO-NH2 at different fields in 0.1 M pH 7.4 KP buffer and 310 K.

Our data show that the TEMPO-TMV conjugates are efficient T_1 and T_2 contrast agents at low field, and present remarkable properties as T_2 agents at high field,[35] with the greatest enhancement seen for *ex*TEMPO-TMV (Table 5.2). Indeed, *ex*TEMPO-TMV shows an enhancement of r_1 and

r_2 at low-field nearly one order of magnitude higher than the corresponding small molecule TEMPO-NH$_2$ and at high-field the r_2 shows a 13-fold increase compared to TEMPO-NH$_2$. A comparison of r_1 and r_2 values for *ex*TEMPO-TMV and *in*TEMPO-TMV (Figures 5.10) show that the exterior functionalization yields higher relaxivity values at all fields and both r_1 and r_2 relaxivities compare very favorably to existing polymeric ORCAs and small molecule contrast agents (Table 5.3). These data suggest that the TEMPO spins located on the inner cavity of the TMV macromolecule may have less access to bulk water preventing optimal exchange between the inner-sphere water molecules and those in the close vicinity of the TEMPO spin.[81]

Table 5.3. Comparison of T_1 and T_2 with ORCA and metal-based MRI imaging agents

Contrast agent	Contrast agent (CA) per particle	r_2 per CA (mM^{-1}s^{-1})	r_1 per CA (mM^{-1}s^{-1})	r_2 per particle (mM^{-1}s^{-1})	r_1 per particle (mM^{-1}s^{-1})	r_2/r_1	Field (T)	Ref.
*ex*TEMPO-TMV	~2130	5.2	0.4	~11076.0	~852	13	9.4	This work
*in*TEMPO-TMV	~3919	2.3	0.2	~9014.2	783.8	11.5	9.4	This work
TEMPO-NH$_2$	1	0.3	0.2	0.3	0.2	1.5	9.4	This work
3-CP	1	0.17	0.15	0.17	0.15	1.13	7	35
chex-MM	N/A	0.30	0.21	N/A	N/A	1.42	7	33
chex-dendrimer	N/A	0.86	0.44	N/A	N/A	1.95	7	39
chex-bottlebrush	N/A	0.82	0.32	N/A	N/A	2.56	7	33
BASP-ORCA1	N/A	4.67	0.41	N/A	N/A	11.39	7	35
Dy-DTPA-PcHexPh$_2$	1	3.0	0.11	3.0	0.11	27	7	80
Gd(DOTA)	1	5.0	3.0	5.0	3.0	1.67	1.5	58
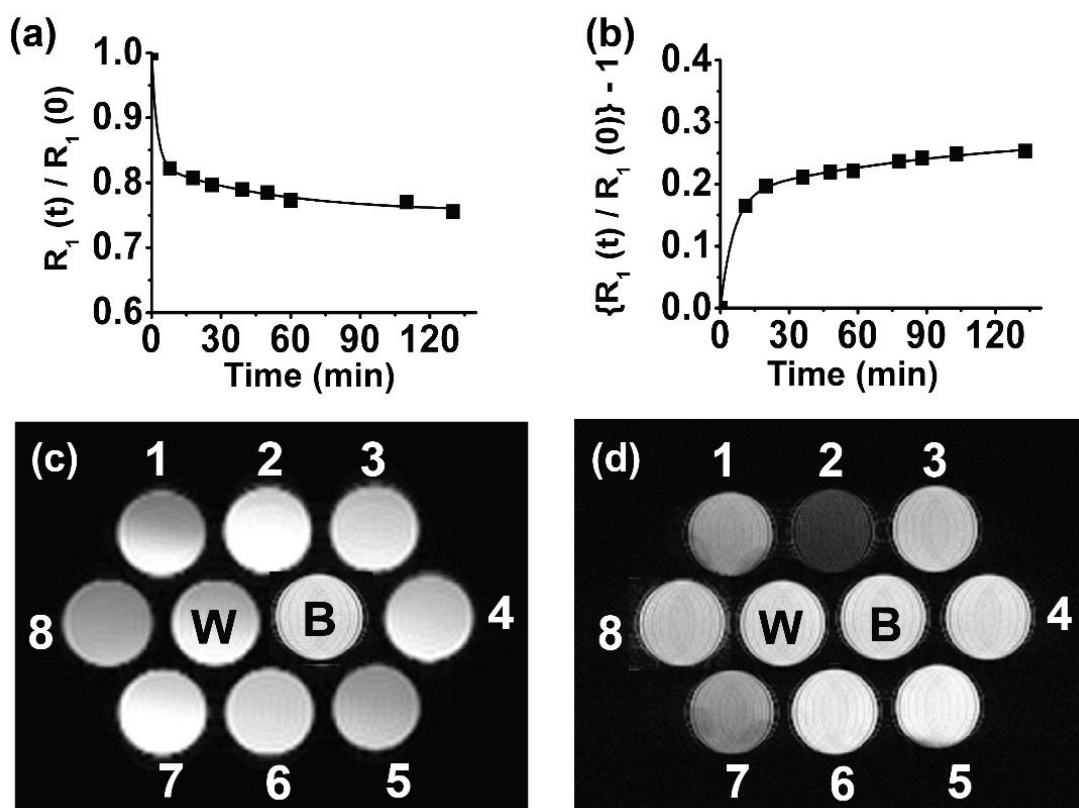
Figure 5.11. (a) Evolution of the relative water proton paramagnetic relaxation rate of a 0.14 mM aqueous solution of exTEMPO-TMV in the presence of 100-fold molar excess of ascorbate. Plot normalized to the initial value R1(t)/R1(0) as a function of the time (min) and measured at 23 MHz, 0.1 M pH 7.4 KP buffer, 310 K. (b) Evolution of the relative water proton paramagnetic relaxation rate of a 0.14 mM aqueous solution of exTEMPO-TMV (reduced) in the presence of 100-fold molar excess KO$_2$. Plot normalized to ($R_1^{(t)}/R_1^{(0)}$ -1) as a function of the time (min) and measured at 23 MHz, 0.1 M pH 7.4 KP buffer, 310 K. The solid lines through the data points represent the pseudo-first order reaction fits. (c) T_1 weighted and (d) T_2 weighted fast spin-echo images (TE = 200 ms) of 1) exTEMPO-TMV oxidized with KO$_2$, 2) exTEMPO-TMV (0.14 mM/TEMPO), 3) exTEMPO-TMV reduced with ascorbate, 4) Ascorbate in PBS, 5) TEMPO-NH$_2$ (1.4 mM), 6) TEMPO-NH$_2$ (0.14 mM), 7) inTEMPO-TMV (0.14 mM/TEMPO), 8) KO$_2$ in PBS, W) water at pH 7.0, B) PBS buffer at pH 7.0 taken at 9.4 T and 293 K.

Nitroxide-based ORCAs typically undergo rapid reduction to diamagnetic hydroxylamines in the

presence of reducing agents such as ascorbate.[82,83] Relaxometric studies of exTEMPO-TMV,

shown in Figure 5.11a, confirm that, in the presence of an equimolar amount of ascorbate, about

20% of the paramagnetic TEMPO spins on the exTEMPO-TMV are reduced within a few minutes.

This was also confirmed by EPR spectroscopy (Figure 5.12a). As proof of principle that TEMPO-

TMV compounds could be used as potent indicators of strong ROS, we performed the relaxometric experiments over the same time span, but in the presence of an excess of KO_2 at 0.4 T. In this case, the T_1 of water protons recovered to nearly the original values (Figure 5.11b). This same re-oxidation experiment was confirmed using EPR spectroscopy (Figure 5.12b). We investigated the rate of reduction of the *ex*TEMPO-TMV under pseudo-first-order conditions using a 10-fold excess of ascorbate in pH 7.4 phosphate-buffered saline (PBS). Fits were obtained for relaxometric data collected over a two-hour period. Pseudo-first order rate constants, *k'*, were obtained by following the decay of the $R_1^{(t)}/R_1^{(0)}$ determined by proton relaxometry. Excellent agreement with literature values was found for *ex*TEMPO-TMV and other macromolecules ($k' = 17 \times 10^{-4} \pm 2.3$ s^{-1}) as shown in the Table 5.4.[33,35,39] Conversely, the oxidation of the reduced *ex*TEMPO-TMV hydroxylamine with an excess of KO_2 also showed a quite extensive reaction with a calculated $t_{1/2}$ ~ 408 s.
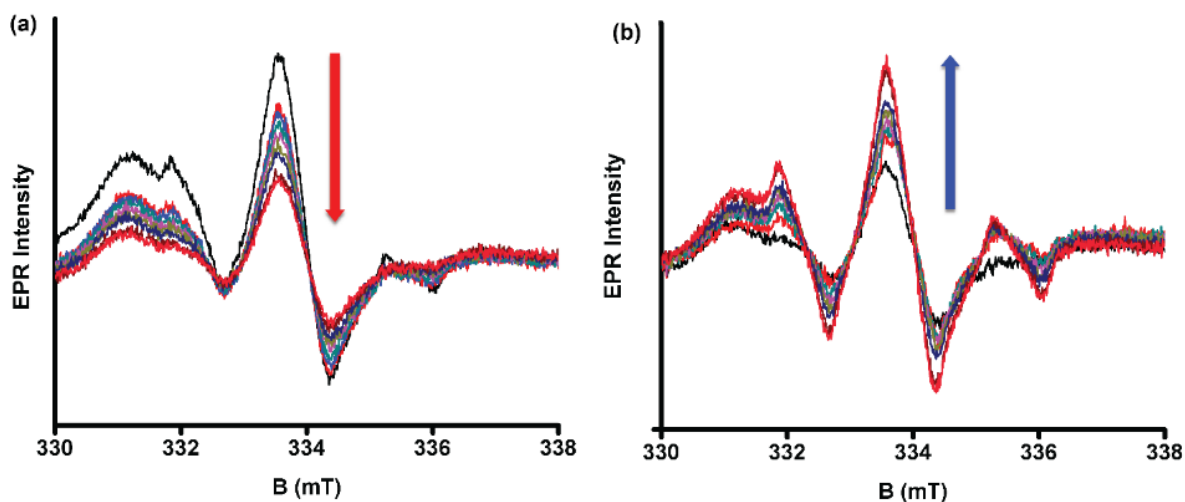
Figure 5.12. (a) EPR data for reduction of 2.52 mg/mL of exTEMPO-TMV with 10 eq of sodium ascorbate (1.40 mM). Data were collected for 2 h at 10 min time intervals. (b) EPR data for oxidation of reduced exTEMPO-TMV (2.52 mg/mL) with 100 eq (14.0 mM) of KO2. Data were collected for 2 h at 10 min time intervals.

Table 5.4. Kinetics of the reduction of nitroxides with excess of sodium ascorbate and oxidation of the hydroxylamine with excess of KO_2. Numerical fits to pseudo-first order rate equation (k') for the relaxometric data of the reaction.

Agent	Reduction with ascorbate			Oxidation with KO_2		
	k' ($\times 10^{-4}$ s^{-1})	k ($\times 10^{-2}$ M^{-1}s^{-1})	R^2	k' ($\times 10^{-4}$ s^{-1})	k ($\times 10^{-2}$ M^{-1}s^{-1})	R^2
*ex*TEMPO-TMV	17 ±0.1	12±0.1	0.97	16 ± 0.1	11 ± 0.1	0.96
TEMPO-conjugated branched-bottle brush polymer*,[86]	79.1	300	0.99	N/A	N/A	N/A
Chex-MIM*,[33]	3.79	12.6	0.99	N/A	N/A	N/A
P1*,[33]	2.70	2.71	0.97	N/A	N/A	N/A
Dendrimer*,[39]	5.78	5.8	0.98	N/A	N/A	N/A
TEMPOL*,[87]	63.33	633	0.99	N/A	N/A	N/A

*determined with the integrated peak height (IPH) EPR data and for the initial kinetic fits (<1 hour)

5.4.3 In vitro MR Imaging

In support of these experimental observations, we have performed phantom imaging on several samples containing *ex*TEMPO-TMV, *in*TEMPO-TMV, reduced *ex*TEMPO-TMV, oxidized *ex*TEMPO-TMV, and standards. T_2-weighted MR imaging at 9.4 T showed that among the 10 tubes, only those containing the non-reduced TMV-TEMPOs showed enhanced T_2 contrast, whereas the free TEMPO (Figure 5.11d, well 5 and 6) do not show any contrast difference even when we doubled the concentration of free TEMPO sample (Figure 5.11d, well 6). While contrast enhancement is evident in the T_1-weighted images (Figure 5.11c wells 8 vs. 2), the greatest contrast at this field strength comes from the T_2-weighted images (Figure 5.11d wells 8 vs. 2). These results suggest that these TEMPO macromolecular derivatives can detect changes in superoxides at millimolar concentrations. It also shows the potential of using *ex*TEMPO-TMV as a high-field (T_2)

contrast agent. This is particularly relevant, because most of clinical MR scanners operate at low-fields (0.4–3 T), though implementation of clinical high field scanners is progressing.

5.4.4 *in*FITC-*ex*TEMPO-TMV for Bimodal Molecular Imaging
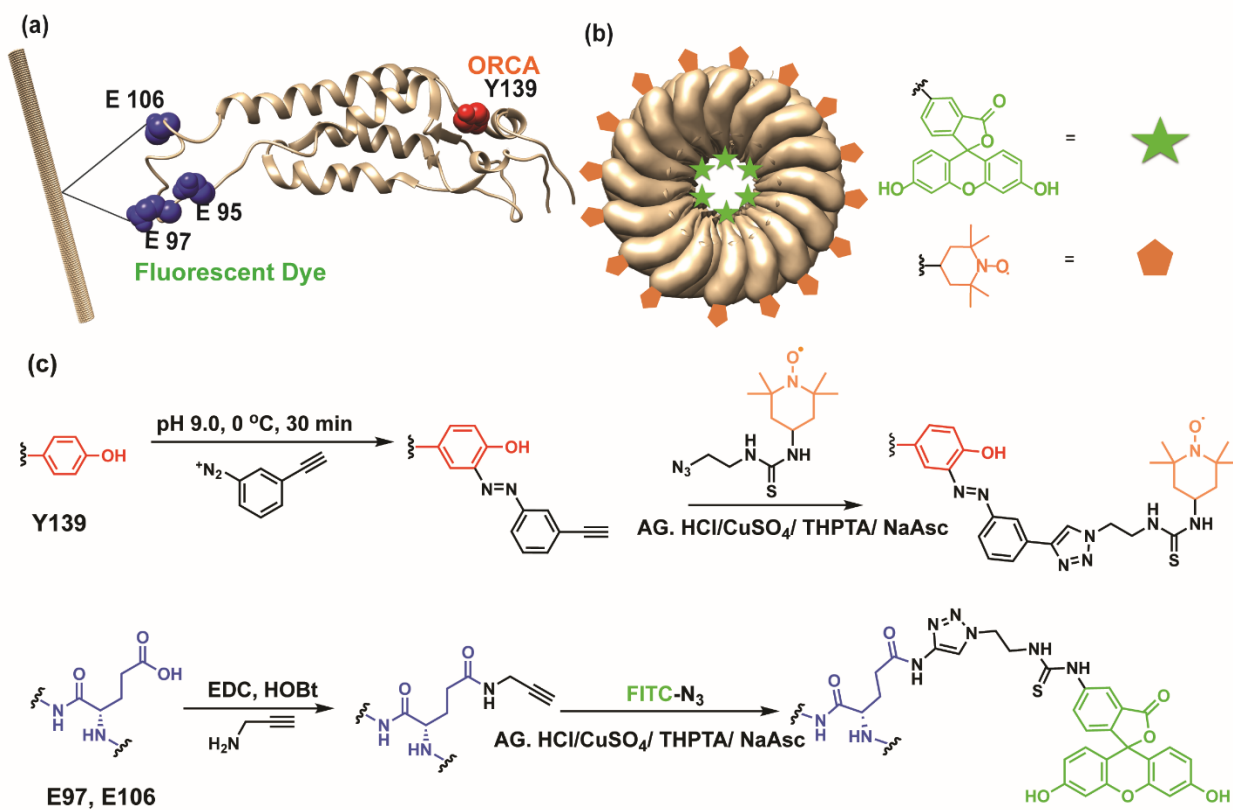
Figure 5.13. *in*FITC-*ex*TEMPO-TMV bimodal imaging probe. (a and b) Diagram of TMV showing the relative placement of the fluorescent dye on the interior residues and the ORCAs on the exterior. (c) The exterior surface was first modified with TEMPO radicals *via* diazonium coupling followed by a CuAAC reaction and, then the Interior surface of TMV was modified by EDC coupling with propargylamine followed by a CuAAC reaction.

After confirming that *ex*TEMPO-TMV exhibits better T_1 and T_2 relaxation characteristics compared to *in*TEMPO-TMV, this compound was used for all additional studies. A second goal of using TMV as a platform was to install a fluorophore for bimodal imaging in a position where it would not be quenched by the TEMPO radicals (Figure 5.13b). The order of the bioconjugation

reactions to the TMV virus surface is important to minimize the redox chemistry on the attached TEMPO.
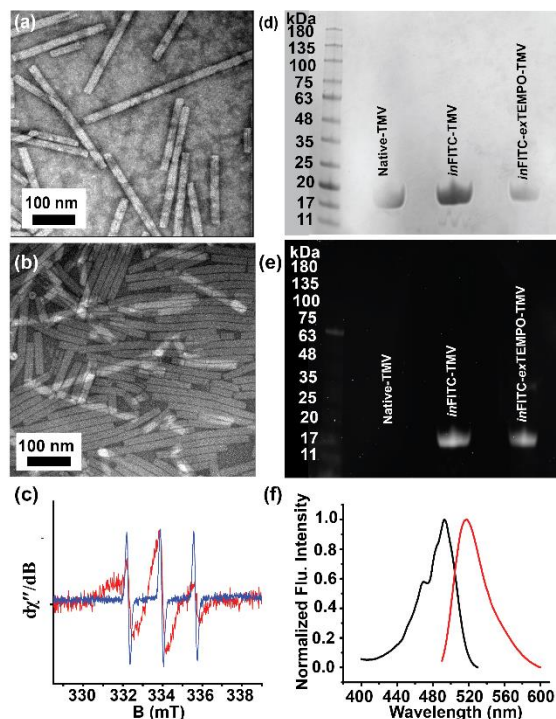
Figure 5.14. Synthesis and characterization of *in*FITC-*ex*TEMPO-TMV; TEM images (a) *in*FITC-TMV (b) *in*FITC-*ex*TEMPO-TMV (c) EPR spectrum of *in*FITC-*ex*TEMPO-TMV (red) and TEMPO-NH$_2$ (blue); SDS-PAGE to confirm that FITC has been successfully attached to TMV. SDS-PAGE was visualized by (d) Coomassie brilliant blue and (e) UV. (f) Excitation (black line) and emission (red) spectra of *in*FITC-*ex*TEMPO-TMV.

We first functionalized the interior surface with FITC using standard CuAAC conditions and then functionalized the exterior surface with TEMPO radicals using our modified procedure. After each bioconjugation reaction, the integrity of the particle was characterized by SEC and TEM (Figure 5.14a-b). Moreover, TEMPO radical attachment to the exterior surface was confirmed by EPR spectroscopy (Figure 5.14c). The attachment of FITC to the interior surface of TMV was confirmed by UV-Vis spectroscopy (Figure 5.15) and SDS-PAGE (Figure 5.14d-e) and fluorescence spectroscopy (Figure 5.14f). To show this quenching process is not dependent on

FITC, we attached a Cyanine dye (Cy 5) to the interior as well, and we again observed minimal quenching from the radical (Figure 5.16-5.18).
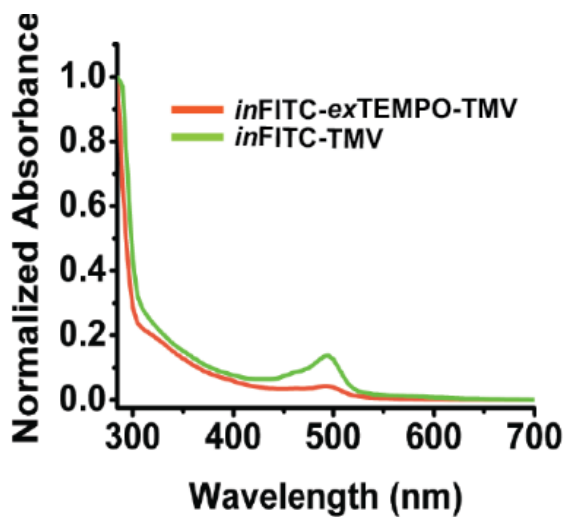
Figure 5.15. UV-Vis spectra of *ex*TEMPO-*in*FITC-TMV and inFITC-TMV.
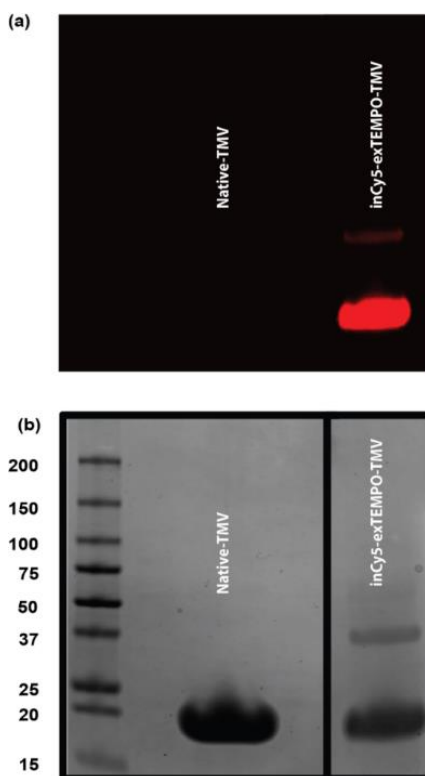
Figure 5.16. Synthesis and characterization of *in*Cy5-*ex*TEMPO-TMV; (a) SDS-PAGE to confirm that Cy 5 has been successfully attached to TMV. SDS-PGE was visualized by (a) UV and Coomassie brilliant blue.
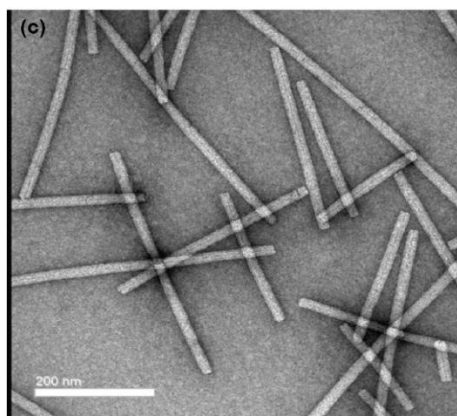
Figure 5.17. TEM image of *in*Cy5-*ex*TEMPO-TMV
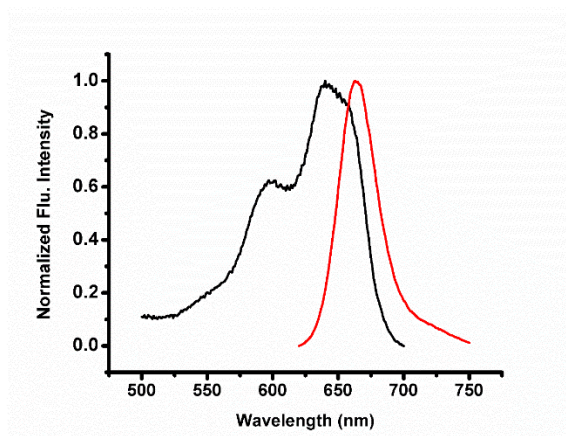
Figure 5.18. Excitation (black) and emission (red) spectra of *in*Cy5-*ex*TEMPO-TMV

Fluorescein and cyanine dyes, like most fluorophores, are known to be quenched by nitroxyl radicals,[33,42,88] and the tube-like architecture of TMV allowed us to attach the MRI imaging agent and the fluorescent dye far enough apart to prevent quenching of the fluorescence emission of the dye (Figure 5.19a). To our satisfaction, we found less than 3% variation in fluorescence when shifting between the oxidized radical to the reduced hydroxylamine (Figure 5.19b) even after an hour following addition of 100 eq of ascorbate. On the other hand, the EPR spectra (Figure 5.19c) confirms that the radicals are completely reduced by the ascorbate under these same conditions. We again conducted the same experiment with *in*Cy5-*ex*TEMPO-TMV and confirmed that the

137

oxidation state of the radical does not affect the emission intensity of Cy 5 (Figure 5.20), showing

the generalizability of this approach with different dyes.
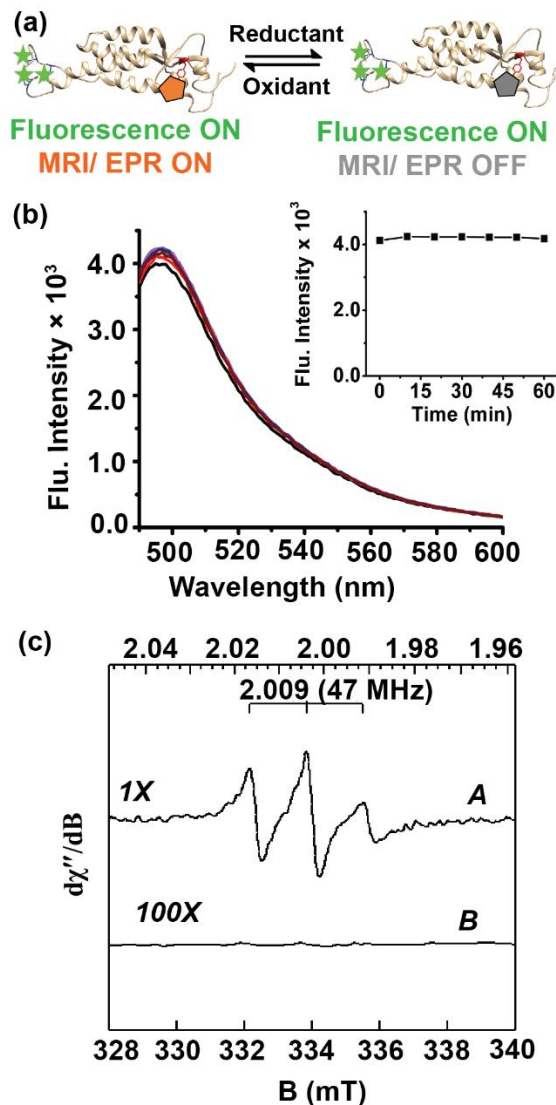
Figure 5.19. Bimodal imaging characteristics of the *in*FITC-*ex*TEMPO-TMV redox probe (a) Protein crystals structure of a single coat protein of TMV showing the attachment of FITC and TEMPO to the inner (glutamate) and outer (tyrosine) surfaces, respectively. (b) Time-dependent emission behavior of *in*FITC-*ex*TEMPO-TMV redox probe upon addition of 100 eq of ascorbate in 0.1 M pH 7.4 KP buffer. (c) EPR spectra of *in*FITC-*ex*TEMPO-TMV redox probe before (A) and 60 min after (B) addition of 100 eq of ascorbate in 0.1 M pH 7.4 KP buffer. An identical experiment on Cy 5 was conducted, and details are in Figure 5.14.

138
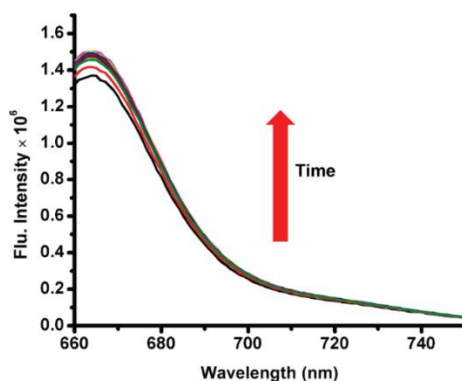
Figure 5.20. Change of fluorescence intensity of 1.0 mgmL^{-1} *in*Cy5-*ex*TEMPO-TMV as a function of time after addition of 100 eq of sodium ascorbate.

5.4.5 *In Vitro in*FITC-*red-ex*TEMPO-TMV Studies
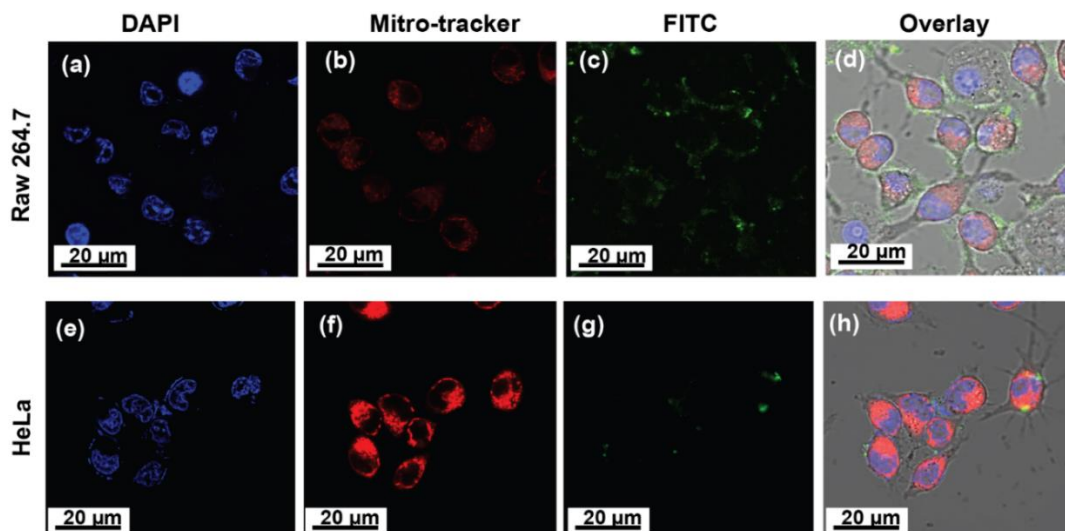
Figure 5.21. Confocal microscopy images of cellular uptake of *in*FITC-*red-ex*TEMPO-TMV redox probe with (a-d) RAW 264.7 cells and (e-f) HeLa cells. Color code: blue, Hoechst 33342; red, MitoTracker Deep Red; green, *in*FITC-*red-ex*TEMPO-TMV.

While the ultimate goal is *in vivo* imaging, in these early studies, we found it important to ascertain their behavior in cells and in serum. Cellular uptake could potentially result in trafficking to organelles normally high in superoxide concentrations, such as mitochondria, and could create an unwanted background signal. Further, uptake by macrophages, which are a known to efficiently remove macromolecules and nanoparticles, could potentially reduce the circulatory half-life of

these particles and may lead to the formation of antibodies against our probe making their

clearance faster.
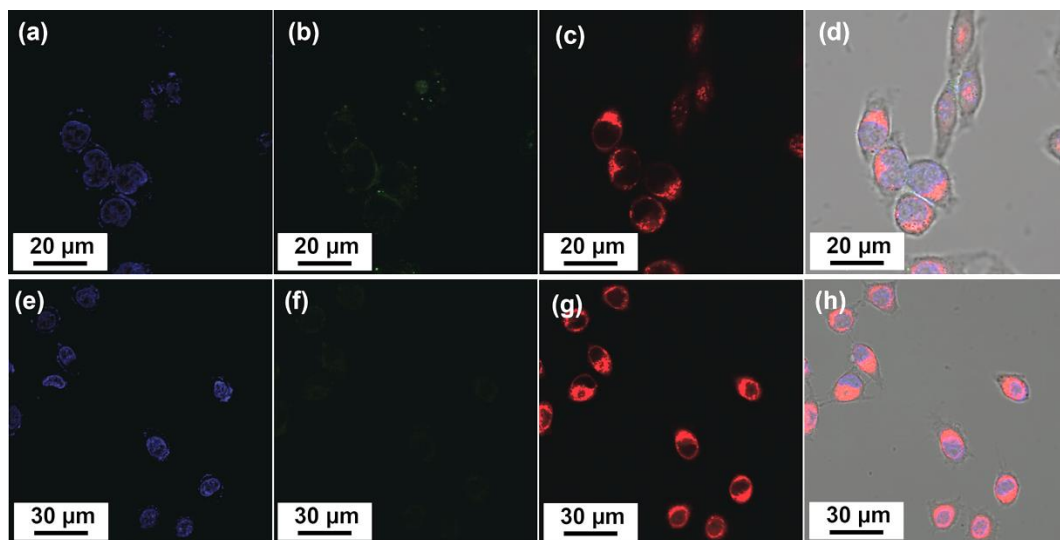
Figure 5.22. Confocal microscopy images of HeLa cells showing that *in*FITC-TMV accumulated on the cell membrane. Color code: blue, Hoechst 33342; green, *in*FITC-TMV; red, MitoTracker Deep Red.
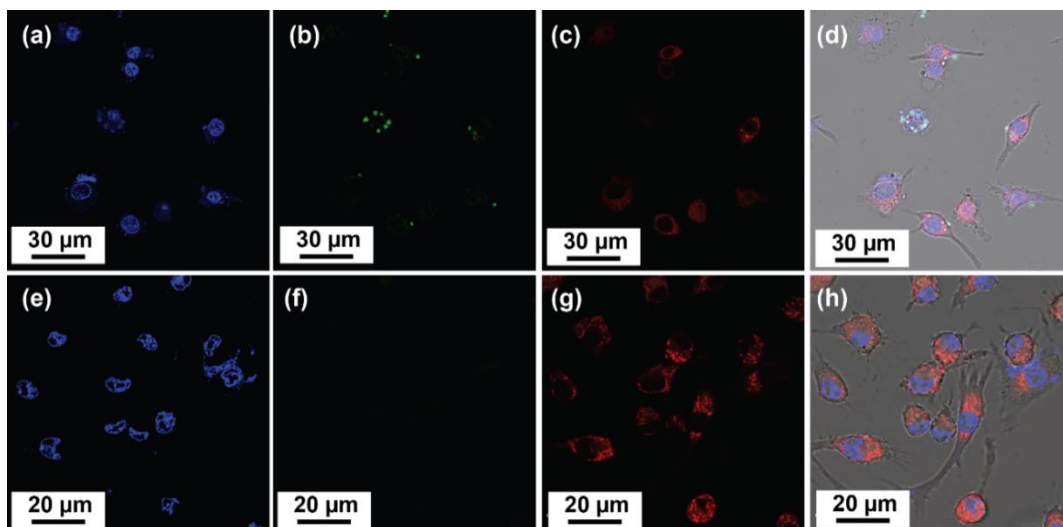
Figure 5.23. Confocal microscopy images of Raw 264.7 cells showing that *in*FITC-TMV accumulated on the cell membrane. Color code: blue, Hoechst 33342; green, *in*FITC-TMV; red, MitoTracker Deep Red.
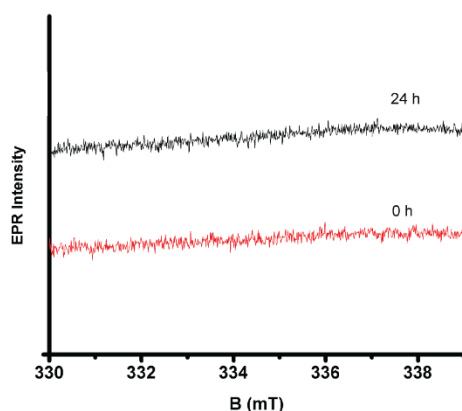
Figure 5.24. Changes of the EPR spectra when *red-ex*TEMPO-TMV is added to the simulated HeLa cells and spectra was recorded over 24 h.

Studies have shown that macrophages as well as HeLa cells interact less effectively with high aspect ratio nanoparticles and TMV in particular has been extensively studied.[52,89,90] We were curious if we would see uptake with reduced *in*FITC-*ex*TEMPO-TMV (*in*FITC-*red-ex*TEMPO-TMV) nanoparticles and if this would cause changes in the oxidation state of the ORCA following uptake. We used confocal microscopy on our "quenchless" system to investigate the interaction between *in*FITC-*red-ex*TEMPO-TMV and macrophages. The confocal microscopy data shows that *in*FITC-*red-ex*TEMPO-TMV (Figure 5.21d) associates with macrophages by adhering to the surface with no obvious fluorescence inside the cells and, in particular, the mitochondria, which are stained red in Figure 5.21b. We also investigated the cellular uptake of *in*FITC-*red-ex*TEMPO-TMV by HeLa cells (Figure 5.21e-5.21g) and found no significant fluorescence signal coming from cells (Figure 5.21g). The lack of interaction with mitochondria was corroborated by EPR spectroscopy. To ensure we would observe signal if any trafficking to mitochondria occurs at all, we stimulated the HeLa and macrophages with the superoxide promotor phorbol 12-myristate 13-acetate (PMA)[91-93] and then incubated these cells with *red-ex*TEMPO-TMV for an hour. Cells were collected and EPR spectra were recorded as a function of time. A lack of an EPR signal over

141

time confirms that *red-ex*TEMPO-TMV has not been uptaken by cells (Figure 5.24). If the *red-ex*TEMPO-TMV had been taken up by the cells and trafficked to an area of ROS activity, we would expect to observe an increase in the EPR signal intensity with time, particularly when the cells were stimulated by PMA.[91] These results are promising as it suggests that background signal from cellular metabolism is minimal.

5.4.6   *red-ex*TEMPO-TMV Performance in Serum

Serum is very rich in a variety of proteins that may interfere with superoxide detection either by (i) directly reducing TEMPO to its EPR silent form or (ii) by covering the probe with a layer of protein—commonly called a protein corona—which would inhibit the 'turn on' response. To ascertain if our sensor functions in a biological environment, which might mimic detection of superoxide from tissue damage, for instance, we tested *red-ex*TEMPO-TMV in serum solution using enzymatically produced superoxide. Xanthine/xanthine oxidase (X/XO) was employed as a superoxide generating agent as it has been shown [93,94] to be a good model of cell-free superoxide generation via EPR/MRI.[1]
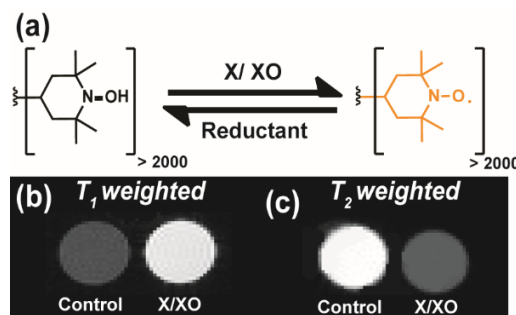
Figure 5.25. (a) schematic showing the redox behavior of *red-ex*TEMPO-TMV (b) T_1-weighted phantom images and (c) T_2-weighted phantom images before and after addition of X/XO. The concentration of TMV sample was 5.0 mgmL^{-1} and the reaction mixture consist of 50% of serum by volume.

First, the *red-ex*TEMPO-TMV was made by reduction of *ex*TEMPO-TMV with 0.1 M sodium ascorbate in a suspension of PBS, which was then purged with nitrogen gas to prevent re-oxidation. Xanthine (final concentration 0.05 mM) and *red-ex*TEMPO-TMV (final concentration of 5.0 mgmL^{-1}) were mixed in fetal bovine serum (FBS). Finally, xanthine oxidase (final concentration 0.1 U/mL) was added to the mixture. EPR spectra were recorded over 24 hours and MR phantom images were obtained from the same samples. Re-oxidation of the probe was evident immediately. The T_1-weighted images and T_2-weighted images for the *red-ex*TEMPO-TMV sample with and without X/XO shows a huge contrast difference (Figure 5.19b-c) clearly indicating that the serum did not prevent detection of superoxide. These changes were confirmed by EPR, which also showed the regeneration of the TEMPO radical by the superoxide formed from X/XO (Figure 5.25) in the serum solution.
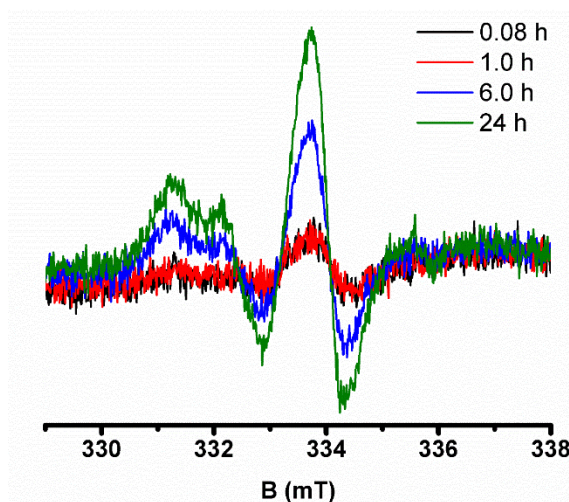
Figure 5.20. EPR spectra for 5.0 mgmL^{-1} of reduced *ex*TEMPO-TMV in the presence of 0.5 mM xanthine and 0.1 U/mL xanthine oxidase. The spectra were recorded over 24 h.

5.5 Conclusions

This was a fundamental study of the synthesis, magnetic, and optical characterizations, and *in vitro* analyses of a new type of a fluorescent/MRI active superoxide sensor that works at both high and

low magnetic fields. Our ORCA conjugated VNP-based nanoparticle probe appears promising for use at both clinical (<3 T) and pre-clinical (>3 T) MRI fields. Attachment of ORCA to TMV rods resulted in a 10-fold increase in r_1 and a 13-fold increase in r_2 compared to the small molecule ORCAs. We have proposed that these increases in relaxivity are ascribed to a decrease in molecular rotation and diffusional motions brought about by attachment of the ORCA to the large rod-shaped particle. The distinct 'inner' and 'outer' topology of the TMV permits the creation of a "quenchless" ORCA-based bimodal probe for combined MRI and fluorescence imaging. The probe shows 'turn-on' functionality toward enzymatically produced superoxide in the presence of serum yet does not show appreciable changes in EPR intensity even when endocytosed by cells, suggesting this probe would be ideal for imaging diffuse tissue injury as may be the case in deep tissue diabetic ulceration or coronary heart disease.

5.6   References

1. Bakalova, R.; Georgieva, E.; Ivanova, D.; Zhelev, Z.; Aoki, I.; Saga, T. Magnetic Resonance Imaging of Mitochondrial Dysfunction and Metabolic Activity, Accompanied by Overproduction of Superoxide. *ACS Chem. Neurosci.* **2015,** *6*, 1922-1929.

2. Sabharwal, S. S.; Schumacker, P. T. Mitochondrial ROS in cancer: initiators, amplifiers or an Achilles' heel? *Nat. Rev. Cancer* **2014,** *14*, 709-721.

3. Desideri, E.; Vegliante, R.; Ciriolo, M. R. Mitochondrial dysfunctions in cancer: Genetic defects and oncogenic signaling impinging on TCA cycle activity. *Cancer Lett.* **2015,** *356*, 217-223.

4. Pinto, M.; Moraes, C. T. Mitochondrial genome changes and neurodegenerative diseases. *Biochim. Biophys. Acta* **2014,** *1842*, 1198-1207.

5. Yadav, A.; Agarwal, S.; Tiwari, S.; Chaturvedi, R. Mitochondria: Prospective Targets for Neuroprotection in Parkinson's Disease. **2014,** *20*, 5558-5573.

6. Giacco, F.; Brownlee, M. Oxidative stress and diabetic complications. *Circ. Res.* **2010,** *107*, 1058-1070.

7. Lowell, B. B.; Shulman, G. I. Mitochondrial dysfunction and type 2 diabetes. *Science* **2005,** *307*, 384-387.

8. Campuzano, V.; Montermini, L.; Molto, M. D.; Pianese, L.; Cossee, M.; Cavalcanti, F.; Monros, E.; Rodius, F.; Duclos, F.; Monticelli, A.; Zara, F.; Canizares, J.; Koutnikova, H.; Bidichandani, S. I.; Gellera, C.; Brice, A.; Trouillas, P.; De Michele, G.; Filla, A.; De Frutos, R.; Palau, F.; Patel, P. I.; Di Donato, S.; Mandel, J. L.; Cocozza, S.; Koenig, M.; Pandolfo, M. Friedreich's Ataxia: Autosomal Recessive Disease Caused by an Intronic GAA Triplet Repeat Expansion. *Science* **1996,** *271*, 1423-1427.

9. Mascialino, B.; Leinonen, M.; Meier, T. Meta-analysis of the prevalence of Leber hereditary optic neuropathy mtDNA mutations in Europe. *Eur. J. Ophthalmol*. **2012,** *22*, 461-465.

10. Montagna, P.; Gallassi, R.; Medori, R.; Govoni, E.; Zeviani, M.; Di Mauro, S.; Lugaresi, E.; Andermann, F. MELAS syndrome: characteristic migrainous and epileptic features and maternal transmission. *Neurology* **1988,** *38*, 751-754.

11. Wallace, D. C.; Zheng, X.; Lott, M. T.; Shoffner, J. M.; Hodge, J. A.; Kelley, R. I.; Epstein, C. M.; Hopkins, L. C. Familial mitochondrial encephalomyopathy (MERRF): Genetic, pathophysiological, and biochemical characterization of a mitochondrial DNA disease. *Cell* **1988,** *55*, 601-610.

12. Hayashi, G.; Cortopassi, G. Oxidative stress in inherited mitochondrial diseases. *Free Radic. Biol. Med.* **2015,** *88*, 10-17.

13. Rahman, S.; Blok, R. B.; Dahl, H. H.; Danks, D. M.; Kirby, D. M.; Chow, C. W.; Christodoulou, J.; Thorburn, D. R. Leigh syndrome: clinical features and biochemical and DNA abnormalities. *Ann. Neurol.* **1996,** *39*, 343-351.

14. Abbas, K.; Hardy, M.; Poulhes, F.; Karoui, H.; Tordo, P.; Ouari, O.; Peyrot, F. Detection of superoxide production in stimulated and unstimulated living cells using new cyclic nitrone spin traps. *Free Radic. Biol. Med.* **2014,** *71*, 281-290.

15. Mrakic-Sposta, S.; Gussoni, M.; Montorsi, M.; Porcelli, S.; Vezzoli, A. Assessment of a standardized ROS production profile in humans by electron paramagnetic resonance. *Oxid. Med. Cell Longev.* **2012,** *2012*, 973927.

16. Krotz, F.; Sohn, H. Y.; Pohl, U. Reactive oxygen species: players in the platelet game. *Arterioscler. Thromb. Vasc. Biol.* **2004,** *24*, 1988-1996.

17. Apel, K.; Hirt, H. eactive oxygen species: metabolism, oxidative stress, and signal transduction. *Annu. Rev. Plant Biol.* **2004,** *55*, 373-399.

18. Kanofsky, J. R. Singlet oxygen production by biological systems. *Chem.-Biol. Interact.* **1989,** *70*, 1-28.

19. Kayama, Y.; Raaz, U.; Jagger, A.; Adam, M.; Schellinger, I. N.; Sakamoto, M.; Suzuki, H.; Toyama, K.; Spin, J. M.; Tsao, P. S. Diabetic Cardiovascular Disease Induced by Oxidative Stress. *Int. J. Mol. Sci.* **2015,** *16*, 25234-25263.

20. Cai, L.; Wang, J.; Li, Y.; Sun, X.; Wang, L.; Zhou, Z.; Kang, Y. J. Inhibition of Superoxide Generation and Associated Nitrosative Damage Is Involved in Metallothionein Prevention of Diabetic Cardiomyopathy. *Diabetes* **2005,** *54*, 1829-1837.

21. Woods, M.; Woessner, D. E.; Sherry, A. D. Paramagnetic lanthanide complexes as PARACEST agents for medical imaging. *Chem. Soc. Rev.* **2006,** *35*, 500-511.

22. Viswanathan, S.; Kovacs, Z.; Green, K. N.; Ratnakar, S. J.; Sherry, A. D. Alternatives to gadolinium-based metal chelates for magnetic resonance imaging. *Chem. Rev.* **2010,** *110*, 2960-3018.

23. Sherry, A. D.; Woods, M. Chemical exchange saturation transfer contrast agents for magnetic resonance imaging. *Annu. Rev. Biomed. Eng.* **2008,** *10*, 391-411.

24. Spasojević, I. Electron Paramagnetic Resonance - A Powerful Tool of Medical Biochemistry in Discovering Mechanisms of Disease and Treatment Prospects. *J. Med. Biochem.* **2010,** *29*, 175-188.

25. Ratnakar, S. J.; Soesbe, T. C.; Lumata, L. L.; Do, Q. N.; Viswanathan, S.; Lin, C. Y.; Sherry, A. D.; Kovacs, Z. Modulation of CEST images in vivo by T_1 relaxation: a new approach in the design of responsive PARACEST agents. *J. Am. Chem. Soc.* **2013,** *135*, 14904-14907.

26. Zhang, L.; Martins, A. F.; Zhao, P.; Wu, Y.; Tircso, G.; Sherry, D. Lanthanide-based T_{2ex} and CEST complexes provide new insights into the design of pH sensitive MRI agents. *Angew. Chem.* **2017***, 56,* 16626 –16630.

27. Zhang, L.; Martins, A. F.; Mai, Y. Y.; Zhao, P. Y.; Funk, A. M.; Jordan, M. V. C.; Zhang, S. R.; Chen, W.; Wu, Y. K.; Sherry, A. D. Imaging Extracellular Lactate In Vitro and In Vivo Using CEST MRI and a Paramagnetic Shift Reagent. *Chem. Eur. J.* **2017,** *23*, 1752-1756.

28. Song, B.; Wu, Y.; Yu, M.; Zhao, P.; Zhou, C.; Kiefer, G. E.; Sherry, A. D. A europium(III)-based PARACEST agent for sensing singlet oxygen by MRI. *Dalton Trans.* **2013,** *42*, 8066-8069.

29. Do, Q. N.; Ratnakar, J. S.; Kovacs, Z.; Sherry, A. D. Redox- and hypoxia-responsive MRI contrast agents. *ChemMedChem* **2014,** *9*, 1116-1129.

30. Hyodo, F.; Matsumoto, K.; Matsumoto, A.; Mitchell, J. B.; Krishna, M. C. Probing the intracellular redox status of tumors with magnetic resonance imaging and redox-sensitive contrast agents. *Cancer Res.* **2006,** *66*, 9921-9928.

31. Prescott, C.; Bottle, S. E. Biological Relevance of Free Radicals and Nitroxides. *Cell Biochem. Biophys.* **2017,** *75*, 227-240.

32. Liu, S. J.; Zhou, N.; Chen, Z. J.; Wei, H. J.; Zhu, Y. N.; Guo, S.; Zhao, Q. Using a redox-sensitive phosphorescent probe for optical evaluation of an intracellular redox environment. *Opt. Lett.* **2017,** *42*, 13-16.

33. Sowers, M. A.; McCombs, J. R.; Wang, Y.; Paletta, J. T.; Morton, S. W.; Dreaden, E. C.; Boska, M. D.; Ottaviani, M. F.; Hammond, P. T.; Rajca, A.; Johnson, J. A. Redox-responsive branched-bottlebrush polymers for in vivo MRI and fluorescence imaging. *Nat. Commun.* **2014,** *5*, 5460.

34. Merbach, A.; Helm, L.; Toth, E. *The Chemistry of Contrast Agents in Medical Magnetic Resonance Imaging*. 2nd ed.; John Wiley & Sons: United Kingdom, 2013.

35. Nguyen, H. V.; Chen, Q.; Paletta, J. T.; Harvey, P.; Jiang, Y.; Zhang, H.; Boska, M. D.; Ottaviani, M. F.; Jasanoff, A.; Rajca, A.; Johnson, J. A. Nitroxide-Based Macromolecular Contrast Agents with Unprecedented Transverse Relaxivity and Stability for Magnetic Resonance Imaging of Tumors. *ACS Cent. Sci.* **2017**, *3*, 800-811.

36. Garmendia, S.; Mantione, D.; Alonso-de Castro, S.; Jehanno, C.; Lezama, L.; Hedrick, J. L.; Mecerreyes, D.; Salassa, L.; Sardon, H. Polyurethane based organic macromolecular contrast agents (PU-ORCAs) for magnetic resonance imaging. *Polym. Chem.* **2017**, *8*, 2693-2701.

37. Chan, J. M. W.; Wojtecki, R. J.; Sardon, H.; Lee, A. L. Z.; Smith, C. E.; Shkumatov, A.; Gao, S. J.; Kong, H.; Yang, Y. Y.; Hedrick, J. L. Self-Assembled, Biodegradable Magnetic Resonance Imaging Agents: Organic Radical-Functionalized Diblock Copolymers. *ACS Macro Lett.* **2017,** *6*, 176-180.

38. Haugland, M. M.; Anderson, E. A.; Lovett, J. E. Tuning the properties of nitroxide spin labels for use in electron paramagnetic resonance spectroscopy through chemical modification of the nitroxide framework. **2016**, *25*, 1-34.

39. Rajca, A.; Wang, Y.; Boska, M.; Paletta, J. T.; Olankitwanit, A.; Swanson, M. A.; Mitchell, D. G.; Eaton, S. S.; Eaton, G. R.; Rajca, S. Organic radical contrast agents for magnetic resonance imaging. *J. Am. Chem. Soc.* **2012**, *134*, 15724-15727.

40. Yamada, K.; Mito, F.; Matsuoka, Y.; Ide, S.; Shikimachi, K.; Fujiki, A.; Kusakabe, D.; Ishida, Y.; Enoki, M.; Tada, A.; Ariyoshi, M.; Yamasaki, T.; Yamato, M. Fluorescence probes to detect lipid-derived radicals. *Nat. Chem. Biol.* **2016**, *12*, 608-613.

41. Anderson, E. A.; Isaacman, S.; Peabody, D. S.; Wang, E. Y.; Canary, J. W.; Kirshenbaum, K. Viral nanoparticles donning a paramagnetic coat: conjugation of MRI contrast agents to the MS2 capsid. *Nano lett.* **2006**, *6*, 1160-1164.

42. Chen, Z.; Li, N.; Li, S.; Dharmarwardana, M.; Schlimme, A.; Gassensmith, J. J. Viral chemistry: the chemical functionalization of viral architectures to create new technology. *WIREs Nanomed. Nanobiotechnol.* **2016,** *8*, 512-534.

43. Scholthof, K. B.; Adkins, S.; Czosnek, H.; Palukaitis, P.; Jacquot, E.; Hohn, T.; Hohn, B.; Saunders, K.; Candresse, T.; Ahlquist, P.; Hemenway, C.; Foster, G. D. Top 10 plant viruses in molecular plant pathology. *Mol. Plant Pathol.* **2011,** *12*, 938-954.

44. Harrison, B. D.; Wilson, T. M. Milestones in the research on tobacco mosaic virus. *Philos. Trans. Royal Soc. B* **1999,** *354*, 521-529.

45. Klug, A. The tobacco mosaic virus particle: structure and assembly. *Philos. Trans. Royal Soc. B* **1999,** *354*, 531-535.

46. Sitasuwan, P.; Lee, L. A.; Li, K.; Nguyen, H. G.; Wang, Q. *Front. Chem.* **2014,** *2*, 31.

47. Miller, R. A.; Stephanopoulos, N.; McFarland, J. M.; Rosko, A. S.; Geissler, P. L.; Francis, M. B., RGD-conjugated rod-like viral nanoparticles on 2D scaffold improve bone differentiation of mesenchymal stem cells. *J. Am. Chem. Soc.* **2010**, *132*, 6068-6074.

48. Datta, A.; Hooker, J. M.; Botta, M.; Francis, M. B.; Aime, S.; Raymond, K. N. Dual-surface modification of the tobacco mosaic virus. High relaxivity gadolinium hydroxypyridonate-viral capsid conjugates: nanosized MRI contrast agents. *J. Am. Chem. Soc.* **2008,** *130*, 2546-2552.

49. Schlick, T. L.; Ding, Z.; Kovacs, E. W.; Francis, M. B. *J. Dual-surface modification of the tobacco mosaic virus. Am. Chem. Soc.* **2005,** *127*, 3718-23.

50. Li, S.; Dharmarwardana, M.; Welch, R. P.; Ren, Y.; Thompson, C. M.; Smaldone, R. A.; Gassensmith, J. J. Template-Directed Synthesis of Porous and Protective Core–Shell Bionanoparticles. *Angew.Chem.* **2016**, *55*, 10691 –10696.

51. Li, S.; Dharmarwardana, M.; Welch, R. P.; Benjamin, C. E.; Shamir, A. M.; Nielsen, S. O.; Gassensmith, Investigation of Controlled Growth of Metal−Organic Frameworks on Anisotropic Virus Particles. *ACS Appl. Mater. Interfaces*, **2018.**

52. Bruckman, M. A.; Randolph, L. N.; Gulati, N. M.; Stewart, P. L.; Steinmetz, N. F. Silica-coated Gd(DOTA)-loaded protein nanoparticles enable magnetic resonance imaging of macrophages. *J. Mater. Chem. B* **2015,** 7503-7510.

53. Bye, N.; Hutt, O. E.; Hinton, T. M.; Acharya, D. P.; Waddington, L. J.; Moffat, B. A.; Wright, D. K.; Wang, H. X.; Mulet, X.; Muir, B. W. Nitroxide-loaded hexosomes provide MRI contrast in vivo. *Langmuir* **2014,** *30*, 8898-8906.

54. Hu, H.; Zhang, Y.; Shukla, S.; Gu, Y.; Yu, X.; Steinmetz, N. F. Dysprosium-Modified Tobacco Mosaic Virus Nanoparticles for Ultra-High-Field Magnetic Resonance and Near-Infrared Fluorescence Imaging of Prostate Cancer. *ACS nano* **2017,** *11*, 9249-9258.

55. Bruckman, M. A.; Hern, S.; Jiang, K.; Flask, C. A.; Yu, X.; Steinmetz, N. F. Tobacco mosaic virus rods and spheres as supramolecular high-relaxivity MRI contrast agents. *J. mater. chem. B* **2013,** *1*, 1482-1490.

56. Bruckman, M. A.; Jiang, K.; Simpson, E. J.; Randolph, L. N.; Luyt, L. G.; Yu, X.; Dual-modal magnetic resonance and fluorescence imaging of atherosclerotic plaques in vivo using VCAM-1 targeted tobacco mosaic virus. *Nano lett.* **2014,** *14*, 1551-1558.

57. Prasuhn, D. E., Jr.; Yeh, R. M.; Obenaus, A.; Manchester, M.; Finn, M. G. V Viral MRI contrast agents: coordination of Gd by native virions and attachment of Gd complexes by azide-alkyne cycloaddition. *Chem. commun.* **2007**, 1269-1271.

58. Liepold, L.; Anderson, S.; Willits, D.; Oltrogge, L.; Frank, J. A.; Douglas, T.; Young, M. Viral capsids as MRI contrast agents. *Magn. reson. med.* **2007**, *58*, 871-879.

59. Garimella, P. D.; Datta, A.; Romanini, D. W.; Raymond, K. N.; Francis, M. B. Multivalent, high-relaxivity MRI contrast agents using rigid cysteine-reactive gadolinium complexes. *J. Am. Chem. Soc.* **2011,** *133*, 14704-14709.

60. Hooker, J. M.; Datta, A.; Botta, M.; Raymond, K. N.; Francis, M. B. Magnetic resonance contrast agents from viral capsid shells: a comparison of exterior and interior cargo strategies. *Nano lett.* **2007,** *7*, 2207-2210.

61. Raymond, K. N.; Pierre, V. C. Next generation, high relaxivity gadolinium MRI agents. *Bioconjugate chem.* **2005,** *16*, 3-8.

62. Allen, M.; Bulte, J. W.; Liepold, L.; Basu, G.; Zywicke, H. A.; Frank, J. A.; Young, M.; Douglas, T. Paramagnetic viral nanoparticles as potential high-relaxivity magnetic resonance contrast agents. *Mag. Res. Med.* **2005,** *54*, 807-812.

63. Qazi, S.; Liepold, L. O.; Abedin, M. J.; Johnson, B.; Prevelige, P.; Frank, J. A.; Douglas, T. P22 viral capsids as nanocomposite high-relaxivity MRI contrast agents. *Mol. Pharmaceutics* **2013,** *10*, 11-17.

64. Bruckman, M. A.; Steinmetz, N. F. Chemical modification of the inner and outer surfaces of Tobacco Mosaic Virus (TMV) *Methods mol. biol.* **2014,** *1108*, 173-185.

65. Weil, J. A.; Bolton, J. R.; Wertz, J. E., Electron Paramagnetic Resonance. Elementary Theory and Practical Applications. 1st ed.; Wiley: 1994.

66. Eaton, G. R.; Eaton, S. S.; Salikhov, K. M., *Foundations of Modern EPR*. World Scientific: 1998.

67. Abragam, A.; Bleaney, B., Electron Paramagnetic Resonance of Transition Ions (International Series of Monographs on Physics). 1970; p 912.

68. Golombek, A. P.; Hendrich, M. P. Quantitative analysis of dinuclear manganese(II) EPR spectra. *J. Magn. Reson.* **2003,** *165*, 33-48.

69. Hong, V.; Presolski, S. I.; Ma, C.; Finn, M. G. Analysis and optimization of copper-catalyzed azide-alkyne cycloaddition for bioconjugation. *Chem.* **2009,** *48*, 9879-9883.

70. Park, J. W.; Kim, Y.; Lee, K. J.; Kim, D. J. Novel cyanine dyes with vinylsulfone group for labeling biomolecules. *Bioconjugate Chem.* **2012,** *23*, 350-362.

71. Bruckman, M. A.; Kaur, G.; Lee, L. A.; Xie, F.; Sepulveda, J.; Breitenkamp, R.; Zhang, X.; Joralemon, M.; Russell, T. P.; Emrick, T.; Wang, Q. Surface modification of tobacco mosaic virus with "click" chemistry. *Chembiochem* **2008,** *9*, 519-523.

72. Franchi, P.; Lucarini, M.; Pedrielli, P.; Pedulli, G. F. Nitroxide Radicals as Hydrogen Bonding Acceptors. An Infrared and EPR Study. *ChemPhysChem* **2002,** *3*, 789-793.

73. Caravan, P.; Farrar, C. T.; Frullano, L.; Uppal, R. nfluence of molecular parameters and increasing magnetic field strength on relaxivity of gadolinium- and manganese-based T_1 contrast agents. *Contrast media mol. imaging* **2009,** *4*, 89-100.

74. Maliakal, A. J.; Turro, N. J.; Bosman, A. W.; Cornel, J.; Meijer, E. W. Relaxivity Studies on Dinitroxide and Polynitroxyl Functionalized Dendrimers: Effect of Electron Exchange and Structure on Paramagnetic Relaxation Enhancement. *J. Phys. Chem. A* **2003,** *107*, 8467-8475.

75. Halle, B.; Wennerström, H. Nearly exponential quadrupolar relaxation. A perturbation treatment. *J. Magn. Reson.* **1981,** *44*, 89-100.

76. The narrowing condition is defined for these systems when one of the two portions of the inner-sphere T_2 and T_1 converge to one of the sides depending on the rate of the proton exchange, T_e, tumbling, chemical shift that is proportional the magnetic field.

77. NMR of Paramagnetic Molecules in Biological Systems (Physical Bioinorganic Chemistry Series) by Luchinat, C., Bertini, Ivano: Benjamin-Cummings Pub Co 9780805307801 Hardcover -HPB-Ohio https://www.abebooks.com/Nmr-Paramagnetic-Molecules-Biological-Systems-Physical/19300712627/bd (accessed Nov 2, 2017).

78. Vander Elst, L.; Roch, A.; Gillis, P.; Laurent, S.; Botteman, F.; Bulte, J. W.; Muller, R. N. Dy-DTPA derivatives as relaxation agents for very high field MRI: the beneficial effect of slow water exchange on the transverse relaxivities. *Magn. Reson. Med.* **2002,** *47*, 1121-1130.

79. Caravan, P.; Greenfield, M. T.; Bulte, J. W. Molecular factors that determine Curie spin relaxation in dysprosium complexes. *Magn. Reson. Med.* **2001,** *46*, 917-22.

80. Swift, T. J.; Connick, R. E. NMR-Relaxation Mechanisms of O^{17}in Aqueous Solutions of Paramagnetic Cations and the Lifetime of Water Molecules in the First Coordination Sphere. *J. Chem. Phys.* **1962,** *37*, 307-320.

81. Bertini, I.; Luchinat, C.; Parigi, G. *NMR of Paramagnetic Molecules Applications to Metallobiomolecules and Model.* 2ⁿᵈ ed.; Elsevier; Amsterdam, **2017**

82. Pereira, G. A.; Ananias, D.; Rocha, J.; Amaral, V. S.; Muller, R. N.; Elst, L. V.; Tóth, É.; Peters, J. A.; Geraldes, C. F. G. C. NMR relaxivity of Ln^{3+}-based zeolite-type materials. *J. Mater. Chem.* **2005,** *15*, 3832.

83. Hyodo, F.; Soule, B. P.; Matsumoto, K.; Matusmoto, S.; Cook, J. A.; Hyodo, E.; Sowers, A. L.; Krishna, M. C.; Mitchell, J. B. Assessment of tissue redox status using metabolic responsive contrast agents and magnetic resonance imaging. *J. Pharm. Pharmacol.* **2008,** *60*, 1049-1060.

84. Bobko, A. A.; Kirilyuk, I. A.; Grigor'ev, I. A.; Zweier, J. L.; Khramtsov, V. V. Reversible reduction of nitroxides to hydroxylamines: roles for ascorbate and glutathione. *Free Radic. Biol. Med.* **2007,** *42*, 404-12.

85. Sato, S.; Endo, S.; Kurokawa, Y.; Yamaguchi, M.; Nagai, A.; Ito, T.; Ogata, T. Synthesis and fluorescence properties of six fluorescein-nitroxide radical hybrid-compounds. *Spectrochim. Acta A* **2016,** *169*, 66-71. 14.

86. Burts, A. O.; Li, Y. J.; Zhukhovitskiy, A. V.; Patel, P. R.; Grubbs, R. H.; Ottaviani, M. F.; Turro, N. J.; Johnson, J. A. The Impact of Aspect Ratio on the Biodistribution and Tumor Homing of Rigid Soft-Matter Nanorods. *Macromolecules* **2012,** *45*, 8310-8318.

87. Paletta, J. T.; Pink, M.; Foley, B.; Rajca, S.; Rajca, A. Synthesis and reduction kinetics of sterically shielded pyrrolidine nitroxides. *Org. lett.* **2012,** *14*, 5322-5325.

88. Shukla, S.; Eber, F. J.; Nagarajan, A. S.; DiFranco, N. A.; Schmidt, N.; Wen, A. M.; Eiben, S.; Twyman, R. M.; Wege, C.; Steinmetz, N. F. The Impact of Aspect Ratio on the Biodistribution and Tumor Homing of Rigid Soft-Matter Nanorods. *Adv. Healthcare Mater.* **2015,** *4*, 874-82.

89. Liu, X.; Wu, F.; Tian, Y.; Wu, M.; Zhou, Q.; Jiang, S.; Niu, Z. Size Dependent Cellular Uptake of Rod-like Bionanoparticles with Different Aspect Ratios. *Sci Rep* **2016,** *6*, 24567.

90. Dikalov, S. I.; Kirilyuk, I. A.; Voinov, M.; Grigor'ev, I. A. EPR detection of cellular and mitochondrial superoxide using cyclic hydroxylamines. *Free Radic. Res.* **2011,** *45*, 417-430.

91. Yapici, N. B.; Jockusch, S.; Moscatelli, A.; Mandalapu, S. R.; Itagaki, Y.; Bates, D. K.; Wiseman, S.; Gibson, K. M.; Turro, N. J.; Bi, L. New rhodamine nitroxide based fluorescent probes for intracellular hydroxyl radical identification in living cells. *Org. Lett.* **2012,** *14*, 50-53.

92. Abbas, K.; Hardy, M.; Poulhes, F.; Karoui, H.; Tordo, P.; Ouari, O.; Peyrot, F. Detection of superoxide production in stimulated and unstimulated living cells using new cyclic nitrone spin traps. *Free Radic. Biol. Med.* **2014,** *71*, 281-90.

93. Fridovich, I. Q. Quantitative Aspects of the Production of Superoxide Anion Radical by Milk Xanthine Oxidase. *J. Biol. Chem.* **1970,** *245*, 4053-4057.

94. McCord, J. M.; Fridovich, I. The Reduction of Cytochrome c by Milk Xanthine Oxidase. *J. Biol. Chem.* **1968,** *243*, 5753-5760.

CHAPTER 6

EFFECT OF SURFACE CHARGE OF VIRUS PARTICLES ON CONTROLLED

GROWTH OF METAL ORGANIC FRAMEWORKS[1]

Authors: Madushani Dharmarwardana, Shaobo Li, Raymond P. Welch, Candace E. Benjamin,
Alexandra M. Shamir, Steven O. Nielsen, and Jeremiah J. Gassensmith

The Department of Chemistry, BE26

The University of Texas at Dallas

800 West Campbell Road

Richardson, Texas 75080-3021

6.1 Summary

Biomimetic mineralization with metal-organic frame-works (MOF), typically zeolitic imidazolate framework-8 (ZIF-8), is an emerging strategy to protect sensitive biological substances against denaturing environmental stressors like heat and proteolytic agents. Additionally, this same biomimetic mineralization process has the potential of being used to create distinct core-shell architectures using genetically or chemically modified viral nanoparticles. Despite the proliferation of examples for ZIF-8 growth on biological or proteinaceous substrates, systematic studies of these processes are few and far be-tween. Herein, we employed the tobacco mosaic virus (TMV) as a model biological template to investigate the biomimetic mineralization of ZIF-8, which has been proven to be a robust MOF for encasing and protecting inlaid biological substances. Our study shows that surface charge of viral nanoparticle has no significant effect on the formation of core-shell bionanoparticles unless the surface of the virus is modified with high loading of positive charges.

6.2 Introduction

The *in-situ* crystallization of metal-organic frameworks (MOFs) on biological macromolecules, otherwise called bio-mimetic mineralization of MOFs, has emerged in recent years as a promising strategy to offer robust protection to encapsulated biological materials against environmental stresses.[1-7] MOFs are a family of porous crystalline materials constructed of metal nodes linked by organic ligands to form porous and high surface area crystals.[8-10] The tunable pore sizes and distribution confers potentially valuable properties in mass transfer, storage, sensing, and catalysis.[11-22] Among the previously reported MOF candidates for biomimetic mineralization,

154

zeolitic imidazolate frameworks (ZIFs)[9]—in particular ZIF-8 with its constituent organic ligand being 2-methylimidazole (HMIM)—has shown tremendous flexibility in the syntheses on a broad variety of biological templates from enzymes,[23-38] to viruses,[3] to living yeast cells.[39-40] The ubiquity of ZIF-8 in biomimetic mineralization is owed, at least partially, to its hydrolytic and thermal stability and being readily prepared in pure aqueous solutions under ambient conditions. The resulting enzyme and viral composites[3, 26] demonstrate enhanced stability toward organic solvents and even boiling water. In addition to affording stability, the ZIF-8 shell allows reactants to travel through the pores and undergo catalysis by the inlaid enzyme under conditions normally leading to protein denaturation or to modify the surface of the protein in a bioconjugation reaction. This has excited researchers as it presents unique opportunities to make enzymes function even under extreme environmental conditions.[41-44]

A curious difference in the resulting morphology of the biomimetic mineralization process emerges using ZIF-8 at the size and length scale of viral nanoparticles. As illustrated in Scheme 1, a single 300×18 nm tobacco mosaic virus (TMV),[45-48] forms an exoskeleton of very fine ZIF-8 crystals, which creates a core-shell bionanoparticle (CSBN). In contrast, many enzymes, which are typically < 10 nm, become entrapped in a single crystal that retains the micron-sized rhombic dodecahedral (r.d.) morphology of pristine ZIF-8. The fact that CSBNs retain the underlying morphology of the virus following their biomimetic mineralization process is intriguing as it is not clear why TMV should form CSBNs and not end up trapped in larger regular crystals *en masse*, as illustrated in Scheme 1d. Nevertheless, CSBNs offer an approach to the articulated interest[49-51] of combining mesoscale and microscale pore structure in the formation of MOF films and composites. One means of getting to such structures is via exploitation of recent advances in viral

nanotechnology.[52-53] In particular, TMV can be engineered to create proteinaceous nanoparticles of custom lengths and very specific shapes like nano-stars, short nanorods and nanospheres.[54-56] This makes TMV an ideal model biological template to study the biomimetic mineralization of ZIF-8, the understanding of which could guide the fabrication of biology@MOF composite materials as drug carriers, biosensors, and biocatalysts.

6.3   Experimental

6.3.1   Chemicals

All the solvents and reagents for buffers were purchased from Fisher Scientific. Ethylenediaminetetraacetic acid (EDTA), 1-methylimidazole, 2-methylimidazole, zinc acetate dihydrate, 2-bromoethylamine hydrobromide, 2-chloro-N,N-dimethylethylamine hydrochloride, anhydrous magnesium sulphate, iodomethane, 6-bromohexanoic acid, methyl acrylate, 1,2-diaminoethane, Poly(ethylene glycol) methyl ether (PEG-2000), *p*-toluenesulfonyl chloride, sodium nitrite, *p*-toluenesulfonic acid monohydrate, 3-ethynylaniline, cupric sulfate pentahydrate, sodium ascorbate, aminoguanidine hydrochloride, 1-(3-dimethylaminopropyl)-3-ethylcarbodiimide hydrochloride (EDC), 1-hydroxybenzotriazole hydrate (HOBt), propargylamine, triethylamine, fluorescein isothiocyanate isomer I (FITC), sodium azide, β-mercaptoethanol, polyethylene glycol 8000 (PEG-8000), and Triton X-100 surfactant were purchased from Alfa Aesar, Acros Organics, Fisher Scientific, or Sigma Aldrich, and used without further purification. Protein concentration was measured using a Pierce™ Modified Lowry Protein Assay Kit (Thermal Fisher Scientific, Waltham, MA).

6.3.2 Instrumentation

Scanning Electron Microscopy (SEM)

SEM was done on a Zeiss Supra 40 at 2.5 kV with SE2 detector. Samples were prepared by either drop-casting 5 µL of the sample suspension onto a clean silicon substrate or by mixing a small amount of sample powder in a pipette tip with a 5 µL drop of ultrapure water by repeatedly pipetting up and down. The drop was then wicked off with Whatman #2 filter paper and dried in air.

Transmission Electron Microscopy (TEM)

TEM was done on a JEOL JEM-1400plus at 120 kV with a Gatan CCD 4K×4K detector. Samples were prepared by applying 5 µL of sample solution onto a 300-mesh Formvar-carbon-coated copper grid (Electron Microscopy Sciences, Hatfield, PA, USA) for at least 30 sec, and wicking off the drop with Whatman #2 filter paper. If negative staining was required, a 5 µL of 2% uranyl acetate (SPI Supplies, West Chester, PA, USA) was then applied to the grid for at least 30 sec, then wicked off with filter paper as above. The grids were then dried in air and stored under ambient conditions until imaged.

Powder X-ray Diffraction (PXRD)

PXRD data for all the samples shown in Figure 3 and Figure S5-S8 were collected by using a Rigaku SmartLab X-ray diffractometer with CuKα (1.54060 Å) at 40 kV and 30 mA. The scans were performed for 2θ from 5° to 55° with a step size of 0.01°.

High Resolution Powder Diffraction

PXRD data that is shown in Figure S31 were collected from the 11-BM beamline at the Advanced Photon Source at Argonne National Laboratory. The samples were characterized using a wavelength of 0.457676 Å that scans 2θ from 0.5° to 50° with a step size of 0.001°.

Nuclear Magnetic Resonance (NMR)

NMR spectra were measured using a Bruker AVANCE III 500 MHz spectrometer with $Si(CH_3)_4$ used as a reference standard.

Size Exclusion Chromatography (SEC)

Analytical SEC was performed using an Agilent 1100 series HPLC system on a GS400SWXL (7.8 mm $\times$ 300 cm) column with 100 mM pH 7.4 KP buffer with 0.05% NaN_3.

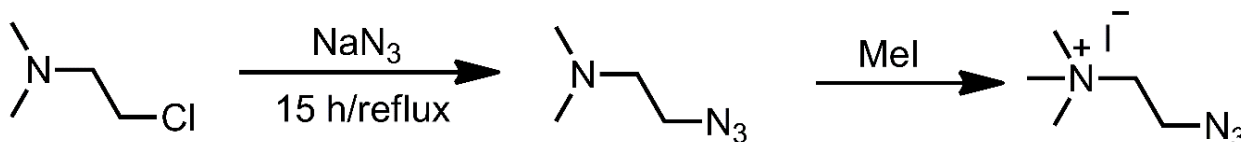## 6.3.3　Synthesis of R-N₃ linkers for Surface Modification on TMV

Figure 6.1. Synthesis of 1C linker

Synthesis of 2-azido-N,N-dimethylethylamine

The compound 2-azido-N,N-dimethylethylamine was synthesized following a published procedure.[57] 2-chloro-N,N-dimethylethylamine hydrochloride (0.907 g, 6.30 mmol) and sodium azide (0.829 g, 12.6 mmol) were dissolved in 20.0 mL of water and heated at 75 °C for 15 hrs. The reaction mixture was cooled in an ice bath and 0.400 g of NaOH was added to allow phase separation and the organic phase was removed. The aqueous phase was washed with diethyl ether. The organic phases were combined, dried with $MgSO_4$, and concentrated down to an oil (0.311 g,

2.70 mmol, 43.0%). ^{1}H-NMR (500 MHz, CDCl$_3$) δ ppm 2.25 (s, 6H), 2.48 (t, J=6.20, 2H), 3.33 (t,

J=6.18, 2H). ^{13}C-NMR (125 MHz, CDCl$_3$) δ ppm 58.05, 48.96, 45.39.

Synthesis of 2-Azido-N,N,N-trimethylethylammonium Iodide (1C)

The compound 1C was synthesized following a published procedure.[57] To a solution of 2-azido-

N,N-dimethylethylamine (0.314 g, 2.72 mmol) in 3.0 mL of dry acetonitrile was added an excess

of iodomethane (0.617 g, 4.35 mmol) at 0 °C, and the resulting mixture was stirred for 24 hrs at

room temperature. After removal of the solvent *in vacuo*, a pale white solid (0.300 g, 1.20 mmol,

42.9%) was obtained. ^{1}H-NMR (DMSO-d$_6$) δ ppm 3.12 (s, 9H), 3.55 (t, J=5.75, 2H), 3.96 (t,

J=5.52, 2H); ^{13}C-NMR (125 MHz, DMSO-d$_6$) δ ppm 44.78, 53.33, 63.88.
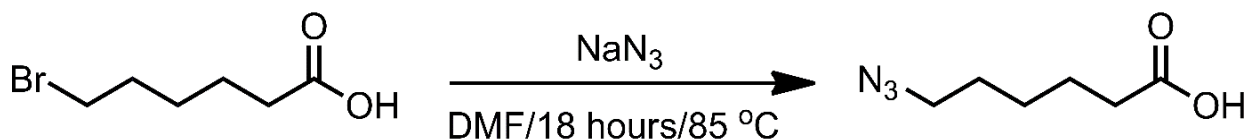

Figure 6.2. Synthesis of 1A linker

The compound 1A was synthesized according to a previously published procedure.[58]

Synthesis of 2-azidoethylamine (**1**)

The compound 2-azidoethylamine was synthesized according to a previously published

procedure.[59]

Synthesis of PAMAM-D$_0$

The compound PAMAM-D$_0$ was synthesized following a published procedure.[60] A solution of 2-

azidopropylamine (0.258 g, 3.00 mmol) in methanol (2.5 mL) was added dropwise to a stirred

solution of methyl acrylate (0.650 g, 7.50 mmol) in methanol (2.5 mL) over a period of 1 hr in an

ice-water bath. The resulting solution was stirred for 30 min in an ice-water bath and then allowed

to warm to room temperature and stirred for further 48 hrs. The volatiles were removed under

reduced pressure and crude product was purified by column chromatography (ethyl acetate/hexane) to afford the PAMAM-D$_0$ (0.120 g, 0.465 mmol, 15.50%) as a colorless oil. ^{1}H-NMR (500 MHz, CDCl$_3$) δ ppm 3.62 (s, 6H), 3.20 (t, J=5.9, 2H), 2.76 (t, J=6.92, 4H), 2.60 (t, J=5.90, 2H), 2.42 (2H, J=6.92, 4H); ^{13}C-NMR (125 MHz, CDCl$_3$) δ ppm 172.74, 53.76, 51.59, 49.63, 49.14, 32.60.
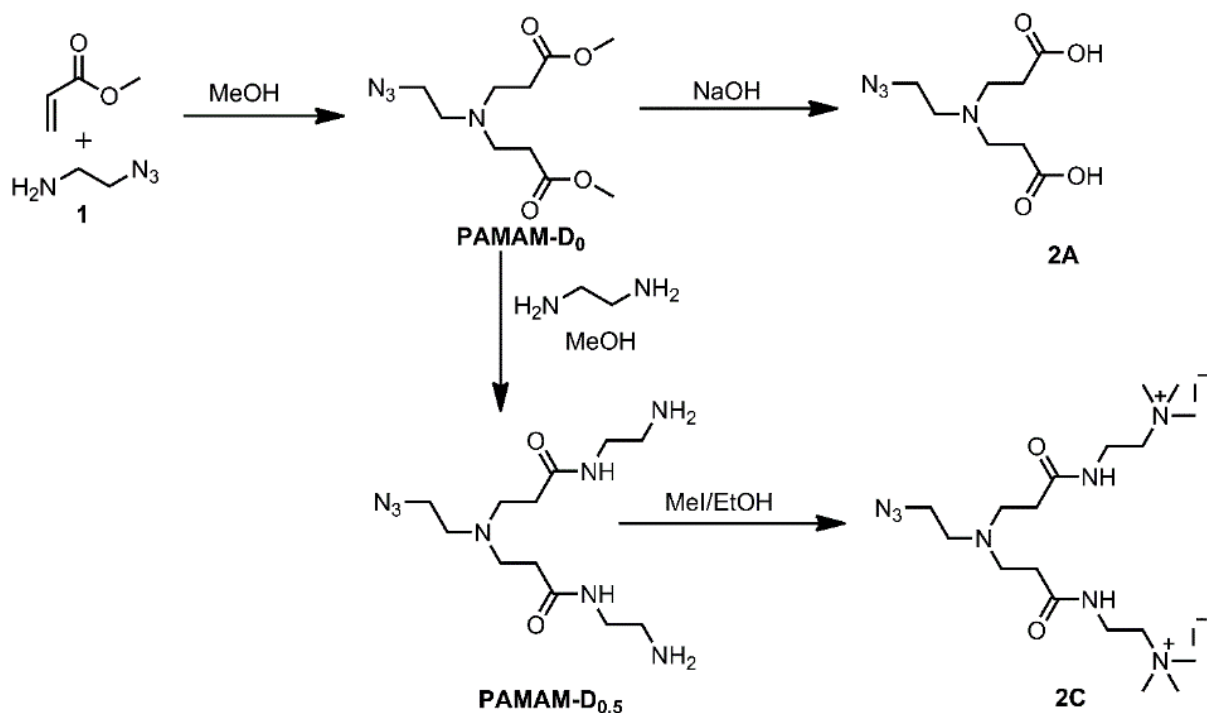

Figure 6.3. Synthesis of 2C and 2A linkers

Synthesis of PAMAM-D$_{0.5}$

The compound PAMAM-D$_{0.5}$ was synthesized following a published procedure.[60] A solution of PAMAM-D$_0$ (0.120 g, 0.464 mmol) in methanol (5.0 mL) was added dropwise to a stirred solution of 1,2-diaminoethane (0.696 g, 11.6 mmol) in methanol (5.0 mL) over a period of 1 hr in an ice-water bath. The resulting solution was allowed to warm to room temperature and stirred for further 7 days at room temperature. The solvent was removed under reduced pressure maintaining the temperature not higher than 40 °C and then the excess 1,2-diaminoethane was removed using

mixture of toluene and methanol (9:1). The remaining toluene was removed using methanol to afford PAMAM-D$_{0.5}$ (0.168 g, 0.535 mmol, 99.0%) as a yellow oil. ^{1}H-NMR (500 MHz, CDCl$_3$) δ ppm 3.36 (t, J= 5.65, 2H), 3.29 (t, J=5.80, 4H), 2.83 (t, J=5.87, 4H), 2.77 (t, J=6.07, 4H), 2.62 (t, J=6.92, 4H), 2.38 (t, J=6.07, 2H). ^{13}C-NMR (150 MHz, CDCl$_3$) δ ppm 172.56, 63.89, 53.25, 50.36, 42.10, 41.32, 34.21.

Synthesis of 2A linker

The compound 2A was synthesized following a published procedure.[61] In a 25-mL round bottom flask, PAMAM-D$_0$ (0.280 g, 1.08 mmol) was dissolved in 280 µL MeOH, 280 µL H$_2$O, and 2.52 mL THF. Then, NaOH (0.840 g, 21.0 mmol) were added and the solution was stirred for 2 hrs. The solution was acidified (pH = 2) by addition of 1M HCl, and the organic component was removed by under vacuum. The remaining aqueous slurry was diluted with a small volume of H$_2$O, transferred to a 30-mL separatory funnel, and extracted 5 times with *n*-butanol. The butanol fractions were combined, dried over Na$_2$SO$_4$, and the butanol removed by rotary evaporation to afford 2A (0.130 g, 0.565 mmol, 52.0%) as a colorless oil. ^{1}H-NMR (500 MHz, MeOD) δ ppm 3.93 (t, J= 6.50, 2H), 3.52 (t, J=6.48, 4H), 3.41 (t, J=6.50, 2H), 2.90 (t, J=6.45, 4H); ^{13}C-NMR (125 MHz, MeOD) δ ppm 172.86, 52.69, 50.16, 45.60.

Synthesis of 2C linker

In a round bottom flask, PAMAM-D$_{0.5}$ (0.230 g, 0.890 mmol), MeI (2.525 g, 17.80 mmol) and K$_2$CO$_3$ (1.000 g, 7.230 mmol) were mixed with 10.0 mL of ethanol and stirred for 2 days at room temperature excess K$_2$CO$_3$ was removed by filtration. Solvent was removed, and the resultant solid was washed with diethyl ether and hexane to yield 2C (0.500 g, 0.764 mmol, 85.9%) as an off-white solid. ^{1}H-NMR (500 MHz, D$_2$O) δ ppm 4.00 (m, 4H), 3.87 (t, 4H), 3.77 (t, 2H), 3.72 (m,

4H), 3.30 (bs,18 H), 2.93 (t, 2H); ^{13}C-NMR (125 MHz, D$_2$O) δ ppm 175.36, 64.25, 62.06, 53.62,

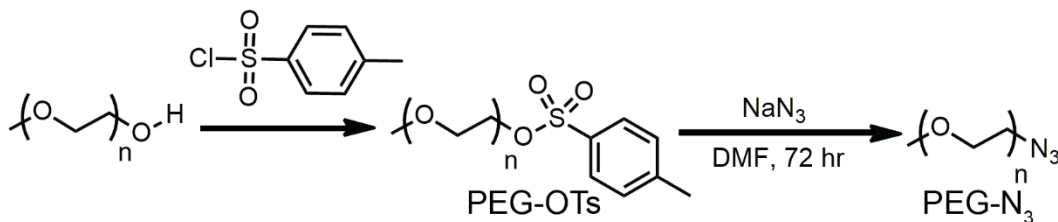51.69, 48.90, 33.68, 32.72. ESI-MS: Mass calculated for [M/2]$^+$ 200.16, observed 200.20.

Figure 6.4. Synthesis of PEG linker

Synthesis of PEG-OTs

The compound PEG-OTs was synthesized following a published procedure.[62] Poly(ethylene

glycol) methyl ether (PEG-2000, 2.00 g, 1.00 mmol) and *p*-toluenesulfonyl chloride (1.90 g, 10.0

mmol) were dissolved in 25 mL CH$_2$Cl$_2$. The resulting solution was cooled to 0 °C on ice and

triethylamine (1.41 mL, 10.0 mmol) was added dropwise to above solution. The solution was

stirred for 24 hrs at room temperature. The resultant solution was diluted to 200 mL with

dichloromethane and extracted with water. The organic phase was dried with anhydrous MgSO$_4$

and concentrated under the reduced pressure, then it was precipitated into 200 mL of diethyl ether

and the precipitate was filtered and dried under vacuum to afford PEG-OTs (1.48 g, 0.740 mmol,

74.0%) as a white solid. ^{1}H-NMR (500 MHz, CDCl$_3$) δ ppm 7.76 (d, J= 8.30, 2H), 7.30 (d, J=8.05,

2H), 4.12 (t, J=4.82, 2H), 3.74 (t, J=4.88, 2H), 3.64 (t, J=4.85, 2H), 3.60 (s, 180H), 3.54 (s, 3H),

3.51 (t, J=5.26, 2H), 3.46 (t, J=4.88, 2H), 3.34 (s, 3H) ; ^{13}C-NMR (125 MHz, CDCl$_3$) δ ppm

144.77,133.02, 129.82, 127.97, 71.92, 70.73, 70.56,69.23, 68.66, 59.02, 45.92.

Synthesis of PEG-N$_3$

The compound PEG-N$_3$ was synthesized following a published procedure.[62] Sodium azide (0.585

g, 9.00 mmol) was added to a dry DMF (10 mL) solution of PEG-OTs (1.84 g, 0.900 mmol) under

a N_2 atmosphere, then the reaction mixture was heated to 105 °C and stirred for 12 hrs. The solution was cooled to room temperature and filtered. DMF solvent was removed under reduced pressure, and then the product was dissolved in 100 mL of dichloromethane. The mixture was extracted with 5 wt% NaCl solution and distilled water, dried with anhydrous $MgSO_4$, precipitated in diethyl ether to afford PEG-N_3 (0.680 g, 0.340 mmol, 36.9%) as a white solid. ^{1}H-NMR (500 MHz, $CDCl_3$) δ ppm 3.75 (t, J= 4.90, 2H), 3.61 (s, 180 H), 3.52 (t, J=4.70, 2H), 3.47 (t, J=4.90, 2H), 3.35 (t, J=5.27, 2H), 3.34 (s, 3H); ^{13}C-NMR (125 MHz, $CDCl_3$) δ ppm 71.96, 70.60, 70.05, 59.04, 50.71.

Synthesis of FITC-N_3

FITC-N_3 was synthesized was synthesized according to a previously published procedure.[3]

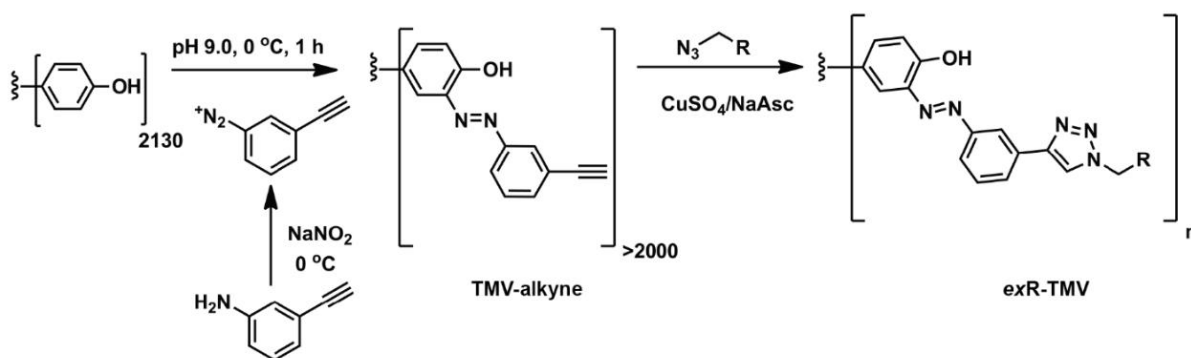Exterior surface modification of TMV with R-N_3 Linkers

Figure 6.5. Exterior surface modification TMV with linkers.

Preparation of ethynylphenyldiazenylphenol-TMV (TMV-alkyne)

3-ethynylaniline diazonium salt was prepared by adding 400 µL of 0.3 M *p*-toluenesulfonic acid monohydrate, 75 µL of 0.68 M 3-ethynylaniline and 25 µL of 3.0 M sodium nitrite. The resultant mixture was cooled on ice for 1 h. Next, 142 µL of stock TMV solution (14.10 mg/mL) was diluted to 2 mg/mL with 808 µL of 0.1 M pH 8.8 borate buffer and cooled on ice. To this solution, 50 µL

of *in situ* prepared 3-ethynylaniline diazonium salt was added and kept on ice for 1 hr. Next, the resultant straw-colored solution (TMV-alkyne) was purified with a PD MidiTrap G-25 column and the solutions were concentrated to 10 mg/mL with a 10K MWCO Pierce™ Protein Concentrator.

General procedure for the preparation of *ex*R-TMV

200 µL of TMV-alkyne (10 mg/mL) was mixed with 730 µL of 0.1 M pH 7.4 KP buffer. Then, 10 µL of 0.01 M R-N$_3$ (10 eq per coat protein) and 10 µL of 0.1 M aminoguanidine hydrochloride were added to the TMV solution. Then, 10 µL of 0.1 M CuSO$_4$, 10 µL of 0.5 M Tris(3-hydroxypropyltriazolylmethyl)amine (THPTA) were mixed and added to above TMV stock solution. Finally, 10 µL of sodium ascorbate was added to the mixture and the resulting solution was incubated at room temperature for 2 h and 10 µL of 0.5 M EDTA was added to the reaction and incubated another 10 min. The reaction mixture was then purified with a PD MidiTrap G-25 column and the solutions were concentrated to 10 mg/mL with a 10K MWCO Pierce™ Protein Concentrator.

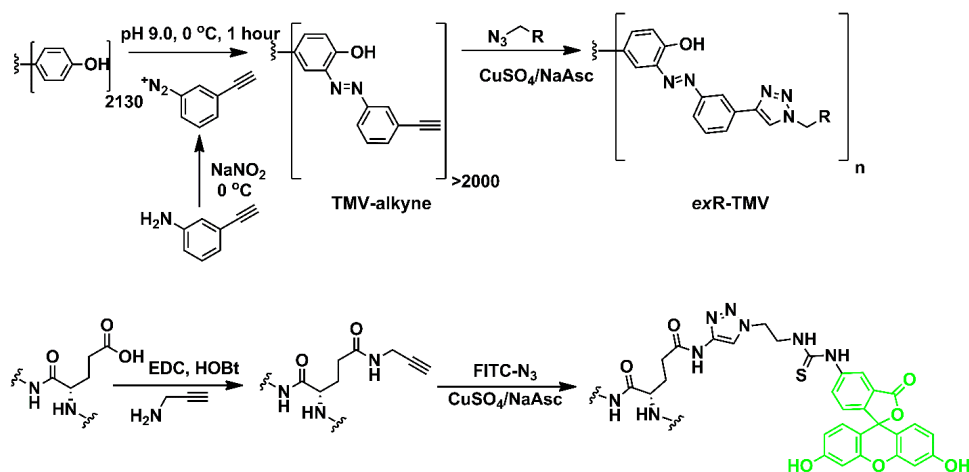Dual surface modification with R-N$_3$ and FITC (exR-inFITC-TMV)

Figure 6.6. Dual surface modification of TMV with R-N$_3$ and FITC-N$_3$.

164

Preparation of *ex*R-*in*FITC-TMV

The exterior surface of TMV was modified with R-N$_3$ as described in the "Exterior surface modification of TMV with R-N$_3$ Linkers" section. Then the interior surface was modified with propargyl amine using an EDC coupling reaction. 142 µL of stock *ex*R-TMV solution (10.0 mg/mL) was diluted to 2 mg/mL with 632 µL of 0.1 M pH 7.4 HEPES buffer at room temperature followed by the addition of 130 µL of 0.1 M TEMPO-NH$_2$, 3 mg of HOBt, and 96 µL of 0.1 M EDC. The reaction mixture was incubated at room temperature for 24 hrs, purified with a PD MidiTrap G-25 column, and the solutions were concentrated to 10 mg/mL with a 10K MWCO Pierce™ Protein Concentrator to yield interior alkyne modified exR-TMV (*ex*R-*in*PA-TMV). FITC-N$_3$ was then attached by the CuAAC reaction. 200 µL of *ex*R-*in*PA-TMV (10 mg/mL) was mixed with 750 µL of 0.1 M pH 7.4 KP buffer. Then, 10 µL of 0.01 M FITC-N$_3$ (10 eq per coat protein) and 10 µL of 0.1 M aminoguanidine hydrochloride were added to the *ex*R-*in*PA-TMV solution. Next, 10 µL of 0.1 M CuSO$_4$ and 10 µL of 0.5 M THPTA were mixed together and was added to the above solution. Finally, 10 µL of sodium ascorbate was added to this solution, the reaction mixture was incubated at room temperature for 2 hrs, 10 µL of 0.5 M EDTA was added to the reaction, and the solution was incubated for another 10 min. The reaction mixture was then purified with a PD MidiTrap G-25 column and the solutions were concentrated to 10 mg/mL with a 10K MWCO Pierce™ Protein Concentrator to yield *ex*R-*in*FITC-TMV.

Preparation of *ex*R-TMV@ZIF-8 CSBNs and *ex*R-*in*FITC-TMV@ZIF-8 CSBNs

Desalted *ex*R-TMV or *ex*R-*in*FITC-TMV (R= 1C/2C/1A/2A/PEG, 0.0625 mg) was added into a 1.5 mL Eppendorf tube, followed by 500 µL of 400 mM HMIM aqueous solution and 500 µL of 20 mM Zn(OAc)$_2$ aqueous solution (P-II [20-20] condition). After shaking for 20 sec the mixture

was set on the bench overnight under ambient conditions. All the mixtures formed flocculates right after shaking except the samples contain *ex*2C-TMV and *ex*2C-*in*FITC-TMV. The precipitates were collected by centrifugation at 2656 ×*g* for 10 min. The product was washed by ultrapure water twice.

Determination of free TMV after ZIF-8 crystallization

Table 6.1. Free *ex*R-*in*FITC-TMV in the supernatant after overnight reaction that is determined by fluorimeter.

Sample	Exp-1 free%	Exp-2 free%	Exp-3 free%	Ave	Stdev
*in*FITC-TMV	19.4	12.2	8.5	13.4	4.5
*ex*1A-*in*FITC-TMV	11.1	15.1	5.3	10.5	4.0
*ex*2A-*in*FITC-TMV	9.5	4.6	5.2	6.4	2.2
*ex*PEG-*in*FITC-TMV	12.0	4.9	3.9	6.9	3.6
*ex*1C-*in*FITC-TMV	7.6	3.1	4.5	5.1	1.9
*ex*2C-*in*FITC-TMV	38.0	25.5	22.0	28.5	6.9

First, *ex*R-*in*FITC-TMV@ZIF-8 CSBNs were prepared as described above. After overnight reaction, the mixtures were centrifuged at 2656 ×*g* for 10 min. Then, 600 µL of supernatant was carefully collected with a pipette. The collected supernatant was further centrifuged at 2656 ×*g* for 10 min to ensure the small particles were completely pelleted down. Later, 500 µL of supernatant was thoroughly mixed with 500 µL of ultrapure water and 1500 µL of 0.5 M EDTA (pH 7.0). The as-prepared sample solution was transferred to a quartz cuvette and directly tested on spectrofluorometer. Additional dilution may be needed if the excitation intensity exceeded the range. The emission spectrum was collected from 500 nm to 700 nm with excitation at 480 nm. The emission intensity was collected at 519 nm and brought to the pre-determined standard curve to calculate the concentration of free *ex*R-*in*FITC-TMV in the supernatant. The percentage of free *ex*R-*in*FITC-TMV was calculated by weight of free *ex*R-*in*FITC-TMV (calculated concentration

times the volume of original reaction mixture) divided by the original weight of *ex*R-*in*FITC-TMV (0.0625 mg).

6.4   Results and Discussion

The isoelectric point (IP) of TMV is 3.5, and in our experiments, under all growth conditions, the surface of TMV has a negative charge, owing to the alkaline nature of HMIM. We hypothesized somewhat intuitively that the induced crystallization was driven by electrostatic interactions between the negatively charged viral particles and metal cations. Because bioconjugation of organic substrates is a very common way to add functionality to viral nanoparticles and biomacromolecules in general, we wondered how the yield of biomimetic mineralization would be impacted by common changes of surface charge induced by typical bioconjugation reactions on the surface of the virus. TMV possesses a tyrosine on the exterior surface, which can be modified via diazonium coupling.[63] The virus also contains glutamate residues on the interior surface, which can be modified by EDC coupling.[63] In this way, we could add a green fluorescent FITC tag to the interior after modifying the exterior to produce *ex*R-*in*FITC-TMV conjugates (where *ex*R-TMV, R= 1C/2C/1A/2A/PEG in Figure 6.1c). Surface charges were varied by attaching to the exterior one or two anionic carboxylate-terminated functional groups (*ex*1A-TMV and *ex*2A-TMV) to enhance the surface negative charge and one or two cationic tetraalkylammonium-terminated functional groups (*ex*1C-TMV and *ex*2C-TMV) to introduce positive charge. We also introduced a PEG2000 (*ex*PEG-TMV*)* polymer to the surface as a charge neutral—though sterically encumbering—functional group.
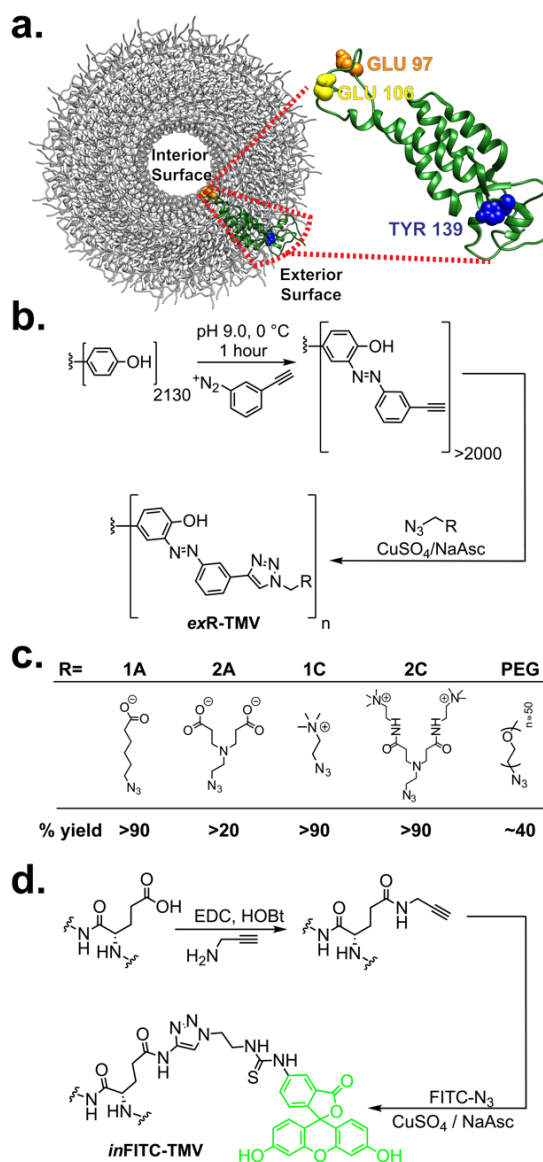
Figure 6.7. a) Crystallographic (PDB ID: 2TMV) structure of TMV with known reactive residues highlighted. b) The bio-conjugation strategy used to functionalize the exterior of TMV at Y139 with linkers to produce *ex*R-TMV where R is defined in c) the table of linkers, which also indicated the percentage of modification to the TMV. d) Shows the bio-conjugation strategy used to functionalize the interior of TMV at E97 and E106 with FITC-N$_3$ to produce *in*FITC-TMV. When the two syntheses are conducted sequentially on the same TMV, the product is denoted as *ex*R-*in*FITC-TMV.
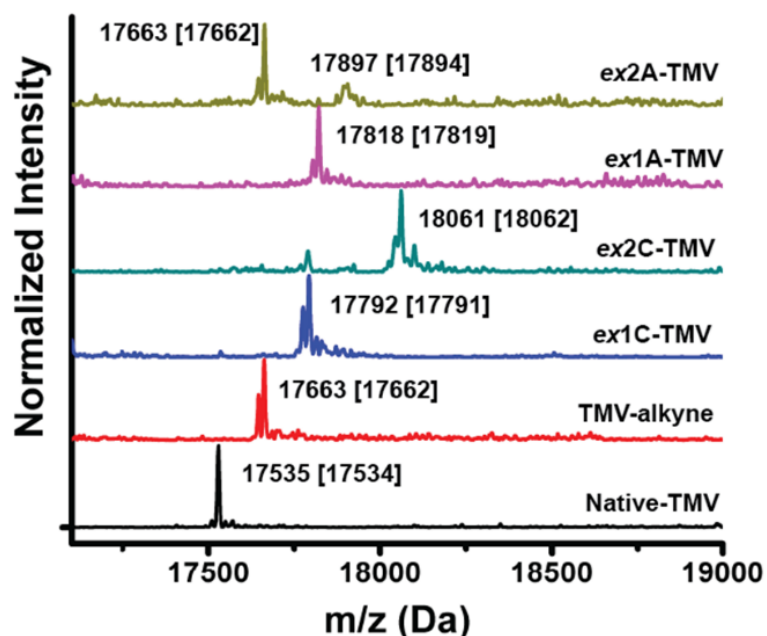
Figure 6.8. ESI-MS of *ex*R-TMV conjugates.

In a typical bioconjugation reaction, we first treated TMV with *in situ* prepared diazonium salt of 3-ethynylaniline to introduce an alkyne group to the exterior of TMV (Figure 6.7b). We used high-performance liquid chromatography/electrospray ionization mass spectrometry (HPLC/ESI-MS) data (see SI) to determined that >90% of the TMV coat protein monomers were converted to the alkyne derivative. We then used a Cu(I)-catalyzed azide-alkyne cycloaddition (CuAAC) reaction to attach the functionalized azides (Figure 6.7c) to the TMV surface. From our HPLC/ESI-MS data (Figure 6.8), we found generally good yields—in excess of 90%—with the exception of the doubly-anionic carboxylate *ex*2A-TMV, and *ex*PEG-TMV; however, these yields are in line with literature values (Figure 6.9).[64]

Following exterior functionalization, the interior was conjugated via a routine procedure using a modified FITC-N_3 tag. The surface charge of TMV after these surface modifications was qualitatively analyzed by agarose gel band shift assay (Figure 6.8a). Compared to native TMV, the cationic ammonium-functionalized TMV (*ex*1C-*in*FITC-TMV and *ex*2C-*in*FITC-TMV) shows

retarded mobility towards the positive electrode at the bottom of the gel while the anionic carboxylate-functionalized TMV (*ex*1A-*in*FITC-TMV and *ex*2A-*in*FITC-TMV) demonstrated enhanced mobility towards the positive electrode.
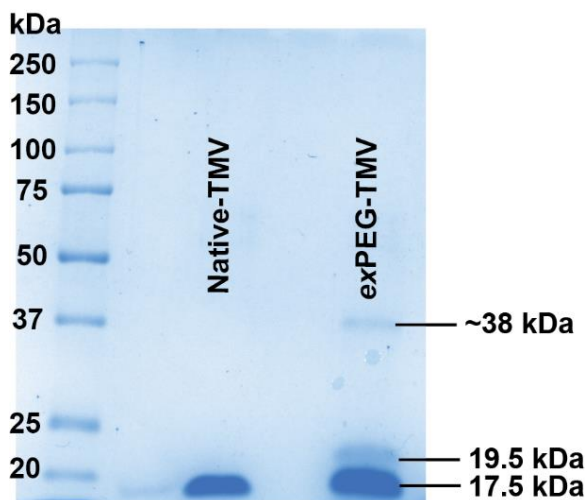

Figure 6.9. SDS page of TMV-PEG; The band at ~38 kDa at the *ex*PEG-TMV line could be due to the dimerization of coat proteins, showing the intertwining of PEG chains.[7]
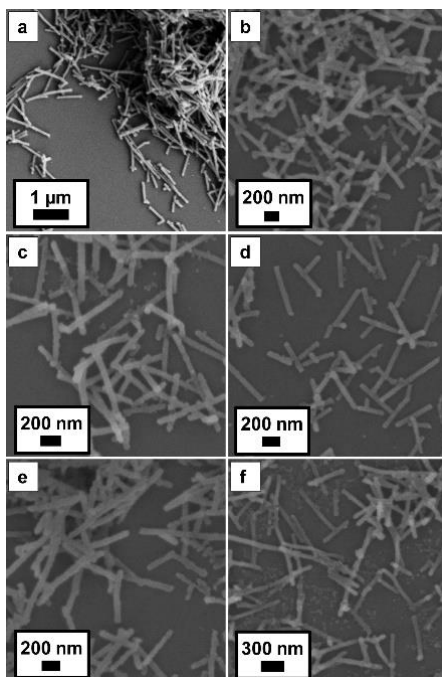

Figure 6.10. SEM micrographs of as-prepared TMV@ZIF-8 with using a) *in*FITC-TMV; b) *ex*PEG-*in*FITC-TMV; c) *ex*1A-*in*FITC-TMV; d) *ex*2A-*in*FITC-TMV; e) *ex*1C-*in*FITC-TMV and f) *ex*2C-*in*FITC-TMV.

To ascertain CSBN yields of each conjugate, the doubly modified *ex*R-*in*FITC-TMV conjugates were individually added to ZIF-8 precursors under identical conditions (M-II [20-20]) and the resultant solutions centrifuged, and the products characterized by SEM and PXRD (Figure 6.10 and Figure 6.11) after they were activated by soaking in methanol. The samples did not show any difference in terms of morphology and crystallinity—each sample contained pristine ZIF-8 coated CSBNs—however, there was a noticeable difference in the yield between each batch. Yields were determined via fluorescence spectroscopy of the reaction solution after all solids were removed and these data are plotted in Figure 6.12b as the amount of free TMV.
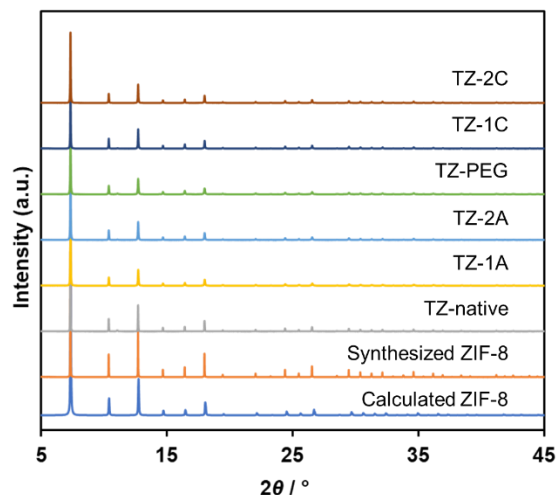
Figure 6.11. PXRD patterns of as-prepared ZIF-8 and TMV@ZIF-8 with using *in*FITC- TMV (TZ-native); *ex*1A-*in*FITC-TMV (TZ-1A); *ex*2A-*in*FITC-TMV (TZ-2A); *ex*PEG-*in*FITC-TMV (TZ-PEG); *ex*1C-*in*FITC-TMV (TZ-1C); and *ex*2C-*in*FITC-TMV (TZ-2C), respectively.

The TMV featuring the most positive charges (*ex*2C-*in*FITC-TMV) shows the highest free TMV content after crystallization, while the other modifications do not appear to affect the yield. This is instructive, as it suggests that CSBN formation proceeds in very good yields (~90%) under most circumstances, unless the surface is highly positively charged, in which case the yield is still ~70%. Interestingly, the yield of the CSBN on *ex*PEG-*in*FITC-TMV appeared unaffected by the PEG2000

chain. This was modestly surprising as PEG coatings are routinely used to inhibit antibody recognition[65-66] of TMV by blocking the protein surface from antibody recognition. Molecular dynamics (MD) computer simulations of a TMV with 45% PEG 2000 coverage (namely 22 of the 49 proteins in the MD unit cell have PEG attached to their modified TYR-139 residue) were performed to quantify the exposure of the protein outer cylinder surface. The actual exposure is 72% using a small probe size, 44% using a medium probe size, and 11% using a large probe size. Which probe size is appropriate depends on the context: since antibodies are large, the low exposure for the large probe size suggests, correctly, that this PEG coverage is sufficient to inhibit antibody recognition. On the other hand, using a smaller probe size would suggest, again in agreement with the experimental data, that this PEG coverage is inadequate to prevent biomimetic mineralization. Together, this indicated that ZIF-8 could be an effective capping strategy for highly functionalized biomaterials—even those with functionality that can evade antibody binding.
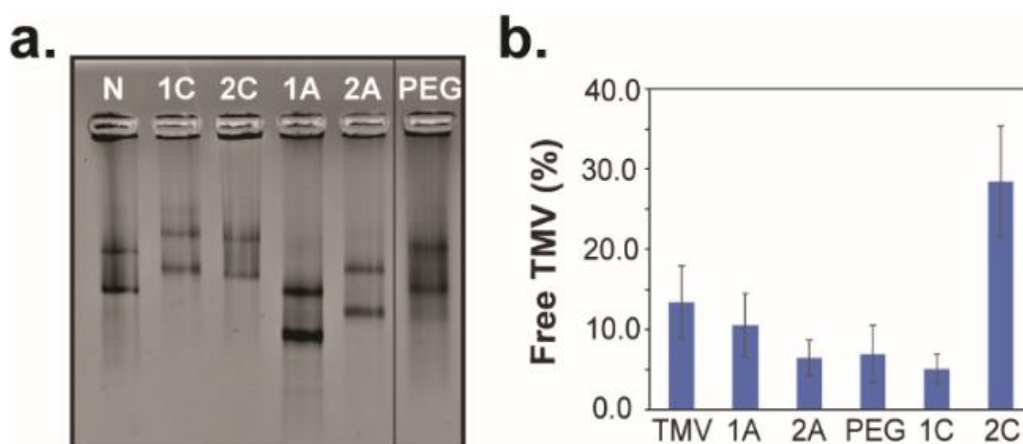

Figure 6.12. a) Band shift assay by agarose gel electrophoresis comparing native TMV (N= *in*FITC-TMV) and TMV functionalized with one of the five linkers (1C= *ex*1C-*in*FITC-TMV; 2C= *ex*2C-*in*FITC-TMV; 1A= *ex*1A-*in*FITC-TMV; 2A= *ex*2A-*in*FITC-TMV and PEG= *ex*PEG-*in*FITC-TMV). Migration toward the positive electrode at the bottom corresponds to more negatively charged TMV assuming functional groups do not significantly affect the size of the original virus. b) Encapsulation efficiency, as determined by fluorescence of the remaining supernatant from CSBN formation, as the surface charge is altered.

6.5   Conclusions

The formation of CSBNs is sufficiently rugged that modification of surface charge or even steric encumbrance still produces decent yields of CSBNs, unless a high loading of positive charge is installed on the exterior of viral particles. This suggests that CSBN formation and biomimetic mineralization processes with ZIF-8 are a viable strategy for a wide variety of proteins making this a highly amenable method for many different protein surfaces.

6.6   References

1.   Liang, K.; Carbonell, C.; Styles, M. J.; Ricco, R.; Cui, J.; Richardson, J. J.; Maspoch, D.; Caruso, F.; Falcaro, P. Biomimetic Replication of Microscopic Metal–Organic Framework Patterns Using Printed Protein Patterns. *Adv. Mater*. **2015**, 27, 7293-7298.

2.   Li, P.; Moon, S.-Y.; Guelta, M. A.; Harvey, S. P.; Hupp, J. T.; Farha, O. K. Encapsulation of a Nerve Agent Detoxifying Enzyme by a Mesoporous Zirconium Metal–Organic Framework Engenders Thermal and Long-Term Stability. *J. Am. Chem. Soc.* **2016**, *138*, 8052-8055.

3.   Li, S.; Dharmarwardana, M.; Welch, R. P.; Ren, Y.; Thompson, C. M.; Smaldone, R. A.; Gassensmith, J. J. Template-Directed Synthesis of Porous and Protective Core–Shell Bionanoparticles. Angew. *Chem., Int. Ed*. **2016**, *55*, 10691–10696.

4.   Doonan, C.; Riccò, R.; Liang, K.; Bradshaw, D.; Falcaro, P. Metal–Organic Frameworks at the Biointerface: Synthetic Strategies and Applications. *Acc. Chem. Res.* **2017**, 50, 1423-1432.

5.   Lian, X.; Fang, Y.; Joseph, E.; Wang, Q.; Li, J.; Banerjee, S.; Lollar, C.; Wang, X.; Zhou, H.-C. Enzyme-MOF (metal-organic framework) composites. *Chem. Soc. Rev*. **2017**, *46*, 3386-3401.

6.   Majewski, M. B.; Howarth, A. J.; Li, P.; Wasielewski, M. R.; Hupp, J. T.; Farha, O. K. Enzyme encapsulation in metal-organic frameworks for applications in catalysis. *CrystEngComm* **2017**, *19*, 4082-4091.

7.   Riccò, R.; Liang, W.; Li, S.; Gassensmith, J. J.; Caruso, F.; Doonan, C.; Falcaro, P. Metal–Organic Frameworks for Cell and Virus Biology: A Perspective. *ACS Nano* **2018**, *12*, 13-23.

8.   Yaghi, O. M.; O'Keeffe, M.; Ockwig, N. W.; Chae, H. K.; Eddaoudi, M.; Kim, J. Reticular synthesis and the design of new materials. *Nature* **2003**, *423*, 705.

9.   Park, K. S.; Ni, Z.; Côté, A. P.; Choi, J. Y.; Huang, R.; Uribe-Romo, F. J.; Chae, H. K.; O'Keeffe, M.; Yaghi, O. M. Exceptional chemical and thermal stability of zeolitic imidazolate frameworks. *Proc. Natl. Acad. Sci. U. S. A*. **2006**, *103*, 10186-10191.

10.   Furukawa, H.; Cordova, K. E.; O'Keeffe, M.; Yaghi, O. M. The Chemistry and Applications of Metal-Organic Frameworks. *Science* **2013**, *341*, 1230444.

11.   Abánades Lázaro, I.; Haddad, S.; Sacca, S.; Orellana-Tavra, C.; Fairen-Jimenez, D.; Forgan, R. S. Selective Surface PEGylation of UiO-66 Nanoparticles for Enhanced Stability, Cell Uptake, and pH-Responsive Drug Delivery. *Chem* **2017**, *2*, 561-578.

12.   Li, Q.; Zhang, W.; Miljanić, O. Š.; Sue, C.-H.; Zhao, Y.-L.; Liu, L.; Knobler, C. B.; Stoddart, J. F.; Yaghi, O. M. Docking in Metal-Organic Frameworks. *Science* **2009**, 325, 855.

13.   Karagiaridi, O.; Lalonde, M. B.; Bury, W.; Sarjeant, A. A.; Farha, O. K.; Hupp, J. T. Opening ZIF-8: A Catalytically Active Zeolitic Imidazolate Framework of Sodalite Topology with Unsubstituted Linkers. *J. Am. Chem. Soc*. **2012**, *134*, 18790-18796.

14.   Lu, G.; Farha, O. K.; Zhang, W.; Huo, F.; Hupp, J. T. Engineering ZIF-8 Thin Films for Hybrid MOF-Based Devices. *Adv. Mater*. **2012**, *24*, 3970-3974.

15.   Gándara, F.; Furukawa, H.; Lee, S.; Yaghi, O. M. High Methane Storage Capacity in Aluminum Metal–Organic Frameworks. *J. Am. Chem. Soc.* **2014**, *136*, 5271-5274.

16.   He, C.; Lu, K.; Lin, W. Nanoscale Metal–Organic Frameworks for Real-Time Intracellular pH Sensing in Live Cells. *J. Am. Chem. Soc.* **2014**, *136*, 12253-12256.

17.   Kornienko, N.; Zhao, Y.; Kley, C. S.; Zhu, C.; Kim, D.; Lin, S.; Chang, C. J.; Yaghi, O. M.; Yang, P. Metal–Organic Frameworks for Electrocatalytic Reduction of Carbon Dioxide. *J. Am. Chem. Soc*. **2015**, *137*, 14129-14135.

18.   Marshall, R. J.; Griffin, S. L.; Wilson, C.; Forgan, R. S. Single-Crystal to Single-Crystal Mechanical Contraction of Metal–Organic Frameworks through Stereoselective Postsynthetic Bromination. *J. Am. Chem. Soc.* **2015**, *137*, 9527-9530.

19.   McGuirk, C. M.; Katz, M. J.; Stern, C. L.; Sarjeant, A. A.; Hupp, J. T.; Farha, O. K.; Mirkin, C. A. Turning on Catalysis: Incorporation of a Hydrogen-Bond-Donating Squaramide Moiety into a Zr Metal–Organic Framework. *J. Am. Chem. Soc*. **2015**, 137, 919-925.

20. Mondloch, J. E.; Katz, M. J.; Isley Iii, W. C.; Ghosh, P.; Liao, P.; Bury, W.; Wagner, G. W.; Hall, M. G.; DeCoste, J. B.; Peterson, G. W.; Snurr, R. Q.; Cramer, C. J.; Hupp, J. T.; Farha, O. K. Destruction of chemical warfare agents using metal–organic frameworks. *Nat. Mater.* **2015**, *14*, 512.

21. Orellana-Tavra, C.; Marshall, R. J.; Baxter, E. F.; Lazaro, I. A.; Tao, A.; Cheetham, A. K.; Forgan, R. S.; Fairen-Jimenez, D. Drug delivery and controlled release from biocompatible metal-organic frameworks using mechanical amorphization. *J. Mater. Chem. B* **2016**, *4*, 7697-7707.

22. Lim, J.; Lee, E. J.; Choi, J. S.; Jeong, N. C., Diffusion Control in the in-Situ Synthesis of Iconic Metal–Organic Frameworks within an Ionic Polymer Matrix. *ACS Appl. Mater. Interfaces* **2018**, *10*, 3793-3800.

23. Lykourinou, V.; Chen, Y.; Wang, X.-S.; Meng, L.; Hoang, T.; Ming, L.-J.; Musselman, R. L.; Ma, S. Immobilization of MP-11 into a Mesoporous Metal−Organic Framework, MP-11@mesoMOF: A New Platform for Enzymatic Catalysis. *J. Am. Chem. Soc.* **2011**, *133*, 10382−10385.

24. Lyu, F.; Zhang, Y.; Zare, R. N.; Ge, J.; Liu, Z. One-Pot Synthesis of Protein-Embedded Metal−Organic Frameworks with Enhanced Biological Activities. *Nano Lett.* **2014**, *14*, 5761−5765.

25. Chulkaivalsucharit, P.; Wu, X.; Ge, J. Synthesis of enzyme-embedded metal-organic framework nanocrystals in reverse micelles. *RSC Adv.* **2015**, *5*, 101293-101296.

26. Liang, K.; Ricco, R.; Doherty, C. M.; Styles, M. J.; Bell, S.; Kirby, N.; Mudie, S.; Haylock, D.; Hill, A. J.; Doonan, C. J.; Falcaro, P. Biomimetic Mineralization of Metal-Organic Frameworks as Protective Coatings for Biomacromolecules. *Nat. Commun.* **2015**, *6*, 7240.

27. Shieh, F.-K.; Wang, S.-C.; Yen, C.-I.; Wu, C.-C.; Dutta, S.; Chou, L.-Y.; Morabito, J. V.; Hu, P.; Hsu, M.-H.; Wu, K. C. W.; Tsung, C.-K. Imparting Functionality to Biocatalysts via Embedding Enzymes into Nanoporous Materials by a de Novo Approach: Size-Selective Sheltering of Catalase in Metal–Organic Framework Microcrystals. *J. Am. Chem. Soc.* **2015**, *137*, 4276-4279.

28. Wu, X.; Ge, J.; Yang, C.; Hou, M.; Liu, Z. Facile synthesis of multiple enzyme-containing metal-organic frameworks in a biomolecule-friendly environment. *Chem. Commun.* **2015**, *51*, 13408-13411.

29. Wu, X.; Hou, M.; Ge, J. Metal-organic frameworks and inorganic nanoflowers: a type of emerging inorganic crystal nanocarrier for enzyme immobilization. *Catal. Sci. Technol.* **2015**, *5*, 5077-5085.

30. Wu, X.; Yang, C.; Ge, J.; Liu, Z. Polydopamine tethered enzyme/metal-organic framework composites with high stability and reusability. *Nanoscale* **2015**, *7*, 18883-18886.

31. Li, P.; Modica, Justin A.; Howarth, Ashlee J.; Vargas L, E.; Moghadam, Peyman Z.; Snurr, Randall Q.; Mrksich, M.; Hupp, Joseph T.; Farha, Omar K. Toward Design Rules for Enzyme Immobilization in Hierarchical Mesoporous Metal-Organic Frameworks. *Chem* **2016**, *1*, 154-169.

32. Liang, K.; Coghlan, C. J.; Bell, S. G.; Doonan, C.; Falcaro, P., Enzyme encapsulation in zeolitic imidazolate frameworks: a comparison between controlled co-precipitation and biomimetic mineralisation. *Chem. Commun*. **2016**, *52*, 473-476.

33. Cui, J.; Feng, Y.; Lin, T.; Tan, Z.; Zhong, C.; Jia, S. Mesoporous Metal–Organic Framework with Well-Defined Cruciate Flower-Like Morphology for Enzyme Immobilization. *ACS Appl. Mater. Interfaces*, **2017**, *9*, 10587-10594.

34. Hou, M.; Zhao, H.; Feng, Y.; Ge, J. Synthesis of patterned enzyme–metal–organic framework composites by ink-jet printing. *Bioresour Bioprocess*. **2017**, *4*, 40.

35. Wang, Q.; Zhang, X.; Huang, L.; Zhang, Z.; Dong, S. GOx@ZIF-8(NiPd) Nanoflower: An Artificial Enzyme System for Tandem Catalysis. *Angew.Chem. Int. Ed*. **2017**, *56*,16082 – 16085.

36. Wu, X.; Yang, C.; Ge, J., Green synthesis of enzyme/metal-organic framework composites with high stability in protein denaturing solvents. *Bioresour Bioprocess*. **2017**, *4*, 24.

37. Zhang, C.; Wang, X.; Hou, M.; Li, X.; Wu, X.; Ge, J. Immobilization on Metal–Organic Framework Engenders High Sensitivity for Enzymatic Electrochemical Detection. *ACS Appl. Mater. Interfaces*, **2017**, *9*, 13831-13836.

38. Liang, W.; Ricco, R.; Maddigan, N. K.; Dickinson, R. P.; Xu, H.; Li, Q.; Sumby, C. J.; Bell, S. G.; Falcaro, P.; Doonan, C. J., Control of Structure Topology and Spatial Distribution of Biomacromolecules in Protein@ZIF-8 Biocomposites. *Chem. Mater*. **2018**, *30*, 1069-1077.

39. Liang, K.; Richardson, J. J.; Cui, J.; Caruso, F.; Doonan, C. J.; Falcaro, P. Metal–Organic Framework Coatings as Cytoprotective Exoskeletons for Living Cells. *Adv. Mater*. **2016**, *28*, 7910-7914.

40. Liang, K.; Richardson, J. J.; Doonan, C. J.; Mulet, X.; Ju, Y.; Cui, J.; Caruso, F.; Falcaro, P. An Enzyme-Coated Metal–Organic Framework Shell for Synthetically Adaptive Cell Survival. *Angew.Chem. Int.Ed*. **2017**, *56*, 8510-8515.

41. DiCosimo, R.; McAuliffe, J.; Poulose, A. J.; Bohlmann, G. Industrial use of immobilized enzymes. *Chem. Soc. Rev*. **2013**, *42*, 6437-6474.

42. Liese, A.; Hilterhaus, L. Evaluation of immobilized enzymes for industrial applications. *Chem. Soc. Rev*. **2013**, *42*, 6236-6249.

43. Min, K.; Yoo, Y. J. Recent progress in nanobiocatalysis for enzyme immobilization and its application. *Bioresour Bioprocess*. *2014*, *19*, 553-567.

44. Hou, M.; Ge, J. Chaper Three-Armoring Enzymes by Metal–Organic Frameworks by the Coprecipitation Method. In Methods in Enzymology, Kumar, C. V., Ed. Academic Press; 2017; Vol. 590, pp 59-75.

45. Shenton, W.; Douglas, T.; Young, M.; Stubbs, G.; Mann, S. Inorganic–Organic Nanotube Composites from Template Mineralization of Tobacco Mosaic Virus. *Adv. Mater*. **1999**, *11*, 253-256.

46. Schlick, T. L.; Ding, Z.; Kovacs, E. W.; Francis, M. B., Dual-Surface Modification of the Tobacco Mosaic Virus. *J. Am. Chem. Soc*. **2005**, *127*, 3718-3723.

47. Niu, Z.; Liu, J.; Lee, L. A.; Bruckman, M. A.; Zhao, D.; Koley, G.; Wang, Q. Biological Templated Synthesis of Water-Soluble Conductive Polymeric Nanowires. *Nano Lett*. **2007**, *7*, 3729-3733.

48. Chen, Z.; Li, N.; Li, S.; Dharmarwardana, M.; Schlimme, A.; Gassensmith, J. J. Viral chemistry: the chemical functionalization of viral architectures to create new technology. *Wiley Interdiscip. Rev. Nanomed. Nanobiotechnol*. **2016**, *8*, 512-534.

49. Furukawa, H.; Müller, U.; Yaghi, O. M. "Heterogeneity within Order" in Metal–Organic Frameworks. *Angew. Chem. Int. Ed*. **2015**, *54*, 3417-3430.

50. Ji, H.; Hwang, S.; Kim, K.; Kim, C.; Jeong, N. C. Direct in Situ Conversion of Metals into Metal–Organic Frameworks: A Strategy for the Rapid Growth of MOF Films on Metal Substrates. *ACS Appl. Mater. Interfaces*. **2016**, *8*, 32414-32420.

51. Li, G.; Sun, H.; Xu, H.; Guo, X.; Wu, D. Probing the Energetics of Molecule–Material Interactions at Interfaces and in Nanopores. J. Phys. Chem. C. 2017, 121, 26141-26154.

52. Chen, Z.; Li, N.; Chen, L.; Lee, J.; Gassensmith, J. J. Dual Functionalized Bacteriophage Qβ as a Photocaged Drug Carrier. *Small* **2016**, *12*, 4563-4571.

53. Chen, Z.; Boyd, S. D.; Calvo, J. S.; Murray, K. W.; Mejia, G. L.; Benjamin, C. E.; Welch, R. P.; Winkler, D. D.; Meloni, G.; D'Arcy, S.; Gassensmith, J. J. Fluorescent Functionalization across Quaternary Structure in a Virus-like Particle. *Bioconjugate Chem. 2017*, **28**, 2277-2283.

54. Atabekov, J.; Nikitin, N.; Arkhipenko, M.; Chirkov, S.; Karpova, O. Thermal Transition of Native Tobacco Mosaic Virus and RNA-free Viral Proteins into Spherical Nanoparticles. *J. Gen. Virol*. **2011**, *92*, 453-456.

55. Mueller, A.; Eber, F. J.; Azucena, C.; Petershans, A.; Bittner, A. M.; Gliemann, H.; Jeske, H.; Wege, C. Inducible Site-Selective Bottom-Up Assembly of Virus-Derived Nanotube Arrays on RNA-Equipped Wafers. *ACS Nano* **2011**, *5*, 4512-4520.

56. Eber, F. J.; Eiben, S.; Jeske, H.; Wege, C. Bottom-Up-Assembled Nanostar Colloids of Gold Cores and Tubes Derived from Tobacco Mosaic Virus. *Angew. Chem. Int. Ed*. **2013**, *52*, 7203-7207.

57. Joo, Y.-H.; Gao, H.; Zhang, Y.; Shreeve, J. n. M. Inorganic or Organic Azide-Containing Hypergolic Ionic Liquids As poster published in 1st Korean International Symposium on High Energy Materials, Incheon, Korea, October 6−9, 2009. *Inorg. Chem.* **2010**, *49*, 3282-3288.

58. Chen, Z.; Li, N.; Chen, L.; Lee, J.; Gassensmith, J. J. Dual Functionalized Bacteriophage Qβ as a Photocaged Drug Carrier. *Small* **2016**, *12*, 4563-4571.

59. Li, S.; Dharmarwardana, M.; Welch, R. P.; Ren, Y.; Thompson, C. M.; Smaldone, R. A.; Gassensmith, J. J., Template-Directed Synthesis of Porous and Protective Core–Shell Bionanoparticles. *Angew. Chem., Int. Ed.* **2016**, *55*, 10691–10696.

60. Ng, D. Y. W.; Fahrer, J.; Wu, Y.; Eisele, K.; Kuan, S. L.; Barth, H.; Weil, T. Efficient Delivery of p53 and Cytochrome C by Supramolecular Assembly of a Dendritic Multi-Domain Delivery System. *Adv. Healthcare Mater*. **2013**, *2*, 1620-1629.

61. Nichols, A. J.; Roussakis, E.; Klein, O. J.; Evans, C. L. Click-Assembled, Oxygen-Sensing Nanoconjugates for Depth-Resolved, Near-Infrared Imaging in a 3 D Cancer Model. *Angew. Chem., Int. Ed*. **2014**, *53*, 3671-3674.

62. Yu, C.; Qian, L.; Ge, J.; Fu, J.; Yuan, P.; Yao, S. C. L.; Yao, S. Q. Cell-Penetrating Poly(disulfide) Assisted Intracellular Delivery of Mesoporous Silica Nanoparticles for Inhibition of miR-21 Function and Detection of Subsequent Therapeutic Effects. *Angew. Chem., Int. Ed*. **2016**, *55*, 9272-9276.

63. Hu, H.; Zhang, Y.; Shukla, S.; Gu, Y.; Yu, X.; Steinmetz, N. F. Dysprosium-Modified Tobacco Mosaic Virus Nanoparticles for Ultra-High-Field Magnetic Resonance and Near-Infrared Fluorescence Imaging of Prostate Cancer. *ACS Nano* **2017**, *11*, 9249-9258.

64. Bruckman, M. A.; Steinmetz, N. F. In Virus Hybrids as Nanomaterials: Methods and Protocols, Lin, B.; Ratna, B., Eds.; Humana Press: Totowa, NJ, 2014; Chapter 13, pp 173-185.

65. Bruckman, M. A.; Randolph, L. N.; VanMeter, A.; Hern, S.; Shoffstall, A. J.; Taurog, R. E.; Steinmetz, N. F. Biodistribution, pharmacokinetics, and blood compatibility of native and PEGylated tobacco mosaic virus nano-rods and -spheres in mice. *Virology* **2014**, *449*, 163-173.

66. Veronese, F. M.; Mero, A. The Impact of PEGylation on Biological Therapies. *BioDrugs* **2008**, *22*, 315-329.

67. Steinmetz, N. F.; Manchester, M. PEGylated Viral Nanoparticles for Biomedicine: The Impact of PEG Chain Length on VNP Cell Interactions In Vitro and Ex Vivo. *Biomacromolecules* **2009**, *10*, 784-792.

68. Cravillon, J.; Nayuk, R.; Springer, S.; Feldhoff, A.; Huber, K.; Wiebcke, M. Controlling Zeolitic Imidazolate Framework Nano- and Microcrystal Formation: Insight into Crystal Growth by Time-Resolved in Situ Static Light Scattering. *Chem. Mater*. **2011**, *23*, 2130-2141.

69. Tang, N.; Skibsted, L. H. Zinc Bioavailability from Whey. Enthalpy-Entropy Compensation in Protein Binding. *Food Res. Int*. **2016**, *89*, 749-755.

CHAPTER 7

SUMMARY OF FINDING AND DIRECTIONS FOR FUTURE STUDIES

7.1   Summary of Findings

Smart materials, also known as stimuli-responsive materials, are fascinating and an emerging research area of scientific interest. Thermo-responsive materials are one of the mostly studied area of smart materials. While there was an enormous interest for thermo-responsive polymeric systems in the past, thermo-responsive molecular crystals are increasingly become popular owing to their interesting properties, however, there are very few class of thermo-responsive molecular crystals are reported. Redox-responsive materials are another emerging class of smart materials that have found many applications in biological systems. Up to date, polymeric systems have been manly used as functional backbone for redox moieties for designing redox responsive materials. Introduction of dual functionality to the polymeric systems can be challenging due to the synthetic limitations. Thus, it is important to introduce novel functional scaffolds for engineering smart materials with improved properties.

This dissertation has described the engineering of several emerging classes of smart materials for industrial and biological applications. The main scope of this work is to introduce some novel classes of smart materials that are not polymer-based materials. Chapters 2-4 presents the fabrication and properties of thermo-responsive alkoxyphenyl naphthalene diimides. These emerging class of materials exhibits several interesting properties including thermochromism, thermo-mechanical and colossal anisotropic thermal expansion. Furthermore, thermo-mechanical properties of BNDI molecular crystals can be used to lift metal ball ~100 times heavier than the crystal itself. The thermochromic behavior of alkoxyphenyl naphthalene diimides is not limited to

the single crystalline state but has also been demonstrated when incorporated to polymeric systems. Furthermore, this dissertation also describes the use of non-synthetic polymeric scaffold for conjugating redox responsive moieties for in vivo ROS sensing applications. Biological macromolecules such as viral nanoparticles provide several advantages over polymeric systems as a functional scaffold including monodispersity, multivalency and ease of fabrication. The synthesized redox responsive organic radical contrast agent conjugated TMV has shown very good proton relaxivity properties as well ability of detection of ROS *in vitro*. Our group has demonstrated that TMV can act as a template for ZIF-8 growth resulting core shell bio nanoparticles (CSBNs). Additionally, in chapter 6 we investigate the responsiveness for formation of CSBNs by TMV when its surface charge is altered.

7.2   Ongoing Research

7.2.1   Thermo-responsive DNDI as an electrical switch

While the thermo-mechanical properties of compounds BNDI-M, ONDI, HNDI and NNDI can be potentially applicable as actuators and sensors, there are a few limitations of these materials. Firstly, irreversible phase transition behaviour allows us to use these single crystals as single use actuators or sensors. Secondly, the working temperatures are quite high making these only applicable for high temperature sensing applications. Thus, single crystals with lower transition temperatures and reversible phase transitions would be ideal for applications such as electrical switches. Single crystals of decoxyphenyl N-substituted naphthalene diimide (DNDI) exhibits reversible phase transition around 43 °C with a clearly visible size change in the crystal. Thus, DNDI will be an ideal candidate to use in temperature sensitive switching applications.
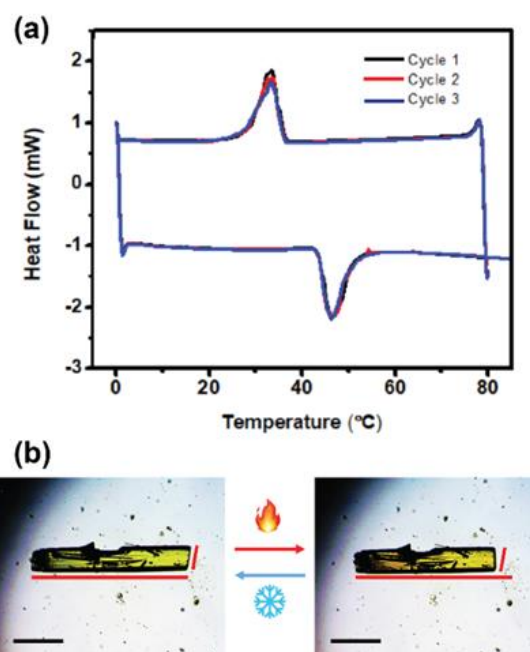
Figure 7.1. Thermo-responsive behaviour of DNDI (a) Thermal profiles of DNDI (b) optical micrographs of before and after the phase transition

7.2.2 *in*TEMPO-TMV as a CEST/MRI bimodal sensor for superoxides
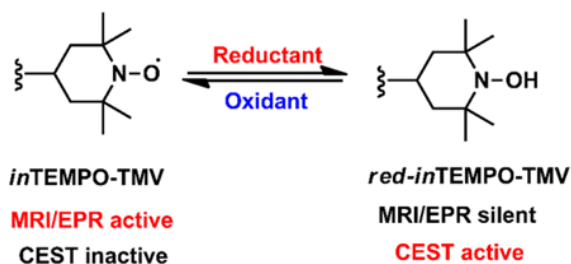
Figure 7.2. inTEMPO-TMV as a bimodal sensing of CEST and MRI/EPR

Our preliminary data shows that reduced inTEMPO-TMV (*red-in*TMEPO-TMV) exhibits CEST

behavior and we also showed that inTEMPO-TMV has very good proton relaxation properties.

We could combine these two behaviors to create bimodal sensor for ROS to be detected by both

CEST and MRI modalities. Additionally, the exterior surface of TMV can be also modified with

near infrared dye (NIR) dye for NIR imaging.

182

7.3　Future Perspectives

Thermo-mechanically responsive organic molecular crystals are bound to play an important role in materials research. These perfectly-ordered and dynamic crystals have potential for fast and efficient conversion of heat energy to mechanical motion, making them useful many applications such as organic electronics, actuators, and soft robotics. More importantly, the remarkable mechanical properties of these molecular crystals will allow scientists to understand the relationship between weak intermolecular interactions and macroscopic responses of molecular crystals when designing novel actuating materials.

Similarly, redox-responsive organic radical contrast agents (ORCAs) will have a greater impact on biomedical imaging research as they are versatile and non-toxic compared to existing, metal-based contrast agents. When ORCAs are incorporated into biological macromolecules such as viral nanoparticles, not only will their contrast properties be enhanced, but they will also be able to be utilized in multimodal imaging such as NIR fluorescence imaging and CEST imaging. Furthermore, the redox behavior of these virus-based ORCA nanoparticles will potentially allow the scientific community to appropriate them as sensors for oxidative stress in diabetic patients.

APPENDIX A

NMR SPECTAR FOR CHAPTER 2
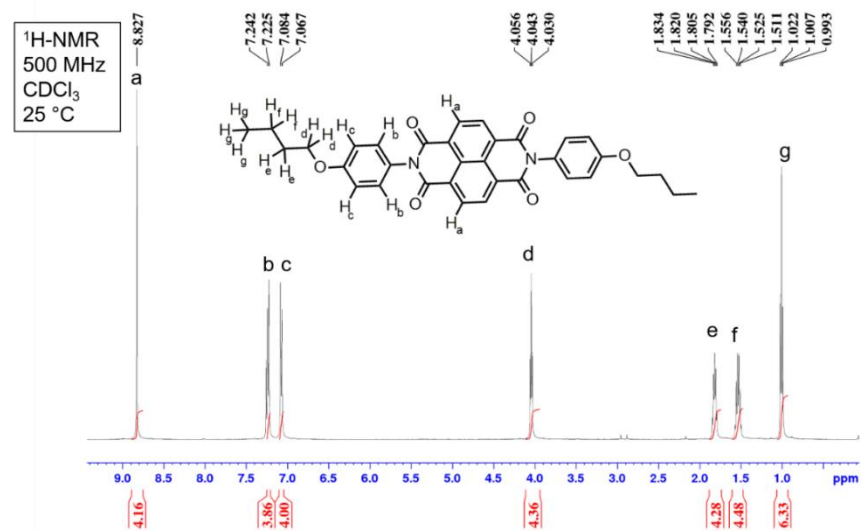
Figure A1. ^{1}H-NMR spectrum of BNDI
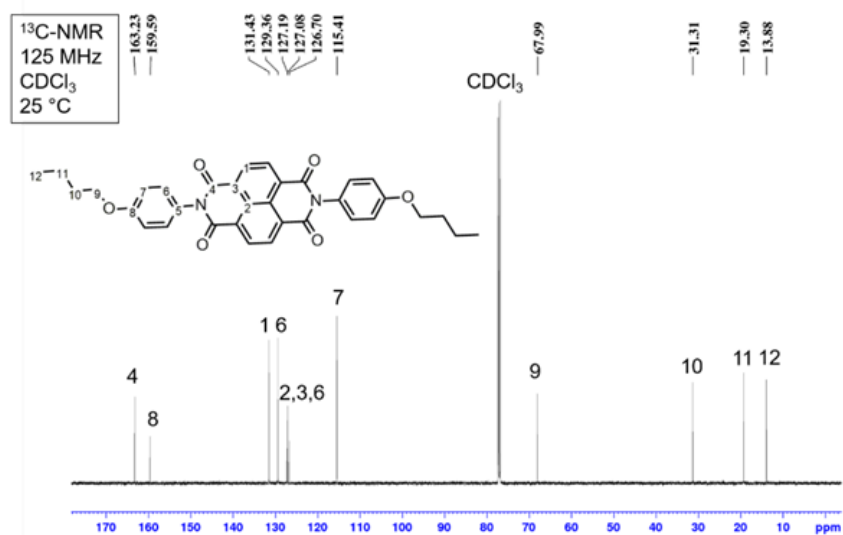
Figure A2. ^{13}C-NMR spectrum of BNDI

NMR AND PXRD SPECTRA FOR CHAPTER 3
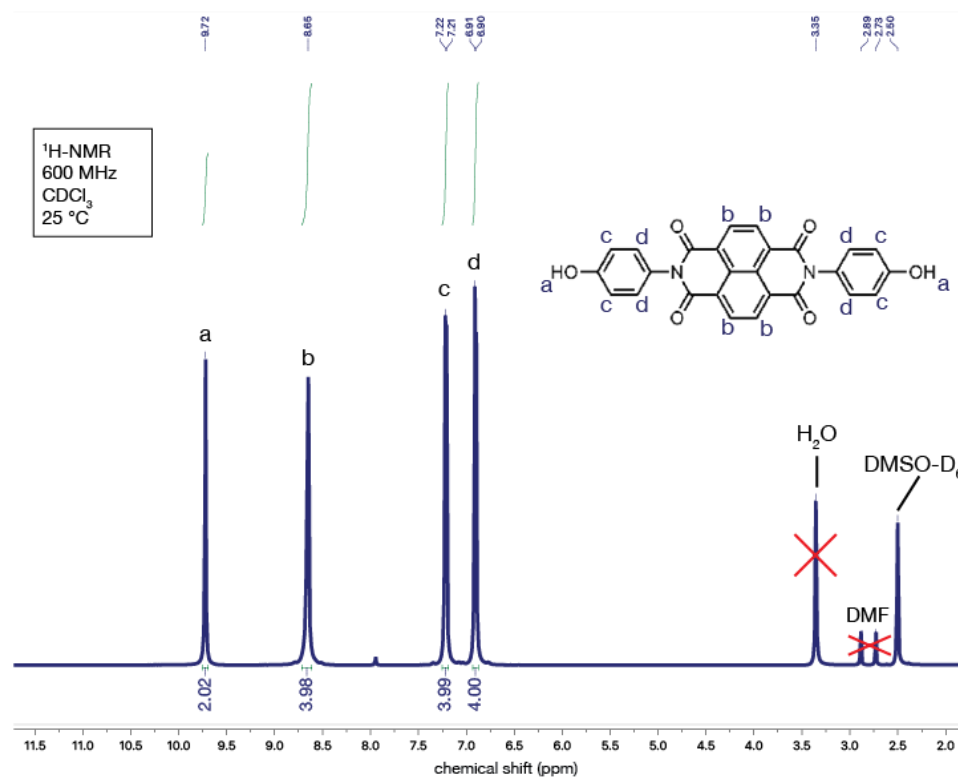
Figure B1. ^{1}H NMR spectrum of NDI-Ph.
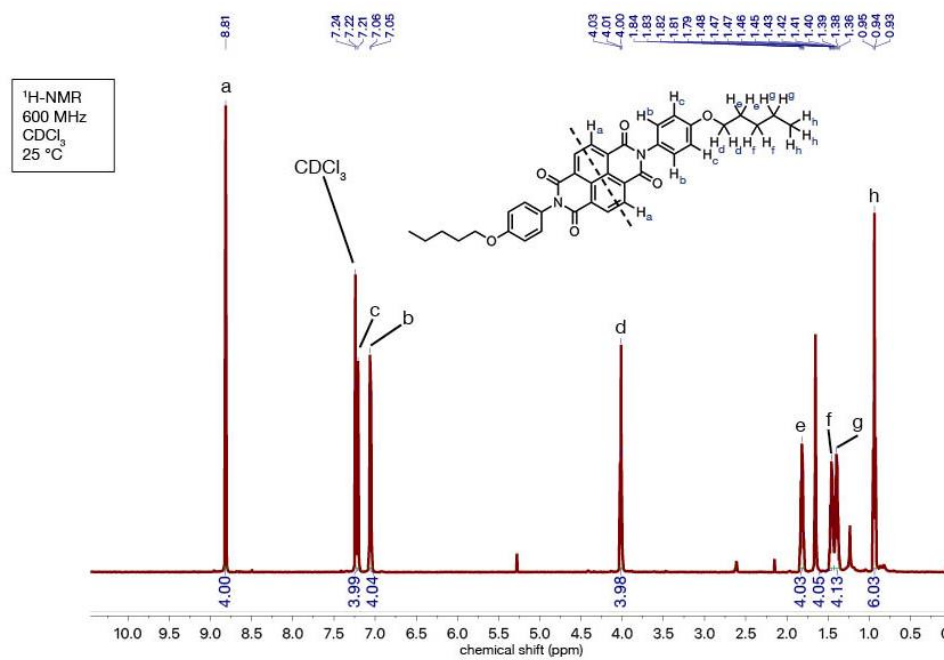
Figure B2. ^{1}H NMR spectrum of PNDI
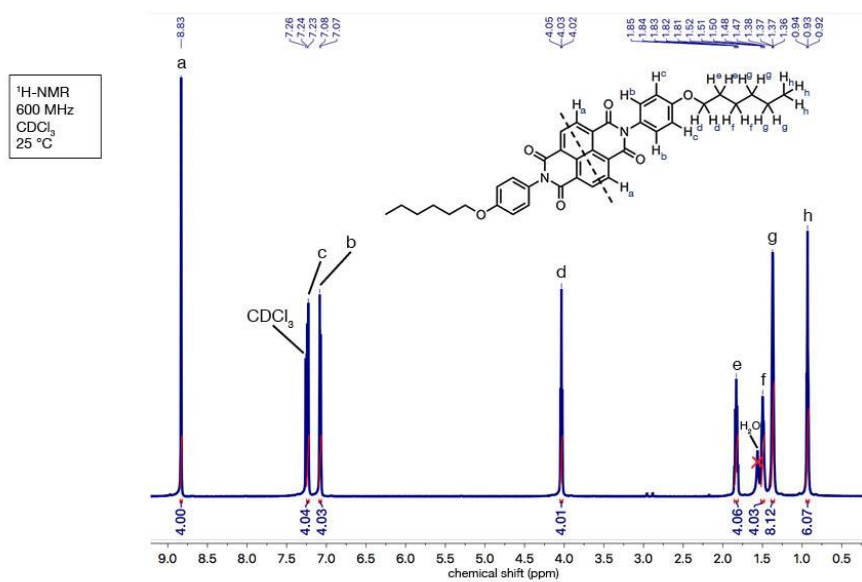
Figure B3. ^{1}H NMR spectrum of HxNDI
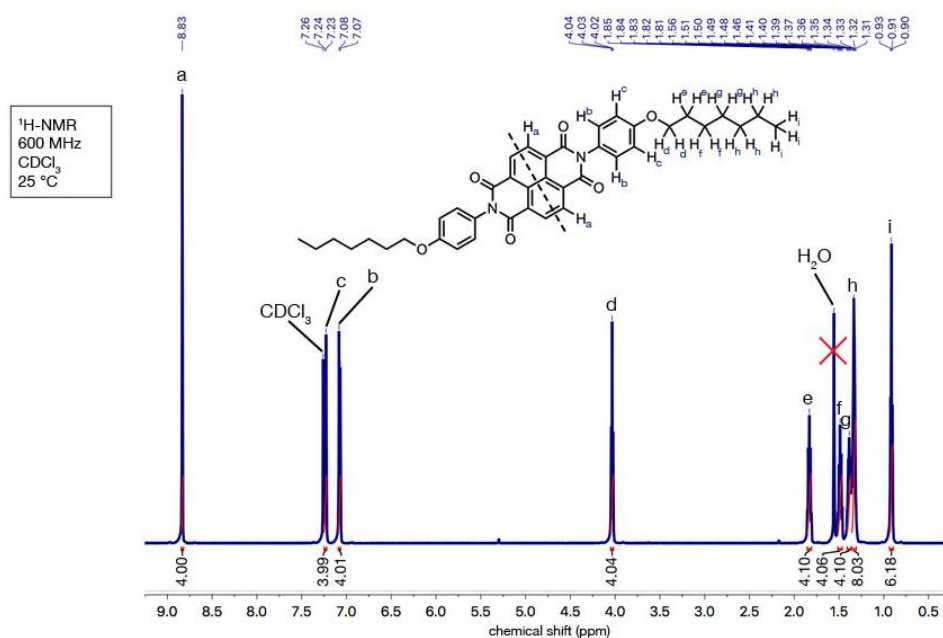
Figure B4. ^{1}H NMR spectrum of HNDI
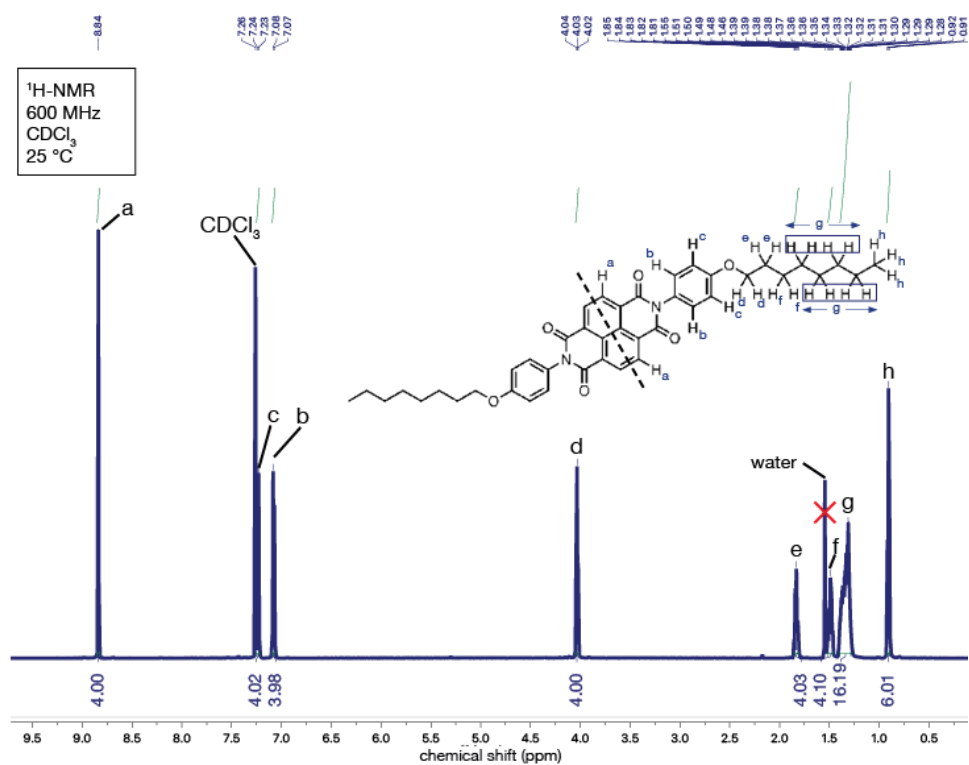
Figure B5. ^{1}H NMR spectrum of ONDI

187
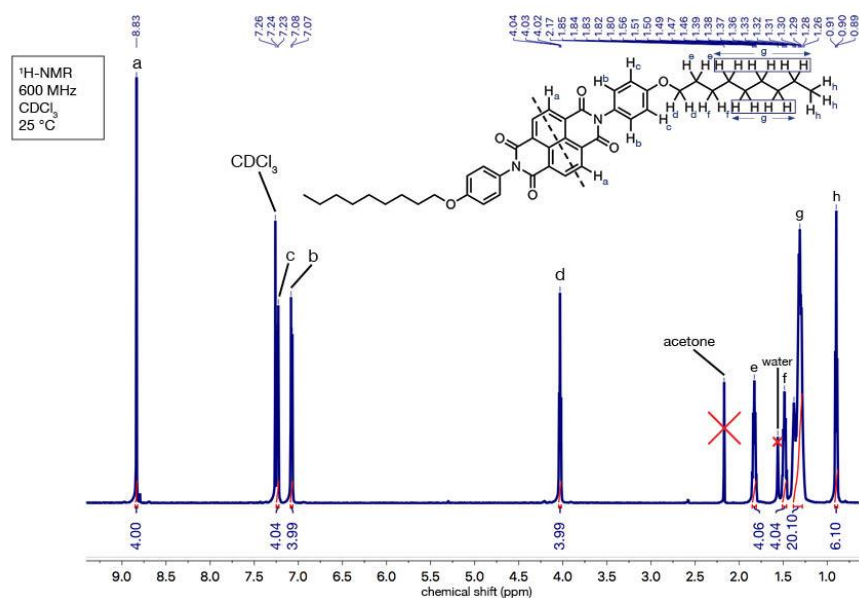
Figure B6. ¹H NMR spectrum of NNDI
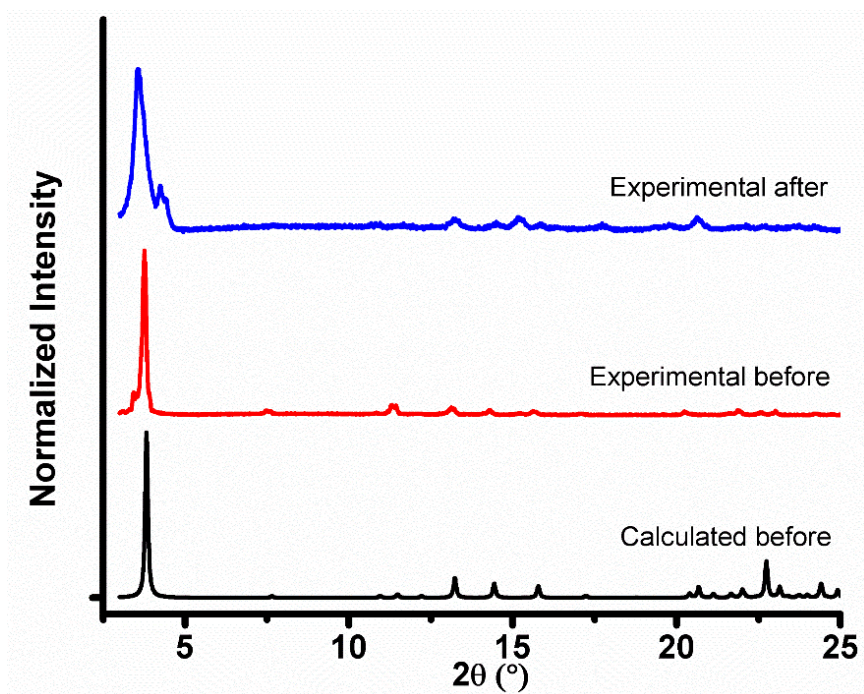
Figure B7. PXRD for HNDI before and after irreversible phase transition
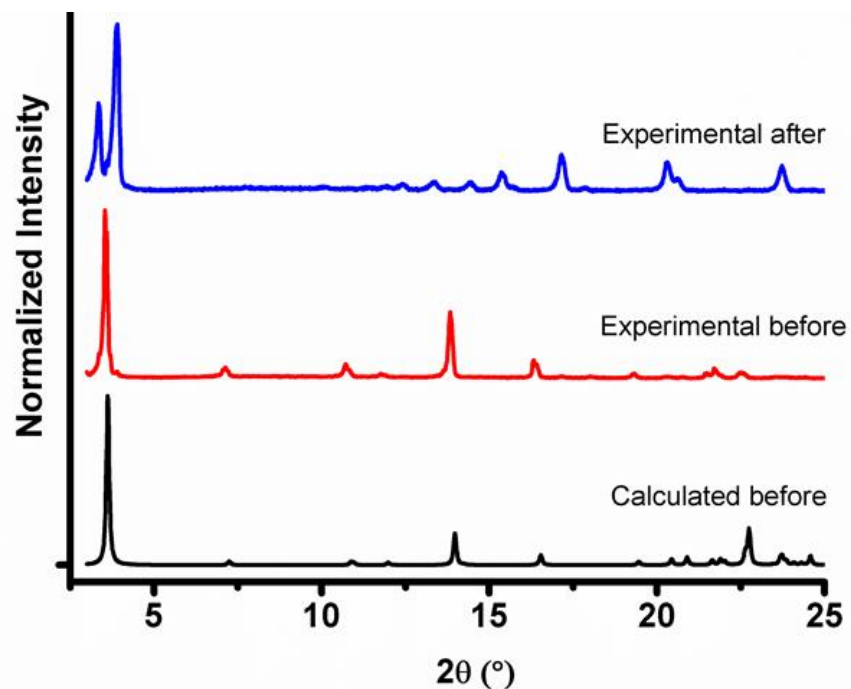
Figure B8. PXRD for ONDI before and after irreversible phase transition
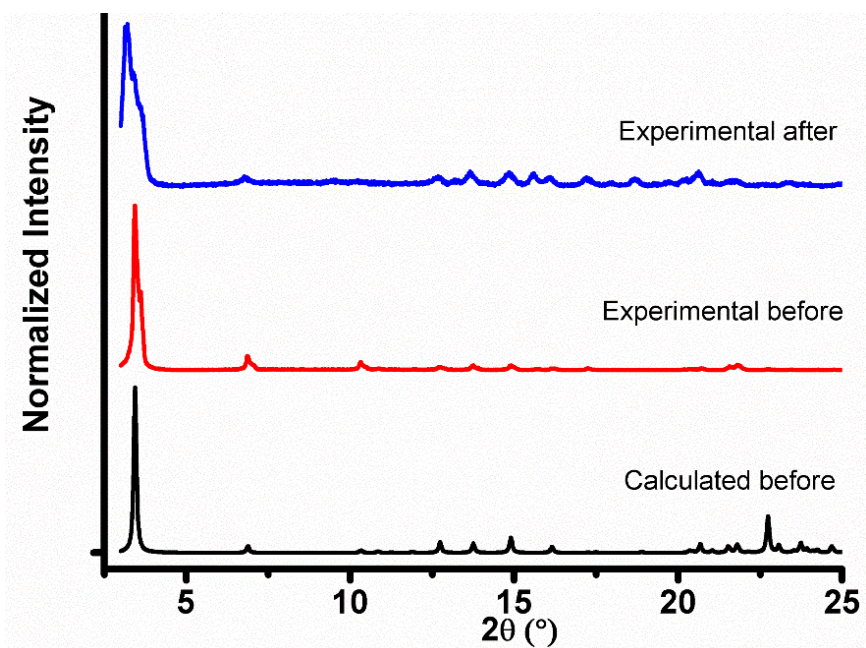
Figure B9. PXRD for NNDI before and after irreversible phase transition

NMR SPECTRA FOR CHAPTER 5
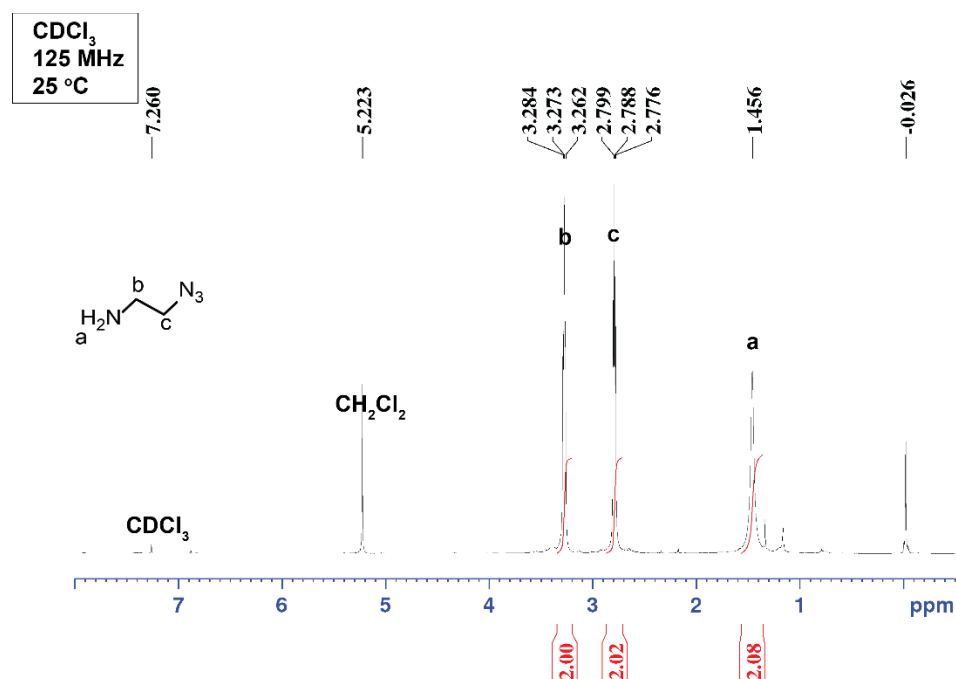
Figure C1. ^{1}H-NMR of 2-azioethylamine
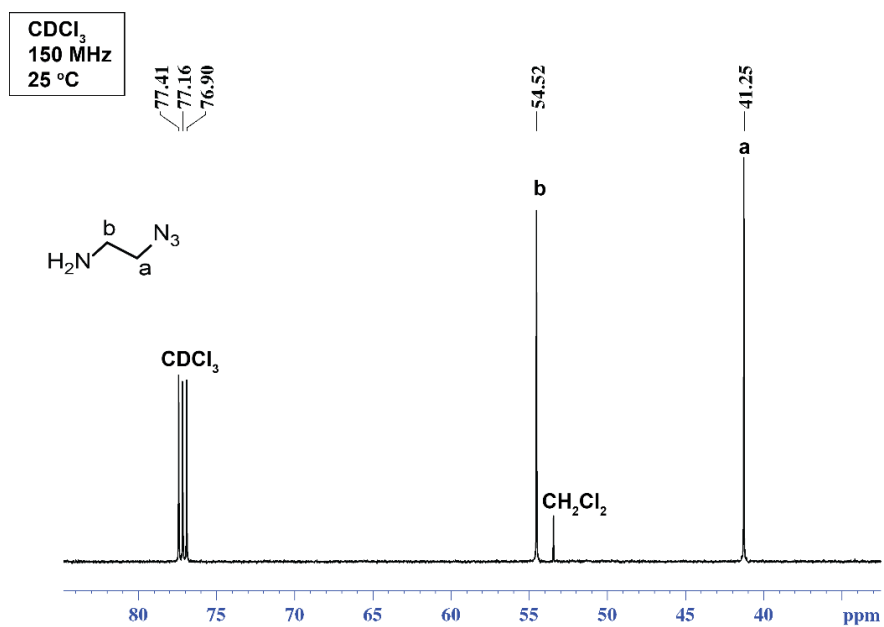
Figure C2. ^{13}C-NMR of 2-azioethylamine
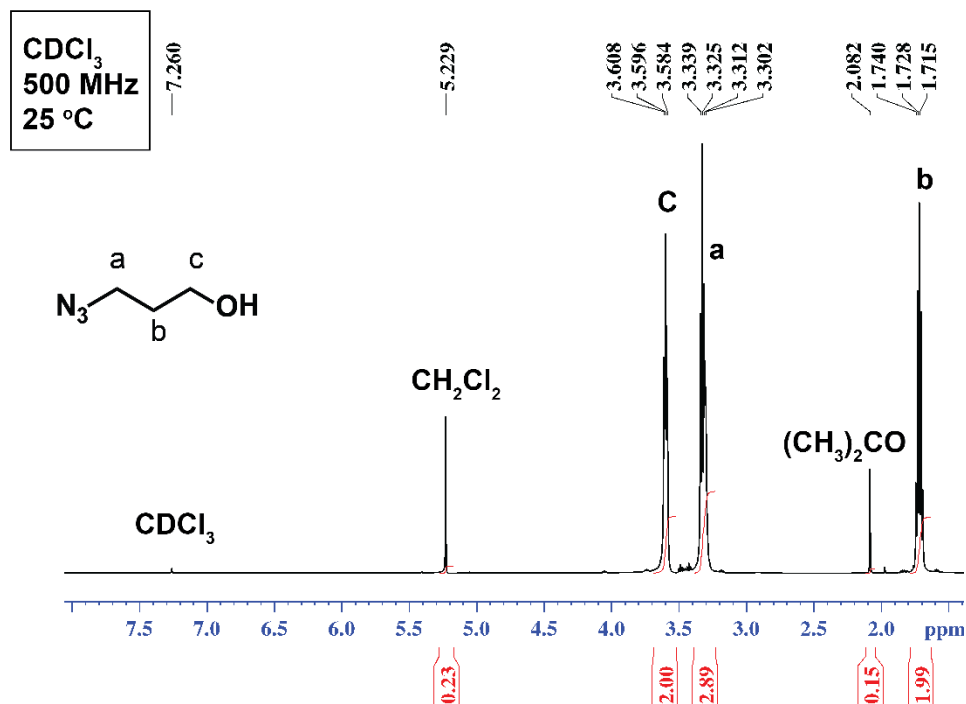
Figure C3. ^{1}H-NMR of 3-azido-1-propanol
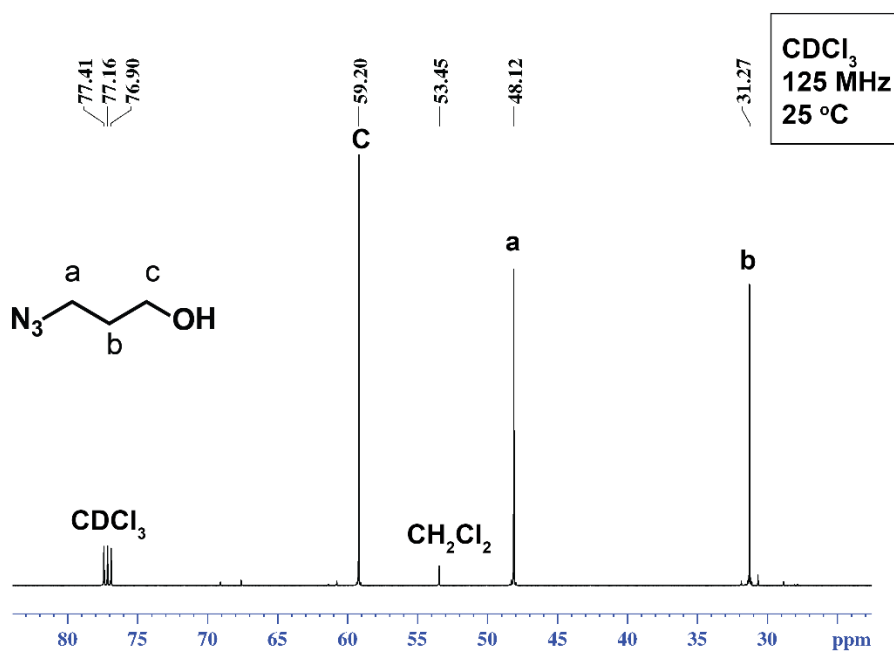
Figure C4. ^{13}C-NMR of 3-azido-1-propanol
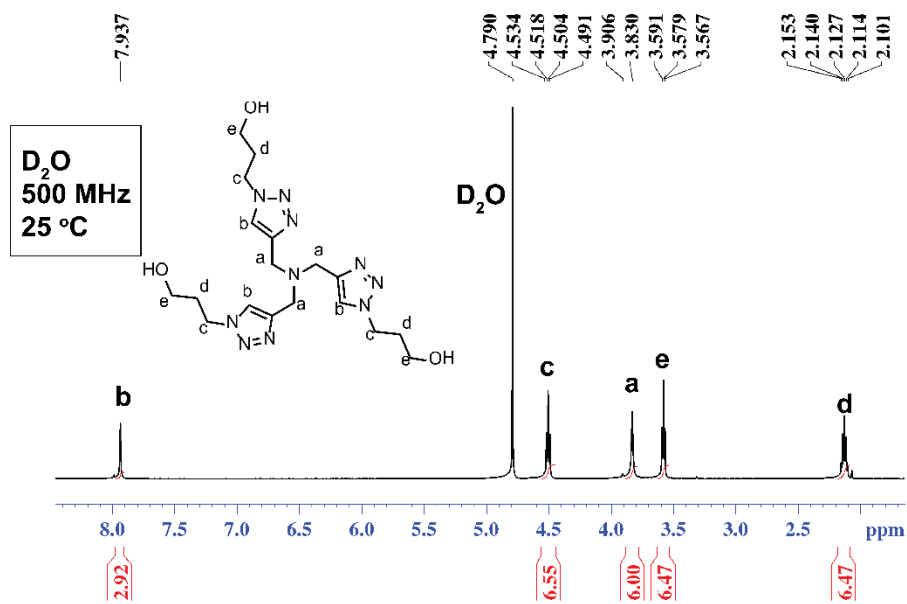
Figure C5. ^{1}H-NMR of THPTA
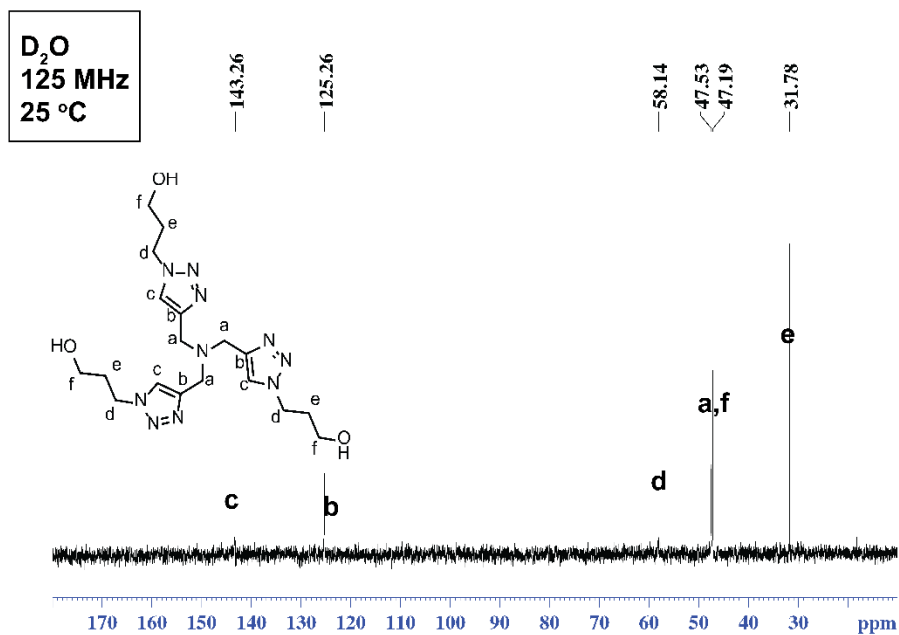
Figure C6. ^{13}C-NMR of THPTA

192
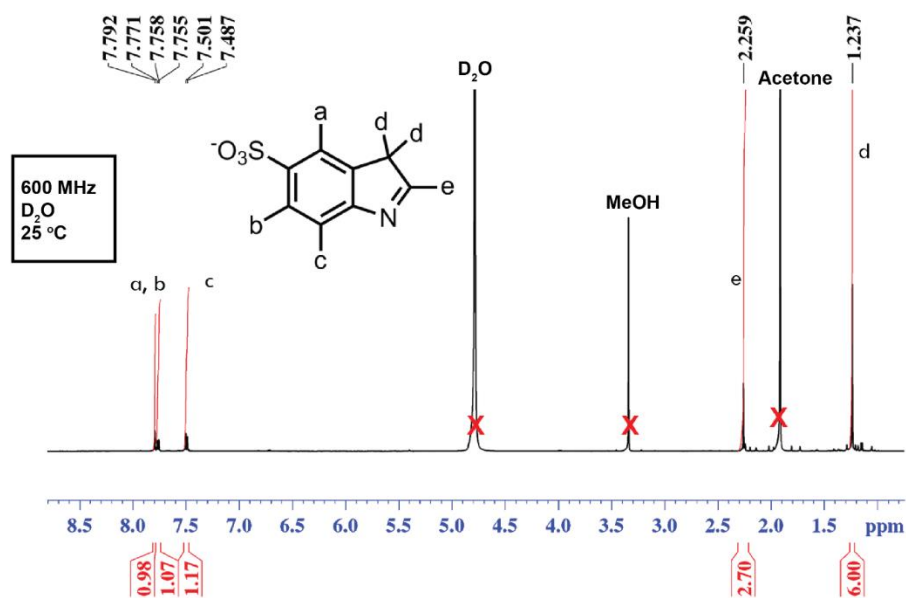
Figure C7. ^{1}H-NMR of 3H-Indole-2,3,3-trimethyl-5-sulfonic Acid, Potassium Salt (**1**)
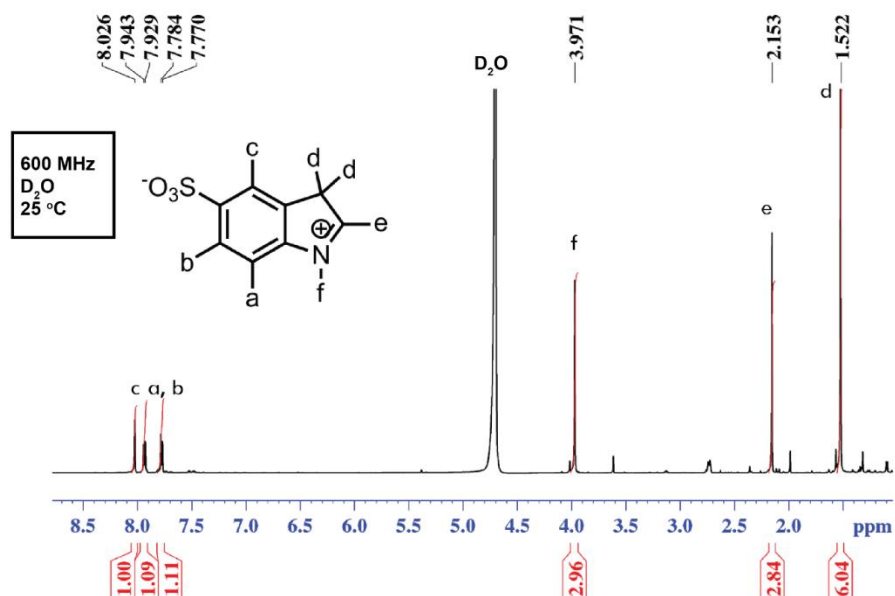
Figure C8. ^{1}H-NMR of 3H-Indolium, 1-Methyl-2,3,3-trimethyl-5-sulfonate (**2**)
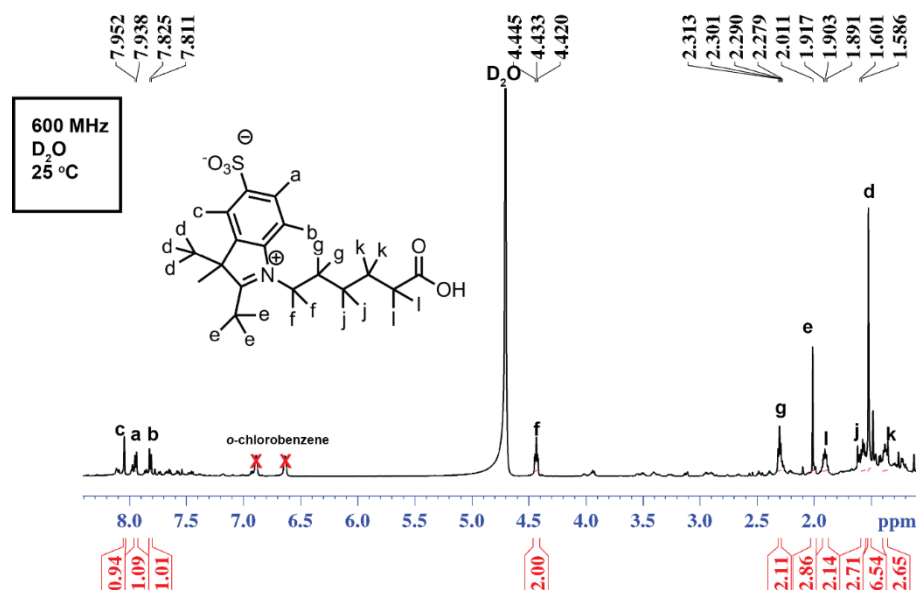
Figure C9. ^{1}H-NMR of 3H-Indolium, 1-(5-Carboxypentyl)-2,3,3-trimethyl-5-sulfonate (**3**)
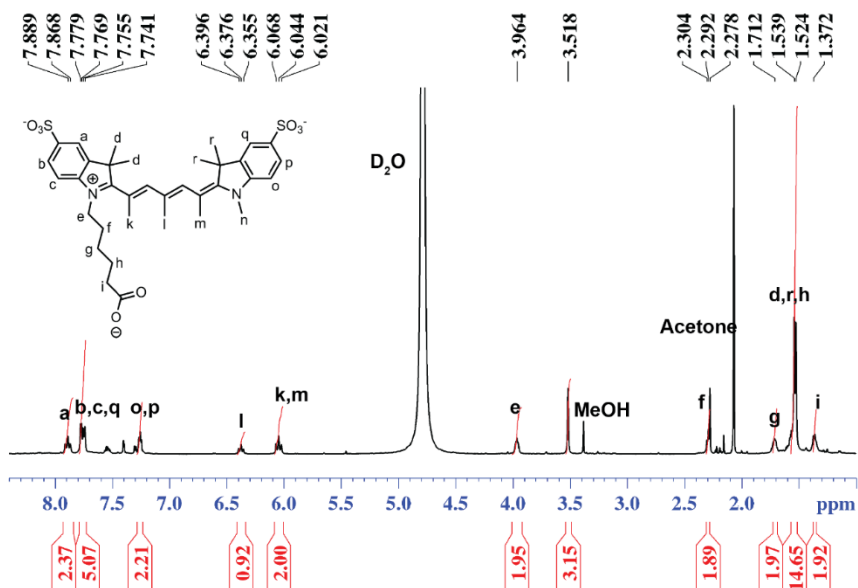
Figure C10. ^{1}H-NMR of 3H-Indolium, 2-[5-[1-(5-Carboxypentyl)-1,3-dihydro-3,3- dimethyl-5-

sulfo-2H-indol-ylidene]-1,3-pentadien-1-yl]-1-methyl-3,3-dimethyl-5-sulfonate (**4**)

194

NMR SPECTRA AND TEM MICROGRAPHS FOR CHAPTER 6
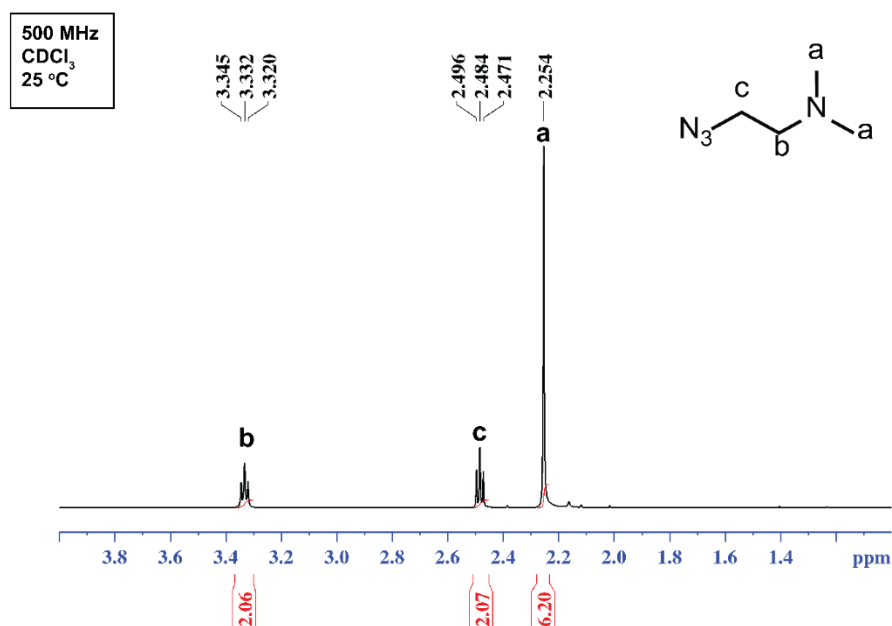
Figure D1. ^{1}H- NMR of 2-azido-N,N-dimethylethylamine
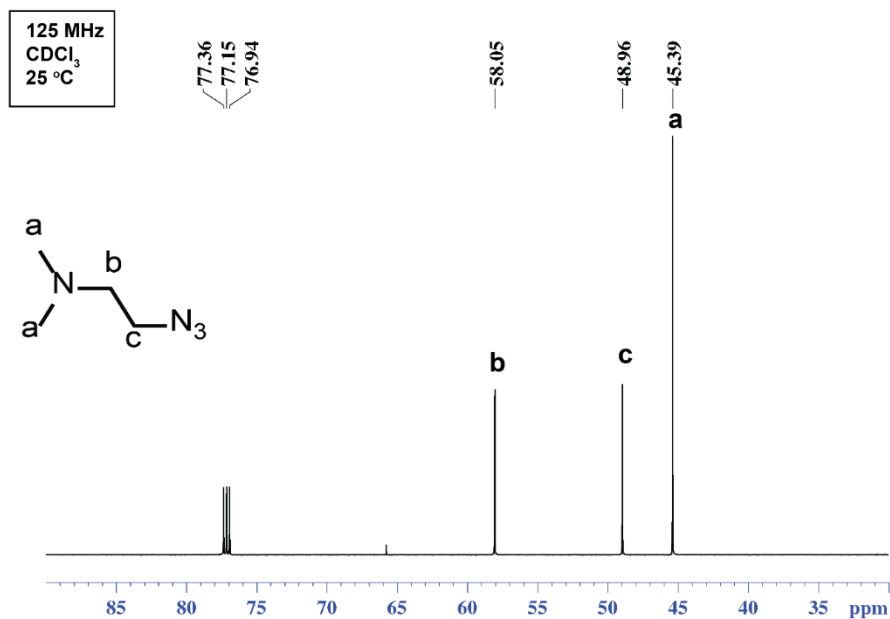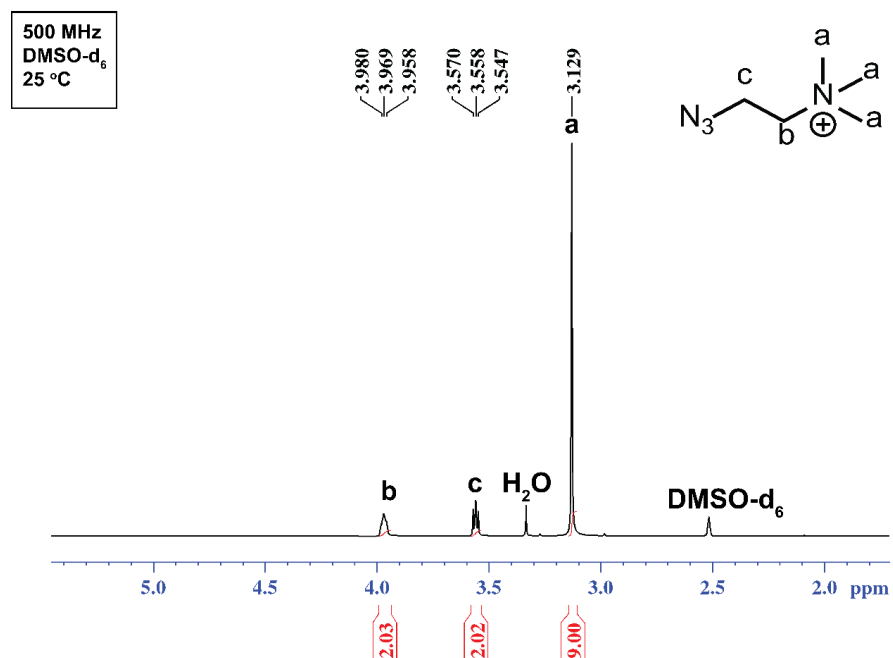

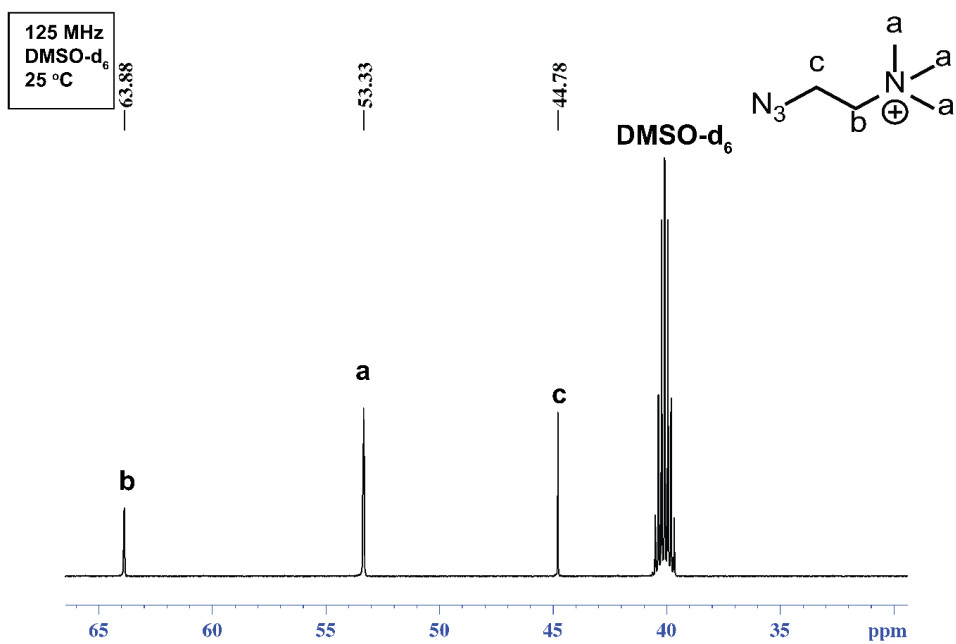Figure D2. ^{13}C- NMR of 2-azido-N,N-dimethylethylamine

Figure D3. ^{1}H- NMR of 1C

Figure D4. ^{13}C-NMR of 1C
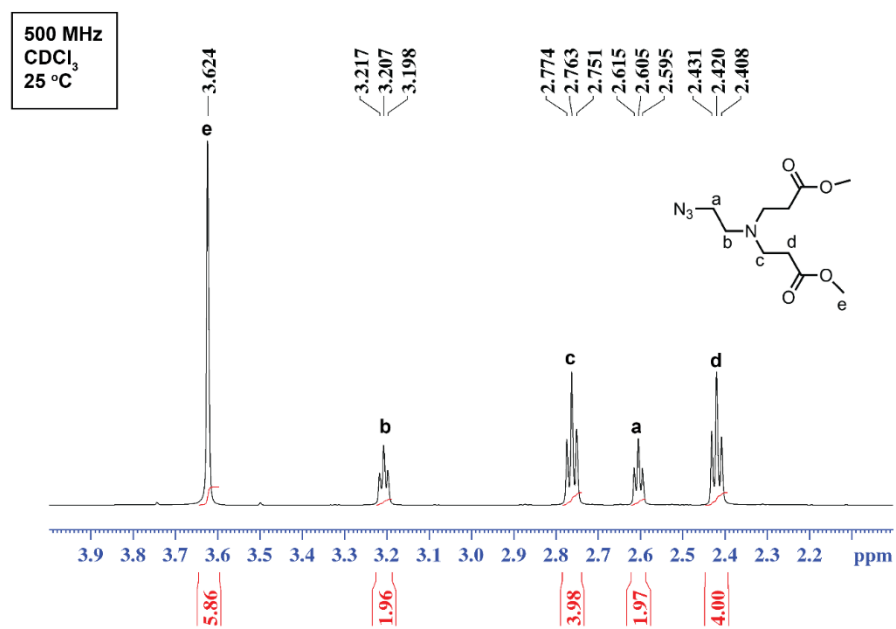
Figure D5. ^{1}H- NMR of PAMAM-D$_0$
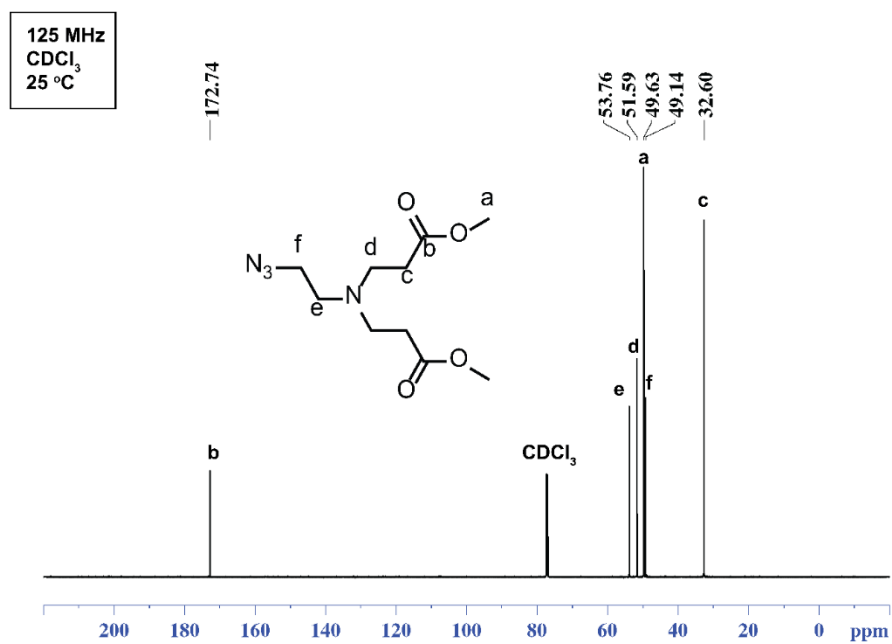
Figure D6. ^{13}C- NMR of PAMAM-D$_0$

197
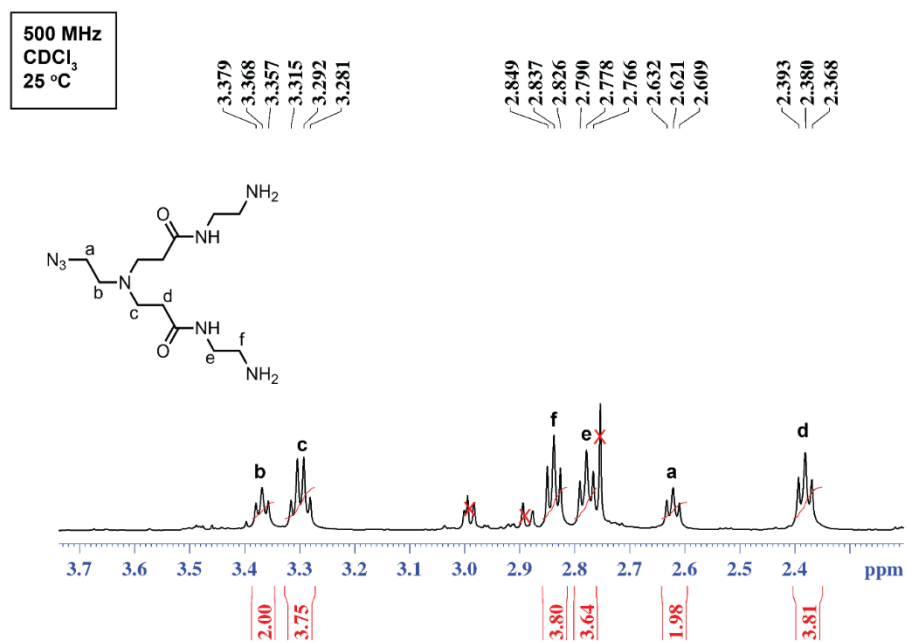
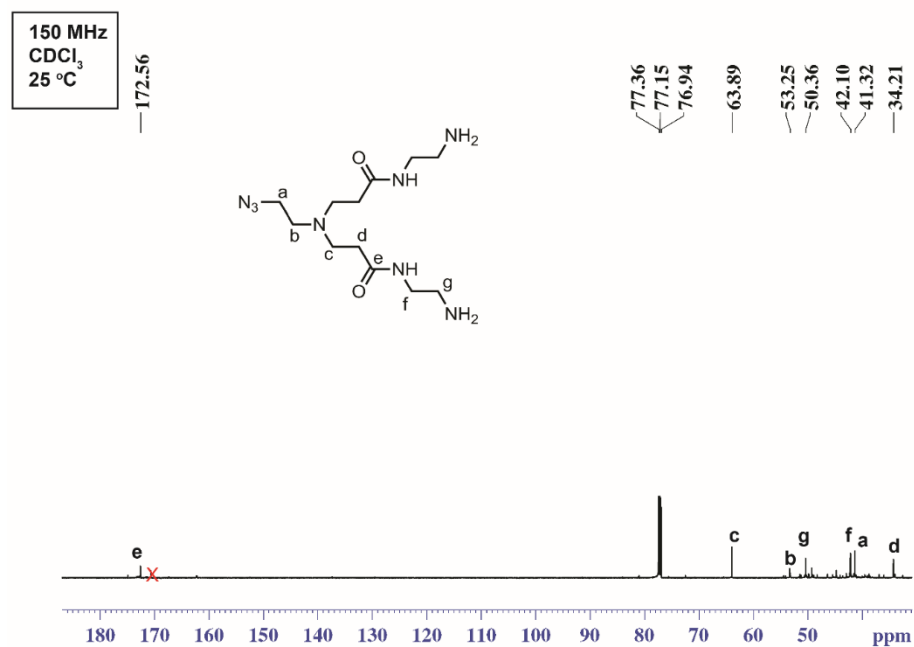Figure D7. ^{1}H- NMR of PAMAM-D$_{0.5}$

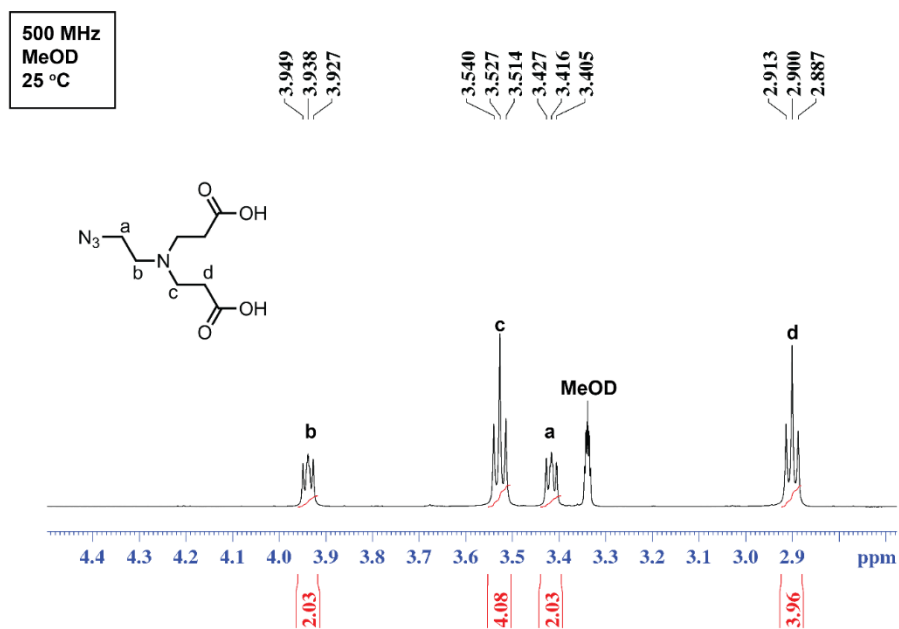Figure D8. ^{13}C- NMR of PAMAM-D$_{0.5}$

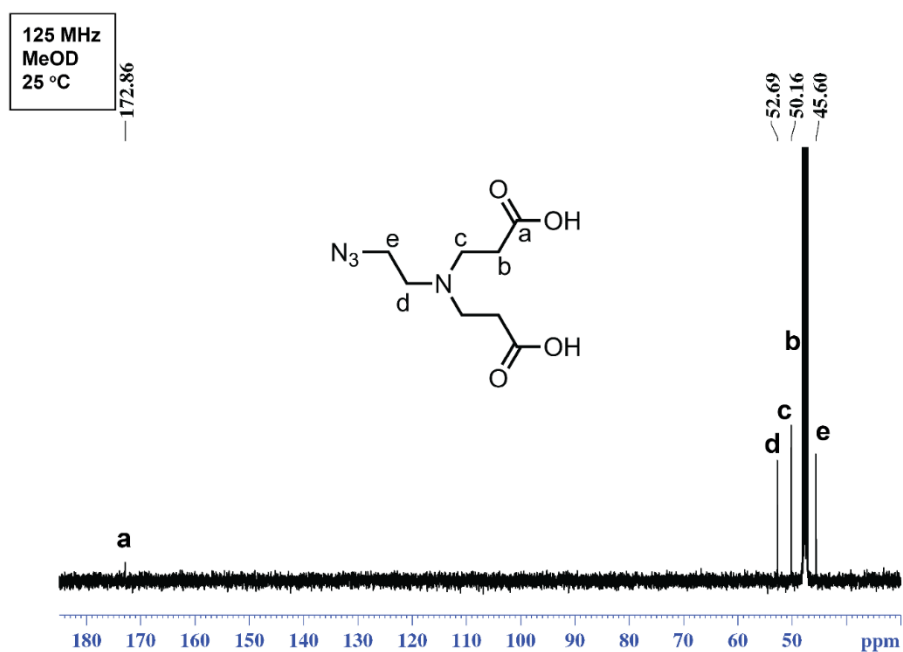Figure D9. ^{1}H- NMR of 2A
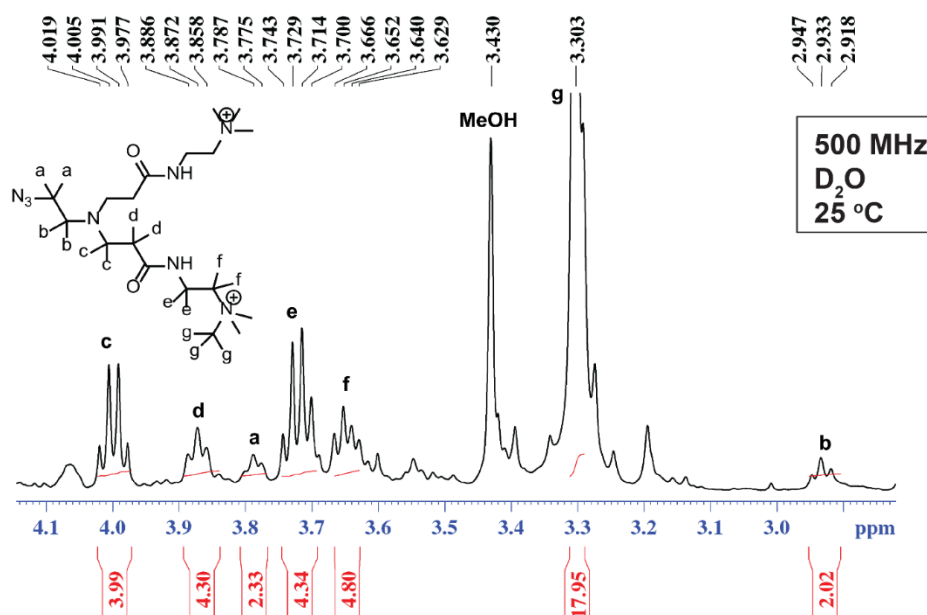

Figure D10. ^{13}C- NMR of 2A

Figure D11. ^{1}H- NMR of 2C
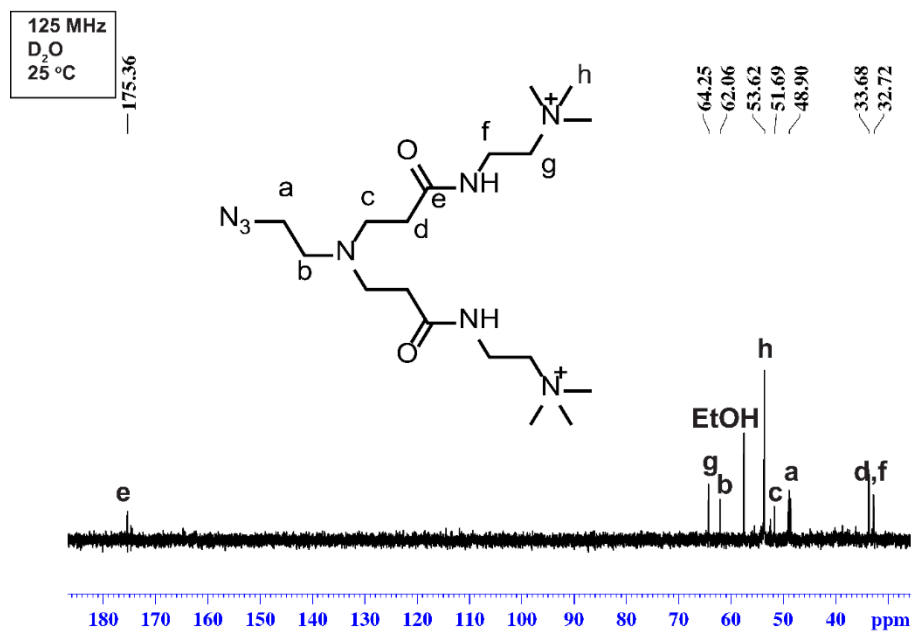
Figure D12. ^{13}C- NMR of 2C
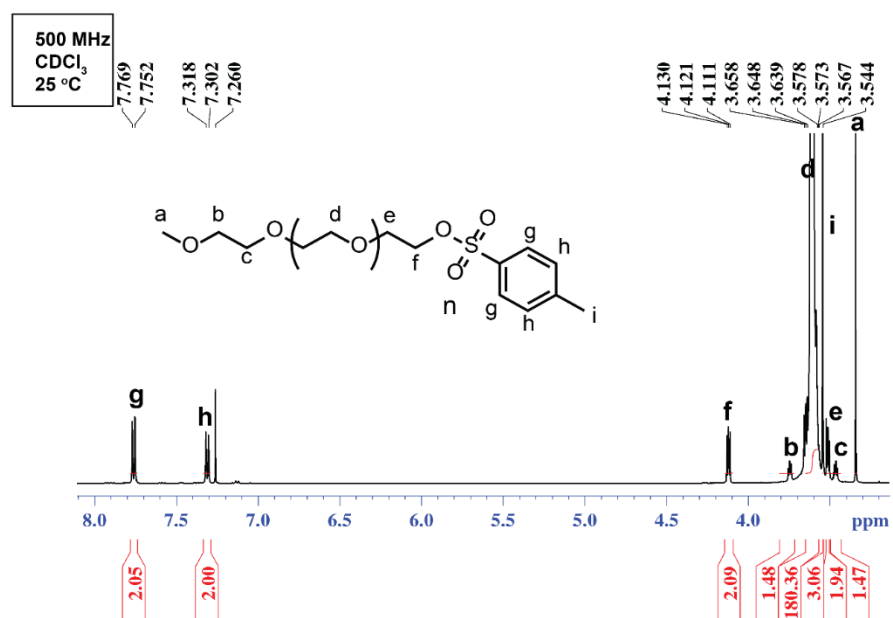
Figure D13. ^{1}H- NMR of PEG-OTs
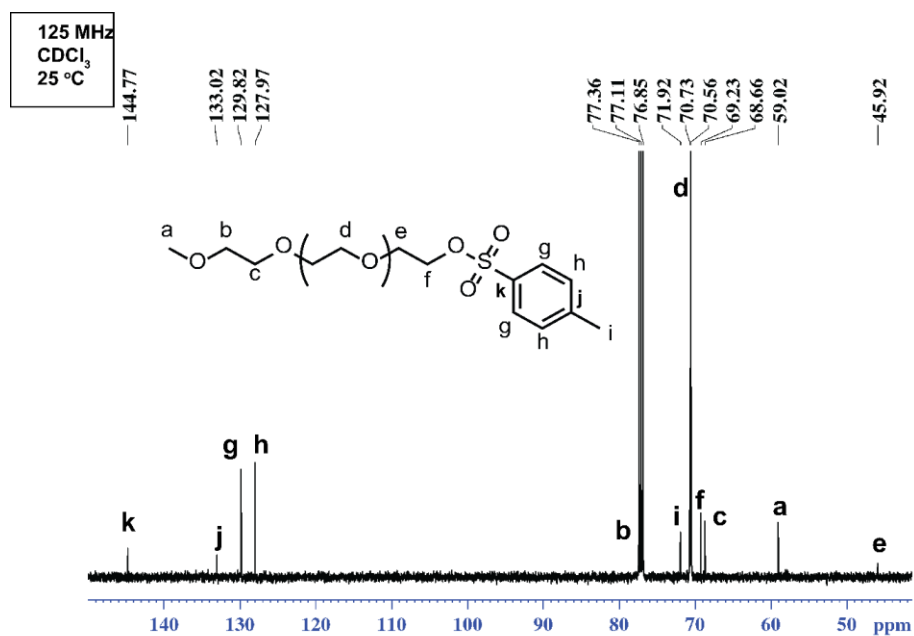
Figure D14. ^{13}C- NMR of PEG-OTs
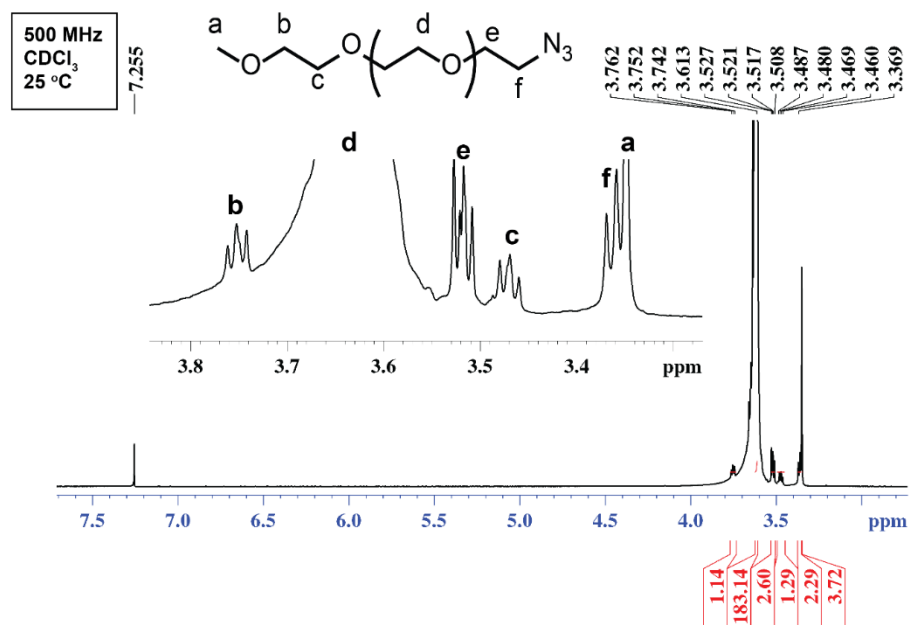
Figure D15. ^{1}H- NMR of PEG-N$_3$
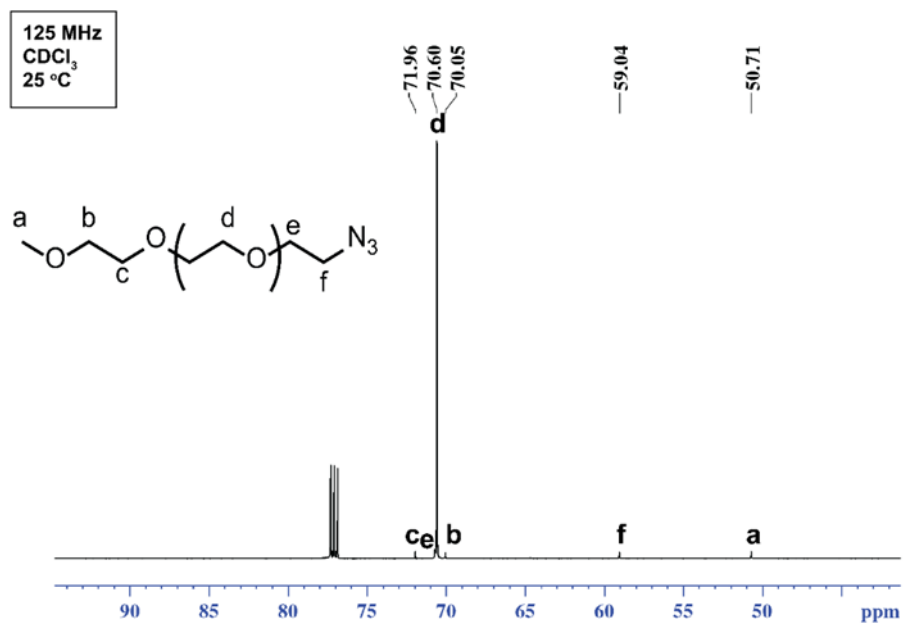
Figure D16. ^{13}C- NMR of PEG-N$_3$
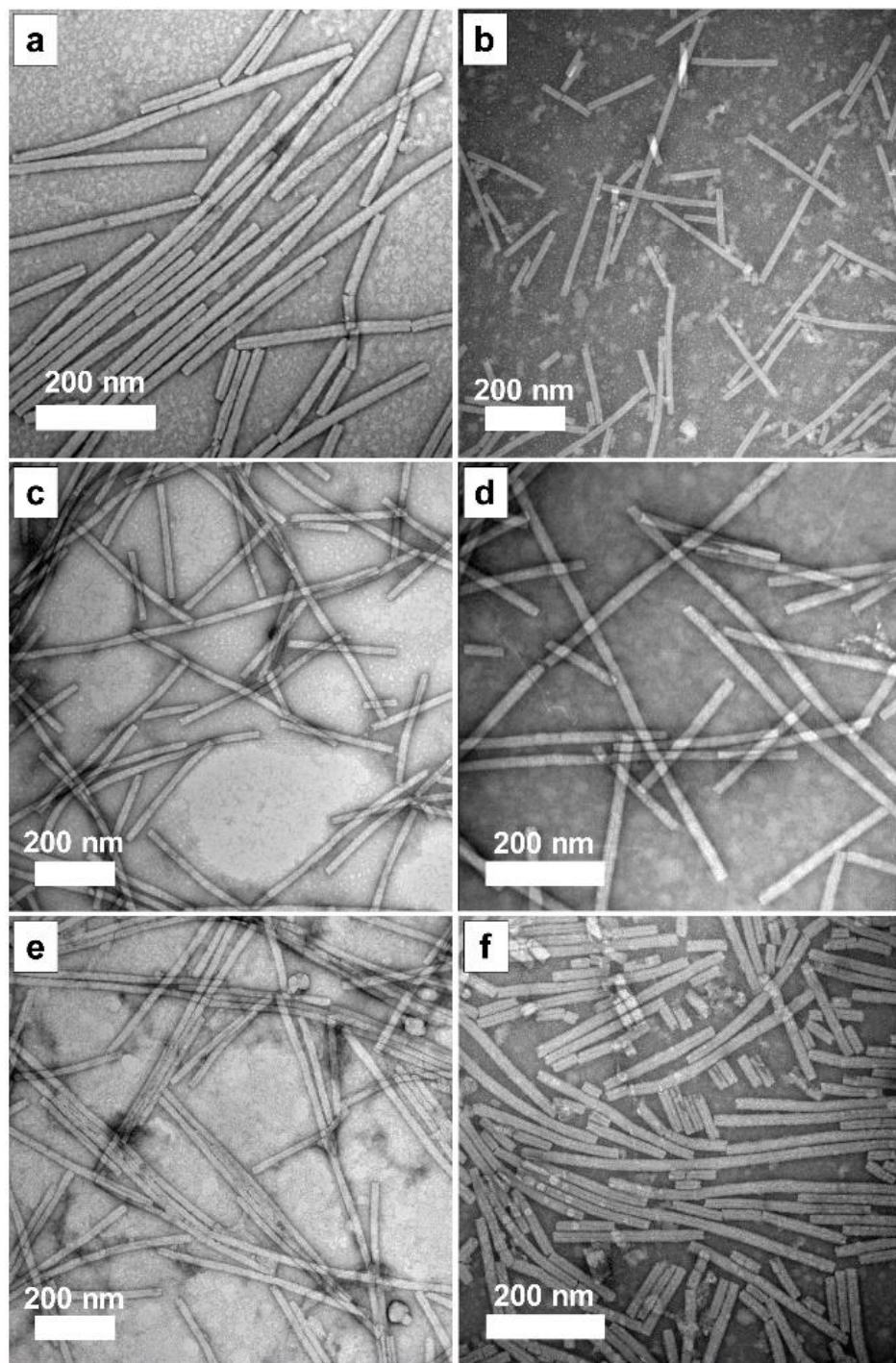
Figure D17. TEM images of TMV conjugates; a) native-TMV; b) *ex*PEG-TMV; c) *ex*1A- TMV
d) *ex*2A-TMV; e) *ex*1C- TMV; and f) *ex*2C-TMV.

BIOGRAPHICAL SKETCH

Madushani Dharmarwardana was born in 1985 in Kandy, Sri Lanka. She obtained her bachelor's degree in Chemistry (Hons) from The University of Peradeniya, Sri Lanka in 2009. Then she joined The University of Peradeniya as an undergraduate teaching assistant in September 2009. In 2011, she began working in a high school as a chemistry teacher. After two years of teaching, she decided to continue her graduate studies in the United States of America. In 2013, she joined The University of Texas at Dallas to pursue her PhD in Chemistry under the supervision of Dr. Jeremiah J. Gassensmith.

CURRICULUM VITAE

MADUSHANI DHARMARWARDANA

EDUCATION

Candidate for Doctor of Philosophy in Chemistry (Expected August 2018)
University of Texas at Dallas, Richardson, TX, USA
Advisor: Professor Jeremiah. J. Gassensmith

Bachler of Science (Honors) in Chemistry (2009)
University of Peradeniya, Sri Lanka
Advisor: Dr. V.N. Senevitane
Honors Thesis Title: "Chemistry of demethylacrovestone from *Acronychia Pedunculata* fruits"

RESEARCH EXPERIENCES

University of Texas at Dallas, Aug 2013 - Present
Department of Chemistry and Biochemistry; Research Advisor: Professor Jeremiah. J. Gassensmith
Graduate student studying properties of contrast agent/NIR dye modified biomacromolecules for the applications in MRI/EPR and NIR imaging. The focus of this project is to use Tobacco Mosaic Virus (TMV) as a functional scaffold for MRI/EPR contrast agents and NIR dyes for *in vivo* MRI and NIR imaging. Other projects involve studying organic soft materials for the applications in organic electronics devices and sensors. The focus of this project is to study the stimuli responsive behavior of single crystalline Naphthalene Diimdies (NDIs) derivatives.

University of Peradeniya, March 2011 - Oct 2011
Department of Chemistry, Sri Lanka; Advisor: Dr. Champika Hettiarachchi
Worked as a researcher on synthesis and characterization of thermochromic fulgides for memory devices.

University of Peradeniya, Aug 2008 - Aug 2009
Department of Chemistry, Sri Lanka; Advisor: Dr. V.N. Senevitane
Undergraduate Researcher worked on isolation, modification and bioactivity of natural products from *Acronychia Pedunculata* fruits. Isolated natural products were characterized by NMR and GC-MS. Pure natural products were tested for antifungal and antibacterial activity.

Vortex Lanka PVT Limited, Sri Lanka, June 2008 - Aug 2008
Research internship on paint development and optimization of existing paint formulations.
PEER-REVIEWED PUBLICATIONS

1. **Dharmarwardana, M.;** Martins, A. F.; Chen, C.; Palacios, P. M.; Novak, C.; Welch, R. P.; Li, S.; Luzuriaga, M. A. Bleris, L.; Pierce, B. S.; Sherry, A. D.; Gassensmith, J. J. "Nitroxyl Modified Tobacco Mosaic Virus as a Metal-Free High-Relaxivity MRI and EPR Active Superoxide Sensor". *Mol. Pharm.* **2018**, Just Accepted. *Invited article in honor of Prof. M.G. Finn.*
2. Lee, H.; Benjamin C. E.; Nowak, C. M.; Tuong, L. H.; Welch, R. P.; Chen, Z.; **Dharmarwardana**, **M**.; Murray, K. W.; Bleris, L.; D'Arcy, S.; Gassensmith, J. J. Regulating the Uptake of Viral Nanoparticles in Macrophage and Cancer Cells by a pH Switch. *Mol. Pharm.* **2018**, Just Accepted. *Invited article in honor of Prof. M.G. Finn.*
3. S. Li, **M. Dharmarwardana**, R. P. Welch, C. E. Benjamin, A. M. Shamir, S. O. Nielsen, J. J. Gassensmith "Investigation of Controlled Metal Organic Frameworks on Anisotropic Virus Particles." *ACS Appl. Mater. Interfaces*, **2018**, Accepted. *Selected to be on the Cover*
4. **M. Dharmarwardana**, R. P. Welch, S. Kwon, V. K. Nguyen, G. T. McCandless, M. A. Omary, J. J. Gassensmith "*Thermo-Mechanically Responsive Crystalline Organic Cantilever.*" *Chem. Commun.* **2017**, *53*, 9890–9893. Featured in *Chemistry World* (Sept 11, 2017)
5. Li, S.; **Dharmarwardana, M.**; Welch, R. P.; Ren, Y.; Thompson, C. M.; Smaldone, R. A.; Gassensmith, J. J. "Template-Directed Synthesis of Porous and Protective Core–Shell Bionanoparticles." *Angew. Chem.* **2016**, *55*, 10691–10696.
6. Chen, Z.; Li, Na.; Li, S.; **Dharmarwardana, M**.; Schlimme, A.; Gassensmith, J.J. "Dual Functionalized Bacteriophage Qβ as a Photocaged Drug Carrier." *WIREs Nanomed. Nanobiotechnol.* **2016**, *8,* 512–534.

SUBMITTED MANUSCRIPTS AND MANUSCRIPTS IN PREPARATION

1. **Dharmarwardana, M**.; Bhargav, A. S.; Luzuriaga, M. A.; Lee, H.; McCandless, G. T.; Appuhamillage, G. A.; Smaldone, R. A.; Gassensmith, J.J. "Thermochromic, Thermo-mechanical and Colossal Anisotropic Thermal Expansion Behavior of Alkoxyphenyl N-substituted Naphthalene Diimdies" *Invited article for CrystEngComm 2018: New Talent themed issue. Submitted.*
2. **Dharmarwardana, M.**; Ghimire, M. T.; Fallah, H.; Kapia, U.; Bhargav, A. S.; McCandless, G. T.; Omary, M. A.; Cundari, T. R; Gassensmith, J.J. "Colossal Anisotropic Thermal Expansion and Thermochromism in a Single Crystal Organic Semiconductor: An Interrelated Structural, Photophysical, and Computational Study." Manuscript in preparation.
3. Welch, R. P.; Luzuriaga, M. A.; **Dharmarwardana, M.**; Li, S.; Ramos, J.; Gassensmith, J. J "Enhance d stability of MOF encapsulated vaccine and immunogenic response *in vivo*. Manuscript in preparation.

MEETING AND CONFERENCES

1. **M. Dharmarwardana,** A. F. Martins, Z. Chen, P. M. Palacios, C. M. Novak, R. P. Welch, S. Li, M. A. Luzuriaga, L. Bleris, B. S. Pierce, A. D. Sherry, J. J. Gassensmith, contributed poster on "*Nitroxyl Modified Tobacco Mosaic Virus as a Metal-Free High-Relaxivity MRI and EPR Active Superoxide Sensor*". Annual symposium on Imaging Metabolism in Brain Disease, UT Southwestern Medical Center, Dallas, TX, USA. January 31 - February 1, **2018.**

2. B. S. Arimilli, **M. Dharmarwardana**, G. T. McCandless, J. J. Gassensmith. Contributed lecture on "*Investigating the Thermochromic Properties of Single Crystal Naphthalene Diimide Derivatives.*" Gulf Coast Undergraduate Research Symposium, Rice University, Houston, TX, USA. November 4, **2017**.

3. **M. Dharmarwardana**, R. P. Welch, S. Kwon, V. K. Nguyen, G. T. McCandless, M. A. Omary, J. J. Gassensmith "*Thermo-Mechanically Responsive Crystalline Organic Cantilever.*" Texas Soft Matter Conference, Houston, TX, USA. August 18, **2017.**

4. S. Li, **M. Dharmarwardana**, R. Welch, M Luzuriaga, J. J. Gassensmith. Poster on *"MOF Vaccines: Toward Storage and Delivery of Biological Agents."* The GRC on Nanoporous Materials & Their Applications, Andover, NH, USA. August 6–10, **2017**.

5. **M. Dharmarwardana**, R. P. Welch, S. Kwon, V. K. Nguyen, G. T. McCandless, M. A. Omary, J. J. Gassensmith "*Thermo-Mechanically Responsive Crystalline Organic Cantilever.*" ACA 67th Annual Meeting, New Orleans, LA, May 26-30, **2017**.

6. **M. Dharmarwardana,** M. T. Ghimire, H. Fallah, U. Kapia, A. S. Bhargav, G. T. McCandless, O. M. Omary, T. R. Cundari, J. J. Gassensmith. Contributed poster on "*Colossal Anisotropic Thermal Expansion and Thermochromism in a Single Crystal Organic Semiconductor.*" FNANO Annual Meeting, Snowbird, UT, April 9-13, **2017**.

7. **Dharmarwardana, M**.; Ghimire, M. T.; Fallah, H.; Kapia, U.; Bhargav, A. S.; McCandless, G. T.; Omary, M. A.; Cundari, T. R; Gassensmith, J.J. **Contributed** Lecture on "*Solid-State Thermochromism in a Single Crystal Organic Semiconductors.*" Texas Soft Matter Annual Meeting, Dallas, TX, USA. August 12, **2016**.

8. **M. Dharmarwardana**, J. J. Gassensmith, **Invited** lecture on "Single Crystal Investigation of Thermochromic Organic Semiconductor Butoxyphenyl N-Substituted Naphthalene Diimide" in the Etter Early Career symposium at ACA Annual Meeting, Denver, CO, USA. July 22-26, **2016**.

9. **M. Dharmarwardana**, S. Li, J. J. Gassensmith, **Contributed** Lecture on "*TMV-dendrimer Bottlebrush Conjugates.*" ACS National Meeting, Boston, MA, USA. August 16-20, **2015**.

10. **M. Dharmarwardana**, J. J. Gassensmith, **Contributed** Poster on "*The Synthesis and Study of the Properties of π–acidic Naphthalene diimides as a Catalytic Agent for Inverse Electron Demand Hetero–Diels Alder Reactions.*" <u>ACS Southwest Regional Meeting</u>, Fort Worth, TX, USA. November 19-22, **2014**.

AWARDS, SCHOLARSHIPS, AND FELLOWSHIPS

1. Etter Student Lecture award, ACA National Meeting (2017)
2. University of Texas at Dallas "Betty and Gifford Johnson Scholarship award" (2017)
3. Invited speaker at the Etter Early Career symposium at ACA Annual Meeting, Denver, CO. (2016)
4. Cambridge Crystallographic Data Centre (CCDC) Travel Award to attend the American Crystallographic Association's Annual meeting in Denver, CO. (2015 - 2016)
5. University of Texas at Dallas Vice President of Research Travel Grant (2014 - 2015)
6. University of Texas at Dallas Graduate Studies Scholarship (2013 - Present)

PROFESSIONAL MEMBERSHIPS
American Chemical Society
American Crystallographic Association
Sigma Xi

TECHNICAL PROFICIENCY
Chemical methods
Organic synthesis, Cell techniques, Chromatographic methods, Organic semiconducting device fabrication

Instrumentation Methods
Atomic Force Microscopy, DSC, EPR, ESI-MS, FT-IR spectroscopy, Fluorescence spectroscopy, GC-MS, HPLC, MALDI-TOF, NMR spectroscopy (1D, 2D), Single crystal and powder X-ray diffraction, SQUID, SEM, TGA, UV-Vis, spectroscopy, Fluorescence spectroscopy, Confocal microscopy

Computer/ IT
Adobe Illustrator, Chemdraw, Computational chemistry program, Microsoft office (Word, Excel, PowerPoint), Origin, Web MO

TEACHING EXPERIENCES
Teaching Assistant for CHEM 3471 "Advance Synthesis Laboratory" Aug 2016 - Dec 2016
University of Texas at Dallas, Professor Jeremiah J. Gassensmith
Teaching Assistant for CHEM 1112 & 1111 "General Chemistry Laboratory" Aug 2013 - Aug 2014
University of Texas at Dallas

High school Chemistry Teacher, Oct 2012 - June 2013
Ranasinghe Premadasa National School, Hasalaka, Sri Lanka
High school Chemistry Teacher, Oct 2011 - Oct 2012
Lyceum International School, Nuwara Eliya, Sri Lanka
Undergraduate Teaching Assistant, Sept 2009 - March 2010
Department of Chemistry, University of Peradeniya, Sri Lanka

REFERENCES

Dr. Jeremiah J. Gassensmith
Assistant Professor
University of Texas at Dallas
Office: 972-883-3596
Email: jjg130230@utdallas.edu

Dr. John Sibert
Associate Professor
University of Texas at Dallas
Office: 972-883-2918
Email: sibertj@utdallas.edu

Dr. Ronald A. Smaldone
Assistant Professor
University of Texas at Dallas
Office: 972-883-2901
Email: ras120030@utdallas.edu